January 2016

Exploring the Mechanistic Landscape of Nitric Oxide Oxidation and Ammonia Selective Catalytic Reduction of Nitric Oxide on Cu-Zeolites via Kinetic and Spectroscopic Characterization

Atish A. Parekh
Purdue University

Recommended Citation

Parekh, Atish A., "Exploring the Mechanistic Landscape of Nitric Oxide Oxidation and Ammonia Selective Catalytic Reduction of Nitric Oxide on Cu-Zeolites via Kinetic and Spectroscopic Characterization" (2016). *Open Access Dissertations*. 1266.
https://docs.lib.purdue.edu/open_access_dissertations/1266

Graduate School Form
30 Updated 12/26/2015

PURDUE UNIVERSITY
GRADUATE SCHOOL
Thesis/Dissertation Acceptance

This is to certify that the thesis/dissertation prepared

By Atish A. Parekh

Entitled

Exploring the Mechanistic Landscape of Nitric Oxide Oxidation and Ammonia Selective Catalytic Reduction of Nitric Oxide on Cu-Zeolites via Kinetic and Spectroscopic Characterization

For the degree of Doctor of Philosophy

Is approved by the final examining committee:

Prof. Fabio H. Ribeiro Co-chair	Dr. Aleksey Yezerets
Prof. W. Nicholas Delgass Co-chair	
Prof. Jeffrey P. Greeley	
Prof. Jeffrey T. Miller	

To the best of my knowledge and as understood by the student in the Thesis/Dissertation Agreement, Publication Delay, and Certification Disclaimer (Graduate School Form 32), this thesis/dissertation adheres to the provisions of Purdue University's "Policy of Integrity in Research" and the use of copyright material.

Approved by Major Professor(s): Prof. Fabio H. Ribeiro

Approved by: Prof. John A. Morgan 5/7/2016

Head of the Departmental Graduate Program Date

EXPLORING THE MECHANISTIC LANDSCAPE OF NITRIC OXIDE OXIDATION AND AMMONIA SELECTIVE CATALYTIC REDUCTION OF NITRIC OXIDE ON CU-ZEOLITES VIA KINETIC AND SPECTROSCOPIC CHARACTERIZATION

A Dissertation
Submitted to the Faculty
of
Purdue University
by
Atish Anil Parekh

In Partial Fulfillment of the
Requirements for the Degree
of
Doctor of Philosophy

August 2016
Purdue University
West Lafayette, Indiana

ACKNOWLEDGEMENTS

First and foremost, I would like to thank my advisors, Prof. Fabio H. Ribeiro and Prof. W. Nicholas Delgass. They have been the pillars of my success throughout graduate school, pushing me to achieve my best under all circumstances. I am grateful to them for their guidance and advice all along right from when I started out as a fledgling new graduate student. They always had my best interest in mind, have instilled an impeccable work ethic in me and helped me develop as a researcher. I consider Prof. Jeffrey T. Miller, who is not formally my research advisor, as my co-advisor. I owe him a lot in terms of professional growth in graduate school. He was the one who always taught me to expand my horizon and look at the bigger picture to put things into perspective first before diving into the details of any work. His analogy, “Look outside the window and tell me if it is day or night” will serve as a valuable lesson throughout my life. He has spent countless hours helping me set up the beamline at Argonne National Laboratory, and teaching the principles and interpretation of results from the x-ray absorption spectroscopy experiments. Every time I sat down with him and discussed ideas, I came out with a clear picture and a plan of action. During our conversations, it seemed so easy to distill everything down to the bare minimum that allowed organization of ideas in a logical manner.

I would like to thank Prof. Rajamani Gounder for the several fruitful discussions during and beyond the NO_x group meetings because of which several experiments performed during my PhD were planned to the minutest detail. His diligence and attention to detail for experimental results and their interpretation and especially, during writing and organizing manuscripts is something that I will always aspire to achieve. Whenever I spoke with him I couldn’t help but realize the idea machine that he really is.

I would like to thank Dr. Aleksey Yezerets deeply for devoting his precious time to serve as a member of my thesis committee and contributing a unique and industrial perspective towards approaching the several challenges in research. It is intriguing that he can seemingly and almost instantly come up with several different ways of looking at the same idea or framing the same question in different ways. I would also like to acknowledge the ideas that came out of the discussions with Dr. Krishna Kamasamudram, Dr. Ashok Kumar and their colleagues during the quarterly meetings with Cummins, Inc.

I have thoroughly enjoyed the stimulating collaboration with Prof. William F. Schneider and his research group at the University of Notre Dame. His insights into the chemistry involved in several reaction sequences always posed challenging questions, which further deepened my understanding and led to refinement of the ideas I proposed. I would like to acknowledge Dr. Yury Zvinevich’s efforts and help on various occasions. Several of the problems I faced in the lab would have taken much longer to resolve without his expertise in multiple areas related to instrumentation. Finally, I would like thank Prof. Jeffrey Greeley for serving as a valuable member on my thesis committee, and his suggestions during the Purdue catalysis center meetings.

I have had the pleasure of working closely with Christopher Paolucci from Prof. William F. Schneider’s group. His understanding of the experiments, marrying it with his own molecular level understanding of the details and persistence on extracting the maximum information out of the existing experimental results always reminded me of the rigor in his approach, and is truly an inspiration going forward. I would like to thank former and current NO_x group members Dr. Vincent F. Kispersky, Dr. Shane A. Bates, Dr. Anuj A. Verma, Jonatan Albarracin, Arthur Shih and Ishant Khurana. Two people that stand out are Dr. Paul J. Dietrich, whom I badgered for help several times with issues related to the beamline, and Viktor J. Cybulskis for his help during the numerous trips to Argonne National Laboratory. Other people that I have had the pleasure of working and interacting with during my graduate career include Dr. Fred Sollberger, Dr. Wen-Sheng Lee, Dr. Michael Detwiler, Dr. Amir Gharachorlou, Dr. Nathan Carter, Dr. Mayank Shekhar, Dr. Sara Yohe, Dr. Vinod Venkatakrishnan, Dr. Zhenglong Lee, Dr. Jun Wang, Jamie Harris, Dr. James Gallagher, Dr. Guanghui Zhang, John R. Di Iorio, Hui Li, McKay Easton, Dr. John Degenstein, Dr. Trunojoyo Anggara and Han-Ting Tseng.

I would like to take this opportunity to thank the following people who have helped me with logistics and business related questions throughout graduate school: Jeffrey Valley, Jason Davenport, Courtney Eddy, Michael Harrington, Amy Hayden, Debra Bowman, Catherine Field, Cristina Farmus, Jenny Olinger, Corwin Green and Beverly Johnson.

I would like to express gratitude towards my colleagues Parth Panchmatia, Ashish Vora, Sumeet Thete, Shankali Pradhan, Vishrut Garg, Gautham Ramapriya, Dr. Krishnaraj Sambath, Dr. Karthikeyan Marimuthu, Dr. Anand Venkatesan, Dr. Vishesh Shah and Dr. Anirudh Shenvi. I am forever indebted to Dr. Kaiwalya D. Sabnis, Dr. Aniruddha V. Kelkar, Dr. Anshu Gupta, Dr. Harshavardhan J. Choudhari, Dr. Dhairya D. Mehta who have kept me sane throughout graduate school, and have been part of the several social outings, including playing cricket near the co-rec.

I also interacted with several immensely talented individuals through participation in various student organizations during my stay at Purdue – Purdue Taal, Vertigo42, Indian Classical Musical Association of Purdue (ICMAP), Chemical Engineering Graduate Student Organization (ChE GSO) and ASHA for Education. I will always cherish those special memories for the rest of my life. Special shout out to Vignesh Gouthaman, Aditya Chandramohan, Chetas Joshi, Sahaana Mukundan and Nishtha Sinha for the late night meals at Chauncey Hill, and the discussions and drives that followed.

Lastly and most importantly, I would like to thank my parents and family in India whose relentless support has helped me endure difficult times in graduate school. It was a huge comfort and relief to know that they were always present and stood by me regardless of any difficulties that I faced here. It is solely because of my parents that I have reached this far today.

TABLE OF CONTENTS

Page

APPENDICES

LIST OF TABLES

Table Page

Appendix Table Page

LIST OF FIGURES

Figure Page

Figure Page

Appendix Figure Page

Appendix Figure Page

ABSTRACT

Parekh, Atish A. Ph.D., Purdue University, August 2016. Exploring the Mechanistic Landscape of Nitric Oxide Oxidation and Ammonia Selective Catalytic Reduction of Nitric Oxide on Cu-Zeolites via Kinetic and Spectroscopic Characterization. Major Professors: Fabio H. Ribeiro and W. Nicholas Delgass

Increasingly stringent regulations to reduce emissions of nitrogen oxides (NO_x) from exhausts of heavy-duty diesel engines has set the stage to delve into a detailed investigation of engine after-treatment catalysts in order to understand the chemistry during their operation and design the next generation of catalytic formulations to meet future requirements. Small-pore Cu- and Fe-exchanged SSZ-13 catalysts with chabazite (CHA) topology are able to sustain high catalytic rates for selective catalytic reduction (SCR) even after exposure to harsh hydrothermal conditions present in diesel exhaust. Probing the redox behavior and the active site requirements for standard SCR on Cu-SSZ-13 catalysts using a combination of infrared (FTIR) and x-ray absorption (XAS) spectroscopies, kinetic measurements and density functional theory (DFT) calculations forms the basis for this dissertation.

The effect of each standard SCR reactant (NO, NH_3 and O_2) on the Cu(I)-Cu(II) redox chemistry and the reaction rates was studied via steady state *operando* XAS experiments. Systematically changing the feed concentration of one of the NO, NH_3 and O_2 reactants at a time showed that while NH_3 and O_2 participated in the reduction of Cu(II)

to Cu(I) and re-oxidation of Cu(I) to Cu(II), respectively, NO was involved in both parts of the redox cycle. Together, NO and NH_3 acted as the co-reductants (473 K) for Cu(II) to Cu(I) reduction via the NO assisted dissociation of a N-H bond in a Cu-bound NH_3 molecule, while the combination of NO and O_2 (473 K) completed the catalytic cycle re-oxidizing Cu(I) to Cu(II).

We studied the re-oxidation of Cu(I) to Cu(II) in the standard SCR mechanism by O_2 and NO_2 titration experiments. Two Cu-SSZ-13 catalysts with the same Cu:Al ratio (0.08-0.09) and structurally equivalent exchanged Cu^{2+} ions charge-compensated by a pair of framework Al atoms but different Si:Al ratio (4.5, 15) were reduced with NO and NH_3 (473 K) to Cu(I). Following this reduction, both catalysts were oxidized either in 10% O_2 or 90 ppm NO_2 under isothermal conditions. Oxidation with O_2 followed second order kinetics in the instantaneous Cu(I) fraction for both catalysts, suggesting the involvement of two Cu(I) moieties for O_2 oxidation. Further, a smaller second order rate constant (1.79 min^{-1}) and a greater final Cu(I) fraction (0.26) for the low Al (Si:Al = 15) catalyst compared to the corresponding values (8.16 min^{-1} and 0.15) for the high Al (Si:Al = 4.5) catalyst implied an underlying dependence of the Cu(I) oxidation with O_2 on the Al distribution and hence, the proximity of Cu ions. In contrast, oxidation with NO_2 was a first order process with identical rate constants of 0.8 min^{-1} for both catalysts, demonstrating that NO_2 oxidation was independent of the Al distribution or Cu proximity, and occurred on isolated Cu(I) ions. Thus, standard SCR, which involves oxidation with O_2, is limited by the pairing ability of Cu ions at dilute Cu or Al contents and hence, controlled by the oxidation half-cycle. Fast SCR, on the other hand, proceeds via oxidation with NO_2, engaging all the Cu ions in the catalyst independent of its location or concentration within the zeolite.

Additionally, a second type of isolated Cu species, $[CuOH]^+$ ions charge-compensated at isolated Al sites, are exchanged in catalysts with dilute Al contents (i.e. high Si:Al) following the saturation of paired Al sites with Cu^{2+} ions, which are thermodynamically preferred over isolated Al sites during Cu ion exchange. NH_3 titration differentiated between the two sites and showed that two protons were replaced per exchanged Cu^{2+}, whereas one proton was replaced per exchanged $[CuOH]^+$ ion. Further, reduction of each Cu^{2+} generated an additional proton, whereas $[CuOH]^+$ ions did not generate extra protons. FTIR spectra on a series of samples with Si:Al = 15 detected the O-H vibration associated with $[CuOH]^+$ ions at 3651 cm^{-1}, and showed a quantitative increase in its peak area with Cu loading beyond the saturation limit of Cu^{2+} (Cu:Al = 0.1, Si:Al = 15). *In situ* oxidizing (20% O_2, 673 K) or reducing (He, 673 K or 3.5% H_2, 523 K) treatments for two representative samples consisting of exclusively Cu^{2+} or predominantly $[CuOH]^+$ (i.e. 80% of the total exchanged Cu) ions exposed differences in their chemical behavior and showed that $[CuOH]^+$ ions are more reducible compared to Cu^{2+}. The two Cu species, however, are indistinguishable for low temperature (473 K) standard SCR catalysis based on the measured apparent kinetics (E_{app}, apparent orders for NO, NH_3, O_2 and turnover rates per Cu), steady state Cu(I)-Cu(II) fractions from *operando* XAS spectra and DFT energetics for the standard SCR pathway on both sites when operating in a kinetic regime that is not limited by the re-oxidation of Cu(I) to Cu(II). DFT calculations rationalized these observations by showing that solvation of Cu by NH_3 under reaction conditions nullified the differences between the two types of Cu species.

The importance of nitrates for the oxidation of NO by O_2 on Cu-ZSM-5 under dry conditions was determined in a separate study using steady state isotope transient kinetic

experiments in a custom-designed *operando* FTIR reactor. Three different nitrate peaks at 1626 cm^{-1}, 1601 cm^{-1} and 1567 cm^{-1} were observed under steady state dry NO oxidation conditions. Simultaneous monitoring of the surface nitrates using FTIR and the reactor effluent using mass spectrometer (MS) showed that NO_2 was produced from the decomposition of surface nitrates by NO. ^{15}NO labeling experiments confirmed that NO and NO_2 were in quasi-equilibrium through nitrates on the catalyst surface, and suggested that the bridged/bidentate nitrate at 1626 cm^{-1} is a likely intermediate for dry NO oxidation on Cu-ZSM-5.

CHAPTER 1. INTRODUCTION

1.1 NO_x Emissions and Control Strategies

The environmental protection agency (EPA) introduced national air quality standards for NO_x, SO_x, CO, unburnt hydrocarbons, photochemical oxidants and particulate matter for the first time in 1971 [1]. The regulatory requirements for each of these classes of pollutants have become more stringent since then in an effort to limit the pollution levels and protect public health and the environment from smog and acid rain [2-4]. Diesel is used for long distance transportation mainly because of the fuel economy advantage it offers over gasoline – powered vehicles [5, 6], especially under lean conditions. i.e. greater than air to fuel stoichiometric ratio. However, the combustion process leads to NO_x emissions from exhausts of lean burn diesel – powered engines on highways, which are a major concern. Figure 1.1.1 shows that combustion of fossil fuels in automobiles contribute to more than half of the total NO_x pollution [7, 8]. Figure 1.1.2 shows the NO_x emission requirements set by the EPA over the past few decades to mitigate this problem. Several strategies such as engine management and combustion control that have been employed in the past are inadequate to comply with the regulations expected in the future [4, 7, 9]. This highlights the importance of implementing after – treatment lean NO_x systems on automobiles.

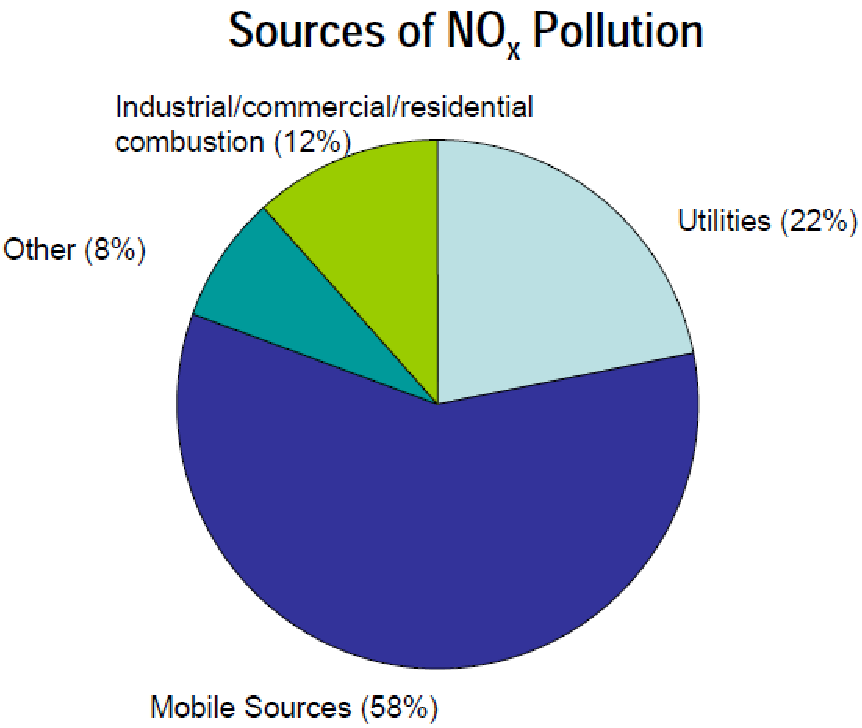

Figure 1.1.1 Sources of NO$_x$ Pollution [3]

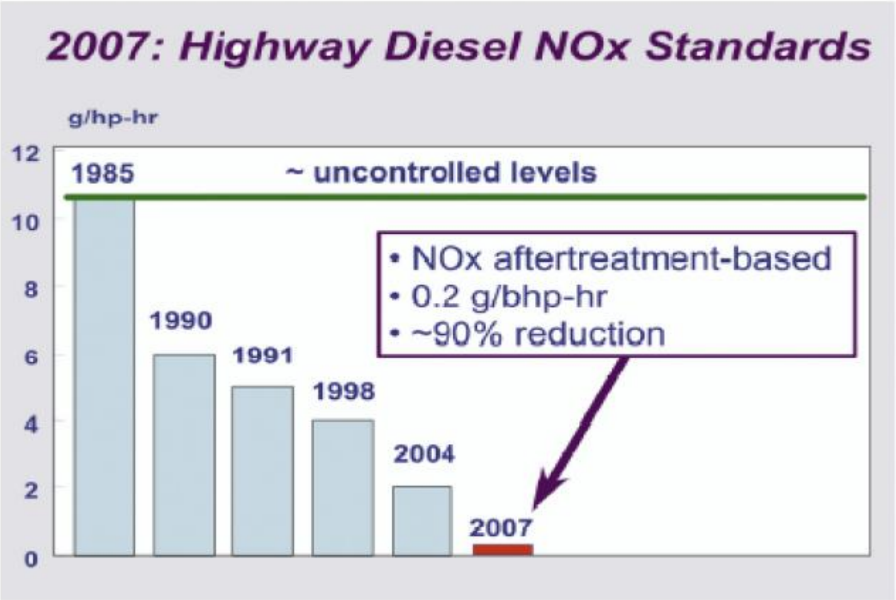

Figure 1.1.2 Current highway diesel NO$_x$ emission standards [10]

Three way catalysts (TWC) are used to meet the current emission standards, and accomplish the combined task of oxidizing CO as well as unburnt hydrocarbons while simultaneously reducing NO_x to N_2. But TWC do not deliver the expected performance under lean operating conditions that are used to improve the overall fuel economy [6]. Consequently, several other technologies such as NO decomposition, lean NO_x traps and selective catalytic reduction (SCR) using both hydrocarbons and ammonia have been explored [6-8, 11-13]. NO decomposition to N_2 and O_2 is the cleanest way of reducing NO_x without any byproduct formation or the need for additives. However, it is kinetically a slow process even though it is thermodynamically favored, and the catalyst is poisoned by the O_2 produced from the decomposition of NO itself. Hence no catalyst with an appreciable NO conversion under the conditions prevalent in a diesel exhaust has been found to date [7, 11, 13]. NO_x storage traps, developed by Toyota [8, 14], consist of a basic oxide like BaO supported on alumina that stores NO_x during lean cycles of operation while Pt oxidizes CO and unburnt hydrocarbons. Periodic regeneration under rich conditions releases the stored NO_x and reduces the hydrocarbons. Hydrocarbon SCR is an alternative way of reducing NO_x emissions using the onboard fuel but it lowers the overall fuel economy because a portion of it is used for after-treatment control. Hydrocarbon combustion in the presence of excess oxygen prevalent under lean conditions is a competing side reaction and reduces selectivity towards NO_x reduction [15]. Ammonia SCR, however, does not suffer from these drawbacks and has been used for stationary applications such as power plants, boilers and turbines in Japan since the 1970’s [16]. Titania supported vanadia formulations, which were sulfur resistant because the anatase phase of titania is only weakly and reversibly sulfated, were originally used for this purpose

[8]. However, the instability of vanadia based catalysts for mobile applications [5] raised concerns due to their toxicity and volatility at the thermal regeneration temperatures used to regenerate particulate filters [17].

Copper (Cu) exchanged zeolites are safer and more viable alternative catalysts for ammonia SCR [13, 18-22]. Cu-ZSM-5 has been the subject of several investigations over the past two decades [7, 11, 23] after it was first reported to be active for NO decomposition by Iwamoto et al [24]. Zeolites are a class of solid acid catalysts wherein a portion of the tetravalent Si^{4+} sites in its framework structure are replaced by trivalent Al^{3+} sites, consequently, causing a deficiency of positive charge that can be compensated by a variety of extra-framework ions (H^+, Cu^{2+}, Fe^{2+}, Fe^{3+}, Co^{2+}, etc.). Cu-ZSM-5, however, suffer from severe degradation in structure and performance under the harsh hydrothermal conditions present in a diesel exhaust. Small pore SSZ-13 and SAPO-34 zeolites show exceptional hydrothermal stability even after aging and exposure to several high temperature regenerative cycles compared to the medium pore ZSM-5 and large pore BEA zeolites [21, 25]. Thermal degradation in medium and large pore zeolites is proposed to occur by dealumination that leads to the formation of octahedrally coordinated, extra – framework aluminum oxides or copper aluminates. However, these species cannot exit the small pores of the SSZ-13 structure because of the inherent size limitations and hence, are proposed to re – attach to the zeolite framework upon cooling, thus imparting these small pore zeolites their hydrothermal stability [25].

1.2 Ammonia SCR

The three types of ammonia SCR reactions, depending on the NO/NO_2 ratio are described below:

$$4NH_3 + 4NO + O_2 \rightarrow 4N_2 + 6H_2O \ldots\ldots 1.1$$

$$4NH_3 + 2NO + 2NO_2 \rightarrow 4N_2 + 6H_2O \ldots\ldots 1.2$$

$$8NH_3 + 6NO_2 \rightarrow 7N_2 + 12H_2O \ldots\ldots 1.3$$

Since a typical diesel exhaust stream contains NO_x mainly in the form of NO [2, 7, 9, 26], standard SCR (equation 1.1) is directly relevant to such mobile applications. However, if some of the NO is pre – oxidized to NO_2 such that equimolar amounts of NO and NO_2 are present, then the resulting fast SCR reaction (equation 1.2) has a higher reaction rate compared to that for standard SCR [9, 22] while simultaneously broadening the temperature window of operation for catalysts to lower temperatures [22, 27], and obviates the need for participation of O_2 in the SCR reaction. A typical disadvantage when significant amount of NO_2 is fed to the SCR catalyst is the formation of ammonium nitrate, which is an unwanted side product, can accumulate and block the active sites for SCR at low temperatures as shown by infrared spectroscopy, and decomposes to N_2O, which is an undesirable greenhouse gas [9, 22]. In the presence of excess NO_2, slow SCR (equation 1.3) takes over and NO_2 reacts directly with NH_3 to produce N_2 and H_2O.

1.2.1 Mechanistic Aspects of Standard SCR

Isolated Cu(II) sites are now accepted as the active site for the standard SCR reaction on Cu-SSZ-13 catalysts [18-20, 28]. Deka et al. [19] argued that mononuclear Cu(II) species was the active species for standard SCR because they did not observe Cu(I) during their *in situ* x-ray absorption spectroscopy (XAS) experiments. However, *operando* XAS experiments performed by Ribeiro and co – workers [20, 28-30] showed a mixture of Cu(I) and Cu(II) during low temperature (473 K) standard SCR while neither the Cu(I) or Cu(II) fraction correlated with the standard SCR reaction rate. Further, two types of ion exchanged, isolated Cu(II) species, namely Cu^{2+} ions that are charge-compensated by a pair of framework Al atoms and $[CuOH]^+$ ions that are charge-compensated by isolated Al atoms in the zeolite, are suggested to be present in zeolites depending on their composition (Si/Al and Cu/Al ratios) ([31, 32]) but it is not clear how these two isolated Cu(II) species behave under SCR conditions.

Paolucci et al. [30] demonstrated via O_2 cutoff experiments that the reduction of Cu(II) to Cu(I) during standard SCR (473 K) required both NO and NH_3 as the co-reductants, and occurred via the NO assisted N-H bond dissociation of a Cu-bound NH_3 ligand while simultaneously generating a proximal Brønsted acid site per Cu^{2+} reduced. The authors speculated that the re-oxidation of Cu(I) to Cu(II) to close the catalytic cycle occurred via the *in situ* reaction of NO and O_2 to the form a nitrite (NO_2^-) anion that subsequently reacted with the NH_4^+ ions to produce N_2 and H_2O. The proposed redox mechanism for standard SCR to account for the experimental observations is shown in Figure 1.2.1.

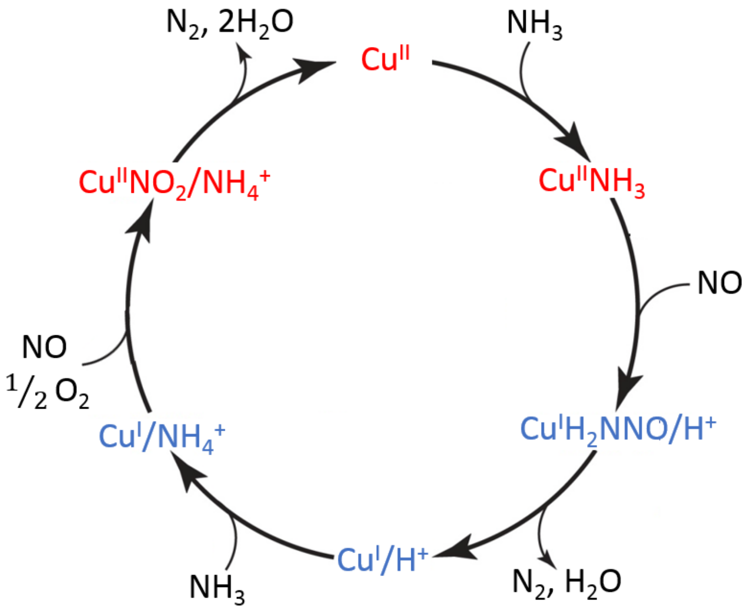

Figure 1.2.1 Proposed standard SCR redox mechanism on isolated Cu^{2+} ions at paired Al sites [30].

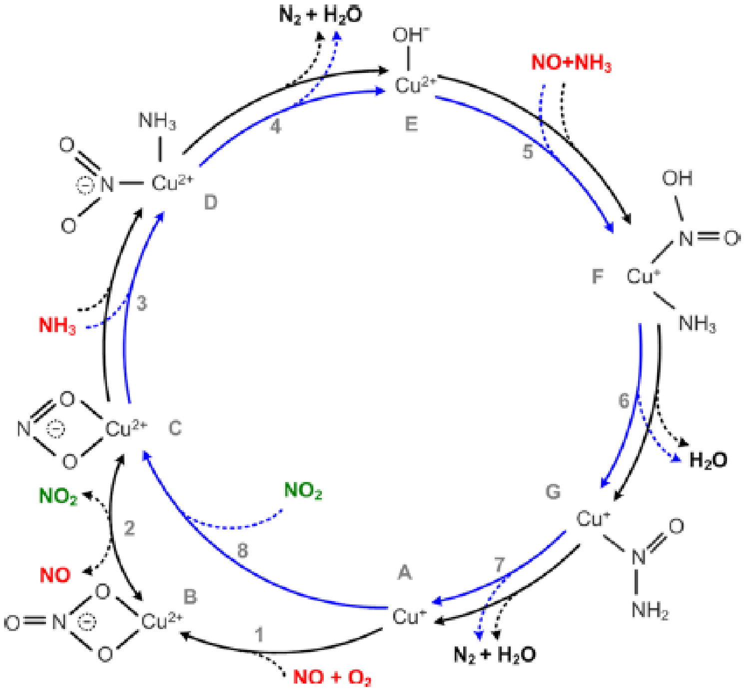

Figure 1.2.2 Coupled standard (black) and fast (blue) standard SCR redox pathways proposed on $[CuOH]^+$ ions at isolated Al sites [33].

Janssens et al. [33], expanded on the proposed reaction mechanism by suggesting that the re-oxidation of Cu(I) to Cu(II) occurred via the initial formation of a nitrate (NO_3^-) anion from the *in situ* reaction of NO and O_2, which is further reduced by another NO molecule to a nitrite (NO_2^-) anion and a free NO_2 molecule, thus coupling standard and fast SCR reactions (Figure 1.2.2). The entire redox cycle was proposed to occur on a single, isolated, ion-exchange Cu site, which is consistent with the linear correlation obtained for the standard SCR reaction rate (Cu/Al = 0-0.2, Si/Al = 4.5) with the Cu content in catalysts [28]. At low Cu loadings (Cu/Al < 0.02, Si/Al = 6), however, Gao et al. [34] showed that this linear correlation breaks down and in fact, the standard SCR rate (473 K) varies as squared of the total Cu content. The authors reconciled this observation by proposing that Cu exchanged as $[Cu\text{-}O\text{-}Cu]^{2+}$ dimers was the active site at low Cu loadings (Cu/Al < 0.02, Si/Al = 6) while isolated Cu^{2+} ions exchanged at a pair of framework Al atoms in the D6R and became the predominant active sites at higher Cu loadings (Cu/Al > 0.02, Si/Al = 6). However, isolated Cu^{2+} ions at a pair of framework Al atoms is the energetically preferred exchange site [28, 31] and secondly, the preferential formation of Cu dimers at low Cu loadings seems unreasonable because of low Cu contents in those samples. This shows that despite of all the advances, there are gaps in our understanding of the reaction mechanism and the active sites involved in low temperature (473 K) standard SCR catalysis that need further elucidation.

1.3 NO Oxidation

NO oxidation is simply the oxidation of NO by O_2 to produce NO_2 as follows:

$$2NO + O_2 \rightarrow 2NO_2 \ldots\ldots 1.4$$

Metkar et al. [35] and several others [7, 23, 36-40] have suggested that NO oxidation is the rate limiting step for low temperature (473 K) ammonia standard SCR. This was proposed because the SCR reaction rate increases with an increase in the NO_2:NO ratio in the feed. Further, H-ZSM-5 and H-SSZ-13 do not show measurable low temperature (473 K) standard SCR rates whereas the reaction is observed to proceed on the same zeolites upon addition of transition metals such as Cu and Fe [2, 5, 37, 40]. Based on these observations, and similar kinetics for ammonia standard SCR and NO oxidation reactions studied separately [35] [39], the proposed role of the transition metal was to oxidize NO to NO_2. Ribeiro and co-workers have shown that the active sites for dry NO oxidation are Cu_xO_y clusters [41] whereas those for ammonia standard SCR are isolated ion-exchanged Cu species [28], and even their apparent kinetics are different. However, the prime difficulty in ascertaining the role of NO oxidation during standard SCR is the inability to study the reaction under SCR conditions.

Nonetheless, Verma et al. [41] showed that the utility of dry NO oxidation lies in the fact that it can be used a probe reaction to detect clustering of Cu that usually occurs due to sintering upon aging Cu-zeolites. Additionally, the efficiency of NO_x removal is greatly enhanced by the fast SCR reaction if some of the NO fed to the SCR catalyst can be pre-oxidized to NO_2.

1.4 The Importance of Spectroscopy in Catalysis

Kinetic studies measure reaction orders for each reactant, based on the coverage of various species on the catalyst surface and heats of adsorption, can be estimated. However, the reactor is like a black box, for which only the inlet and outlet concentrations of the different gases are known, while the adsorbates on the catalyst surface cannot be observed directly. Spectroscopy, both *in situ* and *operando* are indispensable techniques to probe the state of the catalyst and the adsorbates under catalytic conditions. This can be likened to Figure 1.4.1, similar to taking a photograph of the catalyst surface during operation, and provides useful insights into the possible reaction intermediates and the reaction mechanisms and pathways.

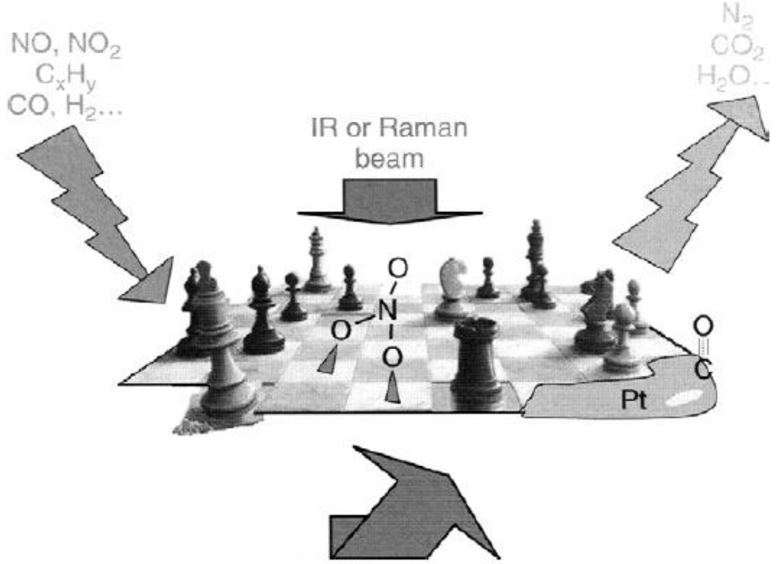

Figure 1.4.1 Analogy of a catalyst with a chessboard, and the utility of spectroscopy [42].

This report uses x-ray absorption (XAS) and infrared (FTIR) spectroscopies to study ammonia SCR and dry NO oxidation reactions. XAS directly probes the oxidation state and the local environment of Cu and hence, is a useful tool to understand the response of the Cu active site under varying gas conditions. Infrared (FTIR) spectroscopy, on the other hand, is useful to identify various types of intermediate species adsorbed on a catalyst surface during reaction. Both *in situ* and *operando* techniques have been used for the purposes of this report with an emphasis on *operando* because spectroscopic information about the catalyst is obtained in real time while monitoring the products formed by the reaction. This is useful for determining structure-activity relationships where changes in certain spectroscopic features can be related to changes in the catalytic performance.

Furthermore, additional mechanistic information is furnished by steady-state isotope transient experiments wherein, at steady state, one reactant is replaced with its isotopically labeled analog. Assuming that the transport and thermodynamic properties of the isotope and the unlabeled gas are the same, these experiments provide a way to keep the catalyst surface at a kinetic steady state while giving us the ability to monitor the isotopic label on the catalyst surface using FTIR and in the final product using a mass spectrometer (MS) as the reactant molecule passes through surface intermediates to form products. Several reports that involve isotopic labeling of one reactant species exist in literature [43-47], where the shapes of the product curves obtained as a function of time are modeled to extract quantitative information about the number of pools of reactive intermediates, their average lifetime on the catalyst surface and the turnover frequency. For example, isotopic labeling experiments have proven that N_2 produced in the standard SCR reaction on V_2O_5/TiO_2 catalysts contains one atom nitrogen from NO and the other from NH_3 [45]. However, a majority of these studies monitor the various isotopic species only in the reactor effluent and not on the catalyst surface. The added advantage in the study of hydrocarbon SCR by Chansai et al. [47], compared to the other studies is that the isotopic label was followed on the catalyst surface using FTIR, and in the reactor outlet using an online MS, thus providing direct evidence for the active intermediates participating in the reaction. Keeping this in mind, a reactor setup capable of performing steady state isotope switching experiments was designed to identify potential intermediates involved in the reaction pathway to form NO_2 by the oxidation of NO.

1.5 Research Objectives

The first objective of this study was to ascertain the effect of each reactant on the state of Cu in Cu-SSZ-13 catalyst during low temperature (473 K) standard SCR. Transient cutoff experiments [30] elucidated the redox behavior of Cu during standard SCR. However, because of the inherent transient nature of these experiments, it was difficult to ascertain whether the changes in Cu oxidation state were catalytic or because of the absence of one reactant in the feed mixture. Further, because a combination of two reactants was always present after cutting off one reactant in the feed, it was unclear as to what role each of the individual reactant molecules played in the standard SCR mechanism. Thus, steady state *operando* experiments were performed in chapter 3 by systematically varying the partial pressure of one reactant at a time while simultaneously measuring the standard SCR reaction rates and collecting x-ray absorption near edge structure (XANES) spectra to observe the change in the Cu(I)-Cu(II) surface coverages, and relate that to the role of each reactant in the standard SCR mechanism.

Even though NO and O_2 are proposed to be involved in the oxidation half-cycle in the standard SCR mechanism, how the 4-electron oxidation with O_2 occurs during standard SCR is not well understood. On the other hand, NO_2 is considered as the oxidant during fast SCR. Consequently, we probed the oxidation half-cycle in the SCR mechanism by reducing and trapping two Cu-SSZ-13 catalysts, which contained structurally equivalent, isolated Cu^{2+} ions charge balanced by a pair of framework Al atoms but with diffeingt Si/Al ratios, in their Cu(I) state, and then followed the rate of Cu(I) re-oxidation by XANES upon flowing either 10% O_2 or 90 ppm NO_2 to elucidate whether there were any differences or similarities between the oxidation behavior of Cu(I) during the two SCR reactions. A secondary objective was also to determine the effects of the zeolite composition i.e. Si/Al ratio and the proximity of exchanged Cu ions on the oxidation reactions with O_2 and NO_2, if any.

Furthermore, two types of isolated Cu(II) species – Cu^{2+} and $[CuOH]^+$ – are proposed (section 1.2.1) to be active for standard SCR. Hence, it was of interest to first detect and quantify their relative amounts in our catalysts. Subsequently, differences in their chemical behavior were investigated under a variety of *ex situ* oxidizing and reducing environments using XANES, extended x-ray absorption fine structure (EXAFS) and first-principles density functional theory (DFT) calculations in chapter 2. The goal was understand whether these *ex situ* characterizations correlated with and could be extrapolated to the behavior of these two species during standard SCR reaction conditions.

Finally, the relevance of nitrates for dry NO oxidation was probed in chapter 4 using a custom-built *operando* FTIR reactor and a unit capable of performing isotope labeling experiments. These experiments demonstrate that steady-state isotope transient kinetic analysis is a powerful technique to identify potential reactive intermediates for the reaction being investigated.

CHAPTER 2. CATALYSIS IN A CAGE: CONDITION – DEPENDENT SPECIATION AND DYNAMICS OF EXCHANGED CU CATIONS IN SSZ-13 ZEOLITES

“Reprinted (adapted) with permission from Catalysis in a Cage: Condition-Dependent Speciation and Dynamics of Exchanged Cu Cations in SSZ-13 Zeolites, Chrisopher Paolucci, Atish A. Parekh, Ishant Khurana, John R. Di Iorio, Hui Li, Jonatan D. Albarracin Caballero, Arthur J. Shih, Trunojoyo Anggara, W. Nicholas Delgass, Jeffrey T. Miller, Fabio H. Ribeiro, Rajamani Gounder, William F. Schneider, Journal of the American Chemical Society, doi: 10.1021/jacs.6b02651. Copyright (2016) American Chemical Society.” (http://pubsdc3.acs.org/articlesonrequest/AOR-RJXD4RdZNiXNX7anz7hE)

The computational work in this chapter has been performed by Christopher Paolucci and Hui Li from Prof. William F. Schneider’s group at the University of Notre Dame.

2.1 Abstract

The relationships among the macroscopic compositional parameters of a Cu-exchanged SSZ-13 zeolite, the types and numbers of Cu active sites, and activity for the selective catalytic reduction (SCR) of NO_x by NH_3 are established through experimental interrogation and computational analysis of materials across the catalyst composition space. Density functional theory, stochastic models, and experimental characterizations demonstrate that under the synthetic conditions applied here, Al randomly distribute on the SSZ-13 lattice subject to Löwenstein’s rule and that exchanged Cu(II) ions first populate 2

Al sites within six-membered-rings before populating remaining 1 Al sites as Cu(II)OH. These sites are distinguished and enumerated *ex situ* through vibrational and x-ray absorption spectroscopies (XAS) and chemical titrations. *In situ* and *operando* XAS follow Cu oxidation state and coordination environment as a function of environmental conditions including low temperature (473 K) SCR catalysis and are rationalized through first-principles thermodynamics and *ab initio* molecular dynamics. Experiment and theory together reveal that the Cu sites respond sensitively to exposure conditions, and in particular that Cu species are solvated and mobilized by NH_3 under SCR conditions. While Cu sites are spectroscopically and chemically distinct away from these conditions, they exhibit the same turnover rates, apparent activation energies and apparent reaction orders at the SCR conditions, even on zeolite frameworks other than SSZ-13.

2.2 Introduction

In 1925 [48], Hugh Scott Taylor theorized that specific groups of atoms were responsible for the rate enhancing capacity of heterogeneous catalyst surfaces, from the he coined the phrase “active site”. This concept has become ubiquitous in modern catalysis science and has proven indispensable to the emergence of rational catalyst design. Most heterogeneous catalysts, however, are structurally heterogeneous at the molecular scale. They contain a distribution of active sites of different catalytic activity [49-51], reflecting non – uniformities in active site coordination and local environment [52, 53], response to external stimuli [54, 55], and interactions with reacting molecules [56-59]. The integration of density functional theory (DFT) computational models and experimental *operando* spectroscopies that interrogate active sites during catalysis can provide powerful insights into the coupling between active site composition, reaction environment, and the reaction mechanism [60, 61]. In this work, we demonstrate how this approach enables the identification, quantification, and characterization of distinctly different active sites in a macro- and microscopically heterogeneous zeolite catalyst. We show through *operando* characterization that the composition and structure of active sites changes dynamically during reaction, differs from their *ex situ* states, and that such reaction-environment-induced modifications are integral to observed catalytic performance.

We demonstrate this capability in the context of Cu-exchanged zeolite catalysts. Zeolites are crystalline, nanoporous aluminosilicates constructed of corner-sharing SiO_4 and AlO_4 tetrahedra, or T-sites. Framework substitution of Si^{4+} by Al^{3+} introduces an anionic charge into the oxide lattice that must be charge-compensated by extralattice cations. The Al sites are in general not ordered, so that at a given Si:Al ratio a zeolite presents a distribution of local Al environments [62-66]. The common oxidation states of Cu are 1+ and 2+, and thus, a single Cu ion can in principle charge-compensate one or two Al T-sites [67-74]. The exact form of this exchange and charge compensation can depend on Cu oxidation state, overall framework structure, and local Al siting. In addition, Cu is observed to form multinuclear oxo-complexes and oxide clusters that further enrich its exchange chemistry and catalysis [41, 75-79].

Cu-exchanged zeolites have been explored for a variety of partial oxidations [77, 78, 80-90] and NO_x chemistries [91-93]. Cu-zeolites have long been known to be active for the selective catalytic reduction (SCR) of NO_x with NH_3 [5, 7, 22, 24, 60, 94-98]. SCR catalysts promote the reduction of NO_x by NH_3:

$$4NH_3 + 4NO + O_2 \rightarrow 6H_2O + 4N_2 \ldots\ldots.2.1$$

over the competing and undesired oxidation of NH_3:

$$4NH_3 + 3O_2 \rightarrow 6H_2O + 2N_2 \ldots\ldots 2.2$$

Small pore Cu-exchanged SSZ-13, in particular, is able to satisfy all the practical requirements of an SCR catalyst and is now in commercial use [99-102]. However, the relationships between zeolite composition, reaction conditions, active site(s), and mechanism remain to be elucidated.

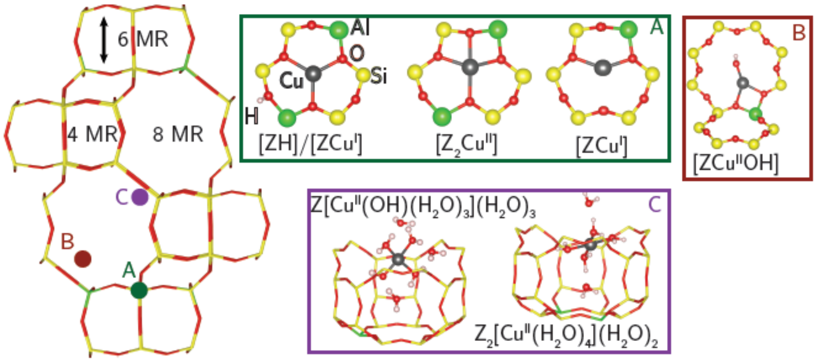

Figure 2.2.1 (left) side view of the chabazite cage. (right) HSE06-optimized structures of (A, B) dehydrated oxidized and reduced Cu sites and (C) hydrated oxidized sites. Label indicates location of Cu ion within the chabazite cage.

SSZ-13 has the chabazite topology. The single symmetry-distinct T-site organizes into 4-, 6- and 8-membered rings (Figure 2.2.1, right) that form a cage ≈8 Å in diameter [103]. SSZ-13 can be prepared in elemental compositions from highly enriched (Si:Al = 2) to infinitely dilute (Su:Al = ∞) in Al sites. The H-form (i.e. Al charge-compensated by H^+) can be exchanged to various Cu:Al ratios, and the locations and forms of these exchanged Cu ions have received considerable attention [19, 25, 28, 32, 33, 41, 104-116]. X-ray absorption (XAS), UV-visible (UV-Vis), and infrared (IR) spectra of zeolites [28, 32, 34, 41, 88, 110, 117] all suggest that exchanged Cu ions are present as hydrated and oxidized [Cu(II)(H_2O)$_6$] [118] at ambient conditions regardless of zeolite composition and topology.

The homogeneity of Cu sites under ambient conditions gives way to a rich variety of Cu species after high temperature and oxidative removal of H_2O. X-ray diffraction (XRD) reveals monomeric Cu ions in SSZ-13 that occupy either 6MR A sites [19, 109], or both A and B sites [104, 113] (Figure 2.2.1). We have reported that high Al content Cu-SSZ-13 zeolites (Si:Al = 5) contain exclusively Cu(II) in the (A) site under dry oxidizing conditions up to Cu:Al = 0.2 [28, 30], as demonstrated through the 4-fold coordination of Cu with the zeolitic oxygen in extended x-ray absorption fine structure (EXAFS) spectra and titrations of residual Brønsted acid sites that reveal a 2:1 H^+:Cu^{2+} exchange stoichiometry. In contrast, Borfecchia et al. [105] report 3-fold Cu coordination under similar conditions on their Si/Al = 13, Cu/Al = 0.4 sample. Giordanino et al. [32, 105] report IR features attributable to Cu hydroxyl ([Cu(II)OH]$^+$) on Si:Al = 13, Cu:Al = 0.4, whereas Gao et al. [114] only observe this band on a subset of Si:Al = 6 samples. DFT calculations generally indicate that isolated, unligated Cu(I) and Cu(II) ions prefer the A site (Figure 2.2.1, left) regardless of the location of Al [20, 28, 30, 105, 108, 119-122].

H_2 temperature programmed reduction (TPR) [114, 123] experiments are consistent with the existence of at least two types of exchanged Cu(II) with differing susceptibility to reduction. Borfecchia et al. [105] similarly observe only a fraction of Cu(II) ions to reduce in He at 673 K. Chemical probes including NO, NO_2 and CO [33, 123-128] will thus see a different mixture of Cu sites depending on sample history. For instance, NO adsorbs strongly with vacuum-reduced Cu(II) → Cu(I) sites [123, 124] but more weakly and dynamically on Cu(II) sites [30, 106]. The relevance of the *ex situ* probes to catalytic conditions has yet to be established.

Standard SCR is a redox reaction, as evidenced by the observation of both Cu(I) and Cu(II) in *operando* experiments [20, 33, 129] and thus the *ex situ* reducibility of catalysts might be expected to correlate with observed activity. However, catalysts with different *ex situ* properties exhibit similar SCR characteristics. Reactant cutoff experiments demonstrate that both NO and NH_3 are necessary for the Cu(II) → Cu(I) half-cycle across samples of various compositions [30, 33]. Apparent activation energies are the same (≈ 70 kJ mol^{-1}) and 473 K SCR turnover rates are linear in Cu content (Cu:Al = 0.08 – 0.2) on Si:Al = 5 samples [28, 30, 130]. Samples with compositions nearer to those studied by Borfechhia et al. present the same Cu(I)/Cu(II) fractions in *operando* XAS [33] and similar apparent activation energies [114] as the Si:Al = 5 samples but different susceptibilities to Cu reduction in H_2 TPR [114].

Thus, while there is general agreement that various isolated, exchanged Cu ions are present and contribute to the SCR catalysis, the precise nature, number and reactivity of different cationic species, their dependence on zeolite composition (Si:Al and Cu:Al ratios) and framework topology, sample treatment history and environment, and their spectroscopic signatures under *ex situ* vs. *in situ* conditions, remain unknown. Here, we report a coordinated computational (stochastic simulation, *ab initio* dynamics and free energy) and experimental (synthetic, spectroscopic and titrimetric) analysis of Cu speciation under *ex situ* conditions, and *in situ* and *operando* SCR conditions as a function of catalyst composition over a wide range of zeolite chemical composition space. We demonstrate that the types, numbers and chemical characteristics of Cu sites depend on bulk composition of the zeolite, can be predicted through first-principles-based models, can be distinguished in the laboratory, and depend strongly on the environmental conditions. Environmental conditions have a profound impact on Cu ion siting, coordination and mobility, resulting in SCR turnover rates (473 K) that are independent of the initial Cu cation site and the zeolite framework type. The results rationalize a large body of literature, resolve contradictory findings regarding the active sites for NO_x SCR, and consolidate the understanding of Cu cation speciation in zeolite.

2.3 Results

2.3.1 Cu Cation Speciation in Cu-SSZ-13

2.3.1.1 First-principles Speciation of Cationic

We first created molecular models for isolated Cu exchange sites in SSZ-13 and established their relative free energies under hydrothermal conditions relevant to Cu exchange and catalyst treatment; computational details can be found in appendix A. We used a 12 T-site supercell [20, 28, 30] with a single Al substitution to represent an isolated Al atoms in the CHA framework. Charge compensating Cu(I) ions prefer to sit in the plane of the 6MR [20, 28, 120], and we label this structure as [ZCu(I)] in Figure 2.2.1a to denote charge-compensation of a single Al (Z) by Cu. This notation also emphasizes the formal 1+ oxidation state of Cu, and this structure is used as the Cu(I) reference in relating computed Bader charges to effective Cu oxidation states. An oxidized form of the Cu sites compensating a single framework Al atoms has been proposed [33, 105, 111] to be formed by the addition of an extra-lattice OH ligand, which redirects the Cu into the 8MR according to optimized [ZCu(II)OH] structure shown in Figure 2.2.1b.

Similarly, two proximal framework Al atoms (2Al sites) can be charge compensated by a single Cu(II) ion. The exchange energies of Cu(II) at different potential 2Al sites were previously computed using a 2 x 1 x 1 supercell containing 4 Al atoms distributed to place 2Al sites in each of the 4, 6, and 8MR [28]:

$$Z_4H_4 + Cu(II)_{(aq)} \rightarrow Z_4H_2Cu(II) + 2H^+_{(aq)} \ldots\ldots 2.3$$

Cu(II) exchange at 2Al sites in the 6MR ring is 108 and 145 kJ mol^{-1} more exothermic than exchange at 2Al sites in the 4MR and 8MR, respectively. We adopt a model with 2Al at third-nearest-neighbor (3NN) positions in a 6MR for Cu near 2Al. Cu exchange at the 2NN Al 6MR is coordinatively similar and the exchange energy more endothermic by 22 kJ mol^{-1}. The 3NN Al 6MR structure is labeled [Z_2Cu(II)] in Figure 2.2.1a and is taken as the Bader charge standard for the Cu(II) oxidation state. We previously found that this [Z_2Cu(II)] site can be reduced by addition of H^+ to an Al site proximal to Cu [30], which is the [ZH]/[ZCu(I)] species shown in Figure 2.2.1a. The forward slash emphasizes that these two sites are proximal. Reduction to Cu(I) decreases Cu coordination to the lattice but preserves Cu location within the 6MR.

Motivated by XAS [28, 67, 110], and molecular dynamics [131] evidence that exchanged Cu(II) ions are hydrated under ambient conditions, we first explored H_2O coordination to the [Z_2Cu(II)] and [ZCu(II)OH] ions by computing the structures and successive adsorption energies of H_2O ligands (x = 1 to 6):

$$1Al: ZCu(II)(OH)(H_2O)_{x\text{-}1} + H_2O \xrightarrow{\Delta E_{ads}} ZCu(II)(OH)(H_2O)_x \ldots\ldots 2.4.1$$

$$2Al: Z_2Cu(II)(H_2O)_{x\text{-}1} + H_2O \xrightarrow{\Delta E_{ads}} ZCu(II)(H_2O)_x \ldots\ldots 2.4.2$$

In each simulation, we started from the equilibrated (x-1) H_2O structure, added another H_2O molecule, annealed for 140 ps at 473 K using NVT *ab initio* molecular dynamics (AIMD) at the GGA level, quenched and evaluated the energy with HSE06 functional including Tkatchenko Scheffier van der Waals (TSvdw) corrections (section 2.6.1). Energy and Cu coordination number results are summarized in Table 2.3.1, where CN is defined as the number of heavy atoms within 2.3 Å of Cu. H_2O adsorption energies are on the order of -70 kJ to -90 kJ mol^{-1} and are generally more exothermic on [$Z_2Cu(II)$] than on [ZCu(II)OH] sites. The computed Cu oxidation state is insensitive to added H_2O. On [$Z_2Cu(II)$], successive H_2O ligands generally displace framework oxygen (O_f) from the first coordination sphere, until at x = 4 the Cu(II) ion is fully coordinate by H_2O; additional H_2O molecules form a second coordination sphere through hydrogen bonds to first shell H_2O. With hydration, the Cu ion moves from within the 6MR (site A, Figure 2.2.1) to the 8MR (site B) to the cage center (site C). The final optimized x = 6 structure is shown in Figure 2.2.1c. The [$Z_2Cu(II)OH$] site behaves similarly with added H_2O; the fully hydrated complex is shown in Figure 2.2.1c.

Table 2.3.1 H_2O adsorption energies (ΔE_{ads}) on Cu sites computed using HSE06-TSvdw. Cage location referenced to Figure 2.2.1. CN and O_f indicate total Cu coordination number and number of close framework O contacts, respectively.

	+x H_2O	1	2	3	4	5	6
Z_2Cu	ΔE_{ads} (kJ mol^{-1})	-84	-94	-108	-84	-90	-73
	Cage Location	A	A	B	C	C	C
	O_f/total CN	3/4	3/4	2/4	0/4	0/4	0/4
ZCuOH	ΔE_{ads} (kJ mol^{-1})	-75	-67	-76	-63	-95	-56
	Cage Location	B	C	C	C	C	C
	O_f/total CN	2/4	0/3	0/3	0/4	0/4	0/4

Exchanged Cu may lose waters of hydration and acquire other ligands during synthesis and after oxidation or reduction treatments. We computed the structures and energies of various combinations of O, OH, H_2O and O_2 ligands on both the 1Al and 2Al models in the nominally oxidized and reduced states. The list of candidate structures was guided by chemical plausibility and includes proposed intermediate species reported elsewhere (e.g. Cu(II)O, Cu(II)$(OH)_2$) [20, 132]. Optimized structures and energies of all 26 species are tabulated in appendix A.

We applied a first-principles thermodynamic analysis to rank the stability of this library of Cu-bound H_xO_y species as a function of temperature, and hydrogen and oxygen potentials. We take O_2 and H_2O as the oxygen and hydrogen references, respectively:

$$\mathrm{ZCu} + \frac{x}{2}\left(\mathrm{H_2O} - \frac{1}{2}\mathrm{O_2}\right) + \frac{y}{2}\mathrm{O_2} \xrightarrow{\Delta G_{\mathrm{form}}} \mathrm{ZCuH_xO_y}\ldots\ldots2.5$$

used the HSE06-TSvdw energies, and applied previously developed correlations [30], to estimate adsorbate entropies. The formation free energies (ΔG_{form}) are computed according to section 2.6.2 and the μ_{H2O} and μ_{O2} related to T and P through the ideal gas relation. Results for an ambient condition (Condition 1, 298 K, 2% H_2O and 20% O_2) representative of an air-exposed catalyst, and an elevated temperature condition (Condition 2, 673 K, 2% H_2O and 20% O_2) representative of an oxidation pretreatment are summarized in Fig. 2. For clarity, species with $\Delta G_{\mathrm{form}} > + 200$ kJ mol^{-1} are not shown in condition 2. The relative energy alignment between Cu near 1Al and 2Al is described in section 2.1.1.2.

At high temperatures (673 K) and high oxygen potentials (20% O_2) of Condition 2, the lowest free energy structure near the 2Al site is the isolated [Z_2Cu(II)] ion. At these conditions, adsorption of a single H_2O ligand is endergonic by 15 kJ mol^{-1}. Other adsorbates on Cu sites near 2Al lead to complexes much higher in free energy, including adsorbed molecule O_2. Similarly, on Cu sites near 1Al, the lowest free energy structure is oxidized [ZCu(II)OH] with normalized Bader charge (appendix A) of +1.8, slightly less than [Z_2Cu(II)]. The reduced form of the site, [ZCu(I)], and its hydrated form, [ZCu(I)(H_2O)], are very close in free energy to the oxidized [ZCu(II)OH] state. Molecular O_2 adsorption on the [ZCu(I)] site is endergonic by 50 kJ mol^{-1} relative to [ZCu(II)OH], and even higher in free energy are other oxidized forms, including [ZCu(II)O] [132] and [ZCu(II)$(OH)_2$] [20]. The primary effect of decreasing temperatures to ambient (Condition 1) is a significant decrease in the free energies of all hydrated Cu states, which causes the most stable species to become the fully hydrated Z_2[Cu(II)$(H_2O)_4$]$(H_2O)_2$ and Z[Cu(II)(OH)$(H_2O)_3$]$(H_2O)_3$ complexes at 2Al and 1Al sites, respectively.

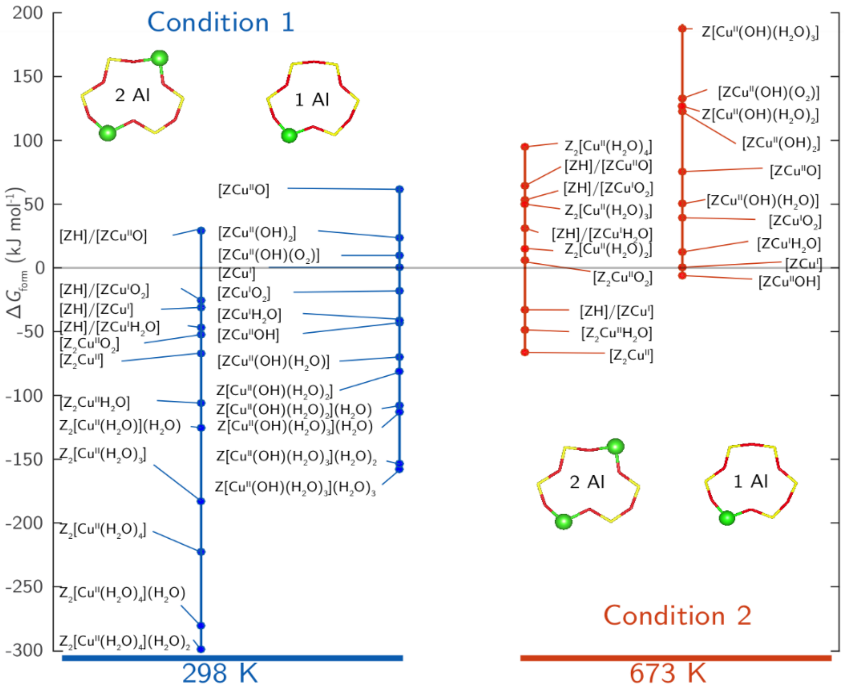

Figure 2.3.1 Formation free energies (ΔG_{form}) CuHxOy species at (left) 298 K, 2% H_2O, 20% O_2 and at (right) 673 K, 2% H_2O, 20% O_2 on the 2Al (Z_2Cu) and 1Al (ZCu) sites. Common energy reference set through equation 2.6

We generalize the analysis in Figure 2.3.1 to a range of temperatures and O_2 pressures at fixed H_2O partial pressures (2%) and plot the lowest free energy species at each set of conditions in Figure 2.3.2 in the form of a phase diagram. For reference, Conditions 1 and 2 of Figure 2.3.1 are labeled with red boxes on Figure 2.3.2. The phase diagrams are insensitive to the H_2O pressure over the range of experimental interest. For comparison, we report the corresponding $T\text{-}P_{H2O}$ diagram in appendix A. As discussed below, these diagrams indicate that the stable Cu state (CN, O_f and oxidation state) depend sensitively on the environmental conditions over the ranges of experimental interest, and that the lowest free energy species differ for Cu complexes that charge compensate 1Al or 2Al sites.

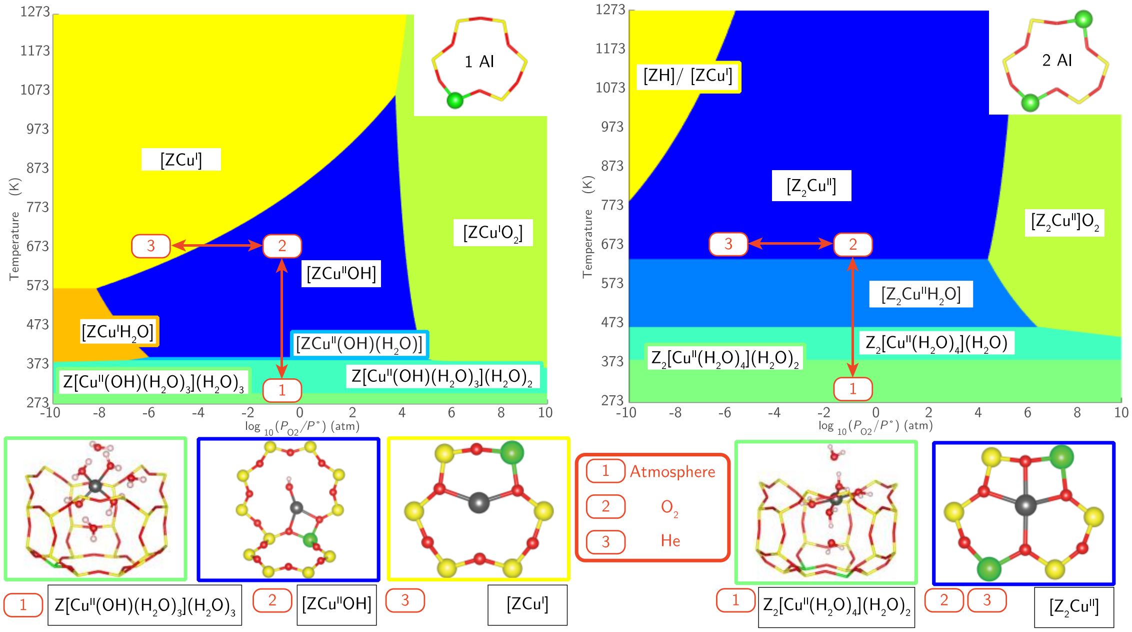

Figure 2.3.2 *Ex situ* Cu speciation phase diagrams based on HSE06-TSvdw calculations on 1Al (left) and 2Al (right) Cu exchange sites. Regions indicate site composition that minimizes free energy at 2% H_2O and given T and P_{O2}. Labeled on the phase diagram and illustrated below are the minimum free energy species at (1) ambient (298 K, 20% O_2), (2) oxidizing (673 K, 20% O_2) and (3) inert (673 K, 10^{-6} atm O_2 in He).

2.3.1.2 1Al and 2Al Cu Exchange Populations

To this point, we have treated the 1Al and 2Al sites independently. To place these two on a common energy scale, we computed the Cu exchange energy between the two sites:

$$[Z_2CuH_2O] + [ZH] \rightarrow [ZH]/[ZH] + [ZCuOH],\ \Delta E = 66\ \mathrm{kJ\ mol^{-1}} \ldots\ldots 2.6$$

We evaluated this energy in a large supercell containing separated Z_2 and Z sites as well as in separate supercells constructed to conserve atomic numbers; results are in close agreement (66 vs. 69 kJ mol^{-1}) and structures are given in appendix A. We used the 66 kJ mol^{-1} result to offset the 0 K energies of [Z_2Cu(II)H_2O] and [ZCu(II)OH], and thus, place the two site types on the same free energy y-axis shown in Figure 2.3.1. The zero of energy is defined as [ZCu(I)]. The free energy associated with Cu near 2Al is substantially lower than Cu near 1Al at both 298 K (-142 kJ mol^{-1}) and at 673 K (-55 kJ mol^{-1}). These results indicate that Cu ions prefer to segregate to 6MR 2Al exchange sites over a wide range of conditions. The relative density of Cu ions in 6MR 2Al sites and in 8MR 1Al sites will depend on the total Cu content and the number of such 2Al and 1Al sites present in a given SSZ-13 sample. We determined the Al distribution as a function of Si:Al ratio by numerical simulation [28, 64] assuming random Al distribution subject to Löwenstein’s rule [133], which prohibits 1NN Al pairs. We then assume that exchanged Cu ion populate all available 2NN and 3NN Al sites as [Z_2Cu(II)] before occupying 1Al sites as [ZCu(II)OH]. Figure 2.3.3 reports the computed fraction of Cu present as [ZCu(II)OH] as a function of Si:Al and Cu:Al ratios. The region below the white line corresponds to a composition space containing exclusively Cu species near 2Al, while the region above the black line contains gradually increasing [ZCu(II)OH] fractions that become the dominant species in the upper right red area. To ensure 2Al 6MR stay charge compensated by a single Cu past the saturation point, we computed the energy of two [ZCu(II)OH] in a 6MR (appendix A):

$$[Z_2CuH_2O] + [ZCuOH] \rightarrow [ZCuOH]/[ZCuOH] + [ZH], \Delta E = 81 \text{ kJ mol}^{-1} \ldots\ldots 2.7$$

Thus, these 6MR 2Al sites will remain populated by [Z_2Cu(II)] as additional Cu is exchanged in the form of [ZCu(II)OH].

To test these model predictions, we prepared and analyzed a series of SSZ-13 catalysts of varying Si:Al and Cu:Al ratio (samples represented by while circles in Figure 2.3.3). An Al-rich SSZ-13 sample (Si:Al = 5) was synthesized using high Al FAU zeolite as the Al source [134] and characterized as reported previously [28, 41, 135, 136], while lower Al content SSZ-13 samples (Si:Al = 15, 25) were synthesized using $Al(OH)_3$ as the Al source [109]. Powder XRD patterns (appendix A) and Ar adsorption isotherms (87 K, appendix A) were consistent with the CHA topology on all H-form SSZ-13 samples. The number of H^+ sites on each SSZ-13 sample was quantified from the NH_3 evolved during TPD of NH_4-form samples, and were 0.65, 1.02, and 0.98 H^+:Al for the Si:Al ratios of 5, 15 and 25, respectively. The high Al H-SSZ-13 sample (Si:Al = 5) contained fewer H^+ sites than its number of framework Al atoms (H^+:Al_f = 0.76) [136], reflecting the imprecision with which *ex situ* methods such as 27Al MAS NMR spectroscopy may characterize structural surrogates for H^+ sites. It also reflects the non-uniformity of SSZ-13 samples prepared using FAU to CHA interconversion methods [134], for which repeat synthesis experiments on crystallized samples that contained H^+:Al ratios that varied between 0.45-0.85 were observed (appendix A).

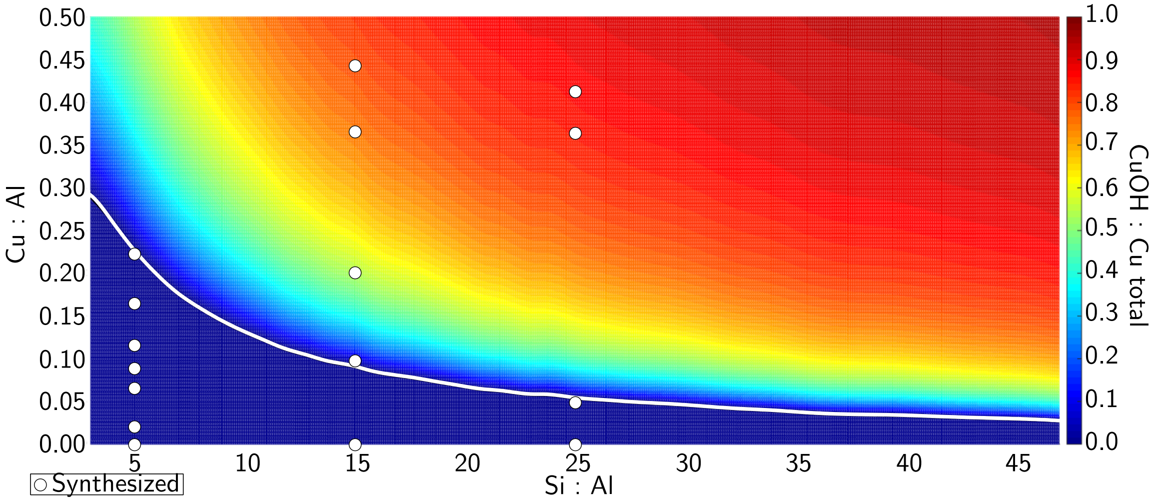

Figure 2.3.3 Predicted Cu site compositional phase diagram vs. Si:Al and Cu:Al ratios. Color scales indicate predicted fraction of CuOH. White line demarcates transition from [Z_2Cu(II)]-only region to mixed [Z_2Cu(II)]/[ZCu(II)OH] region. White circles indicated compositions of synthesized Cu-SSZ-13 samples.

Increasing amounts of Cu were exchanged into these three (Si:Al = 5, 15, 25) H-SSZ-13 samples from aqueous-phase Cu(II)$(NO_3)_2$. The number of residual H^+ sites was quantified using NH_3 TPD, which was performed after samples were saturated with gaseous NH_3 (433 K) and purged in wet helium (3% H_2O, 433 K) to desorb Lewis acid-bound NH_3 and selectively retain NH_4^+ species [135], as illustrated by equation 2.8:

$$\mathrm{ZCuNH_3 + H_2O \rightarrow ZCuH_2O + NH_3}\ldots\ldots 2.8.1$$

$$\mathrm{ZNH_4 + H_2O \rightarrow ZNH_4 + H_2O}\ldots\ldots 2.8.2$$

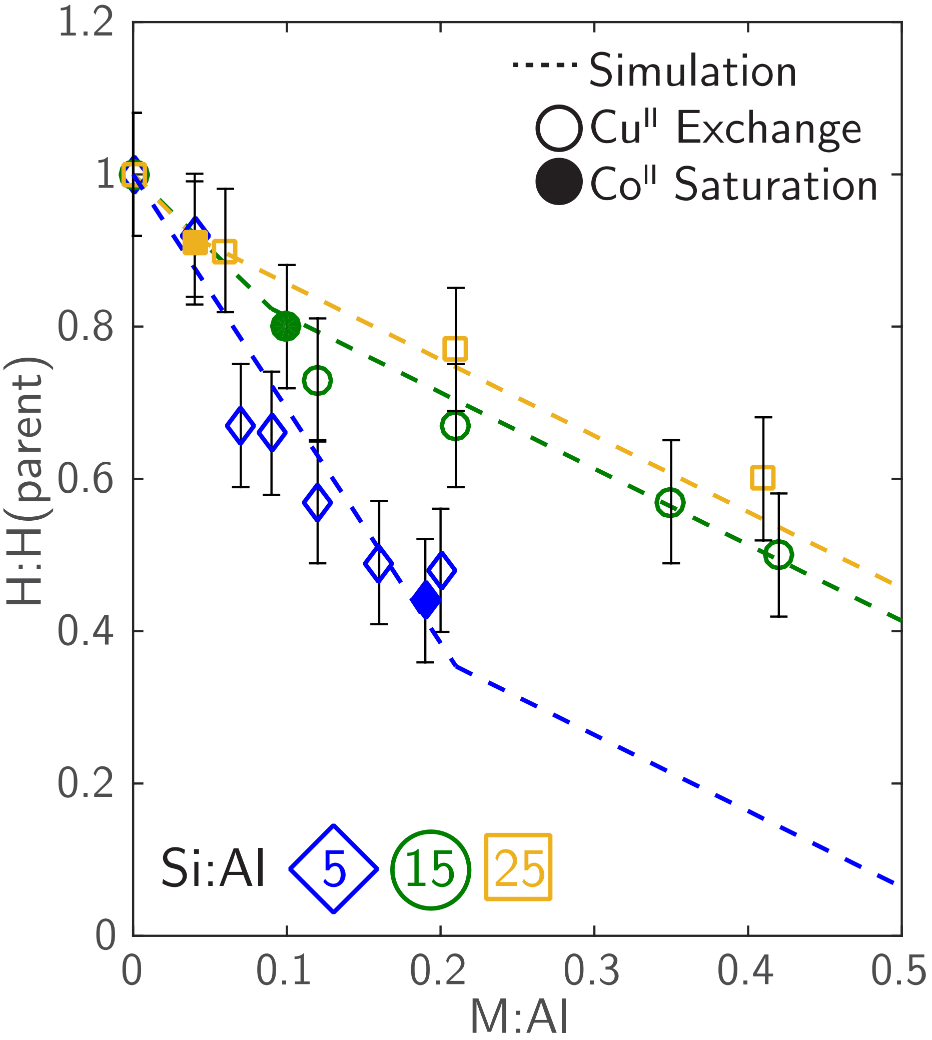

Figure 2.3.4 Residual H^+ sites per parent sample H^+ from NH_3 titrations on oxidized M-SSZ-13 samples vs. extent of M/Al exchange for Si:Al = 5 (blue diamonds), 15 (green circles) and 25 (orange squares). Open and filled symbols denote Cu^{2+} and saturated Co^{2+} exchange, respectively. Dashed lines are model predictions.

Figure 2.3.4 shows the number of residual H^+ sites present on each Cu-SSZ-13 sample after oxidative treatment in flowing air (773 K), normalized by the number of H^+ sites quantified on their respective H-SSZ-13 parent samples after the same oxidative treatment, as a function of Cu:Al ratio. The dashed lines in Figure 2.3.4 represent the number of residual H^+ sites as a function of Cu:Al ratio predicted from the simulation results in Figure 2.3.3. At a Si:Al ratio of 5, each exchanged Cu cation decreased the number of residual H^+ sites by two (on average) up to a Cu:Al ratio of 0.2 (Figure 2.3.4) [135, 136], consistent with the exchange stoichiometry:

$$Z_2H_2 + Cu(II) \rightarrow Z_2Cu + 2H^+ \ldots\ldots 2.9$$

On samples with Si:Al ratios of 15 and 25, each exchanged Cu exchanged two H^+ sites until Cu:Al ratios of 0.1 and 0.04, respectively, but only one additional H^+ site beyond this limit (Figure 2.3.4), consistent with the exchange reaction:

$$ZH + Cu(II)H_2O \rightarrow ZCuOH + 2H^+ \ldots\ldots 2.10$$

These Cu:H^+ exchange stoichiometries provide experimental evidence that cationic Cu species exchange sequentially as [Z_2Cu(II)] sites until saturation and then [ZCu(II)(OH)] sites (Figure 2.3.1).

Figure 2.3.5 shows FTIR quantification of the disappearance of Brønsted ZH species and the appearance of [ZCu(II)OH] as a function of Cu density on the series of Cu-SSZ-13 samples with Si:Al = 15. The H-SSZ-13 spectrum includes four features in the O-H region, including modes at 3605 and 3580 cm^{-1} [137, 138] from Brønsted sites, at 3732 cm^{-1} from isolated silanols, and at 3700 cm-1 from vicinal silanols [139]. The integrated area of the Brønsted ZH peaks of the Cu:Al = 0.12 sample, taking that of the H-SSZ-13 sample as the baseline, decreased with a 2:1 H^+:Cu ratio (appendix A), consistent with equation 2.9. A new, fifth feature appears at 3651 cm^{-1} in Cu:Al $\geq$ 0.21 samples, at a location consistent with previous assignment to [105], and the computed harmonic O-H stretch frequency of [ZCu(II)OH]. The integrated area of this 3651 cm^{-1} band increases linearly across the range Cu:Al = 0.21-0.44, (Figure 2.3.5 inset), and the integrated areas of the Brønsted OH stretches decrease concurrently in a 1:1 H^+:Cu ratio, consistent with equation 2.10. These vibrational data provide strong support for the sequential population of [Z_2Cu(II)] followed by [ZCu(II)OH] sites.

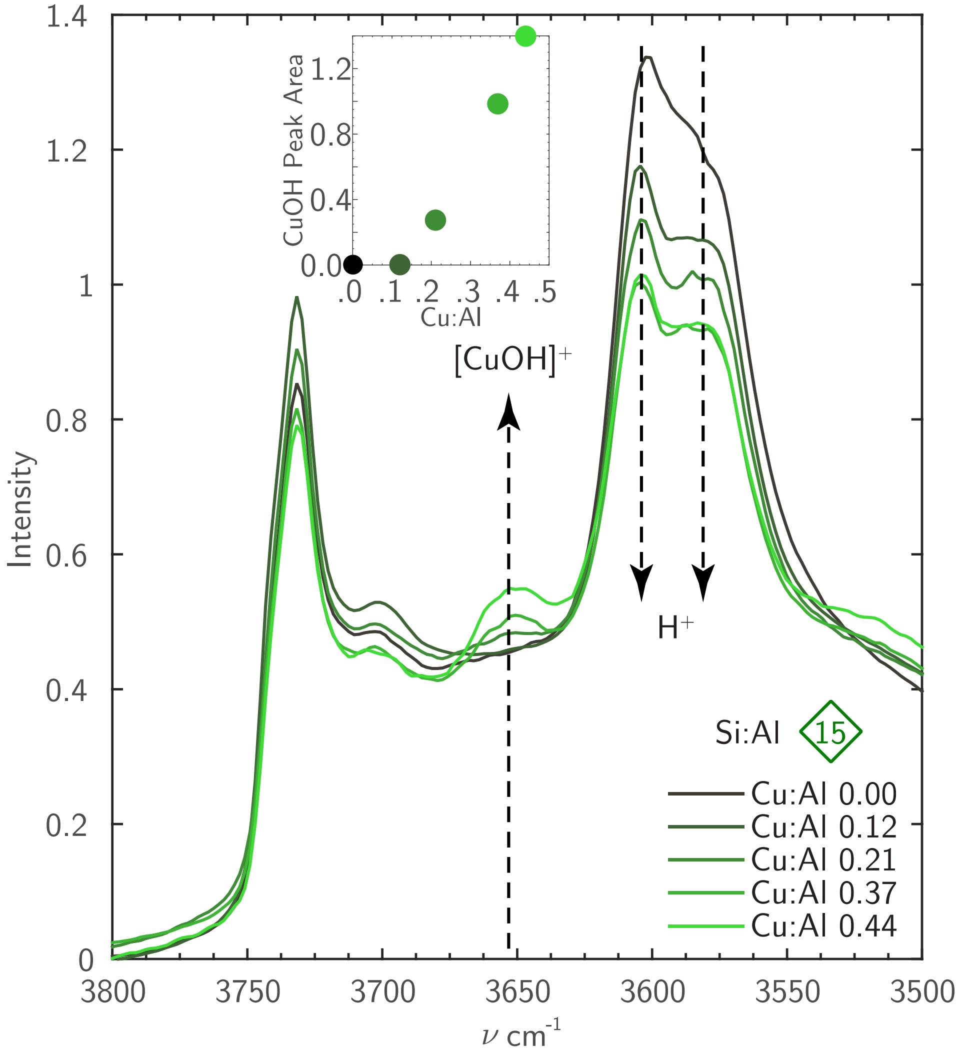

Figure 2.3.5 FTIR spectra of oxidized Cu-SSZ-13 samples (Cu:Al = 0-0.44, Si:Al = 15). Inset: Integrated 3651 cm^{-1} CuO-H area as a function of Cu:Al ratio.

Co(II) exchange provides a third independent enumeration of the number of 2Al 6MR sites on each sample, because Co(II) does not exchange at single Al sites as [ZCo(II)OH] at the exchange pH used here (pH ≈ 3.2) [140]. Samples with Si:Al ratios 5, 15 and 25 were saturated with Co(II) and the Co:Al contents were determined by atomic absorption (appendix A) to be 0.19, 0.1 and 0.04, respectively. These values agree quantitatively with the maximum number of 2Al 6MR sites predicted for each Si:Al ratio in Figure 2.3.3 for a random Al distribution in SSZ-13. Furthermore, the number of residual H^+ sites on Co-saturated H-SSZ-13 samples were quantified by NH_3 titration, and are plotted on Figure 2.3.4 as filled symbols, and agree quantitatively with the transition Cu:Al ratios between exchange of $[Z_2Cu(II)]$ and [ZCu(II)OH] species. These results indicate that isolated Co(II) and Cu(II) exhibit identical preferences for 2Al 6MR sites, and that both cations replace two Brønsted sites via equation 2.9 when exchanged at these sites.

The Cu:Al values that demarcate the transition between formation of $[Z_2Cu(II)]$ sites and [ZCu(II)OH] sites are 0.2, 0.1 and 0.04 for the H-SSZ-13 samples with Si:Al ratios of 5, 15 and 25, respectively (Figure 2.3.4). These Cu:Al values are identical, within error, to the fraction of 2Al 6MR sites predicted from simulation of Al distribution in CHA frameworks at these Si:Al ratios (Figure 2.3.3). Taken together, the experimental and computational findings indicate that under conditions of synthesis applied here [141], Al are distributed randomly in SSZ-13 subject to Löwenstein's rule, that 2Al 6MR are the preferred sites for Cu(II) exchange, and that these sites saturate before remaining 1Al sites are populated with [ZCu(II)OH]. This quantification allows us to identify and contrast the structures, properties and catalytic performance under low temperature (473 K) standard SCR conditions of samples that contain predominantly $[Z_2Cu(II)]$ or [ZCu(II)OH] sites. We chose a sample with Si:Al = 5 and Cu:Al = 0.08 to represent a $[Z_2Cu(II)]$ site and a sample with Si:Al = 15 and Cu:Al = 0.44 to represent [ZCu(II)OH], which we refer to as the "2Al" and "1Al" samples, respectively.

2.3.2 Copper Cation Structure under *ex situ* Conditions

We next combine XAS and AIMD simulations to explore the molecular and the electronic structures of both the model 1Al and 2Al samples as a function of the hydrothermal conditions represented in Figure 2.3.2. Results are summarized in Figure 2.3.6 and Figure 2.3.7, and in Table 2.3.2.

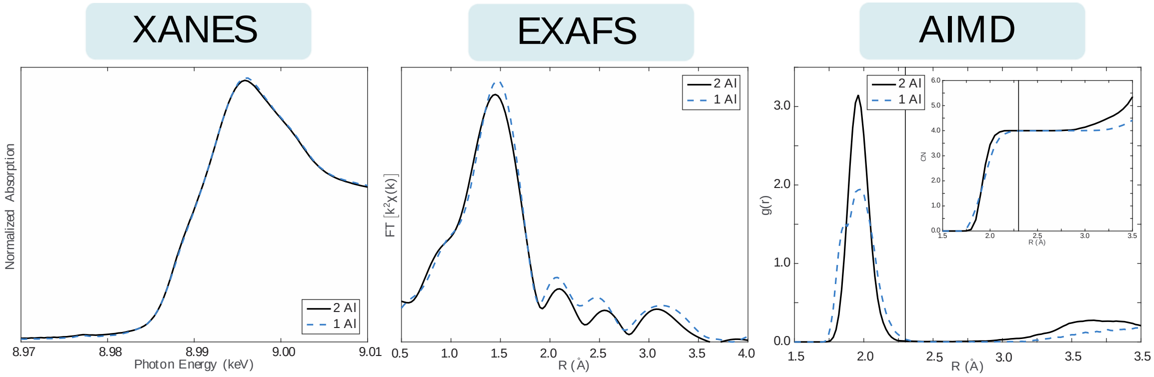

Figure 2.3.6 Left: XANES spectra collected on the 1Al (teal dashes) and 2Al (black lines) Cu-SSZ-13 samples under treatment in 2% H_2O, 20% O_2 at 298 K. Middle: EXAFS spectra at same conditions. Right: 298 K AIMD RDFs and integrated RDFSs (inset).

2.3.2.1 Condition 1: Ambient Atmosphere (XAS/AIMD)

First, both 1Al and 2Al samples were subjected to high temperature oxidative treatments and then exposed to ambient atmosphere at 298 K, corresponding to Condition 1 of Figure 2.3.2. The Cu K-edge X-ray absorption near edge spectra (XANES) collected on both samples were indistinguishable, as shown in Figure 2.3.6, left. A single edge at 8.988 keV corresponds to the 1s → 4p transition of a Cu(II) ion in a distorted square-planar or octahedral coordination [118]. EXAFS spectra of both samples from the same energy scan (Figure 2.3.6, middle) exhibited a high intensity first coordination shell peak at ≈ 1.5 Å (not phase-corrected). The spectra were fitted using a Cu_2O(s) experimental reference to estimate 4 Cu-O bonds (1.94 Å average distance) and 4.2 Cu-O bonds (1.93 Å average distance), respectively on the 2Al and 1Al samples, which are identical within the ±10% error of the fit (appendix A). Higher coordination shells beyond 2.0 Å appear with low intensity on both samples and indicate Cu-O bonds with extra-framework O species, as evidenced by the absence of scattering from Si or Al atoms bound to O_f. The XANES and EXAFS spectra are indistinguishable from each other and that of aqueous Cu(II) complexes [118], which are also known to form a square-planar tetraaquo complex. These observations are in agreement with the phase diagram Condition 1 predictions shown in Figure 2.3.2.

Table 2.3.2 Comparison of AIMD (blue, left) and EXAFS (black, right) characterization of 2Al and 1Al sites, including Cu-X (X = O, N) coordination number (CN), average Cu-X distances and whether second-shell features appear

	AIMD/EXAFS				
Gas Condition	Sample	CN	Avg. Bond Dist.	2nd Shell	Cu mobility[c]
Condition 1 (Ambient)	1Al	4.0/4.2	1.96/1.93	N/N	1.38
	2Al	4.0/4.0	1.96/1.94	N/N	1.00
Condition 2 (O_2)	1Al	3.0/3.0	1.89/1.91	Y/Y	0.11
	2Al	3.9/3.8	2.02/1.94	Y/Y	0.14
Condition 3 (He)	1Al	2.5[a]/2.4	1.92[a]/1.92	Y/Y	0.14a
	2Al	3.7[a]/3.6	2.50[a]/2.4	Y/Y	0.14a
NO + NH_3 473 K	1Al	2.0/2.2	1.89/1.88	N/N	3.26
	2Al	2.0/2.1	1.89/1.88	N/N	1.83
O_2 + NH_3 473 K	1Al	3.3[b]/3.2	1.97[b]/1.92	N/N	2.21[b]
	2Al	3.6[b]/3.5	2.00/1.92	N/N	1.31[b]

[a] XANES weighted average of Cu(I) (ZCu(I)) and Cu(II) (Z_2Cu and ZCuOH) structures obtained from AIMD.

[b] XANES weighted average of Cu(I) ($ZCu(I)(NH_3)_2$) and $ZNH_4/ZCu(I)(NH_3)_2$ and Cu(II) ($Z_2Cu(NH_3)_4$ and $ZCu(OH)(NH_3)_3$) structures obtained from AIMD.

[c] Volume visited by the minimum free energy forms of Cu(I) and Cu(II) () during 90 ps AIMD, normalized to the volume of hydrated Z_2Cu (1.00).

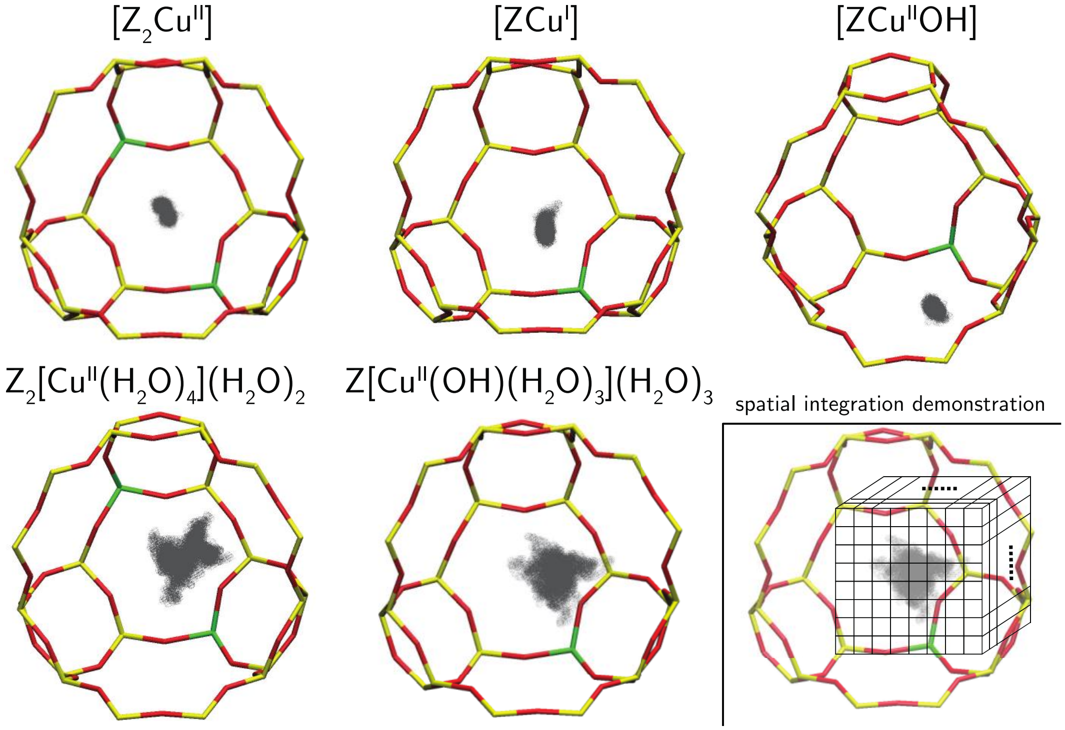

Figure 2.3.7 Cu positions (grey balls) visited during 90 ps of NVT AIMD at 298 K. Fixed zeolite framework shown for ease of visualization; framework was unconstrained during dynamics. Inset illustrates discretization used to compute relative Cu mobilities.

The EXAFS provides an ensemble average of the Cu coordination environment. To extract comparable information from simulation, we performed 298 K AIMD simulations (50 ps of equilibration followed by 90 ps of sampling) on the lowest free energy hydrated forms of [Z_2Cu(II)] and [ZCu(II)OH]. In both cases, Cu remained near the center of the cage (Figure 2.2.1c) and were dynamic. Figure 2.3.7 superimposes the Cu positions relative to the zeolite cage during the 90 ps sampling. To quantify Cu mobility, we discretized the supercell into 0.2 x 0.2 x 0.2 Å cubes, counted the cubes visited at least once during the simulation, scaled by the cube volume, and normalized to the volume visited by Z_2[Cu(II)(H_2O)$_4$](H_2O)$_2$. Results are summarized in Table 2.3.2 and further detailed in appendix A. Z[Cu(II)OH(H_2O)$_3$](H_2O)$_3$ is estimated to be 1.38 times as mobile as

$Z_2[Cu(II)(H_2O)_4](H_2O)_2$, consistent with the weaker electrostatic attraction to a single Al compared to two proximal Al atoms. Throughout the $Z[Cu(II)OH(H_2O)_3](H_2O)_3$ simulation, H atoms are observed to hop between non-framework O with a barrier of ≈20 kJ mol^{-1}, causing O bound Cu to spend time as both OH and H_2O.

The right panel of Figure 2.3.6 shows the computed radial distribution functions (RDFs) between Cu and all heavy atoms. Both RDFs show a prominent peak near 2 Å corresponding to the first coordination shell with peak area corresponding to four O atoms. This first RDF peak corresponds with the first EXAFS peak (the RDF and EXAFS are offset due to the difference between electron scattering and interatomic distances). The 1Al RDF is broadened in comparison to the 2Al due to the presence of both shorted Cu-OH and longer Cu-H_2O bonds that are not resolvable by EXAFS. The RDFs are near-zero between 2.2-3 Å; structure appears beyond 3 Å. The results are consistent with the observation of only low intensity peaks beyond the first major one in the EXAFS and H_2O solvated Cu complexes.

2.3.2.2 Condition 2: 20% O_2, 673 K (XAS/AIMD)

Next, we collected XANES spectra at 298 K on both samples after 1 hr treatment at 673 K in O_2, corresponding to Condition 2 in Figure 2.3.2. The vessels were sealed before cooling to prevent rehydration of Cu. Resultant XANES and EXAFS are shown in Figure 2.3.8. In addition to the 8.988 keV Cu(II) edge feature observed in Figure 2.3.6, an additional feature appears at 8.987 keV that reflects Cu(II) present in a lower than octahedral coordination environment [67]. Further, on the 1Al sample a low intensity peak appears at 8.983 keV that we assign to 5% Cu(I) based on a fit using Cu(I) and Cu(II) references (appendix A).

The EXAFS (Figure 2.3.8, middle) exhibit high intensity peaks at ≈1.5 Å that fit to 3.0 Cu-O bonds at 1.91 Å and 3.8 Cu-O bonds at 1.94 Å on the 1Al and 2Al samples, respectively (Table 2.3.2). Consistent with the higher first-shell coordination and closer proximity to multiple Si:Al, the 2Al sample also exhibits a more distinct second shell peak at ≈2.4 Å than that on the 1Al sample. To ensure reversibility, we cycled samples between Condition 1 and Condition 2, and confirmed that XAS spectra were identical to those shown in Figure 2.3.6.

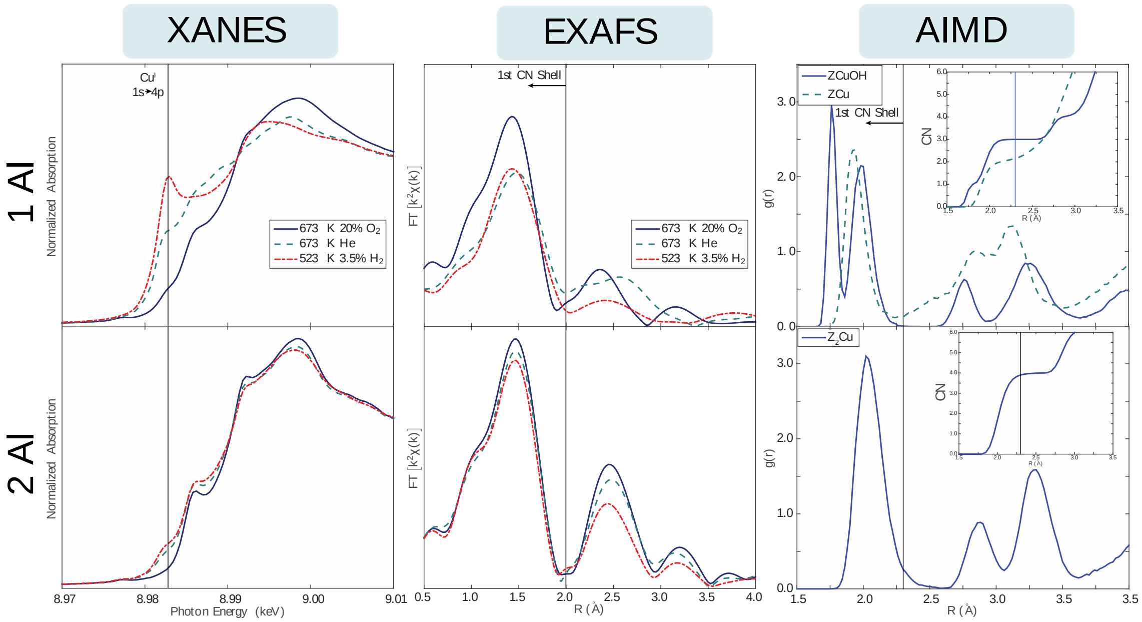

Figure 2.3.8 Left: XANES spectra collected on the 1Al (top) and 2Al (bottom) samples after treatment in 20% O_2 at 673 K (solid blue lines), He at 673 K(dashed teal lines) and in 3% H_2 at 523 K (dot-dashed red lines). Middle: Corresponding EXAFS spectra. Right: AIMD Cu-Si/O/Al RDFs for ZCuOH and ZCu (top) and Z_2Cu (bottom). Insets show integrated RDFs.

These EXAFS features are consistent with those expected for the [Z_2Cu(II)] and [ZCu(II)OH] species predicted to predominate at Condition 2. Cu remain bound to multiple O_f for the duration of AIMD simulations on each, and each are computed to be about 8 times less mobile than the $Z_2[Cu(II)(H_2O)_4](H_2O)_2$ reference. The $[Z_2Cu(II)]$ site oscillates between three nearly isoenergetic minima (appendix A) that differ in the O_f nearest-neighbor to Cu. The 1st shell in RDF (Figure 2.3.8, bottom right) convolutes these three and integrates to a CN = 3.9. By deconvolution of the RDF, we assign the second feature at ≈2.8 Å to one Al and one Si atom nearest Cu (appendix A). The AIMD CN is consistent with the EXAFS fit.

In contrast, [ZCu(II)OH] only exhibits a “wagging” into and out of the 8MR plan during AIMD. The Cu-O_f and Cu-OH pairs appear as sharp features in the RDF (Figure 2.3.8, top right). The integrated RDF and fitted CN are identical. The slightly broad second shell feature at ≈2.75 Å arises from the Al nearest Cu (Figure 2.2.1b). This second shell feature is at 0.25 Å shorter distance and half the integrated area of the $[Z_2Cu(II)]$ second shell, consistent with both the location and magnitude of the EXAFS second shell features.

2.3.2.3 Condition 3: He, 673 K (XAS/AIMD)

As noted above, a small amount of Cu(I) appears in the XANES of the calcined 1Al sample. This auto-reduction feature [32, 105], becomes more prominent after treating the 1Al sample in flowing helium at 673 K for 1 hr following the calcining treatment (Figure 2.3.8, left panel). From spectral deconvolution and EXAFS fitting, we infer 55% of the Cu to be present as Cu(I) and the mean Cu-O coordination number to decrease to 2.4 (Table 2.3.2). In contrast, only 10% Cu(I) is observed on the 2Al sample following the same helium treatment, and the coordination number is unchanged. The Cu(I) feature becomes even more pronounced and the Cu(I) fraction increases to 65% on the 1Al sample treated in 3% H_2 at 523 K [114, 115]; the 2Al sample is changed negligibly by H_2 reduction. These observations of auto-reduction in the 1Al but not the 2Al samples are consistent with the predictions for Condition 3 in Figure 2.3.2. That reduction is not complete on the 1Al sample suggests some kinetic as well as thermodynamic contribution to the auto-reduction process, possibly associated with the mobility of the [ZCu(II)OH]. Re-oxidation of samples after the He purge or H_2 treatment returns the XANES and EXAFS spectra to their post-calcination forms (additional details in appendix A), indicating that reduction and re-oxidation are reversible.

To interpret the observed EXAFS, we used 298 K AIMD to compute the dynamics of the reduced [ZCu(I)] site. The Cu ion stays within the 6MR and retains coordination to the same two O_f atoms; the computed RDF (Figure 2.3.8) is dominated by a Cu-O_f feature at 1.93 Å that integrates to CN 2.1. The Cu mobility is enhanced by about 20% compared to [ZCu(II)OH] and [Z_2Cu(II)], but still roughly 8 times less than hydrated [Z_2Cu(II)]. The second shell feature in EXAFS, spanning from roughly 2-3 Å, is echoed in the broad AIMD RDF past the first coordination shell, a consequence of [ZCu(I)] mobility within the 6MR.

2.3.3 Copper Speciation at SCR Conditions

The *ex situ* characterizations above show that Cu in the 1Al and 2Al samples are identical under ambient and hydrated conditions, exhibit different coordination after high temperature oxidation, and respond differently to high temperature reduction. We next explore the implications under catalytic conditions relevant to low-temperature NO_x SCR.

2.3.3.1 *Operando* XAS Spectra and SCR Kinetics

We used a custom-built reactor [29] designed to collect XAS spectra in *operando* to determine the Cu oxidation states of the 2Al and 1Al samples during steady-state SCR (300 ppm NO, 300 ppm NH_3, 10% O_2, 2% H_2O, 5% CO_2) at 473 K under differential and plug-flow conditions (< 20% NO conversion). Observed SCR turnover rates (TOR, mol NO (mol Cu^{-1}) s^{-1}), apparent NO, O_2 and NH_3 reaction orders, and apparent activation energies (E_{app}) (Table 2.3.3) were identical on the 2Al and 1Al samples, within experimental error, and identical to values measured on these samples in a different plug-flow reactor (section 2.6.5). *Operando* XANES spectra for the two samples (Figure 2.3.9, left, black traces) indicate the presence of 50% and 55% Cu(I) (8.983 keV peak), respectively, that are identical within fitting error (5%). Although the presence of both Cu(II) and Cu(I) species during standard SCR redox cycles is not surprising [20, 30, 33, 96, 129], the identical Cu(I) fractions and kinetic parameters (Table 2.3.3) are unexpected given the different structures, dynamics and reducibility of [Z_2Cu(II)] and [ZCu(II)OH] species in He and H_2. These *operando* characterization results suggest that cationic copper sites are functionally equivalent during low temperature standard SCR at 473 K.

Table 2.3.3 Characterization of 2Al and 1Al Cu-SSZ-13 catalysts during low temperature (473 K) standard SCR: XANES Cu(I)/Cu(II) fraction, SCR rates (per Cu and mol NO) in the *operando* reactor/plug-flow reactor, apparent activation energies and apparent NO, O_2 and NH_3 orders.

	Cu(I)/Cu(II)	TOR[a]	E_{app} (kJ mol^{-1})	NO order	O_2 order	NH_3 order
2Al	50/50 ± 5	8.3/7.3	60 ± 10	0.8/0.8	0.3/0.3	-0.2/-0.1
1Al	55/45 ± 5	9.9/8.0	74 ± 10	n.m./0.7[b]	n.m./0.3[b]	n.m./0.0[b]

[a](mol NO (mol Cu)$^{-1}$ s^{-1}) x 10^{-3} [b]n.m.= not measured, 1 Al orders were measured only in the PFR.

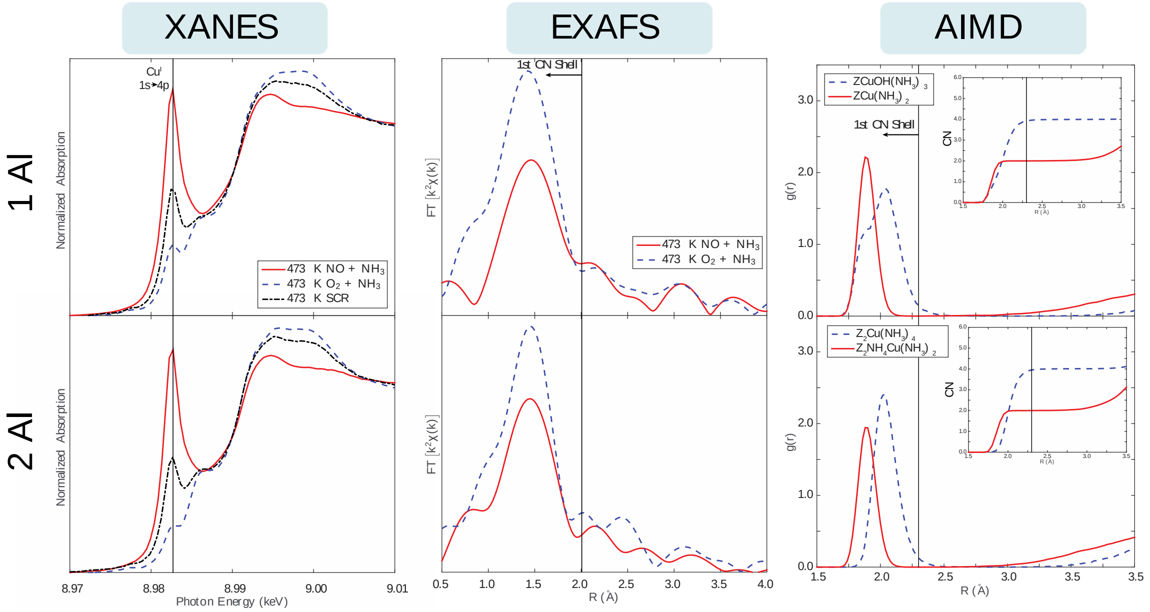

Figure 2.3.9 Left: XANES spectra of the 1Al (top) and 2Al (bottom) Cu-SSZ-13 samples under treatment in 2% H_2O, 10% O_2, 300 ppm NH_3 at 473 K (O_2 + NH_3, blue traces), 2% H_2O and 300 ppm NO/NH_3 at 473 K (NO + NH_3, red lines) and in 2% H_2O, 10% O_2, 300 ppm NO/NH_3 at 473 K (black traces). Middle: EXAFS collected under same conditions. Right: AIMD Cu-Si/O/Al RDFs for the most stable Cu(I) (red lines) and Cu(II) (blue traces) species on the 1Al and 2Al sites in the presence of NH_3. Insets: Integrated RDFs.

2.3.3.2 SCR gas species binding energies

To understand Cu coordination in the SCR gas mixture (H_2O, N_2, NH_3, NO, O_2), we first computed adsorption energies of these species as well as NO_2, which is often proposed as an SCR intermediate [33, 125-128], on the oxidized and reduced forms of the 1Al and 2Al Cu sites using the same AIMD and HSE06-TSvdw quenching protocol. The computed NH_3 binding energy to the [ZH]/[ZCu(I)] Brønsted site is -151 kJ mol^{-1}, quantitatively consistent with NH_3 differential heats observed via microcalorimetry on zeolitic H^+ sites [142-146]:

$$[ZH]/[ZCu(I)] + NH_3 \rightarrow [ZNH_4]/[ZCu(I)] \ldots\ldots 2.11$$

Thus, the NH_4^+ form of this site prevails under SCR conditions, and we used the [ZNH_4]/[ZCu(I)] structure shown in Figure 2.3.10 as the model for a reduced 2Al site.

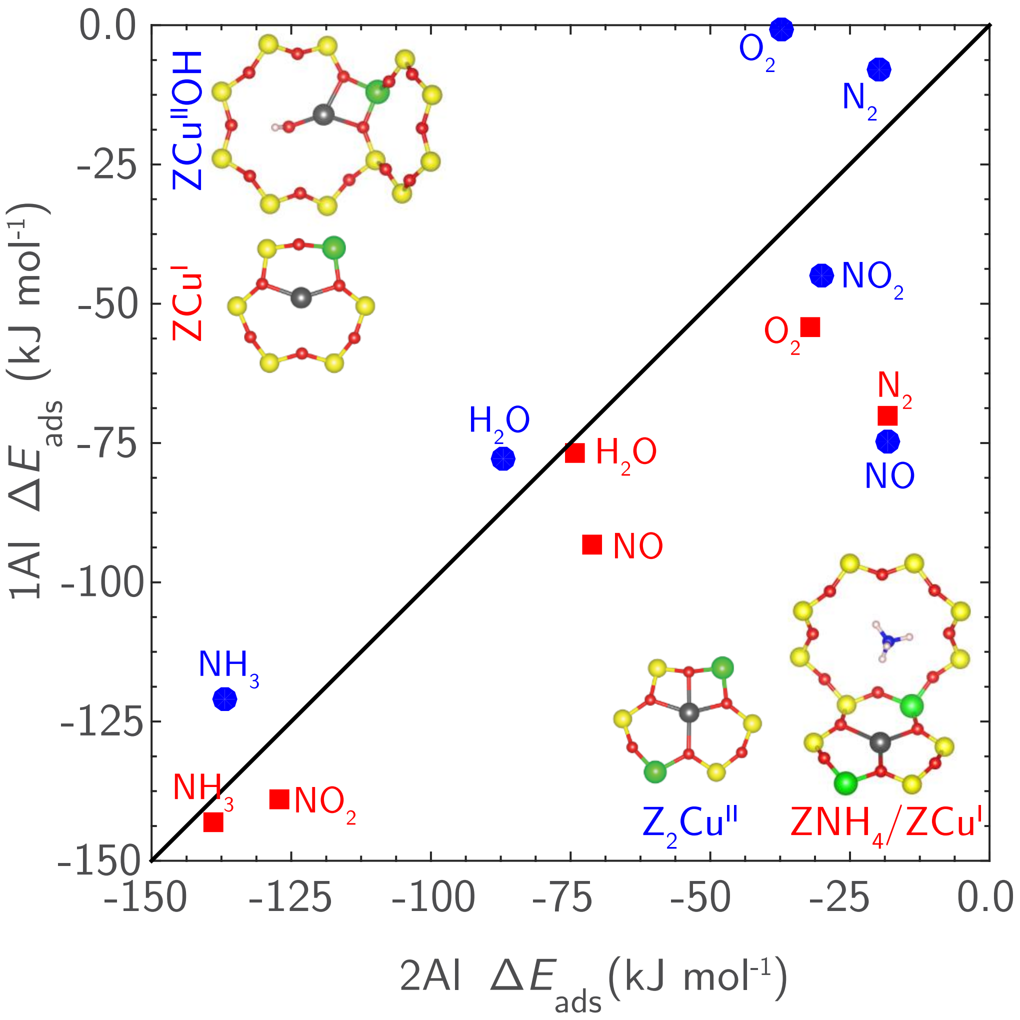

Figure 2.3.10 Parity plot of HSE06-TSvdw-computed binding energies of gaseous species relevant to SCR on 2Al oxidized (Z_2Cu, blue) and reduced (ZNH_4/ZCu, red) vs. the corresponding oxidized (ZCuOH, blue) and reduced (ZCu, red) 1Al sites.

Computed 1Al site binding energies are plotted against 2Al sites in Figure 2.3.10. Binding energies without the TSvdw correction are approximately 20 kJ mol^{-1} more positive. Binding energies (appendix A) and structures on the [Z_2Cu(II)] and [ZCu(II)OH] sites are generally consistent with those for H_2O, NO and NH_3 reported elsewhere [33, 107, 120-122], although the inclusion of hybrid exchange significantly decreases the NO binding relative to the GGA values [33, 107, 120-122]. The 1Al and 2Al binding energies are roughly linearly correlated, although deviations as large as 50 kJ mol^{-1} are evident. O_2 interacts weakly with all sites; H_2O and NO exhibit intermediate binding strengths. NH_3 binds by -120 to -140 kJ mol^{-1} on all four Cu adsorption sites and does not significantly alter the Cu oxidation state. NO= binds strongly to reduced sites (oxidizing the Cu center to form a nitrite) but interacts weakly with oxidized Cu. NO is a notable outlier from the linear correlation: the HSE calculations predict NO to bind weakly to [Z_2Cu(II)] (-25 kJ mol^{-1}) but with intermediate strengths on [ZCu(II)OH] (-75 kJ mol^{-1}). NO locates near the OH ligand rather than Cu, similar to structures for this species reported elsewhere [107], but does not form a HONO-like structure. N_2 more strongly adsorbs to [ZCu(I)] than to other sites.

Because NH_3 out-binds all other species, and is similar in its coordination behavior to H_2O, we explored the sequential binding of additional NH_3 on all four sites:

$$*(NH_3)_{x-1} + NH_3 \xrightarrow{\Delta E_{ads}} *(NH_3)_x \ldots\ldots 2.12$$

using an AIMD anneal at 473 K followed by HSE06-TSvdw optimization, where * represents the Cu site. Results are summarized in Table 2.3.4; structures and normalized Cu Bader charges are detailed in appendix A. Binding energies are roughly constant as NH_3 displaces O_f from the Cu coordination sphere. Cu(I) and Cu(II) retain 2-fold and 4-fold coordination, respectively; additional NH_3 beyond these limits are more weakly bound and not directly associated with Cu, instead forming hydrogen bonds with NH_3 in the first coordination sphere. The only exception is ZCu(II)OH$(NH_3)_2$; this species adopts a square-planar conformation including a single O_f ligand at 0 K, but in the finite T dynamics adopts a trigonal-planar form, free from O_f for ≈90% of the trajectory. Energy and entropy are evidently closely balanced between the two configurations.

Table 2.3.4 HSE06-TSvdw-computed sequential NH3 adsorption structures and energies. Cage location indicates optimized ion location referenced to Figure 2.2.1. CN and Of indicate total Cu coordination number and number of close framework O contacts, respectively.

	+ xNH_3	1	2	3	4
[Z_2Cu(II)]	ΔE_{ads} (kJ mol^{-1})	-132	-136	-123	-132
	Cage Location	A	A	B	C
	O_f/total CN	3/4	2/4	1/4	0/4
[ZNH_4]/[ZCu(I)]	ΔE_{ads} (kJ mol^{-1})	-134	-150	-72	-73
	Cage Location	B	C	C	C
	O_f/total CN	1/2	0/2	0/2	0/2
[ZCu(II)OH]	ΔE_{ads} (kJ mol^{-1})	-117	-119	-116	-47
	Cage Location	B	C, B[a]	C	C
	O_f/total CN	2/4	0/3, 1/4[a]	0/4	0/4
[ZCu(I)]	ΔE_{ads} (kJ mol^{-1})	-137	-151	-75	-41
	Cage Location	B	C	C	C
	O_f/total CN	1/2	0/2	0/2	0/2

[a]Trigonal planar, square planar values.

2.3.3.3 NH_3 Phase Diagrams

We used a first-principles thermodynamic analysis to rang the free energies of the NH_3 species in Table 2.3.4 and H_xO_y structures from Figure 2.3.1, 42 species in total, taking O_2, H_2O and NH_3 as oxygen, hydrogen and nitrogen references, respectively:

$$ZCu + \frac{x}{2}\left(H_2O - \frac{1}{2}O_2\right) + \frac{y}{2}O_2 + z\left(NH_3 - \frac{3}{2}H_2O + \frac{3}{4}O_2\right) \xrightarrow{\Delta G_{form}} ZCuH_xO_yN_z \ldots\ldots 2.13$$

Figure 2.3.11 reports the lowest free energy 1Al and 2Al species as a function of T and O_2 partial pressure at H_2O and NH_3 concentrations of 2% and 300 ppm, respectively, representative of the experimental conditions shown in Figure 2.3.9. We chose O_2 pressure as an independent variable for direct comparison to the experimental results detailed in the preceding section. The resultant phase diagrams are substantially different from the H_xO_y ones in Figure 2.3.2; NH_3-containing species dominate the diagrams up to 773 K, and H_2O is an unimportant adsorbate. The most prominent species in the 1Al and 2Al diagrams are reduced Cu(I) species and oxidized Cu(II) species, respectively, although both oxidized and reduced forms of Cu appear on both diagrams. Both sites are saturated with NH_3 at 473 K, and successively lose NH_3 ligands with increasing temperature. At 473 K, the 2Al phase diagram (Figure 2.3.11, right) shows Cu preferring $Cu(I)(NH_3)_2$ as the O_2 concentration decreases, and $Cu(II)(NH_3)_4$ species as the O_2 concentration increases. The $Cu(I)(NH_3)_2$ complex is the most stable 1Al species over the entire O_2 range examined here. Sidebars in Figure 2.3.11 rank the relative free energies of intermediates at the condition indicated by the chrome spheres in the phase diagrams (473 K and 10% O_2), equivalent to those in Figure 2.3.9. Species with $\Delta G_{form} > 0$ kJ mol^{-1} are excluded for clarity; full results are tabulated in appendix A. The analysis predicts a reduced and NH_3-saturated Cu(I) to be the most stable 1Al species at these conditions. Cu(I) complexes with one or three NH_3 ligands are higher in free energy, and the first Cu(II) species to appear is $Z[Cu(II)(OH)(NH_3)_3]$ at 50 kJ mol^{-1} higher free energy than the most stable species. Thus, these two NH_3-saturated and O_f-liberated complexes are the most likely dominant forms of Cu(I) and Cu(II) under SCR conditions in the 1Al catalyst. The Cu(I)/Cu(II) ordering is reversed at the 2Al site, where the most stable complex is an oxidized and NH_3-saturated $Z_2[Cu(II)(NH_3)_4]$ at 16 kJ mol^{-1} below the reduced and NH_3-saturated $[ZNH_4]/Z[Cu(I)(NH_3)_2]$. The Cu(I)/Cu(II) fractions are the same in the *operando* XANES (Figure 2.3.9) on the 1Al and 2Al samples, and likely kinetically rather than thermodynamically controlled. The thermodynamic screening identifies the species most relevant to catalysis, and highlights the importance of NH_3 coordination under SCR conditions.

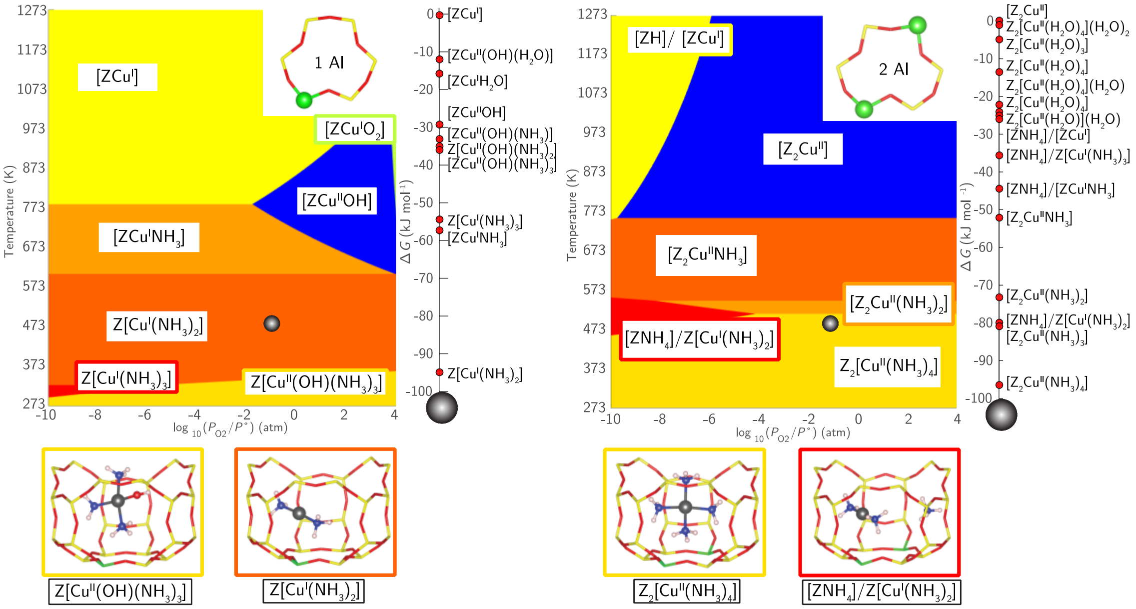

Figure 2.3.11 Phase diagrams for 1Al (left) and 2Al (right) sites with varying T and P_{O2} at 300 ppm NH_3 and 2% H_2O. Relative rankings for all species $\Delta G_{form} < 0$ at 473 K and 10% O_2 (chrome spheres on the phase diagrams) are given to the right of each phase diagram. The structures shown on the bottom are the most stable Cu(I) (red) and Cu(II) (golden) under these conditions.

2.3.3.4 XAS/AIMD for Cu(I)/Cu(II) with NH_3

To explore Cu structure and dynamics under SCR conditions, we collected XAS and AIMD information on both 1Al and 2Al samples prepared with subsets of SCR gas mixes that place them primarily in the Cu(I) and Cu(II) states.

Figure 2.3.9 shows the XANES and EXAFS at 473 K of 1Al and 2Al samples treated in 300 ppm NO plus NH_3. Consistent with previous reports [30, 33, 129], this treatment reduces Cu. In fact, the XANES and EXAFS on both samples are indistinguishable and the XANES fit to a Cu(I) fraction of 100%. A prominent first shell peak at 1.88 Å in the EXAFS fits to 2.1 CN, which EXAFS cannot distinguish between O and N. The EXAFS is absent of longer-range structure.

These XAS results are consistent with the reduced Cu forms highlighted in Figure 2.3.11. We performed 473 K AIMD simulations on [ZNH_4]/Z[Cu(I)(NH_3)$_2$] and [Z[Cu(I)(NH_3)$_2$] for the 2Al and 1Al sites, respectively. The linear Cu(I)(NH_3)$_2$ species are identical in structure and, as evidenced in the dynamics trajectory (Figure 2.3.12) and the volume visited (Table 2.3.2), highly mobile. Computed RDFs between Cu and other heavy atoms are shown in Figure 2.3.9. As in the EXAFS, the lone peak at 1.89 Å integrates to 2.0 CN; the Cu location is completely disordered with respect to the zeolite lattice. To probe the ability of this NH_3-mobilized Cu(I) to diffuse between cages, we used the climbing image nudged elastic band (CI-NEB, appendix A) method to compute the energy to thread a Cu(I)(NH_3)$_2$ ion through the 8MR. The path starts with one NH_3 in the plane of the 8MR, passes over a 37 kJ mol^{-1} transition state in which the Cu is centered within the ring, and ends with the other NH_3 in the 8MR. This modest barrier suggests rather facile transport of reduced NH_3 within the SSZ-13 lattice, as has been inferred from the NH_3-facilitated exchange of Cu(I) [147].

Figure 2.3.9 similarly shows XAS spectra collected on the same samples during exposure to an oxidizing mixture of NH_3 (300 ppm) and O_2 (10%) at 473 K. The XANES are again similar to one another but markedly different from those at the reducing condition. Both samples exhibit a peak at 8.983 keV corresponding to a Cu(I) species, 27% and 17% on the 1Al and 2Al samples, respectively, and a balance of Cu(II) species. EXAFS show prominent first coordination shells at 1.5 Å (not phase-corrected) that fit to 3.2 and 3.5 O or N around Cu at 1.92 Å. Neither EXAFS exhibit second shell coordination in the 2.5-3 Å range. RDFs and AIMD performed at 473 K on Z[Cu(II)(OH)(NH_3)$_3$] and

$Z_2[Cu(II)(NH_3)_4]$, corresponding to the oxidized 1Al and 2Al species at SCR conditions, are also shown in Figure 2.3.9.

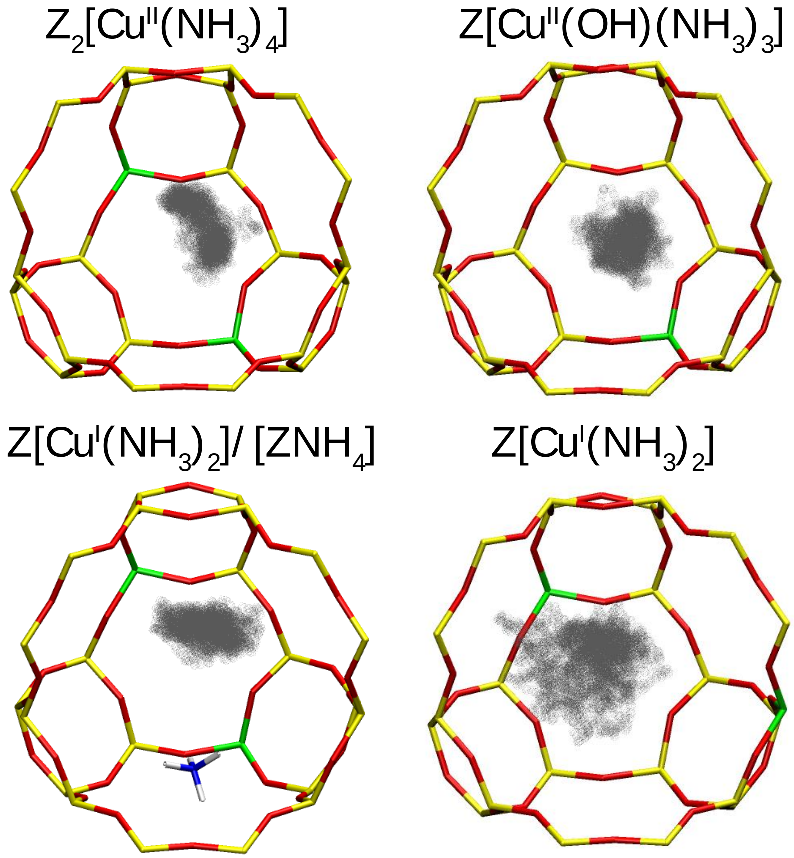

Figure 2.3.12 Cu positions (grey balls) sampled inside the zeolite cage during 90 ps of equilibrated NVT AIMD at 473 K for the most stable NH_3 solvated Cu(I) and Cu(II) species.

As with Cu(I), both are free from framework oxygen and remain fully coordinated to NH_3 through the course of the dynamics. RDFs integrate to ≈3.9 CN; weighting the AIMD RDFs by the XANES-observed fractions of Cu(I) and Cu(II) recovers average coordination numbers of 3.2 and 3.6, close to the EXAFS-fitted values. These species were roughly 50% less mobile than their Cu(I)(NH_3)$_2$ counterparts (Table 2.3.1), and 30% more mobile than their hydrated forms (Table 2.3.2).

Finally, to confirm the transferability of EXAFS spectra collected under the non-catalytic NO + NH_3 and O_2 + NH_3 conditions to catalytic ones, we obtained 473 K SCR *operando* EXAFS on the recently enhanced APS sector 10-ID beamline on a Si:Al = 25, Cu:Al = 0.41 sample similar to the 1Al catalyst (Figure 2.3.3), kinetic details and spectra are provided in appendix A. This catalyst has a 60/40 Cu(I)/Cu(II) ratio, a fit CN of 3.1, and no second shell structure. The CN is consistent with a 60/40 weighted average of 2CN Cu(I) and 4CN Cu(II). The lack of second shell character demonstrates all Cu are NH_3 solvated under the *operando* conditions.

2.3.4 SCR Mechanism

2.3.4.1 Cu(II) → Cu(I) half-cycle

We previously proposed an NO-assisted NH_3 dissociation as the rate-limiting step in Cu(II) to Cu(I) reduction during SCR [30]. We report in Figure 2.3.13 and appendix A the computed CI-NEB pathways for such a step starting from NH_3-saturated Cu(II) identified in the XAS and DFT here. Both reactions proceed by attack of NO on a Cu-bound NH_3 to form a N-N bond. In the process, a proton is transferred to an acceptor and an electron to Cu, leaving an H_2NNO intermediate that can decompose via proton transfers to N_2 and H_2O [30, 148]. In the 1Al case, the Cu-OH ligand acts as the proton acceptor, to form water:

$$\mathrm{Z[Cu(II)(OH)(NH_3)_3 + NO \rightarrow Z[Cu(I)(NH_3)_2(H_2NNO)] + H_2O} \ldots\ldots 2.14$$

In the 2Al case, an O_f plays the role of the acceptor, to form a new, proximal Brønsted site:

$$Z_2[Cu(II)(NH_3)_4] + NO \rightarrow [ZH]/Z[Cu(I)(NH_3)_3(H_2NNO)]……2.15$$

The first path is much more exothermic than the second (-267 vs. -68 kJ mol^{-1}), reflecting the strong driving force for creating H_2O. Nonetheless, the computed barriers for these two paths are a similar 71 and 74 kJ mol^{-1}, respectively, within the HSE06 model. These similarities reflect an early transition state dominated primarily by the partial desorption of NH_3 from Cu to accommodate the attacking NO. The N-N separations at the transition states are over 2 Å and N-H bonds only slightly elongated.

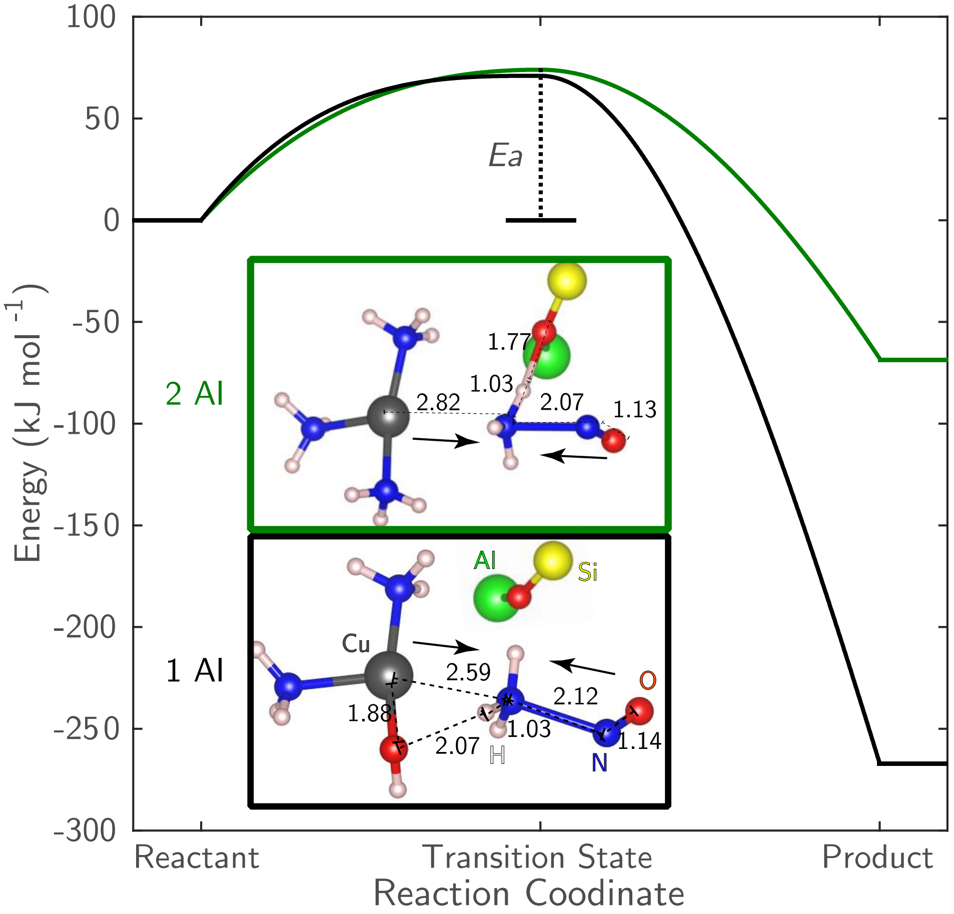

Figure 2.3.13 HSE06 CI-NEB calculated activation (Ea) and reaction energies for NO assisted reduction of NH_3 solvated Cu(II) 1Al (black) and 2Al (green) sites. Transition state structures are shown in boxes. For ease of visualization, most of the zeolite framework is hidden.

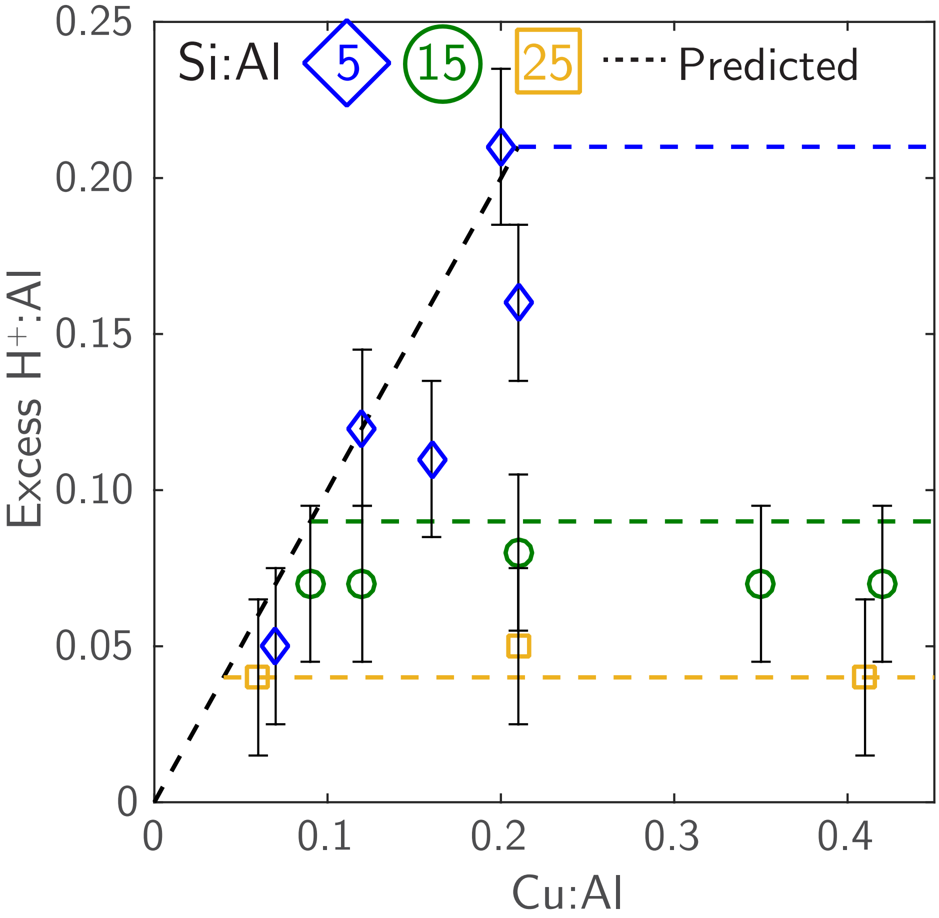

Figure 2.3.14 The number of extra H^+ sites (per Al) formed after reduction of Cu(II) to Cu(I) in flowing NO and NH_3 (473 K) as measured by NH_3 titration and TPD. Dashed lines represent the predicted number of H^+ formed based on the assumption that reduction of only Cu(II) at 2Al sites form a Cu(I)/H^+ site pair.

The key difference between the 1Al and 2Al paths is that NH_3/NO reduction of 2Al Cu(II) should produce new Brønsted sites while 1Al Cu(II) should not. The number of NH_4^+ species on samples treated in flowing NO and NH_3 (473 K) were counted by TPD performed after purging physisorbed and Cu(I)-bound NH_3 species in flowing wet helium (3% H_2O, 433 K) [135]. On all Cu-SSZ-13 samples, a large number of NH_4^+ species were present after reduction treatments than after oxidation treatments (appendix A). Figure

2.3.14 shows the number of additional H^+ sites present after reduction of Cu sites to Cu(I) as a function of the Cu:Al ratio on the Si:Al = 5 (blue diamonds), 15 (green circles) and 25 (orange squares) samples. The dashed lines indicate the excess H^+ expected from the theoretical enumeration of 1Al and 2Al sites (Figure 2.3.3). In line with predictions, one additional H^+ site is formed per Cu(I) formed until all the 2Al sites are filled, beyond which point no additional H^+ sites were formed. Re-oxidation in NO and O_2 (appendix A) returns the samples to the state shown in Figure 2.3.4. The catalytic cycle can thus be closed on both 2Al and 1Al sites.

2.3.4.2 SCR Cycle Energetics

The results above highlight the importance of NH_3 coordination during 473 K SCR. We previously proposed an SCR cycle on [Z_2Cu(II)] sites that accounts for the observed Cu redox [30]. Figure 2.3.15 shows an elaboration of that cycle that incorporates NH_3-solvation inferred from the thermodynamic analysis and EXAFS on 1Al and 2Al sites. The mechanism includes five primary steps, starting from the 12 o'clock position: (1) NH_3 adsorption on Cu(II); (2)NO-assisted NH_3 dissociation concurrent with Cu(II) reduction to Cu(I); (3) N_2 and H_2O desorption from Cu(I); (4) Cu(I) re-oxidation to Cu(II) by NO and O_2 (a non-elementary step); and (5) reaction of adsorbed NO_2^- with NH_3 or NH_4^+ to desorb N_2 and H_2O. Figure 2.3.15 (right) compares the computed reaction energies for each step (details in appendix A). The similar energetics are consistent with the similar standard SCR turnover rates (473 K) measured on the two site types (Table 2.3.3).

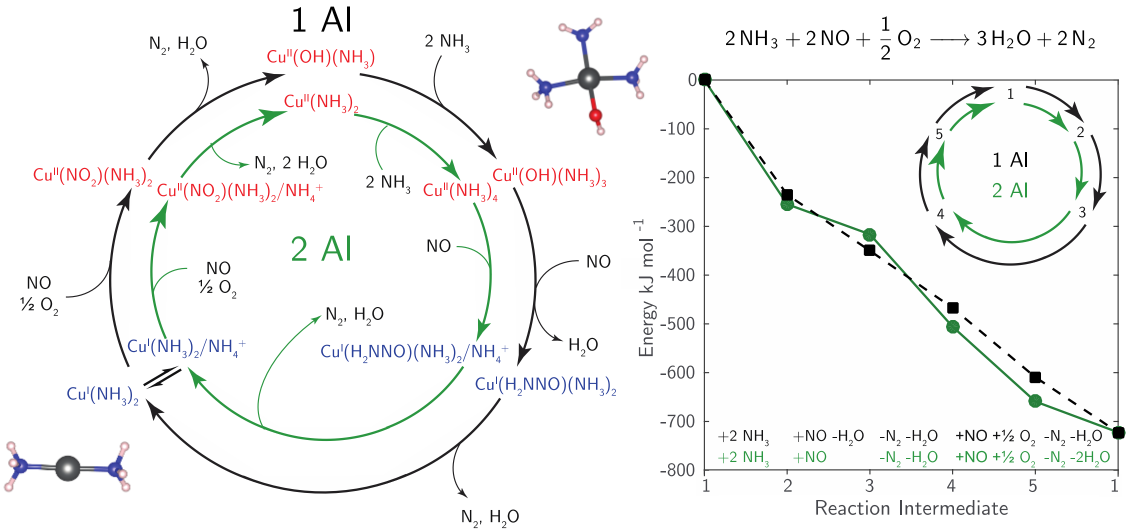

Figure 2.3.15 (Left) Proposed parallel standard SCR cycles for NH_3-solvated Cu ions near 1Al (black) or 2Al (green). (Right) HSE06-TSvdw-computed reaction energies along each step of the proposed cycles. 1-5 correspond to the intermediates in the left panel. Listed are the molecules consumed (+) and generated (-) between each intermediate.

2.3.5 SCR Rates on Other Cu-Zeolites

All the cationic Cu species in these cycles are NH_3-solvated and thus, not sensitive to the location of charge-compensating framework Al. To test the generality of this observation, standard SCR rates were measured on synthesized and commercial Cu-ZSM-5 and Cu-BEA samples of compositions similar to the Si:Al = 15 SSZ-13 samples. Standard SCR rates (per g, 473 K) on Cu-exchanged MFI (Si:Al = 13), BEA (Si:Al = 13) (sample preparation and characterization described in appendix A), and Cu-CHA (Si:Al = 5, 15) are shown in Figure 2.3.16 as a function of the Cu density (per g). The error was calculated by replicate experiments under the same conditions. These SCR rates were measured in a regime uncorrupted by mass or heat transfer artifacts (Koros-Nowak test [130]) and in a kinetic regime characterized by the same apparent reaction orders and apparent activation energies (appendix A). Standard SCR rates (per g_{cat}, 473 K) increased linearly with Cu density (per g_{cat}) on the Cu-CHA samples of different Si:Al ratio (5, 15), as expected from the similar turnover rate measured for Cu at 1Al and at 2Al sites (section 2.3.3.1), and also on C-ZSM-5 and Cu-BEA samples according to the same linear correlation. These data indicate that the catalytic SCR mechanism on Cu sites in these zeolites may be similar and, under the conditions in this kinetic regime, turnover at similar rates that are insensitive to the zeolite support. We surmise that this insensitivity reflects the undetectable bonds between Cu and O_f atoms in the presence of NH_3 at 473 K, which solvate both Cu(II) and Cu(I) species during conditions relevant to low temperature SCR catalysis.

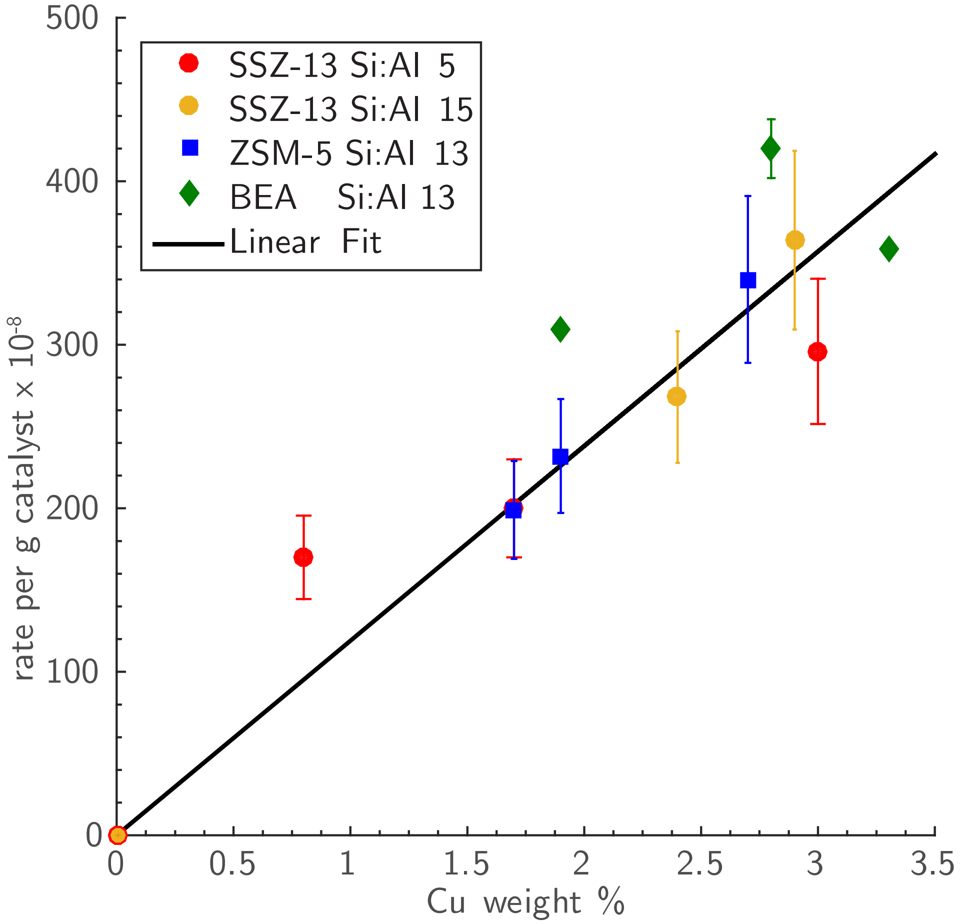

Figure 2.3.16 Standard SCR rates per g_{cat} at 473 K on Cu-exchanged SSZ-13, ZSM-5 and BEA vs. Cu mass density.

2.4 Discussion

2.4.1 Al distribution and Cu speciation *ex situ*

While the apparent macroscopic composition of a heterogeneous catalyst is typically simple to determine, relating that composition to the molecular-scale, functional composition of an active site remains a major challenge. The relevant macroscopic composition variables for the Cu-SSZ-13 materials are the Si:Al and Cu:Al ratio. As reported in Figure 2.3.3 and the supporting experimental results, the two types of Cu sites are present over the composition ranges studied here, and the relative densities of each type of Cu site are a function of both composition variables. Figure 2.3.3 is based on two assumptions: first, that framework Al atoms are randomly sited during zeolite crystallization modulo Löwenstein's rule, and second, that 6MR 2Al sites are populated by Cu(II) cations to saturation before 1Al sites are populated with Cu(II)OH. The close correspondence between these predictions and the experimental characterizations support the mode.

Synthesis conditions are well known to influence Al siting in zeolites [65, 66, 91, 149-159], and specifically in SSZ-13 [141] and thus, the conclusions drawn from the synthetic conditions here cannot be extended to all Cu-zeolites or even to all Cu-SSZ-13 materials. We can, however, compare our findings to SSZ-13 zeolites prepared via procedures equivalent to those used here [28, 109, 134, 160-164]. Fickel et al. [109] concluded, based on XRD and EXAFS, that an SSZ-13 sample with Si:Al = 9 and Cu:Al = 0.18 contained predominantly Cu in the 6MR, in agreement with the models here that predict 80% of [$Z_2Cu(II)$] in such sites. Gao et al. [114, 115, 165] compared the H_2 TPR of SSZ-13 zeolites with Si:Al = 6 and 12, and Cu:Al = 0.1-0.5. Samples we predict to contain

[$Z_2Cu(II)$] shown only a 653 K TPR feature, while samples in the range expected to contain [ZCu(II)OH] also exhibit a 503 K TPR feature, consistent with the easier reducibility of [ZCu(II)OH] sites demonstrated here (Figure 2.3.2 and Figure 2.3.8). FTIR similarly shows only a 895 cm^{-1} Cu-perturbed T-O-T vibration in the composition range dominated by [$Z_2Cu(II)$], supplemented by a 940 cm^{-1} feature in the range containing [ZCu(II)OH] [165]. Davis and co-workers recently showed that these 2Al 6MR sites can be selectively protected against dealumination, and deactivated for methanol-to-olefins (MTO) activity by preferential exchange of Cu(II) ions [166, 167] and Gao et al. [166] used an analogous concept to exchange 2Al 6MR sites with alkaline earth cations.

While this partitioning and counting of [$Z_2Cu(II)$] and [ZCu(II)OH] sites is successful, these sites themselves are not monolithic. A 6MR ring can have 2Al in 2NN and 3NN relative positions, and even for given positions, at finite temperature an exchanged ion is quite dynamic within the site, as illustrated by the AIMD simulations. Capturing these dynamics was important in developing a correspondence between the AIMD and EXAFS results, and are important effects to consider in any DFT models of these systems.

2.4.2 Cu speciation *in situ*

Once microscopic sites are identified and enumerated, a second key challenge is to determine how they respond to environmental, *in situ* conditions. We find from the first-principle thermodynamics and spectroscopies that ambient conditions cause both [$Z_2Cu(II)$] and [ZCu(II)OH] species to exist as hydrated ions, liberated from coordination to zeolite framework oxygens, differing in composition by only a single proton, and differing only slightly in mobility (Figure 2.3.7). These observations are consistent with a large body of literature on Cu-zeolites. XAS and UV-vis spectroscopies of Cu(II)-exchanged SSZ-13 [29, 32, 41, 117, 168], ZSM-5 and BEA zeolites under ambient conditions are identical to the corresponding spectra of aqueous Cu(II) complexes, demonstrating the insensitivity of zeolite topology to solvated ions [32, 118]. Similarly, the perturbed T-O-T vibrations in IR spectra due to the framework-bound Cu(II) disappear upon hydration of Cu(II) under ambient conditions [110]. Electron paramagnetic resonance (EPR) spectra at ambient conditions observed for predominantly [Z_2Cu(II)] samples have been taken as evidence of hydrated and mobile Cu(II) [115]; broadening at 155 K is attributed to loss of that Cu(II) ion mobility [71, 169], and coalescence into a single sharp signal at 523 K to loss of the hydration sphere [34].

The first-principles thermodynamics and XAS spectroscopies are consistent with the loss of water ligands at high temperature in O_2. Similarly, Borfecchia et al. [105] infer this loss from observed changes in EXAFS to a 3CN Cu species, the same behavior the Si:Al = 15 Cu:Al = 0.44 catalyst exhibits (Figure 2.3.8) after dehydration. We and Borfecchia et al. [105] also observe the appearance of Cu(I) under more reducing conditions. We assign this reduced fraction to [ZCu(II)OH] species, based on the comparisons between the 1Al and 2Al samples. The auto-reduction is not complete on any sample, suggesting some kinetic in addition to thermodynamic control of the reduction process. The nominal auto-reduction stoichiometry:

$$4[\mathrm{ZCu(II)OH}] \rightarrow 4[\mathrm{ZCu(I)}] + 2\mathrm{H_2O} + \mathrm{O_2} \ldots\ldots 2.16$$

implies a complicated, multi-step process likely involving Cu dimer or higher-order intermediates [41, 111, 115] and thus, a sensitivity to spatial Cu-Cu (and hence, Al-Al) separations. Consistent with the inference, Gao et al. [114] report that the fraction of reducible [ZCu(II)OH] at constant Cu:Al ratio decreases with increasing Si:Al ratio, or equivalently, increasing the mean [ZCu(II)OH] separation.

Under standard SCR conditions at 473 K, Cu(I) and Cu(II) ions near 1Al or 2Al are all predicted and observed to be fully solvated by NH_3, and further, all Brønsted sites are present as NH_4^+. Both NH_4^+ and Cu-NH_3 are observed in DRIFTS spectra at similar conditions [21, 170, 171] on Cu-SSZ-13 samples. In fact, both vibrational and XAS spectra of NH_3 dosed to a number of Cu-exchanged zeolites are similar to those of aqueous $Cu(I)(NH_3)_2$ and $Cu(II)(NH_3)_4$ [13, 28, 29, 33, 171-175]. The standard SCR active sites at 473 K are NH_3-solvated Cu ions.

NH_3 solvation influences Cu mobility as well as structure, and this effect is insensitive to zeolite topology. NH_3 is observed to promote the exchange of Cu(II) from CuO(s) into a number of zeolite frameworks, and this process is further promoted by *in situ* reduction of Cu(II) to Cu(I) by NH_3 and NO mixtures [147].

2.4.3 Mechanistic Implications for SCR

The SCR reaction is well established to involve Cu(I) ↔ Cu(II) redox cycles [30, 33, 96, 129]. There has been some controversy regarding the species responsible for reduction [7, 30, 33, 124, 128]. Exposure to NO alone at 473 K does not reduce either the 1Al [ZCuOH] (appendix A) or 2Al [Z_2Cu] [30] samples, and the hybrid-exchange DFT results do not predict NO to strongly bind to or reduce either Cu(II) site. We thus find no evidence to support the elementary mechanistic steps:

$$[\mathrm{Z_2Cu(II)}] + \mathrm{NO} \rightarrow \left[\mathrm{ZCu(I)NO^+}\right] \ldots\ldots 2.17$$

$$[ZCu(II)OH] + NO \rightarrow [ZCu(I)HONO] \ldots\ldots 2.18$$

Rather, NO and NH_3 together are necessary to reduce either of these sites. The reaction pathways and activation barriers for these reductions are computed to be quite similar on the [ZCu(II)OH] and [Z_2Cu(II)] sites in the presence of solvating NH_3. At the higher temperatures at which NH_3 ligands are lost, the reduction rates on these two sites may differ.

While NO and NH_3 are most effective at reducing Cu(II), we and others [129, 176], also observe a partial reduction of Cu(II) to Cu(I) in flowing NH_3 and O_2. DFT calculations identified an O_2-assisted NH_3 dissociation pathway that parallels but has much higher barrier than the NO-assisted one NH_3 dissociation reaction [30]. This pathway is unlikely to be catalytically relevant but could be responsible for this reduction.

The results presented here provide indirect mechanistic information about the SCR oxidation half-cycle. We find adsorbed NO_2 to oxidize Cu(I) to Cu(II) as a Cu-bound nitrite:

$$Cu(I) + NO_2 \rightarrow Cu(II)O_2N \ldots\ldots 2.19$$

consistent with many proposals [7, 33, 125-128]. The source of NO_2 and even its presence as a free intermediate during standard SCR is less clear. Janssens et al. [33] proposed NO oxidation to nitrite to occur on a single, isolated Cu site through the intermediacy of a nitrate with the initial step as rate-determining:

$$[ZCu(O_2)(NO)] \rightarrow [ZCuNO_3] \xrightarrow{NO} [ZCuNO_2] + NO_2 \xrightarrow{NH_3} [ZCuOH] + H_2O + N_2 \ldots\ldots 2.20$$

However, computed activation energies and the RDS assumption are inconsistent with experimental activation energies and the observed 50/50 mixture of Cu(I)/Cu(II) for SCR [28, 30, 114, 115]. Rather, as with auto-reduction, NO oxidation may involve participation of more than one Cu species, facilitated by the solvation and high mobility of $Cu(I)(NH_3)$= and its low diffusion barrier between CHA cages. Solvated Cu(I) ions are well known to participate in dimeric Cu oxidation chemistries [67, 177-179], and a second-order dependence of SCR rate on Cu concentration has been observed on Si:Al = 6 Cu-SSZ-13 catalysts at Cu:Al ratios ≤ 0.03 [34]. At higher temperatures, Cu is expected to desolvate (Figure 2.3.11), consistent with the FTIR findings of Giordanino et al [170]. In sharp contrast to 473 K spectra (Figure 2.3.9), EXAFS collected at 673 K in NH_3 and O_2 demonstrate similar second shell character (appendix A) to the dry-oxidized framework bound Cu (Figure 2.3.8). Concurrent with this desolvation, apparent activation energies from 70 kJ mol^{-1} at 473 K to 140 kJ mol^{-1} at 623 K [114], consistent with the dip in NO conversion observed [123] in non-differential measurements. Thus, NH_3 (de)solvation likely has a large impact on SCR oxidation half cycle rates.

2.4.4 Implications for partial methane oxidation

The results and approach described here are useful for the interpretation of the recently observed [89] non-catalytic, stoichiometric partial oxidation of methane (PMO) on Cu-SSZ-13:

$$2CH_4 + O_2 \rightarrow 2CH_3OH\text{……}2.21$$

PMO is carried out in a three step sequence [84-87] that can be understood in part through reference to Figure 2.3.2. In a first step, the Cu-SSZ-13 material is brought to ≈673 K in O_2 (≈20%) and balance inert, corresponding to Condition 2 in the figure. O_2 is then purged by inert, bringing the material to Condition 3. We observe a subset of sites to reduce under these conditions, consistent with the participation of only a fraction of exchanged Cu in

PMO [85]. Subsequent introduction of CH_4 at 473 K results in the production of methanol, which is liberated by returning to percent level H_2O pressures, between Conditions 1 and 2 of Figure 2.3.2.

Wulfers et al. [89] demonstrated PMO on Si:Al = 6 and 12, Cu:Al = 0.35 SSZ-13 materials. The Si:Al = 12 sample has roughly double (mol methanol per mol Cu) the performance of the Si:Al = 6 sample, in precise correlation with the predicted increase in [ZCu(II)OH] sites (Figure 2.3.3). We conclude that [ZCu(II)OH] sites are likely precursors to ZCuOCuZ sites proposed to be responsible for PMO activity [78, 81, 82, 86, 88] and [Z_2Cu(II)] sites are inactive.

$$2\mathrm{ZCuOH} \rightarrow \mathrm{ZCuOCuZ} + \mathrm{H_2O} \ldots\ldots 2.22$$

2.5 Conclusions

While the macroscopic composition of a heterogeneous catalyst is generally straightforward to measure and control, the relationship between this apparent composition and the number and type of catalytically relevant active sites is generally difficult to infer. We illustrate here an example of a non-trivial catalytic system in which it is possible to predict both the speciation and number density of active sites as a function of the relevant synthetic compositional variables. Further, we show that these distinct active sites can be tracked as they evolve under different exposure conditions, from ambient characterization, to dry and inert high temperature, to *operando* reaction conditions. This enumeration and tracking is enabled by site-sensitive spectroscopies that are able to interrogate the catalyst under working conditions and computational approaches that treat the catalyst in a "*operando*" fashion, incorporating reaction conditions and reliable estimates of free energies beyond the standard harmonic approximations into the predictions of site structure and composition.

We show that exchanged, atomically dispersed and isolated Cu ions within the SSZ-13 cages populate two distinct types of sites, distinguished by the number of charge-compensating Al T-sites, and that the structure and dynamics of these two Cu types are strongly influenced by the environment they experience. H_2O solvates both Cu types at ambient conditions, is lost at higher temperatures, and is replaced by NH_3 reactant at 473 K SCR conditions. This NH_3 liberates Cu from the framework, greatly enhances Cu mobility, and masks some of the differences between the two site types. The sites remain distinct, however; while both Cu sites undergo similar redox cycles at similar rates under the conditions studied here, the mechanisms differ in detail, as illustrated by the intermediacy of transient Brønsted sites on one but not the other Cu site type (Figure 2.3.14).

These findings underscore the need for caution in extrapolating from *ex situ* characterizations to catalytic conditions. Reaction conditions can and in this example do have a substantial influence on active site structure and properties. These environment-induced modifications need not be limited to reactants. Surrogate “promoters” that modify active sites (e.g. by mobilizing at different conditions, or that modify redox properties) could provide an alternative to traditional catalytic material modifications for tuning catalytic activity.

2.6 Methods

2.6.1 DFT and AIMD Details

Plane-wave, supercell DFT supercell calculations employed a triclinic SSZ-13 supercell containing 12 T-sites [20] and Si:Al ratios of either 11:1 or 10:2. The first Brillouin zone was sampled at the Γ point only, as appropriate for this insulator. Many of the adsorbate structures considered here have flat potential energy surfaces. To identify representative structures for subsequent optimizations, initial structures were first annealed non-spin-polarized at 473 K for a minimum of 140 ps using the Car-Parrinello molecular dynamics software [180](CPMD), version 3.17.1, the Perdew-Becke-Erzenhof [181] generalized gradient approximation (GGA) exchange-correlation functional, and ultrasoft psuedopotentials [182, 183]. These Born-Oppenheimer molecular dynamics simulations were run in the NVT ensemble using a Nose-Hoover thermostat with a timestep of 0.6 fs. RDFs from the final 90 of 140 ps simulations were constructed from the trajectories of a subset of these species for comparison to EXAFS results. Low energy structures visited during the AIMD simulations were subsequently optimized using the Vienna Ab initio Simulation Package (VASP) [184] version 5.3.5. Calculations were performed spin-polarized using the projector augmented wave (PAW) treatment of core-valence interactions [185, 186] and a plane wave cut off of 400 eV. For computational efficiency, structures were first relaxed within the GGA of Perdew et al. [181] and subsequently relaxed using the hybrid screened-exchange method of Heyd-Scuseria-Ernzerhof (HSE06) [187][Heyd, 2004 #181][188, 189] and the Tkatchenko Scheffier method for van der Waals interactions (TS-vdW) [190]. We converged self-consistent-field (SCF) electronic energies to 10^{-6} eV and atomic forces to less than 0.03 eV/Å. Charge analysis was performed through the method of Bader [191-195]. Cu charges are reported normalized to Cu(II) and Cu(I) references ([Z_2Cu(II)] and [ZCu(I)], respectively), then rounded to I or II reported as a superscript on Cu. Harmonic vibrational frequencies of adsorbed species were calculated at the HSE06-TSvdW level by numerical differentiation of atomic forces with 0.01 Å displacements on the adsorbate atoms and used to compute zero-point vibrational energies (ZPE). All structures can be found in the sitesCONTCARS attachment SI file.

2.6.2 *Ab initio* Free Energies

To relate DFT-computed energies to reaction conditions, we write the formation energies of adsorbed intermediates [196, 197] containing O and H relative to O_2 and H_2O references:

$$\Delta G_{x,y}^{form}\left(T, \Delta\mu_{O_2}, \Delta\mu_{H_2O}\right) = \Delta E_{x,y}^{form} - T\Delta S_{x,y}^{ST}(T) - \frac{x}{2}\left(\Delta\mu_{H_2O} - \frac{1}{2}\Delta\mu_{O_2}\right) - \frac{y}{2}\Delta\mu_{O_2} \ldots\ldots A.1$$

$$\Delta E_{x,y}^{form} = E_{ZCuH_xO_y} - E_{ZCu} - \frac{x}{2}\left(E_{H_2O} - \frac{1}{2}E_{O_2}\right) - \frac{y}{2}E_{O_2} \ldots\ldots A.2$$

The $\Delta\mu$ are free parameters corresponding to the difference in chemical potential between 0 K and the conditions of interest. They can be related to corresponding temperatures and pressures through the ideal gas chemical potential relation. ΔS^{ST} in entropy between a free and adsorbate-covered site. We have previously found that the harmonic oscillator approximation significantly underestimates actual entropies [30], consistent with observations made by others [106, 108, 198]. Comparisons with dynamics simulations suggest a simple heuristic in which the difference is approximated from the Sackur-Tetrode expression:

$$\Delta S^{ST}_{x,y} = \left(S_{ZCuH_xO_y} - S_{ZCu}\right) \approx \frac{2}{3}k_B \ln\left[\left(\frac{2\pi M_{x,y}k_B T}{h^2}\right)^{\frac{3}{2}}\frac{Ve^{\frac{5}{2}}}{N_A}\right] \text{……A.3}$$

where $M_{x,y}$ is the total mass of the adsorbed species and V is the supercell volume. This model roughly treats adsorbed species as retaining 2/3 of their gas-phase translational entropy, similar to that discovered for adsorbates at surfaces [199].

It is straightforward to extend these expressions to ones appropriate in the presence of NH_3, conditions that present nitrogen as well as hydrogen and oxygen to the sites:

$$\Delta G^{form}_{x,y,z}\left(T, \Delta\mu_{O_2}, \Delta\mu_{H_2O}, \Delta\mu_{NH_3}\right) = \Delta E^{form}_{x,y,z} - T\Delta S^{ST}_{x,y,z}(T) - \frac{x}{2}\left(\Delta\mu_{H_2O} - \frac{1}{2}\Delta\mu_{O_2}\right) -$$

$$\frac{y}{2}\Delta\mu_{O_2} - z\left(\Delta\mu_{NH_3} - \frac{3}{2}\Delta\mu_{H_2O} + \frac{3}{4}\Delta\mu_{O_2}\right) \text{……A.4}$$

We retain O_2 and H_2O as oxygen and hydrogen references and adopt NH_3 as nitrogen references.

2.6.3 Zeolite Synthesis and Characterization

Synthesis methods for all zeolites (SSZ-13, BEA, ZSM-5) can be found in appendix A. The crystal topologies of H-zeolites were confirmed from powder X-ray diffraction (XRD) patterns collected on a Rigaku Smartlab X-ray diffractometer equipped with a Cu K x-ray source (1.76 kW), and measured from 4-40° at a scan rate of 0.00833 ° s^{-1} with a step size of 0.01 ° (appendix A). Micropore volumes of H-SSZ-13 zeolites were determined from Ar adsorption isotherms (87 K), and for H-BEA and H-ZSM-5 zeolites were determined from N_2 (77 K), using a Micromeritics ASAP 2020 Surface Area and Porosity Analyzer, and were in reasonable agreement with the values expected for the CHA, BEA, and MFI frameworks and can be found in appendix A. Solid-state ^{27}Al magic angle spinning nuclear magnetic resonance (27Al MAS NMR) spectroscopy was used to estimate the fraction of framework and extraframework Al on H-form zeolites. SS NMR spectra were collected using a Chemagnetics CMX400 400 MHz spectrometer in a wide-bore 9.4 Tesla magnet at ambient conditions from 456 scans with 12.5 μs pulses and a 2 s delay and were measured at 104.24 MHz and MAS rate of 5 kHz. Prior to packing in a 4mm ZrO_2 rotor holding for > 48 h in a desiccator containing a saturated potassium chloride (KCl) solution. All 27Al MAS NMR spectra are referenced to an aqueous 1.0M $Al(NO_3)_3$ spectra and quantification of extraframework Al for all H-zeolite samples can be found in appendix A.

Cu-zeolites were prepared by aqueous-phase Cu ion exchange of H-form zeolites with a $CuII(NO_3)_2$ solution (0.001-0.1 M, 100 cm^3 g_{cat}^{-1}; 99.999 wt.% , Sigma Aldrich) for 4 h and 300 RPM at ambient conditions, during which the pH was controlled to 4.9 ± 0.1 through dropwise addition of a 1.0M NH4OH solution (Sigma Aldrich). Co-SSZ-13 zeolites were prepared by ion exchange of H-SSZ-13 with an aqueous 0.25M $CoII(NO_3)_2$ solution (150 ml g_{cat}^{-1}) for 4 h at ambient conditions, during which the pH was not controlled (pH stabilized between 3.2-3.6 after 4 h). Metal-exchanged zeolites were recovered by centrifugation and washed with deionized water six times (70 ml g catalyst−1 per wash), dried at ambient temperature under flowing air, and then treated in flowing dry air (100 ml g_{cat}^{-1}) to 773 K (0.0167 K s^{-1}) for 4 h. Elemental composition (Si, Al, Cu, Co) was determined using atomic absorption spectroscopy (AAS) on a Perkin-Elmer AAnalyst 300.

2.6.4 NH_3 Temperature Programmed Desorption

Residual H^+ sites on H-zeolites, on Cu- and Co-exchanged zeolites after oxidation treatments in air (20% O_2, balance N_2, 773 K, 4 h), and on Cu-zeolites after reduction treatments (500 ppm NO + 500 ppm NH_3, balance He, 473 K, 2 h) were titrated using the procedure described by Di Iorio et al [135]. This titration method involves saturation of zeolites (≈0.03-0.05 g) with NH_3 at 433 K (500 ppm, balance He, 2 h, 350 ml min^{-1}), followed by removal of physisorbed and Cu-bound NH_3 by treatment in wet helium (2.5-3.0% H_2O/He, 8 h, 350 ml min^{-1}), in order to selectively retain surface NH_4^+ species [135, 136]. NH_3 was then evolved in a subsequent TPD in flowing He (350 ml min^{-1}) to 823 K (0.083 K s^{-1}), and quantified using on-board calibrations in a MKS Multigas 2030 gas-phase FT-IR spectrometer. Further details can be found in appendix A.

2.6.5 Kinetics

Standard selective catalytic reduction (SCR) kinetics were measured on a bench-top tubular glass reactor described elsewhere [28]. All samples were sieved to a nominal size of 125-250 μm and diluted with silica gel to obtain a bed height of ≈2.5 cm. Steady-state kinetic data was collected at NO conversions below 20%, so that the entire bed was exposed to approximately the same gas concentrations, using a reactant gas mixture of 300 ppm NO (3.6% NO/Ar, Praxair), 300 ppm NH_3 (99.5%, Indiana Oxygen), 5% CO_2 (liquid, Indiana Oxygen), 10% O_2 (99.5%, Indiana Oxygen), 2.5% H_2O (deionized, 18.2 MΩ, introduced through saturator), and balance N2 (99.999% UHP, Indiana Oxygen) at 473 K and 1 atm. The total gas flow rate was maintained at 1.5 l min^{-1}. Outlet gas concentrations were analyzed using on-board gas calibrations on an MKS MultigasTM 2030 gas-phase

Fourier Transform Infrared (FTIR) spectrometer and NO, NO_2, NH_3, CO_2 and H_2O concentration data was recorded every 0.95s.

2.6.6 Spectroscopic Methods (XAS, FTIR)

XAS experiments were carried out on the insertion device (ID) and bending magnet (BM) beam lines of the Materials Research Collaborative Access Team (MRCAT, Sector 10) at the Advanced Photon Source (APS) at Argonne National Laboratory. A cryogenically cooled double-crystal Si(111) monochromator was used with an uncoated glass mirror to minimize the presence of harmonics. Spectra were recorded in transmission mode with the ionization chambers optimized for the maximum current with linear response (≈1010 photons s^{-1}) using gas mixtures to give 10% absorption in the incident X-ray detector and 70% absorption in the transmission X-ray detector. A Cu metal foil spectrum were simultaneously collected while measuring sample spectra to calibrate the Cu K-edge to 8979 eV. *Operando* experiments were performed at the 10-ID line in a special glassy carbon tube reactor described by Kispersky et al. [29], in which XAS spectra were collected simultaneously with steady-state standard SCR rate measurements to verify that rates were identical to those measured in separate differential plug-flow reactor experiments. XAS spectra were collected in an energy range between 8700 and 9890 eV for samples held under different gas conditions, and between 8700 eV and 9780 eV for *operando* experiments (additional details in appendix A). Multiple energy scans were taken to ensure the absence of time-dependent change or beam damage to the sample. Spectra were collected under isothermal conditions and normalized using a first-order polynomial in the pre-edge region and a third-order polynomial in the post-edge region. XANES spectra were fitted using a linear combination of Cu(I) and Cu(II) references [20, 28, 30] to determine the fractions of Cu(I) and Cu(II) in certain gas environments and under *operando* conditions. EXAFS data were fit from k = 2.7 to ≈11 $Å^{-1}$ (details of the fitting procedure in appendix A).

FTIR data were collected on zeolite samples using a Nicolet 6700 FTIR spectrometer equipped with a liquid nitrogen-cooled mercury cadmium telluride (MCT) detector. Catalyst samples (≈35-40 mg) were pressed into a self-supporting wafer (≈2 cm in diameter) and placed in a custom-built FTIR cell that has been described elsewhere [200]. Wafers were treated in flowing oxygen (10% O_2, balance He) to 673 K for 30 min and then cooled to 473 K, prior to collecting spectra. Spectra were collected with a resolution of 4 cm^{-1} and averaged over 1000 scans, baseline corrected, and normalized to the framework Si-O-Si combination/overtone band between 2100-1750 cm^{-1} (Additional details can be found in appendix A).

2.7 Acknowledgements

Financial support was provided by the National Science Foundation GOALI program under award number 1258715-CBET (Purdue) and 1258690-CBET (Notre Dame), and The Patrick and Jane Eilers Graduate Student Fellowship for Energy Related Research. Use of the Advanced Photon Source (APS) is supported by the U.S. Department of Energy, Office of Science, and Office of Basic Energy Sciences, under Contract No. DE-AC02-06CH11357. We would like to thank Viktor J. Cybulskis (Purdue) for his help in performing XAS experiments at the APS. We thank the Center for Research Computing at Notre Dame, and EMSL, a DOE Office of Science User Facility sponsored by the Office of Biological and Environmental Research and located at Pacific Northwest National Laboratory, for support of computational resources.

CHAPTER 3. COPPER SITE PROXIMITY REQUIREMENTS FOR OXIDATION WITH DIOXYGEN OR NITROGEN DIOXIDE DURING AMMONIA SELECTIVE CATALYTIC REDUCTION ON CU-SSZ-13

3.1 Abstract

This study is a two part investigation of low temperature selective catalytic reduction (SCR) on Cu-SSZ-13 zeolites. First, steady state *operando* XAS experiments were performed by systematically varying the concentrations of one reactant – NH_3 (0-590 ppm), O_2 (0%-10%) and NO (0-600 ppm) – at a time to determine its effect on the Cu(I)-Cu(II) surface coverages and their role in the standard SCR mechanism. These experiments showed that while O_2 and NH_3 participated in the oxidation and reduction half-cycles, respectively, NO was involved in both parts of the redox cycle. Second, titration experiments with O_2 starting from the reduced, Cu(I) state for two catalysts with the same Cu/Al (0.08-0.09) but different Si/Al ratios (4.5 and 15) followed second order kinetics for Cu(I) re-oxidation but showed differences in the rates of oxidation ($k = 1.79$ min^{-1} for Si/Al = 15 vs. 8.16 min^{-1} for Si/Al = 4.5) and the final fraction of Cu unable to oxidize to Cu(II) (0.26 for Si/Al = 15 vs. 0.15 for Si/Al = 15), even when both samples contained structurally equivalent Cu^{2+} ions exchanged at paired Al sites. This suggested the involvement of two Cu(I) centers for oxidation with O_2 and its underlying dependence on zeolite composition (Si/Al, Cu/Al) and proximity of Cu sites. The lower density of and longer average distances between Cu ions at Si/Al = 15 were used to rationalize differences in the low temperature

(473 K) standard SCR apparent kinetics and steady state XANES spectra between the two samples, which showed that re-oxidation of Cu(I) to Cu(II) was the slow step for the Si/Al = 15 catalyst. In sharp contrast, both samples showed identical rates of oxidation with NO_2 ($k = 0.8$ min^{-1}) and oxidized completely to 100% Cu(II), implying that NO_2 oxidation occurs on isolated Cu(I) sites, thus highlighting the differences between the oxidation half-cycles for standard and fast SCR reactions.

3.2 Introduction

Nitrogen oxides (NO_x, x = 1, 2) in automotive exhaust of lean-burn diesel-powered vehicles pose major environmental hazards, and increasingly stringent environmental regulations are enforced to reduce their emissions [113, 165, 174, 201]. Selective catalytic reduction (SCR) of NO_x by NH_3 (equation 3.1) is a commercial technology that is currently used to meet NO_x emissions standards. Specifically, small-pore, eight-membered ring (8-MR) aluminosilicate (SSZ-13) and silicoaluminophosphate (SAPO-34) molecular sieves of the chabazite (CHA) topology, after exchange with Cu and Fe species, are used in practice because of their resistance towards dealumination and poisoning by residual hydrocarbons. Their much higher hydrothermal stability, compared to metal-exchanged medium- and large-pore zeolites (e.g., Cu-ZSM-5, Cu-Beta) leads to stable catalytic performance in selectively reducing NO_x to N_2, even after experiencing high temperature (> 800 ^{o}C) excursions in the presence of water (7% (v/v)) [5, 25, 99, 109, 161, 171, 202].

Consequently, a molecular-level understanding of the reactive intermediates and active sites involved in the mechanism of NO_x SCR with ammonia on Cu-SSZ-13 catalysts is required to improve modeling of currently-used catalysts, and to develop and design improved catalysts to meet more stringent emission requirements being proposed for the future [203]. Several literature reports have suggested that isolated Cu^{2+} ions in the double 6-MR obtained after ion exchange are the active sites for this reaction [18, 19, 28, 31]. *Operando* XAS experiments have shown that isolated Cu is present as a mixture of Cu(I) and Cu(II) during standard SCR, suggesting that Cu redox chemistry is central to the SCR reaction mechanism [30, 32]. It is generally accepted that the combination of NO and NH_3 are co-reductants involved in the reduction of Cu(II) to Cu(I) during standard SCR (473 K) via the NO assisted dissociation of the N-H bond in a Cu-bound NH_3 molecule [30, 204], and that this one electron reduction half-cycle can occur at each isolated Cu(II) site. This also illustrates the selective nature of NH_3 in reducing NO instead of O_2, even though the latter is present in large excess. It remains unclear how the re-oxidation of Cu(I) to Cu(II) occurs although O_2 is typically considered to be the oxidant during standard SCR. The authors proposed a plausible pathway for the oxidation half-cycle that involved both NO and O_2 via the reaction of a nitrite (NO_2^-) anion with an ammonium cation (NH_4^+) to form N_2 and H_2O so that the stoichiometry was consistent with the overall reaction while the electron balance was maintained for each step. Oxidation with O_2, however, is a 4-electron process, and hence, cannot be accounted for by the oxidation of a single Cu(I) to Cu(II). However, in the case of NO_2, which is a 1-electron oxidant, the oxidation of Cu(I) to Cu(II) can be accounted for by the concomitant formation of a nitrite (NO_2^-) and the complete SCR cycle can occur on an isolated Cu site. This reaction that involves NO_2 as the oxidant instead of O_2 is called fast SCR with an equimolar mixture of NO and NO_2, described by equation 3.2 below.

$$4NH_3 + 4NO + O_2 \rightarrow 4N_2 + 6H_2O\ldots\ldots 3.1$$

$$4NH_3 + 2NO + NO_2 \rightarrow 4N_2 + 6H_2O\ldots\ldots3.2$$

Giordanino et al. [32] suggested the existence of two different isolated, cationic Cu(II) species, namely Cu^{2+} ions that are charge balanced by a pair of framework Al atoms and $[CuOH]^+$ ions that are charged balanced by one framework Al atom. The type and amount of these two different isolated Cu(II) in catalyst samples is dependent on the Al distribution and the Si/Al and Cu/Al ratios [28, 31, 32, 111, 149, 151, 158]. The effect of Si/Al ratio on the speciation of Cu and ammonia standard SCR has also been investigated by Gao et al. [114]. Paolucci et al. [31] confirmed the presence of two isolated Cu(II) species by showing the difference in their chemical behavior when reduced with H_2 or He. The authors used FTIR spectroscopy to detect and quantify the peak at ~3651 cm^{-1}, assigned to the OH stretching vibration on $[CuOH]^+$, and showed that all Cu exchanged as $[CuOH]^+$ species for Cu/Al > 0.12 at Si/Al = 15,. Further, one extra Brønsted acid site is formed upon reduction for each Cu^{2+} ion whereas such additional Brønsted acid sites are not formed upon reduction of a $[CuOH]^+$ ion. Consequently, NH_3 titrations were used to count the total number of Brønsted acid sites after reduction to differentiate between them and quantify the amounts of the two isolated Cu(II) ions present in their samples. .

Apparent reaction orders for NO (75 – 600 ppm), NH_3 (250 – 600 ppm) and O_2 (2.5 – 20%) at 473 K and apparent activation energy (433 – 473 K) measurements for two samples with either bare Cu(II) ions or $[CuOH]^+$ ions were similar, as was the steady state distribution of Cu(I) and Cu(II) under *operando* standard SCR conditions [31]. The authors showed that both types of ion-exchanged Cu(II) reduced to a mobile diamminecopper(I) species with NO (300 ppm) and NH_3 (300 ppm) at 473 K. DFT calculations showed similar energetics pathways for standard SCR (473 K) on both isolated Cu(II) sites, and that solvation by NH_3 nullified the differences between them. Based on these observations, they concluded that low temperature standard SCR (473 K) occurred via similar pathways on both isolated Cu(II) sites and proposed similar standard SCR mechanisms for the two sites At higher temperatures (> 623 K), however, where solvation due to NH_3 is absent [34], differences between their behavior for standard SCR may be observed. A potential advantage of similar standard SCR (473 K) turnover rates on both isolated Cu(II) species is that a greater extent of Cu can be exchanged into the zeolite with $[CuOH]^+$ as the ion exchange species compared to that with Cu^{2+} because charge balance requires two Al per Cu^{2+} ions, whereas only one Al is required per $[CuOH]^+$ ion.

This study explores the effect of Si/Al ratio by focusing on two Cu-SSZ-13 samples that contain predominantly Cu^{2+} ions, and shows that kinetic and spectroscopic differences are observed during standard SCR conditions, even when structurally-equivalent Cu^{2+} species cations are initially present in the two samples. Cu(I) re-oxidation to Cu(II) during standard and fast SCR has been investigated using x-ray absorption spectroscopy (XAS) by *in situ* treatment of the reduced form of the two samples with O_2 and NO_2, and comparing the relative rates and extents of oxidation to Cu(II). The results presented in this study illustrate the effect of Cu proximity for oxidation with O_2. Cu(I) oxidation with NO_2, however, showed no such differences or the effect of Cu proximity. These results have been used as the basis for suggesting different oxidation pathways and actives sites for standard and fast SCR reactions.

3.3 Methods

3.3.1 Catalyst Preparation

H-SSZ-13 zeolites with Si/Al = 4.5 and 15 were synthesized in-house as described previously [31, 136] by following the synthesis procedure outlined by Fickel et al. [109] and Zones et al. [162, 163]. $Cu(NO_3)_2$ (Alfa-Aesar) was used as the precursor to exchange Cu into the zeolite using liquid phase ion exchange. A slurry consisting of ~1-2 g of H-SSZ-13 in 180 ml DI water was heated to 313 K and stirred for 30 min. An aqueous solution of 0.01-0.02 M $Cu(NO_3)_2$ was added in a dropwise manner to the slurry containing H-SSZ-13 during which the pH of the solution was controlled to 4.9 ± 0.1 by dropwise addition of 0.1 M NH_4OH (Sigma Aldrich) while the mixture was allowed to stir for 15 h. The resulting slurry was centrifuged and rinsed three times with deionized (D.I.) water, after which the supernatant liquid was discarded and the catalyst was vacuum dried at ambient temperature in vaccum (-29 in. Hg) for 12 h. After drying, the catalyst was calcined under 80 ml min^{-1} flow of dry air (Commercial Grade, Indiana Oxygen) at 823 K for 6 h with a ramp rate of 0.5 K min^{-1}. Si, Al and Cu content of the samples was measured by atomic absorption spectroscopy (AAS) using the Perkin Elmer AAnalyst 300 spectrometer. ~20-30 mg of each sample was dissolved in 2-3 ml HF (48%, Fisher Scientific) and then diluted with D.I. water before actual measurements. The XRD patterns for both samples can be seen in figure B1 while the BET surface area and micropore volumes measured by Ar for the parent H-SSZ-13 are reported in Table 3.4.1 along with the corresponding Cu wt. %, Cu/Al and Si/Al ratios after Cu exchange. Co^{2+} ion exchange was used as a way to titrate the fraction of total Al present as Al pairs [141] since Co^{2+} exchanges only at Al pairs and not at isolated Al atoms within the zeolite framework.

3.3.2 Steady State X-ray Absorption Spectroscopy (XAS) Experiments

XAS experiments were performed at sector 10 MR-CAT (Materials Research Collaborative Access Team) of the Advanced Photon Source, Argonne National Laboratory. The insertion device beamline at sector 10 (10-ID) was used for the *operando* and *in situ* oxidation experiments due to the high photon flux available at that beamline. Incident and transmitted x-ray intensities were measured in ion chambers filled with 20% He in N_2 and 20% Ar in N_2 respectively to obtain approximately 10% and 70% absorption of the beam before and after the sample respectively. A Cu metal foil reference spectrum (edge energy of 8979 eV), was measured simultaneously with each sample spectrum to calibrate the x-ray beam for spectral measurements at the Cu-K edge. All sample spectra were normalized using 1st and 3rd order polynomials for background subtraction of the pre- and post-edges respectively. Steady state spectra were collected in the quick scan mode with an edge step of 0.5 eV, a dwell time of 0.05 s at each step and an energy range between 8700 and 10000 eV, each spectrum taking 2-3 min to complete. Steady state data were averaged over 3-5 scans depending on the data quality obtained under different experimental conditions.

The Cu K-edge x-ray absorption near edge spectroscopy (XANES) consists of several distinct features indicative of the various electronic transitions for the Cu(I) and Cu(II) oxidation states. The peaks at 8977 eV and 8987 eV are representative of Cu(II), with the first peak centered at 8977 eV due to the symmetry forbidden 1s → 3d transition. It becomes allowed due to mixing of the 3d and 4p orbitals, and has been reported in several studies as a low intensity, pre-edge feature [170, 205-207], while the shoulder at 8987 eV is due to its 1s → 4p electronic transition [170, 208]. The presence of the sharp peak centered around 8983 eV is characteristic of the 1s → 4p transition for a two coordinate Cu(I) complex. This peak has previously been reported in literature in a variety of environments including HC-SCR [209] and NO decomposition [210] on Cu-ZSM-5, thermal reduction of Cu-Mordenite [211], Cu-Y [212], various two coordinate Cu(I) model compound studies [213] and diamminecopper(I) complexes [172, 214, 215]. Since XAS is a bulk technique, each sample spectrum is a linear combination of the corresponding oxidation states. Therefore, a linear combination XANES fitting of the Cu(I) and Cu(II) references was used to obtain the relative amounts of each oxidation state under various conditions. Information about how the Cu(I) and Cu(II) references were generated is provided in our previous publication [30].

The details of the custom *operando* XAS reactor setup used for experiments in this work have been described elsewhere [20, 29, 30]. 7-13 mg of the high Al (Cu/Al = 0.08, Si/Al = 4.5) or 30 mg of the low Al (Cu/Al = 0.09, Si/Al = 15) sample was loaded in the *operando* reactor, after sieving to 125-250 µm, to maintain differential conditions (< 25% conversion). Gases were mixed and introduced into the reactor in a precise manner to avoid any side reactions. D.I. H_2O was introduced into the feed stream by flowing He carrier gas through a heated shell type humidifier (Perma Pure MH-Series). All gas lines downstream of the humidifier were heated to above 373 K to prevent H_2O condensation. After introducing H_2O, NO (3000 ppm in N_2, Matheson Tri-Gas) was introduced into the gas stream followed by the introduction of O_2 (20% in He, Airgas, Inc.). The reaction mixture was then preheated to 473 K. Ammonia (3000 ppm in He, Airgas, Inc.) was introduced through a 1/16” stainless steel tube a few inches above the catalyst bed to minimize the chances of gas phase side reactions. Gas concentrations were measured using a MKS

Multi-Gas 2030 gas analyzer FTIR with a cell temperature of 464 K and based on factory provided calibration files. Standard SCR conditions of 300 ppm NO, 300 ppm NH_3, 10% O_2, 2% H_2O, 5% CO_2, a total flow rate of 500-600 ml min^{-1} and a temperature of 463-473 K was used for all steady state experiments.

3.3.3 Kinetic Order Measurements under *Operando* Conditions

Co-existence of Cu(I) and Cu(II) at steady state during standard SCR [28, 29] and transient cutoff experiments [30] suggested that the reaction occurred via redox mechanism. If standard SCR is truly a redox reaction then changing the feed gas concentrations would be expected to change the steady state Cu(I) – Cu(II) fractions observed under standard conditions. The advantage of performing such *operando* experiments was that XAS spectra were simultaneously collected while measuring reaction orders to obtain correlations between the behavior of the catalyst under varying conditions and the oxidation states of Cu. Standard operating conditions were 300 ppm NO, 300 ppm NH_3, 10% O_2, 2% H_2O, 5% CO_2 and 463 K as mentioned above. For the reaction order measurements only the concentration of the particular gas whose effect was being explored on the catalyst was changed while keeping the same total flow rate, concentrations of other gases in the feed and catalyst temperature. Thus, O_2 concentration was varied from 0% to 10%, NH_3 concentration was varied between 0 ppm to 600 ppm and NO concentration was changed from 0 ppm to 600 ppm, in separate sets of experiments. The resulting XANES spectra were fitted using a linear combination of references as explained in section 3.3.2.

3.3.4 *In situ* Oxidation Experiments with O_2 or NO_2

The reactor setup described above was slightly modified and used to understand the oxidation behavior for the two catalyst samples used in this study, and to determine the link between standard and fast SCR reactions. This modification affected the measurement of sample temperature; determination of sample temperature is described in the appendix B. Both catalysts were first reduced to Cu(I) with 300 ppm NO and 300 ppm NH_3 under a total flow of 500 ml min^{-1} at approximately 447 K. Following the reduction to Cu(I), the two samples were exposed to either 10% O_2 or 90 ppm NO_2 at the same temperature in separate experiments. The Cu(I)-Cu(II) fractions during these transient experiments were followed by collecting XANES spectra in quick scan mode from 8700 to 9700 eV. Each spectrum took 1 min 48 s to complete with a step size of 0.5 eV and a dwell time of 0.05 s.

Rate constants for oxidation of Cu(I) to Cu(II) for the NO_2 experiments were extracted assuming a first order rate law (equation 3.3), solving the resulting equation as follows and fitting the final equation (equation 3.6) to the experimental data.

$$r_{\text{oxidation}} = -\frac{d[\mathrm{Cu(I)}]}{dt} = k[\mathrm{Cu(I)}] \ldots\ldots 3.3$$

$$\int \frac{d[\mathrm{Cu(I)}]}{\mathrm{Cu(I)}} = -k \int dt \ldots\ldots 3.4$$

$$\ln[\mathrm{Cu(I)}_t] = a - kt \ldots\ldots 3.5$$

$$\text{at } t = 0,\ \mathrm{Cu(I)}_t = \mathrm{Cu(I)}_o \rightarrow a = \ln\left[\mathrm{Cu(I)}_o\right]$$

$$\ln\left[\frac{\mathrm{Cu(I)}_t}{\mathrm{Cu(I)}_o}\right] = -kt \ldots\ldots 3.6$$

Rate constants for the oxidation of Cu(I) to Cu(II) for the O_2 experiments were extracted by using a similar procedure as above, except this time a second order rate law (equation. 3.7) was used for the low Al content sample. The corresponding equation was solved as follows

$$r_{oxidation} = -\frac{d[Cu(I)]}{dt} = k[Cu(I)]^2 \ldots\ldots 3.7$$

$$\int \frac{d[Cu(I)]}{Cu(I)^2} = -k\int dt \ldots\ldots 3.8$$

$$Cu(I)_t = \frac{1}{a + kt} \ldots\ldots 3.9$$

An offset term ‘b’ was added to equation 3.9 to account for the fraction of total Cu that was unable to oxidize to Cu(II) at the end of the experiment. These values were 0.26 and 0.15 for the low and high Al content samples, respectively from Figure 3.4.8a.

$$Cu(I)_t = \frac{1}{a + kt} + b \ldots\ldots 3.10$$

$$t = 0,\ Cu(I)_t = Cu(I)_o \rightarrow \frac{1}{a} = Cu(I)_o - b$$

$$\frac{1}{Cu(I)_t - b} - \frac{1}{Cu(I)_o - b} = kt \ldots\ldots 3.11$$

Only those data points that were outside the 5% XANES fitting error of the final steady state value were considered to determine the value of the second order rate constant for the two samples. Since there was not enough time resolution to observe the transient behavior for oxidation with O_2 for the high Al content sample, it was assumed that the oxidation process with O_2 was the same as for the low Al content sample and hence, the same form of the rate law was used to fit the experimental data for the high Al content sample.

3.4 Results

3.4.1 Synthesis of Cu-SSZ-13 zeolites with isolated Cu^{2+} species at different proximity

XANES spectra of both Cu-SSZ-13 samples under ambient conditions were indistinguishable from that of an aqueous solution of $Cu(NO_3)_2$ (Figure 3.4.1), and did not show any evidence of Cu^{1+} (pre-edge peaks ~8983 eV^+ [172, 209-215]) or of Cu_xO_y clusters, as reported previously [28, 110, 111, 115].

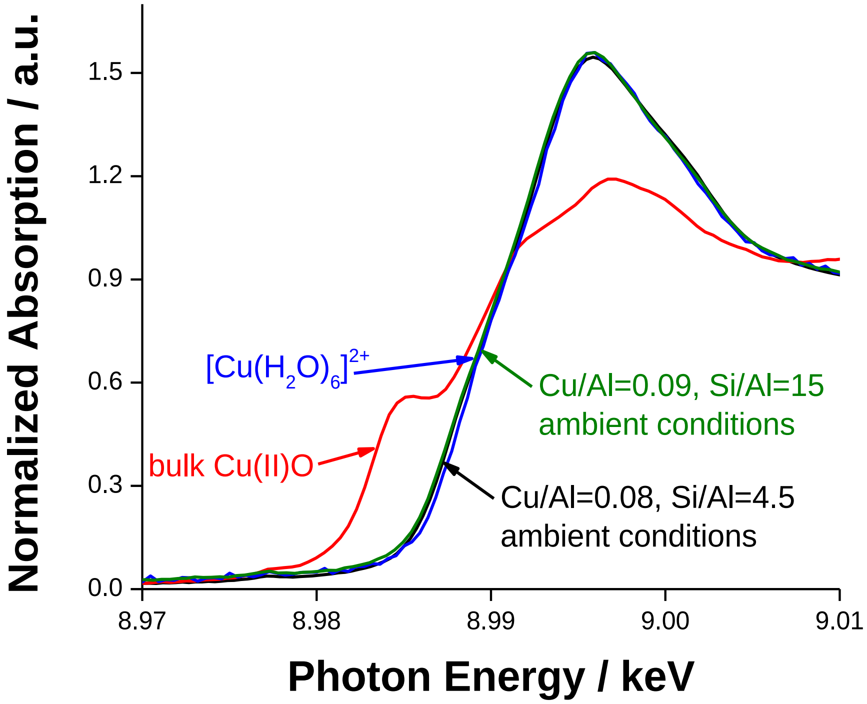

Figure 3.4.1 Comparison of XANES spectrum at ambient conditions with that for bulk CuO and aqueous solution of $Cu(NO_3)_2$ Samples: Cu/Al = 0.08, Si/Al = 4.5 and Cu/Al = 0.09, Si/Al = 15.

Second- and higher-coordination shells were also absent in the EXAFS region [31], indicating that all Cu sites were present as isolated hydrated Cu^{2+} complexes under ambient conditions. These ex-situ XAS characterization techniques indicate that both Cu-SSZ-13 samples contain predominantly isolated divalent cationic copper (Cu(II)), but do not provide further information about the speciation of Cu(II) between divalent Cu^{2+} and monovalent $[CuOH]^+$ complexes.

In CHA zeolites, Cu^{2+} cations exchanged at a paired Al site (6-MR containing 2 Al atoms) are thermodynamically more stable than $[CuOH]^+$ complexes exchanged at isolated Al sites (1 Al per 6-MR) [28, 165]. Therefore, Cu^{2+} cations are preferentially exchanged to saturation prior to exchange of $[CuOH]^+$ complexes, as has been demonstrated elsewhere on SSZ-13 zeolites of varying Si/Al ratio (4.5, 15, 25) [31]. The density of paired Al sites capable of exchanging Cu^{2+} cations decreases with increasing Si/Al ratio, assuming that Al atoms are randomly distributed in the framework according to Löwenstein's rule [133]. The two samples in this study have bulk Si/Al ratios of 4.5 and 15 and were synthesized according to protocols that crystallize SSZ-13 zeolites with randomly distributed Al atoms [141], which should contain 0.25 and 0.09 Al pairs (per total Al) [28]. Saturation Co^{2+} cation exchange levels, which provide an independent quantification of the number of Al pairs in SSZ-13, were 0.21 and 0.09 for the Si/Al = 4.5 and 15 samples, respectively [141], and agreed quantitatively with the number of Al pairs predicted from stochastic simulations. In this study, the Cu/Al ratios on the high Al (Cu/Al = 0.08, Si/Al = 4.5) and low Al (Cu/Al = 0.09, Si/Al = 15) Cu-SSZ-13 samples were less than or equal to the maximum number of divalent cation exchange sites predicted by theory and measured experimentally by Co^{2+} exchange (0.21 and 0.09, respectively), and thus were expected to contain only isolated Cu^{2+} cations.

Table 3.4.1 Elemental analysis, Ar micropore volume and proton count for the parent H-SSZ-13 and oxidized (Cu(II)) and reduced (Cu(I)) forms of the high Al (Cu/Al = 0.08, Si/Al = 4.5) and low Al (Cu/Al = 0.09, Si/Al = 15) content samples.

Si/Al	Cu/Al	Cu wt.%	Ar micropore volume / cm^3 g^{-1}	H^+/Al (H-form)	H^+/Al (Cu(II) form)	H^+/Al (Cu(I) form)
4.5	0.08	1.7	0.16	0.46	0.31	0.36
15	0.09	0.5	0.17	0.98	0.81	0.88

In order to verify the sole presence of isolated Cu^{2+} cations at paired Al sites in each Cu-SSZ-13 sample, the number of residual Brønsted acid sites was quantified by selective titration with NH_3 [135, 136], in which NH_3 saturation steps (433 K) were followed by purging in flowing helium containing 2-3% H_2O (433 K, 8 hr) to desorb Cu-bound NH_3 species prior to temperature programmed desorption. Oxidized forms of the high Al (Cu/Al = 0.08, Si/Al = 4.5) and low Al (Cu/Al = 0.09, Si/Al = 15) content Cu(II)-SSZ-13 samples contained two fewer H^+ sites per ion exchanged Cu(II) than their respective parent H-SSZ-13 samples (by 0.15 and 0.17, respectively, Table 3.4.1). Treatment of both Cu(II)-SSZ-13 samples in flowing NO (300 ppm) and NH_3 (300 ppm) at 473 K caused reduction of all isolated Cu^{2+} ions to Cu^{1+}, as monitored by XANES spectra (figure B2), and as expected for samples containing isolated Cu^{2+} ions [28, 30]. Reduced forms of the high Al (Cu/Al = 0.08, Si/Al = 4.5) and low Al (Cu/Al = 0.09, Si/Al = 15) content Cu(I)-SSZ-13 samples contained 0.05 and 0.07 additional protons relative to their oxidized Cu(II)-SSZ-13 forms (Table 3.4.1). These findings are consistent with the formation of a Cu^+ and H^+ site pair at two framework Al sites upon reduction of isolated Cu^{2+} cations, which occurs via NO-assisted dissociation of an N-H bond in a Cu-coordinated NH_3 ligand [30]. These residual H^+ titration data, which quantify a decrease in two protons per exchanged Cu^{2+} on oxidized forms of Cu(II)-SSZ-13 and the subsequent formation of one new proton per Cu^+ upon reduction to Cu(I)-SSZ-13 [30], confirm the sole presence of isolated Cu^{2+} cations at paired Al sites in both the high and low Al content Cu-SSZ-13 samples.

3.4.2 Differential Standard SCR Kinetics on Cu-SSZ-13 samples

Next, the kinetic details of low temperature (463-473 K) standard SCR were measured under differential conditions (< 25% conversion) on the high and low Al content Cu-SSZ-13 samples in a plug flow reactor (PFR). On the high Al content sample, the steady-state standard SCR rate (473 K) was 7.3 x 10^{-3} mol NO (mol Cu)$^{-1}$ s^{-1}, with apparent reaction orders of 0.8 for NO, -0.1 for NH_3, 0.3 for O_2 and an apparent activation energy of 60 kJ mol^{-1} (Table 3.4.2). Values of these kinetic parameters agree with those reported previously in the literature [28, 34, 115] for high Al content Cu-SSZ-13 samples with a similar composition (Si/Al = 4.5-6, Cu/Al = 0.03-0.2), for which the standard SCR rate (473 K) increased linearly with Cu^{2+} content with a turnover rate (473 K) of 6.5 x 10^{-3} mol NO (mol Cu)$^{-1}$ s^{-1}. Cu-SSZ-13 samples with lower Cu content studied by Bates et al. (Si/Al = 4.5, Cu/Al < 0.02) [28] and by Gao et al. (Si/Al = 6, Cu/Al < 0.03) [34], however, showed lower standard SCR turnover rates (2-4 x 10^{-3} mol NO (mol Cu)$^{-1}$ s-^{1}; 473 K) and subtle differences in apparent activation energies (40-43 kJ mol^{-1}). Given that Cu cations exchange predominantly as isolated Cu^{2+} sites at paired Al at these low Cu/Al ratios, these differences in the kinetic parameters suggest different kinetically-relevant steps or intermediates during standard SCR conditions (473 K) at dilute Cu loadings on SSZ-13.

Table 3.4.2 Standard SCR reaction kinetics for the high Al (Cu/Al = 0.08, Si/Al = 4.5) and low Al (Cu/Al = 0.09, Si/Al = 15) content samples at 300 ppm NO, 300 ppm NH_3, 10% O_2, 5% CO_2, 2% H_2O, 473 K.

Sample	Standard SCR Rate (10^{-6} mol NO g_{cat}^{-1} s^{-1})	NO order (±0.1)	O_2 order (±0.1)	NH_3 order (±0.1)	E_{app} (±5 kJ mol^{-1})
High Al	184	0.8	0.3	-0.1	60
Low Al	18	0.4	0.7	-0.5	50

On the low Al content Cu-SSZ-13 sample, the standard SCR turnover rate (473 K) was 2.3 x 10^{-3} mol NO (mol Cu) $^{-1}$ s^{-1} (Table 3.4.1 and Table 3.4.2), which is 2.8x lower than the value expected (6.5 x 10^{-3} mol NO (mol Cu)$^{-1}$ s^{-1}) from the linear correlation between standard SCR rate and Cu^{2+} content for the high Al content Cu-SSZ-13 samples [28]. On this low Al content sample, the apparent reaction orders were 0.4 for NO, -0.5 for NH_3, and 0.7 for O_2, and the apparent activation energy was 50 kJ mol^{-1} (Table 3.4.2), which seem similar to the apparent kinetic parameters for the low Cu and high Al content SSZ-13 samples (Si/Al = 4.5, Cu/Al = 0.02) reported by Bates et al. [28]. Values of the apparent activation energy in this range (40 – 49 kJ mol^{-1}) have been reported previously [34, 114], but reaction orders for these samples have not been measured previously. The different kinetic parameters measured on the high Al and low Al content Cu-SSZ-13 catalysts under equivalent standard SCR reaction conditions (Table 3.4.2) suggest differences in the active states of their Cu cations, as we probe next with XANES characterization in *operando*.

3.4.3 *Operando* XANES during Steady-State SCR Catalysis

3.4.3.1 Validation of the *Operando* Reactor

The low and high Al content Cu-SSZ-13 samples were studied under *operando* conditions by collecting XANES spectra simultaneously with steady-state SCR rate measurements (463-473 K), in order to determine the origin of the difference in apparent reaction orders and apparent activation energies for the two Cu-SSZ-13 samples. Interpretation of these spectra and their connection to the working state of the catalysts first required establishing the equivalence of kinetic measurements in the *operando* reactor and in the PFR, with reaction rates in both reactors given in Table 3.4.3. Figure 3.4.2 shows an Arrhenius plot for the high Al content Cu-SSZ-13 sample measured in the PFR and in the *operando* reactor, demonstrating reproducibility of SCR rate measurements in the *operando* reactor across a period of several months and in agreement with the PFR rate measurements.

Table 3.4.3 Comparison of standard SCR reaction rates measured in the PFR and the *operando* reactor for the high Al (Cu/Al = 0.08, Si/Al = 4.5) and low Al (Cu/Al = 0.09, Si/Al = 15) content samples and apparent reaction orders for the high Al (Cu/Al = 0.08, Si/Al = 4.5) content sample. Feed contained 5% CO_2, 2% H_2O for all measurements.

Sample	High Al				Low Al
	Rate[a] / 10^{-8} mol NO (g cat)$^{-1}$ s^{-1}	NO order[b] (±0.1)	O_2 order[c] (±0.1)	NH_3 order[d] (±0.1)	Rate[b] / 10^{-8} mol NO (g cat)$^{-1}$ s^{-1}
PFR	184	0.8	0.8	-0.1	18
Operando Reactor	209	0.8	0.8	-0.2	15.3

[a] reaction rates measured at 300 ppm NO, 300 ppm NH_3, 10% O_2, 473 K

[b] NO concentration varied between 120 and 600 ppm, apparent order measured at 463 K

[c] O_2 concentration varied between 2% and 10%, apparent order measured at 463 K

[d] NH_3 concentration varied between 160 and 590 ppm, apparent order measured at 463 K

After performing these experimental validations, the high Al content Cu-SSZ-13 sample was tested by systematically varying the concentration of each standard SCR reactant at a time to explore their role in the standard SCR reaction during steady state standard SCR catalysis.

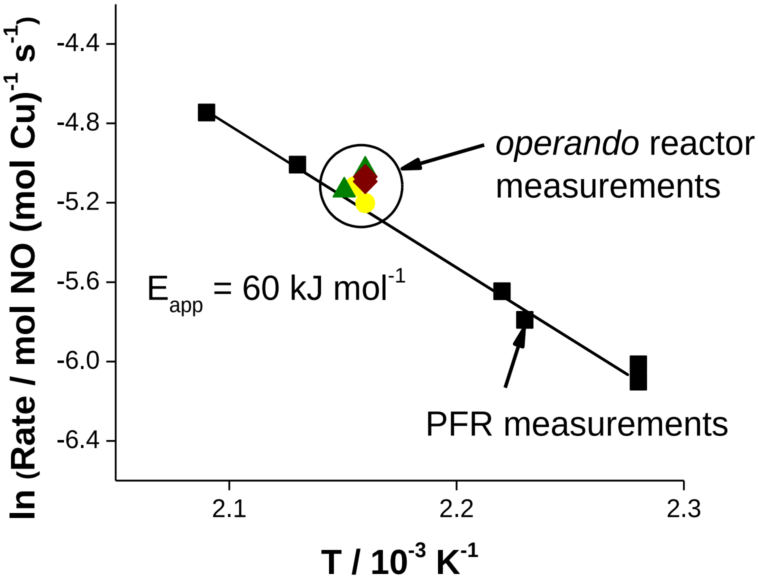

Figure 3.4.2 Activation energy plot (black squares) during standard SCR in the PFR overlayed with the rate measurements in the *operando* reactor (green triangles, yellow circles, maroon diamonds). Feed conditions: 300 ppm NO, 300 ppm NH_3, 10% O_2, 2% H_2O, 5% CO_2, 440 – 479 K. Sample Cu/Al = 0.08, Si/Al = 4.5.

3.4.3.2 Changing Gas Conditions for the High Al (Cu/Al = 0.08, Si/Al = 4.5) Catalyst

3.4.3.2.1 O_2

The first set of experiments involved varying O_2 partial pressure between 0% and 10% holding the partial pressures of other components in the feed constant while simultaneously collecting XANES spectra. *Operando* XANES spectra at standard conditions (300 ppm NO, 300 ppm NH_3, 10% O_2, 5% CO_2, 2% H_2O, 463 K) showed an equimolar mixture of Cu(I) and Cu(II) (Table 3.4.1). Increasing the O2 concentration from 2% to 10% resulted in an increase in the Cu(II) fraction from 36% to 50% (Table 3.4.4 and Figure 3.4.3a), as expected from the involvement of O_2 only in Cu(I) – Cu(II) oxidation half-cycle of the SCR redox mechanism [30]. An apparent reaction order of 0.3 was measured in the *operando* reactor (Figure 3.4.3b), consistent with its value of 0.3 measured in the plug flow reactor (PFR) (Table 3.4.3). The increase in Cu(II) fraction with O_2 pressure during steady state SCR catalysis is also evident from an increase in the white line intensity at ~8995 eV that is representative of Cu(II). 96% Cu(I) was present when O_2 was removed from the feed mixture, confirming that the combination of NO and NH_3 behaved as the reductant during low temperature (463 – 473 K) SCR conditions. Moreover, the Cu(I) species obtained upon reduction with NO and NH_3 is suggested to be diamminecopper(I) because the XANES spectrum for the reduced form of the sample at 0% O_2 resembled that for an aqueous diamminecopper(I) solution obtained at room temperature [214].

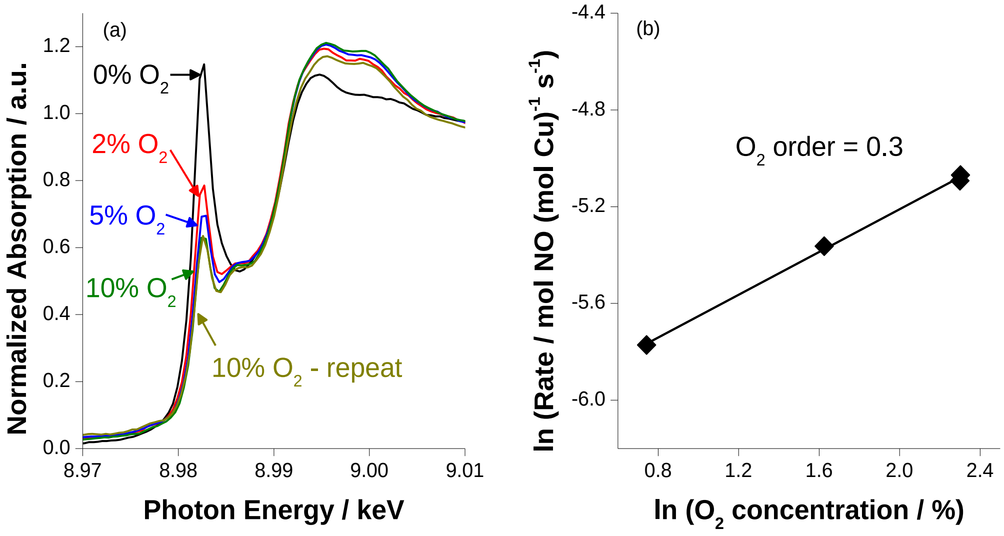

Figure 3.4.3 (a) *Operando* XANES spectra under varying O_2 partial pressures, (b) O_2 reaction order plot collected simultaneously while collecting XANES spectra. Feed conditions: 300 ppm NO, 300 ppm NH_3, 0% – 10% O_2, 2% H_2O, 5% CO_2, 463 K. Sample: Cu/Al = 0.08, Si/Al = 4.5.

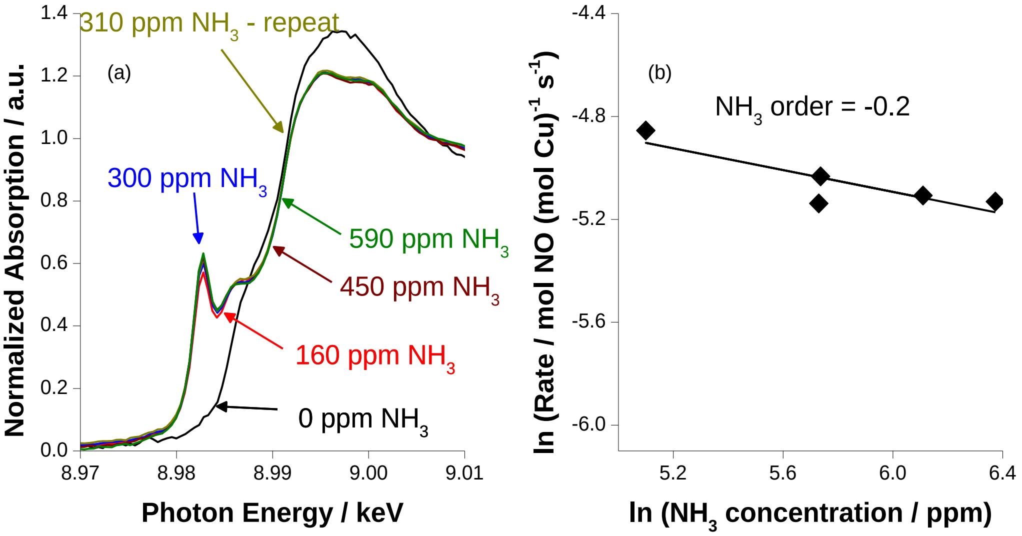

Figure 3.4.4 (a) *Operando* XANES spectra under varying NH_3 partial pressures, (b) NH_3 reaction order plot collected simultaneously while collecting XANES spectra. Feed conditions: 300 ppm NO, 0 – 590 ppm NH_3, 10% O_2, 2% H_2O, 5% CO_2, 463 K. Sample: Cu/Al = 0.08, Si/Al = 4.5.

Table 3.4.4 Quantification of isolated Cu(I) and isolated Cu(II) fractions from XANES spectra with varying O_2 partial pressures. Feed conditions: 300 ppm NO, 300 ppm NH_3, 0% – 10% O_2, 2% H_2O, 5% CO_2, 463 K. Sample: Cu/Al = 0.08, Si/Al = 4.5.

O_2 concentration / %	Isolated Cu(I) (±0.05)	Isolated Cu(II) (±0.05)
0	0.96	0.04
2.1	0.64	0.36
5.1	0.58	0.42
10	0.5	0.5

3.4.3.2.2 NH_3

Next, the NH_3 feed concentration was varied from 160 ppm 590 ppm to understand its effect on the SCR redox mechanism. Figure 3.4.4a showed that XANES spectra did not change for the range of concentrations tested, and quantification showed that the Cu(I) – Cu(II) fractions were constant within the measurement error (Table 3.4.5). An apparent reaction order of -0.2 was measured (Figure 3.4.4b), close to the value of -0.1 obtained in the PFR (Table 3.4.3). 96% Cu(II) was observed in the absence of NH_3 but with NO and O_2 present in the feed, mimicking the end state in the NH_3 cutoff experiment performed by Paolucci et al [30]. This showed that the Cu(I) – Cu(II) coverages on the catalyst surface were independent of the NH_3 gas phase partial pressure, consistent with the measured apparent NH_3 order of close to 0 and the catalyst surface being saturated with NH_3 under reaction conditions.

Table 3.4.5 Quantification of isolated Cu(I) and isolated Cu(II) fractions from XANES spectra with varying NH_3 partial pressures. Feed conditions: 300 ppm NO, 0 – 590 ppm NH_3, 10% O_2, 2% H_2O, 5% CO_2, 463 K. Sample: Cu/Al = 0.08, Si/Al = 4.5.

NH_3 concentration / ppm	Isolated Cu(I) (±0.05)	Isolated Cu(II) (±0.05)
0	0.04	0.96
160	0.48	0.52
310	0.5	0.5
450	0.51	0.49
590	0.52	0.48

3.4.3.2.3 NO

Changing the NO concentration between 0 and 600 ppm showed that the steady state Cu(I) fraction reached an asymptotic value of 0.5 at a concentration of 300 ppm, and was constant between 300 pm and 600 ppm (Figure 3.4.5a). If NO participated only in the reduction of Cu(II) to Cu(I) as proposed in section 3.4.3.2.1 then the Cu(I) fraction would be expected to increase monotonically with NO partial pressure. Further, a positive apparent reaction order of 0.8 (Figure 3.4.5b), consistent with that measured in the PFR

(Table 3.4.3), showed that the reaction rate increased throughout the entire NO concentration range. Thus, a non-monotonic change in the Cu(I) fraction coupled with an increase in the standard SCR suggested that NO was a participant not only in the reduction half-cycle but even in the re-oxidation of Cu(I) to Cu(II) to close the catalytic cycle. The steady state fractions of Cu(I) and Cu(II) at intermediate NO concentrations are shown in

Table *3.4.6*. 20% Cu(I) was observed in the absence of NO and with 300 ppm NH_3 and 10% O_2 because of the partial delocalization of the electron density from the lone pair on the nitrogen atom of the NH_3 molecules bound to Cu(II), thereby causing partial reduction [30].

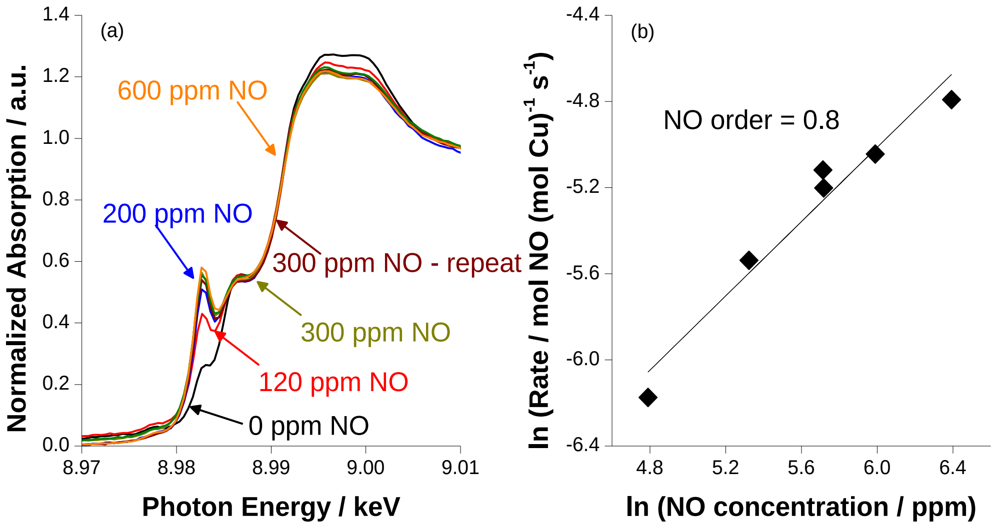

Figure 3.4.5 (a) *Operando* XANES spectra under varying NO partial pressures, (b) NO reaction order plot collected simultaneously while collecting XANES spectra. Feed conditions: 0 – 600 ppm NO, 300 ppm NH_3, 10% O_2, 2% H_2O, 5% CO_2, 463 K. Sample: Cu/Al = 0.08, Si/Al = 4.5.

Table 3.4.6 Quantification of isolated Cu(I) and isolated Cu(II) fractions from XANES spectra with varying NO partial pressures. Feed conditions: 0 – 600 ppm NO, 300 ppm NH_3, 10% O_2, 2% H_2O, 5% CO_2, 463 K. Sample: Cu/Al = 0.08, Si/Al = 4.5.

NO concentration / ppm	Isolated Cu(I) (±0.05)	Isolated Cu(II) (±0.05)
0	0.2	0.8
120	0.35	0.65
200	0.4	0.6
300	0.45	0.55
400	0.45	0.55
600	0.47	0.53

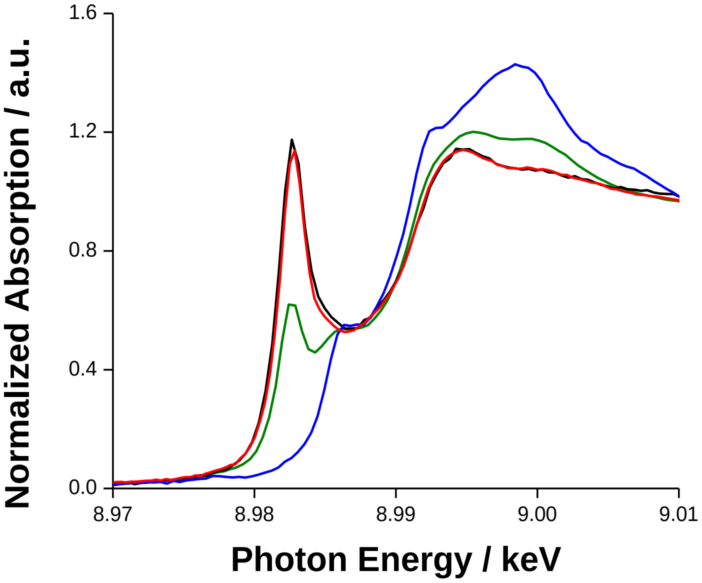

Figure 3.4.6 Steady state *operando* XANES spectra for the **high Al (Cu/Al = 0.08, Si/Al = 4.5, green)** and **low Al (Cu/Al = 0.09, Si/Al = 15, red)** content samples during steady state standard SCR (300 ppm NO, 300 ppm NH_3, 10% O_2, 2% H_2O, 5% CO_2, 463 – 473 K) overlayed with **isolated Cu(I) (black)** and **isolated Cu(II) (blue)** references.

3.4.3.3 Steady State XANES for the Low Al (Cu/Al = 0.09, Si/Al = 15) Catalyst

These findings shown above indicate that, on the high Al Cu-SSZ-13 sample, a mixture of Cu(I) and Cu(II) oxidation states persist during steady-state low temperature SCR catalysis, under standard conditions (300 ppm NO, 300 ppm NH_3, 10% O_2) [28-30].

In sharp contrast, *operando* XANES spectra of the low Al Cu-SSZ-13 sample showed that Cu cations were exclusively present in their reduced form (96% Cu(I)) during steady state standard SCR conditions (Figure 3.4.6). Moreover, these *operando* XANES spectra were indistinguishable from those collected after stoichiometric reduction of both Cu-SSZ-13 samples in flowing NO and NH_3 (447-463 K), and resembled that of an aqueous diamminecopper(I) diammine solution (figure B2) [214]. Diamminecopper(I) was also proposed by Kieger et al. on Cu-FAU samples reduced in NO and NH_3 [204]. These interpretations of *operando* XANES spectra indicate that the most abundant reaction intermediate during standard SCR on the low Al content Cu-SSZ-13 sample is diamminecopper(I) coordinated weakly to the zeolite [31].

Taken together with the different apparent reaction orders and activation energies compared to the analogous parameters measured for high Al content sample (Table 3.4.2), these *operando* XAS data provide clear evidence that standard SCR turnover rates are limited by and reflect that the kinetics depend on Cu(I) → Cu(II) re-oxidation half cycle for the low Al content sample. This shows that the kinetics of Cu(I) re-oxidation with O_2 were sensitive to changes in the catalyst composition, evident in the presence of ~50% and ~100% Cu(I) during standard SCR catalysis on the Si/Al = 4.5 and 15 samples, respectively. Despite the fact that both samples initially contained isolated Cu^{2+} cations at paired framework Al sites, the low Al content Cu-SSZ-13 sample was limited solely by Cu(I) re-oxidation with O_2 while the high Al content Cu-SSZ-13 was not, indicating an influence of the underlying framework Al density and extraframework Cu proximity.

3.4.4 *In situ* Oxidation Experiments with O_2 or NO_2 as the Oxidant

In order to understand the observed differences in Cu(I) re-oxidation behavior between the low Al and the high Al content Cu-SSZ-13 samples during steady-state, low temperature, standard SCR catalysis, stoichiometric oxidation half-reaction experiments were performed on each catalyst using NO_2 and O_2 as the oxidant.

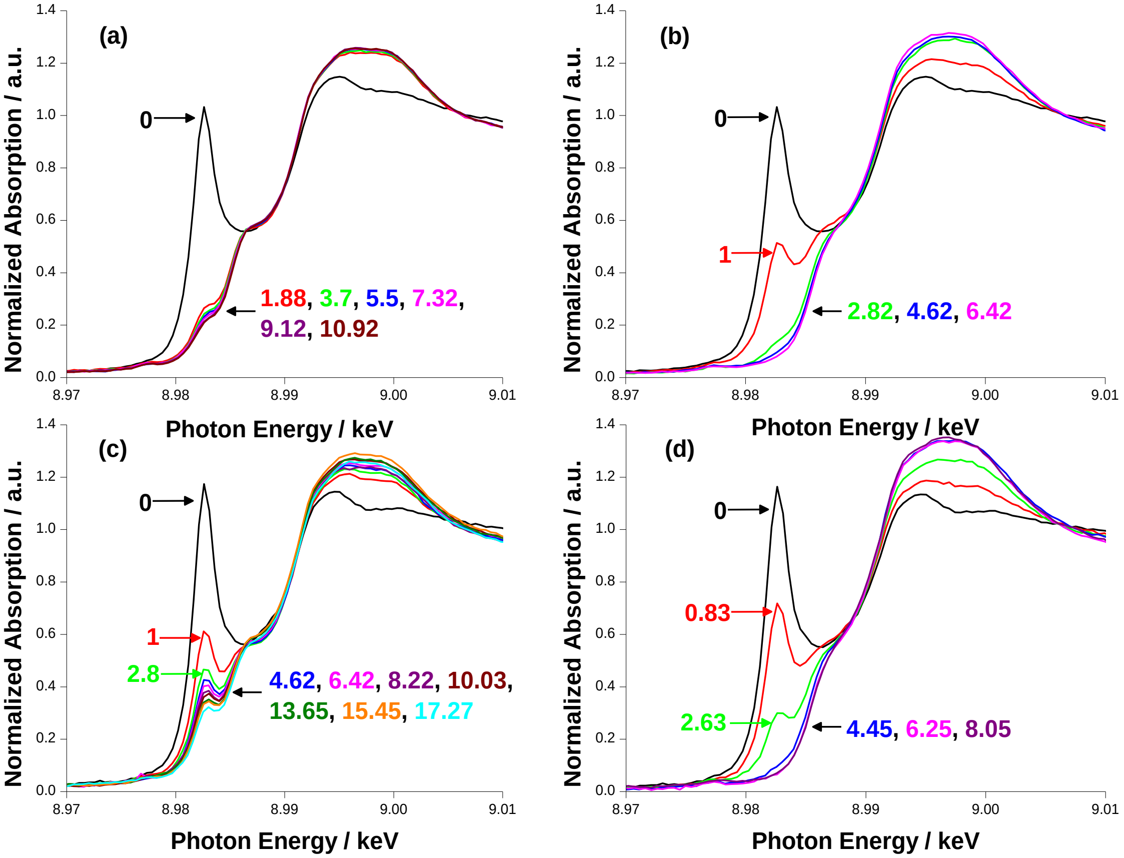

Figure 3.4.7 Transient XANES spectra at 447 K starting from Cu(I) for the (a), (b) high Al (Cu/Al = 0.08, Si/Al = 4.5) and (c), (d) low Al (Cu/Al = 0.09, Si/Al = 15) content samples during oxidation with (a), (c) 10% O_2 and (b), (d) 90 ppm NO_2. Colored numbers with arrows on all four plots correspond to the time stamp (in minutes) when each scan was started relative to when the flow of 10% O_2 or 90 ppm NO_2 began.

Each Cu-SSZ-13 sample was first treated in NO and NH_3 (300 ppm each, 447 K) to fully reduce Cu species to their the Cu(I) state, and then held either in flowing 10% O_2 or 90 ppm NO_2 while measuring the relative rates and extents of Cu(I) re-oxidation to Cu(II). The low and high Al content samples initially contained 97% and 90% Cu(I), respectively.

Transient XANES spectra for the high Al and low Al content Cu-SSZ-13 samples during re-oxidation with O_2 (10%, 447 K) are shown in Figure 3.4.7a and Figure 3.4.7c, respectively. The two samples showed significant differences, with faster re-oxidation of Cu(I) → Cu(II) for the high Al content sample (within 2 min), whereas it was more gradual for the low Al content sample (~10 min) (Figure 3.4.8a). The low Al sample had a Cu(I) fraction of 0.26, which was higher than 0.15 for the high Al content sample, in the final steady state. Biological literature suggests that oxidation of Cu(I) to Cu(II) with O_2 in enzymes occurs via coupling of two Cu(I) centers to form a Cu-oxo-bridged dimer [216-218]. This two electron-transfer process is describe as follows:

$$2[\mathrm{Cu(I)(NH_3)_2}] + \mathrm{O_2} \rightarrow \left[\mathrm{(NH_3)_2Cu(II)}\text{-}\left(\mathrm{O_2^{2-}}\right)\text{-}\mathrm{Cu(II)(NH_3)_2}\right] \ldots\ldots(3.12)$$

If the re-oxidation pathway indeed involved such dimer species, then the change in Cu(I) fraction with time would follow second order kinetics in the number of Cu(I) sites (equation 3.12) i.e. the change in the fraction of Cu(I) sites as a function of time in the stoichiometric oxidation half reaction with O_2 is given by (derivation in section 3.3.4):

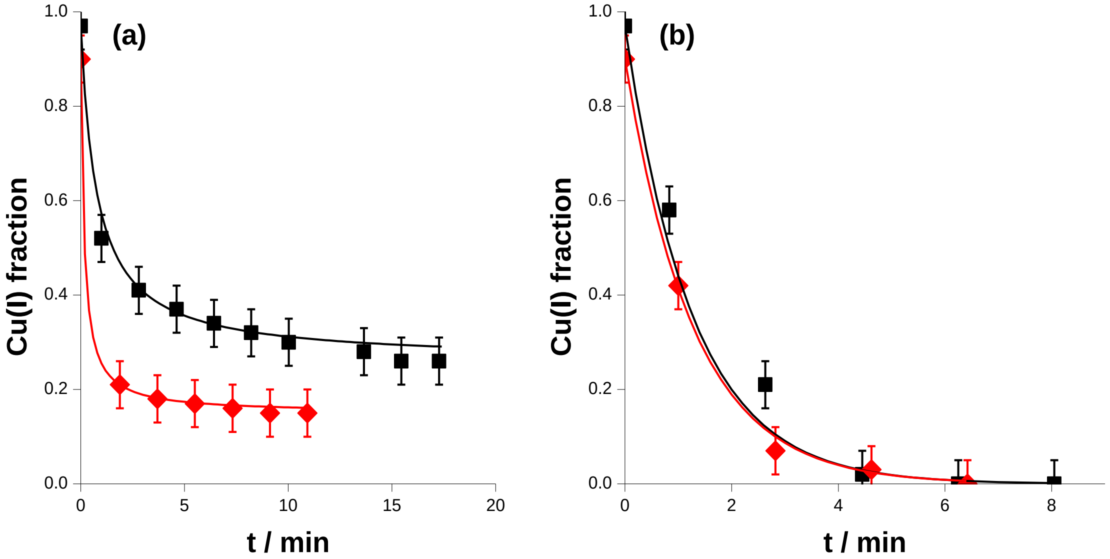

Figure 3.4.8 Variation of Cu(I) fraction with time (symbols) for the **high Al (Cu/Al = 0.08, Si/Al = 4.5, red)** and **low Al (Cu/Al = 0.09, Si/Al = 15, black)** content samples at 447 K starting from Cu(I) overlayed with the appropriate rate law fits (solid lines) during oxidation with (a) 10% O_2 and (b) 90 ppm NO_2.

$$\frac{1}{\mathrm{Cu(I)}_t\text{-b}} - \frac{1}{\mathrm{Cu(I)}_o\text{-b}} = \mathrm{kt}\ldots\ldots 3.13$$

Linear regression of the Cu(I) fraction on both Cu-SSZ-13 samples as a function of the reaction time to equation 3.13 (figure B3) gave second-order rate constants of 1.79 min^{-1} and 8.16 min^{-1} (with b = 0.26 and 0.15) for the low Al and the high Al content samples, respectively. The slower rate of Cu(I) re-oxidation to Cu(II) with O_2 and a greater fraction of Cu(I) in the final steady state for the low Al content sample compared to that for the high Al content sample, despite both catalysts containing Cu^{2+} exchanged at paired Al sites species in their fresh, dehydrated state, imply that Cu proximity and therefore, Al density is of paramount importance for oxidation of Cu(I) to Cu(II) with O_2.

Figure 3.4.7b and Figure 3.4.7d show the time-dependent XANES spectra collected during re-oxidation of the high Al and low Al content samples, respectively, in flowing NO_2 (90 ppm, 447 K). Exposure to flowing NO_2 oxidized all of the Cu in both samples to Cu(II) at a similar rate (Figure 3.4.8a), consistent with the ability of NO_2 to form nitrite (NO_2^-) [30, 33] on single Cu(I) sites with concurrent re-oxidation to Cu(II) via a one electron-transfer process:

$$[\mathrm{Cu(I)(NH_3)_2}] + \mathrm{NO_2} \rightarrow [\mathrm{(NH_3)_2Cu(II)\text{-}NO_2^-}] \ldots\ldots 3.14$$

The fraction of Cu(I) sites on both Cu-SSZ-13 samples, plotted in Figure 3.4.8b as a function of time after exposure to flowing NO_2, decreased at similar rates for the low and high Al content samples, consistent with single-site oxidation behavior. Assuming that the single-electron re-oxidation of isolated Cu(I) sites to Cu(II) with NO_2 (equation 3.14) is a first-order reaction in the number of Cu(I) sites, then the fraction of Cu(I) present as a function of time in the stoichiometric oxidation half-reaction is given by (derivation in section 3.3.4):

$$\ln\left[\frac{\mathrm{Cu(I)_t}}{\mathrm{Cu(I)_o}}\right] = -kt \ldots\ldots 3.15$$

The fractions of Cu(I) sites on both Cu-SSZ-13 samples as a function of reaction time were regressed linearly to the equation 3.15 (figure B4) and gave identical apparent first-order rate constants of 0.8 min^{-1} for NO_2-mediated oxidation, providing quantitative evidence for single-site re-oxidation behavior of isolated Cu(I) complexes with NO_2, irrespective of the Al or Cu density in the sample.

3.5 Discussion

3.5.1 Influence of Cu proximity on oxidation of Cu(I) to Cu(II) with O_2 or NO_2

Ex situ characterization of exchanged Cu cations by XANES spectra and titration of residual H^+ sites by NH_3, together with quantification of the number of paired Al by Co^{2+} exchange and stochastic calculations, demonstrated that both the high Al (Cu/Al = 0.08, Si/Al = 4.5) and low Al (Cu/Al = 0.08, Si/Al = 15) content Cu-SSZ-13 samples studied here contained predominantly Cu^{2+} cations charge-balanced by framework Al pairs. On the high Al content sample, *operando* XANES spectra showed that a mixture of Cu(I) and Cu(II) oxidation states were present during standard SCR catalysis, in agreement with previous reports [28-30]. In sharp contrast, *operando* XANES spectra of the low Al content sample during standard SCR conditions showed ~100% Cu(I), which is the first reported direct observation of a Cu-SSZ-13 catalyst that does not contain a mixture of Cu(I) and Cu(II) oxidation states during steady-state low-temperature standard SCR. Although both the low Al and high Al content Cu-SSZ-13 samples initially contained structurally equivalent, isolated Cu^{2+} cations, they differ in framework Al density and Cu proximity, which influences the re-oxidation behavior of Cu(I) to Cu(II) when O_2 is used as the oxidant in standard SCR redox cycles.

The prevalence of Cu(I) species, which XAS characterization and DFT calculations indicate are linear diamminecopper(I) complexes [31], during low temperature (473 K) standard SCR on the low Al content Cu-SSZ-13 sample indicates that re-oxidation of Cu(I) to Cu(II) is the kinetically-relevant process that limits SCR turnover rates. Yet, diamminecopper(I) ions in solution need to be held under inert atmosphere to prevent their re-oxidation to Cu(II) ammines, which occurs upon exposure to air at ambient conditions

[172, 214]. Thus, the slow re-oxidation (473 K) of Cu(I) species in the low Al content Cu-SSZ-13 sample cannot reflect an intrinsic inability of Cu(I) to oxidize in the presence of dioxygen but because of differences in the Cu distribution and proximity. Second order kinetics for stoichiometric re-oxidation of Cu(I) to Cu(II) with O_2 (Figure 3.4.8, figure B3) suggest the involvement of two diamminecopper(I) complexes in the oxidation process. Since two Cu(I) centers are required for O_2 activation, the rate of Cu(I) re-oxidation to Cu(II) with O_2 would depend on the Cu density and therefore, the Si/Al ratio for each catalyst, consistent with the slower oxidation rate observed for the low Al content sample ($k = 1.79$ min^{-1}) compared to that for the high Al content sample ($k = 8.16$ min^{-1}) with the same Cu/Al ratio.

Since O_2 is a 4-electron oxidant, re-oxidation of a single Cu(I) site to Cu(II) would simultaneously be accompanied by the oxidation of an NO molecule to a nitrate (NO_3^-) on the Cu(II) site, to account for the overall electron balance, as suggested by Janssens et al [33]. However, the calculated activation energy of 1.08 eV for the formation of a nitrate is greater than the range of measured apparent activation energies (60 – 70 kJ mol^{-1}) for low temperature (473 K) standard SCR. Also, if the complete standard SCR cycle occurred on isolated Cu sites, then a linear correlation between the standard SCR reaction rate and the Cu content would be expected, which directly contradicts the non-linear dependence reported by Gao et al [34]. An alternate pathway for Cu(I) re-oxidation to Cu(II) with O_2 during standard SCR catalysis that is consistent with the overall electron balance, oxidation of Cu(I) to Cu(II) in enzymes [216-218] and second order kinetics in Cu(I) for oxidation with O_2 is described by equations 3.16 and 3.17 below:

$$2[\mathrm{Cu(I)(NH_3)_2}] + \mathrm{O_2} \rightarrow \left[\mathrm{(NH_3)_2Cu(II)\text{-}\left(O_2^{2-}\right)\text{-}Cu(II)(NH_3)_2}\right] \ldots\ldots 3.16$$

$$\left[(NH_3)_2Cu(II)\text{-}\left(O_2^{2-}\right)\text{-}Cu(II)(NH_3)_2\right] + 2NO \rightarrow 2[(NH_3)_2Cu(II)\text{-}NO_2^-]\ldots\ldots 3.17$$

The oxidation of two Cu(I) centers to Cu(II) accounts for the transfer of two electrons (one electron per Cu(I) oxidized to Cu(II)) and the remaining two electrons are accounted for by the oxidation of two NO molecules to a nitrite (NO_2^-) each. The requirement of two Cu(I) centers for oxidation with O_2 during standard SCR is in direct contradiction with the proposition by Janssens et al. [33] and others [124, 219] that the complete standard SCR cycle, including reduction of Cu(II) to Cu(I) and the re-oxidation of Cu(I) to Cu(II), occurs on a single Cu site.

The different Al contents for the two samples used in this study meant that on average there would one Al per unit cell at Si/Al ratio of 15 and three Al per unit cell at a Si/Al of 4.5. Consequently, the Cu^{2+} ions would be farther apart for the low Al content sample compared to those in the high Al content sample, which may impose barriers in finding multiple diamminecopper(I) complexes in close proximity that effectively slows down the rate of oxidation during standard SCR for samples with low Al content. Gao et al. [34] and Bates et al. [28] showed that the effects of Cu proximity, evident from the lower apparent activation energy (≤ 473 K) in the range of 40 – 43 kJ mol^{-1}, are observed even in high Al content (Si/Al = 4.5 – 6) samples with very low Cu content (Cu/Al < 0.02). Gao et al [34] also showed that there is a linear correlation of the low temperature (≤ 473 K) standard SCR rate and the squared of the total Cu content (Cu/Al < 0.03), implying that the standard SCR reaction was limited by re-oxidation of Cu(I) to Cu(II) with O_2 for these samples.

This drawback due to the requirement of multiple Cu(I) centers in close proximity and its dependence on the Si/Al ratio can be overcome by using NO_2 as the oxidant instead of O_2. NO_2 being a 1-electron oxidant can oxidize isolated Cu(I) sites, regardless of their proximity as shown in this study, while concomitantly forming a nitrite (NO_2^-) species as follows:

$$[\mathrm{Cu(I)(NH_3)_2}] + \mathrm{NO_2} \rightarrow [\mathrm{(NH_3)_2Cu(II)\text{-}NO_2^-}] \ldots\ldots 3.18$$

Because reduction with NO and NH_3 also occurs on isolated Cu(II) sites [30, 31], the complete redox cycle for fast SCR can occur on isolated Cu sites, whereas standard SCR (473 K) requires one Cu(II) site for reduction with NO and NH_3 and two Cu(I) sites for oxidation with O_2. This suggests that there are two different pools of Cu(I) sites that are obtained after reduction of Cu(II) with NO and NH_3. The first pool consists of sites that are in close proximity with each other and hence, participate in standard SCR by activating O_2 with pairs of Cu(I) centers, while the second pool consists of isolated Cu(I) sites that can only participate in the SCR reaction via oxidation with NO_2 and would otherwise not contribute towards standard SCR. Thus, NO_2 co-feeding would engage all of the Cu sites in the catalyst and ensure optimal performance for maximum NO_x removal rate. Consequently, fast SCR is independent of the density or proximity of Cu in the zeolite and hence, faster than standard SCR on catalysts limited by oxidation with O_2 due to low Cu or Al contents. Thus, even though fast SCR and standard SCR differ stoichiometrically only by the NO oxidation reaction, the active sites and intermediates for the two reactions are different and there is no rigorous link between the two SCR reactions, in contrast to the proposition by Janssens et al [33] that standard and fast SCR reactions both occur on an isolated Cu sites and are linked by the NO oxidation reaction.

3.5.2 Implications of the Mobility of Diamminecopper(I)

An important consequence of the mobility of diamminecopperCu(I) complexes [132, 147, 203] is that it is plausible that at least a fraction of the total Cu can form oxo-bridged dimers by oxidation with O_2 during standard SCR, which are different from the Cu-oxo dimers formed under dry conditions without solvation by NH_3 [41, 75, 114]. DFT calculations show that it is energetically favorable to form such dimers from solvated diamminecopper(I) species. However, they are very reactive upon their formation because they are stabilized only at sub-ambient temperatures between 148 K and 195 K [203].

This knowledge of diamminecopper(I) mobility has recently been used as an alternative to aqueous phase ion exchange of Cu into a variety of zeolites, including SSZ-13, ZSM-5 and BEA, by physically mixing bulk Cu(II)O powder with the corresponding H-zeolite and reducing with NO and NH_3 or by physically mixing bulk Cu(I)O powder with the H-zeolite and flowing NH_3 over the mixture, both of which generate the mobile diamminecopper(I) species that migrate into the zeolite and replace the proton sites to give ion exchanged Cu-zeolites [147, 208]. Paolucci et al. [31] also showed that the mobility of Cu(I) within the zeolite cages is enhanced when coordinated with ammonia.

The mobility of diamminecopper(I), however, does not cause sintering of all the Cu in the samples because these positively charged complexes are held by electrostatic attraction at the negatively charged framework Al sites. Thus, they cannot traverse infinitely far within the zeolite cages from the charge-compensating Al atom. These diamminecopper(I) complexes would, however, lose their mobility due to solvation by NH_3 at temperatures above 623 K and coordinate to the zeolite lattice [31]. Due to the loss of mobility, an O_2 molecule can no longer be activated by two Cu(I) centers and the re-oxidation of Cu(I) to Cu(II) in the standard SCR cycle would necessarily occur on single Cu(I) sites. The standard SCR rate ($\geq$ 623 K, g_{cat}^{-1}) showed a linear correlation with the Cu content (Cu/Al < 0.02, Si/Al = 6) regardless of the Cu proximity and a significantly higher apparent activation energy of 130 – 140 kJ mol^{-1} [34], in line with the higher barrier for O_2 activation on an isolated Cu(I) site calculated by Janssens et al. [33], instead of the squared dependence for the same samples at lower temperatures (< 473 K) and an activation energy in the range of 60 – 70 kJ mol^{-1}. Thus, proximity of Cu(I) sites does not play an important role in the standard SCR mechanism at temperatures above 623 K.

3.6 Conclusions

We report, for the first time, a Cu/SSZ-13 catalyst with ~100% Cu(I) during steady state standard SCR (473 K), where re-oxidation of Cu(I) to Cu(II) is the kinetically relevant step in the standard SCR reaction mechanism. Complete kinetics, including reaction orders for NO, NH_3 and O_2 and the apparent activation energy, were reported for this sample in the oxidation limited kinetic regime, and were different from the corresponding parameters for the high Al content sample that was not limited by oxidation despite both samples containing structurally equivalent, exchanged Cu^{2+} ions charge balanced by a pair of framework Al atoms. Cu(I) stoichiometric re-oxidation to Cu(II) with O_2 obeyed second order kinetics in the fraction of Cu(I) sites, consistent with the formation of a transient Cu dimer during oxidation with O_2, and was dependent on the Cu proximity and therefore, the Si/Al ratio for the sample being tested. Stoichiometric re-oxidation of Cu(I) to Cu(II) with NO_2 obeyed first order kinetics in the fraction of Cu(I) sites and was independent of the sample composition (Cu density and Si/Al ratio), showing that fast SCR occurs on single

Cu sites, unlike standard SCR (473 K) that requires two diamminecopper(I) centers for the oxidation half-reaction with O_2. Thus, even though standard SCR and fast SCR differ stoichiometrically by the NO oxidation reaction, the active sites and the intermediates involved in the two reactions are different. An important implication of the mobility of diamminecopper(I) complexes at low temperatures (473 K) is that the location of the isolated Cu^{2+} ions upon dehydration is inconsequential, and that any modeling effort involving a static Cu^{2+} would not be an accurate description of the active site for low temperature (473 K) standard SCR. The existence of two different pools of Cu sites, ones that can be oxidized with O_2 and thus, participate in standard SCR, while others that are isolated and can only be oxidized with NO_2, has been proposed for the first time and suggests that NO_2 , under fast SCR conditions, engages all of the Cu in the catalysts being tested.

3.7 Acknowledgements

We thank Viktor Cybulskis and Dr. Anuj A. Verma for their help with executing the x-ray absorption experiments at the Advanced Photon Source at Argonne National Laboratory. Financial support was provided by the National Science Foundation GOALI program under award number 1258715 – CBET. MRCAT operations are supported by the Department of Energy and the MRCAT member institutions. This research used resources of the Advanced Photon Source, a U.S. Department of Energy (DOE) Office of Science User Facility operated for the DOE Office of Science by Argonne National Laboratory under Contract No. DE-AC02-06CH11357.

CHAPTER 4. DETERMINING THE ACTIVE INTERMEDIATES FOR NO OXIDATION ON CU-ZSM-5 FROM ^{15}NO LABELING EXPERIMENTS

4.1 Abstract

The objective of this work was to identify the nature of the active intermediate for the NO oxidation reaction on copper (Cu) exchanged ZSM-5 zeolite. *In situ* FTIR experiments (150 ppm NO, 50 ppm NO_2 and 5% O_2, 573 K) revealed the presence of three types of nitrates at 1626 cm^{-1}, 1601 cm^{-1} and 1567 cm^{-1}. NO_2 was produced by reduction of surface nitrates with NO (573 K), demonstrating that nitrates are important intermediates for NO oxidation. Keeping this in mind, fast isotope switching experiments were performed at 543 K, 553 K, 563 K and 573 K in a custom-built, low internal volume *operando* FTIR reactor, where ^{14}NO was replaced with ^{15}NO in the feed stream, to identify the nitrate species responsible for NO_2 production from the oxidation of NO. These experiments allowed us to follow the isotope label on the catalyst surface using FTIR, and in the reactor effluent using a mass spectrometer (MS), furnishing important information about the reaction mechanism for dry NO oxidation on Cu-ZSM-5, and showed that gas phase NO and NO_2 in the reactor are in equilibrium with each other via surface nitrates while the bridged/bidentate nitrate at 1626 cm^{-1} is the likely active intermediate for the NO oxidation reaction.

4.2 Introduction

NO_x emissions from high temperature combustion of fossil fuels in diesel-powered vehicles has spurred interest to discover catalysts that assist in their removal to meet the emission standards set by the EPA [7, 8]. Ammonia selective catalytic reduction (SCR) on copper (Cu) exchanged zeolite catalysts is particularly useful in mitigating these emissions. Cu-ZSM-5 was studied for ammonia SCR [2, 36, 220] following the initial discovery of this catalyst by Iwamoto et al. [11]. However, an important mechanistic aspect still under debate is the relevance of NO oxidation for ammonia SCR.

NO oxidation has been proposed as the rate determining step for standard SCR by various authors in literature [7, 35-37, 39, 221] because increasing the NO_2/NO_x ratio in the feed stream to SCR catalysts increases their efficiency for NO_x removal. Luo et al. [39] proposed this based on similar reaction orders with respect to NO and O_2 for NO oxidation and standard SCR. Devadas et al. [37] argued that H-ZSM-5, which is inactive for standard SCR, shows measurable activity upon introducing an equimolar mixture of NO and NO_2 in the feed. Thus, the authors proposed that the role of the transition metal i.e. Cu, was to oxidize NO to NO_2 to facilitate the standard SCR reaction. Verma et al [41] showed the utility of NO oxidation as a probe reaction to identify clustering of Cu in catalyst samples. Cu_xO_y species were suggested as the active sites for NO oxidation from the linear correlation between the measured dry NO oxidation reaction rates (573 K) and Cu_xO_y quantified from *in situ* x-ray absorption spectroscopy (XAS). Besides, it would be useful to pre-oxidize some of the NO present in the engine exhaust of diesel-powered automobles to NO_2 because fast SCR is more efficient for NO_x removal compared to standard SCR. Hence, it is important to understand the reaction mechanism and the intermediates involved in NO oxidation. Nitrogen oxides are reported to form various types of nitrates/nitrites on Cu/ZSM-5 [13, 36, 222-224] and may play an important role in both ammonia SCR and NO oxidation.

In this work, we have utilized *operando* FTIR spectroscopy to identify whether nitrates are potential reaction intermediates in the NO oxidation pathway, and isotope labeling experiments to determine which of those surface nitrates are the active intermediates and their average lifetime on the catalyst surface. These results allowed us to further expand on the reaction mechanism for NO oxidation proposed by Verma et al [41].

4.3 Experimental Methods

4.3.1 Catalyst Preparation

H-ZSM-5 was obtained by heating NH_4^+-ZSM-5 (CBV3024E, Zeolyst International) to 823 K with a ramp rate of 0.5 K min^{-1} under a 100 ml min^{-1} flow of dry air (Commercial Grade, Indiana Oxygen), followed by a dwell time of 480 min at 823 K. Cu was ion exchanged by stirring 2 g of the H-ZSM-5 support in deionized (D.I.) water for 30 min at 313 K followed by addition of 10 ml 0.1 M $Cu(NO_3)_2$ (Sigma Aldrich). The solution pH was maintained at 5 ± 0.2 by drop-wise addition of 0.1 M NH_4OH (Fisher Chemicals) while the mixture was allowed to stir for 4 h. The resulting slurry was subsequently centrifuged and rinsed three times with D.I. water, and the supernatant liquid was discarded. Following this, the catalyst was vacuum dried overnight at -29 in. Hg and ambient temperature. After drying, the catalyst was calcined once again by heating to 823 K under a 100 ml min^{-1} flow of dry air with a ramp rate of 0.5 K min^{-1}, followed by a dwell time of 360 min. Elemental analysis was performed by atomic absorption spectroscopy (AAS) using a Perkin AAnalyst 300 spectrometer. 20 mg of the sample was dissolved in 2-3 ml HF (48%, Fisher Scientific) followed by dilution with D.I. water prior to the measurement of Cu, Si and Al contents. For the Cu-ZSM-5 sample reported in this study, Cu/Al = 0.3 (1.8 wt.% Cu) and Si/Al = 18.

4.3.2 *Operando* Transmission FTIR – MS Setup

A custom – designed FTIR reactor and aluminum heating block made by Research Machining Services at Purdue University was used for experiments in this work. Detailed CAD drawings are available from previous work in our group [200]. Four 125 W heating cartridges (Catalog No. 279312, Chromalox), 2” long and 0.25” in diameter, were used to heat the reactor to the desired temperature. 40 – 60 mg of the catalyst samples were pressed in the form of 20 mm diameter self – supported wafers using a commercial die (Catalog No. GS03165, Specac, Inc.). CaF_2 windows (25.4 mm diameter, 10 mm thick, ISP Optics Corporation) along with graphite ferrules (Catalog No. SF30.0/25.4/6.0-4.2-G, Chromalytic Technology) were used to seal the reactor. The gas phase species in the reactor effluent stream were monitored using a mass spectrometer (5975C, Agilent) connected via a flexible fused silica capillary column (Catalog No. 2000017, Polymicro Technologies, LLC) and their concentrations measured via a MKS Multigas 2030 gas phas FTIR analyzer. Standard conditions of 150 ppm NO (0.5% in He), 50 ppm NO_2 (1% in He), 5% O_2 (UHP grade, Matheson Tri-Gas), 573 K balanced by He (UHP grade, Matheson Tri-Gas) to a total flow of 50 ml min^{-1} were used for rate measurements, while the temperature was varied between 543 K and 573 K for apparent activation energy measurements. Nicolet

6700 FTIR spectrometer was used to collect infrared spectra at a resolution of 4 cm^{-1}. Rapid scan mode was used in the OMNIC software during the isotope switching experiments to obtain a time resolution of 0.16 min per scan. Each infrared spectrum during these experiments is a single scan.

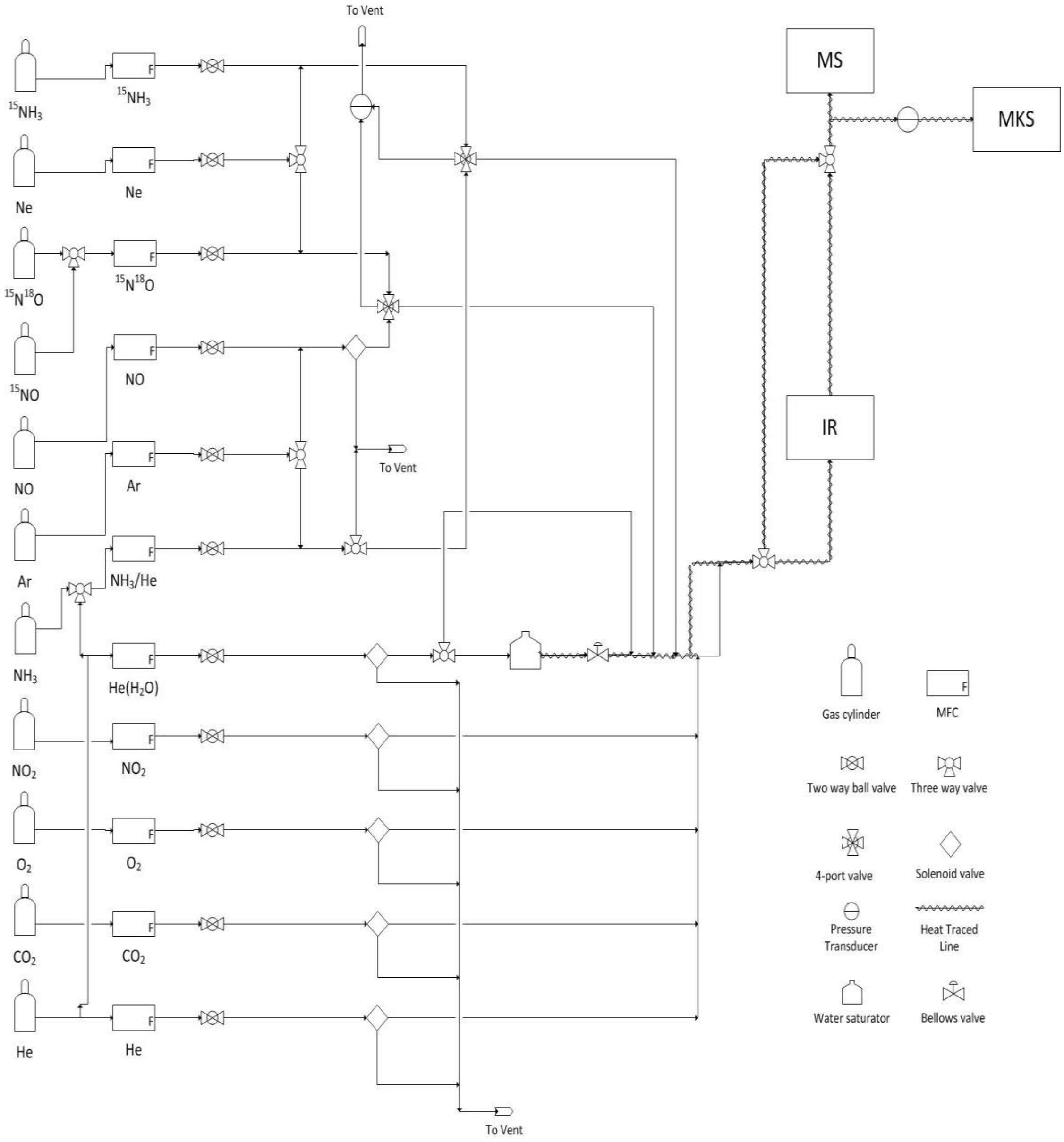

Figure 4.3.1 Flow diagram for the *operando* FTIR-MS isotope switching setup [225].

A flow diagram for the complete setup is shown in Figure 4.3.1. 150 ppm NO, 5% O_2, 573 K at 50 ml min^{-1} total flow was used for isotope switching experiments without NO_2 co – feeding. Ar (UHP grade, Matheson Tri-Gas) was used as the tracer with the unlabeled ^{14}NO gas, whereas Ne (Research grade, Airgas) was the tracer used with the labeled ^{15}NO (0.5% in Ne). A 4-port switching valve (Catalog No. A4C4WE, Vici Valco Instruments Co.) was used to replace ^{14}NO with ^{15}NO at steady state. While performing the switching experiments, the stream containing ^{14}NO and Ar was replaced with that containing ^{15}NO and Ne while keeping the same feed $^{14}NO/^{15}NO$ concentrations and the total flow rate to maintain kinetic steady state for the catalyst sample being tested. Two pressure transducers, one connected at the reactor outlet and the other at the vent line for the 4-port switching valve, were used to adjust the pressure difference and eliminate any pressure spikes upon switching from ^{14}NO to ^{15}NO in the feed stream. The signals at m/z = 46 and 47 were used for tracking $^{14}NO_2$ and $^{15}NO_2$, while the signals at m/z = 30 and m/z = 31 were used to monitor ^{14}NO and ^{15}NO after subtracting the contribution due to fragmentation of $^{14}NO_2$ and $^{15}NO_2$, respectively. Peak fitting of the FTIR spectra was performed using CasaXPS by constraining the full width at half maximum to the same value for the each ^{14}N- and ^{15}N-nitrate pair.

4.4 Results and Discussion

4.4.1 Steady State FTIR Spectra and Peak Assignments

A typical FTIR spectrum obtained during steady state NO oxidation (150 ppm NO, 50 ppm NO_2, 5% O_2, 573 K) shown in Figure 4.4.1 is similar to that obtained on Cu-ZSM-5 catalysts by others [13, 223, 226]. Three distinct peaks at 1626 cm^{-1}, 1601 cm^{-1} and 1567

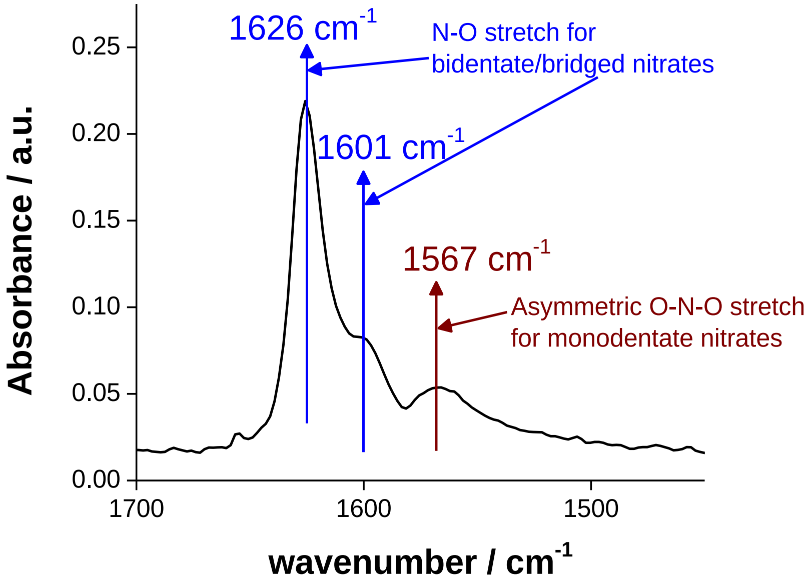

Figure 4.4.1 Typical FTIR spectrum showing the nitrate stretching region with the peak assignments. Feed conditions: 150 ppm NO, 50 ppm NO_2, 5% O_2, 573 K. Sample: Cu/Al = 0.3, Si/Al = 18, Cu-ZSM-5.

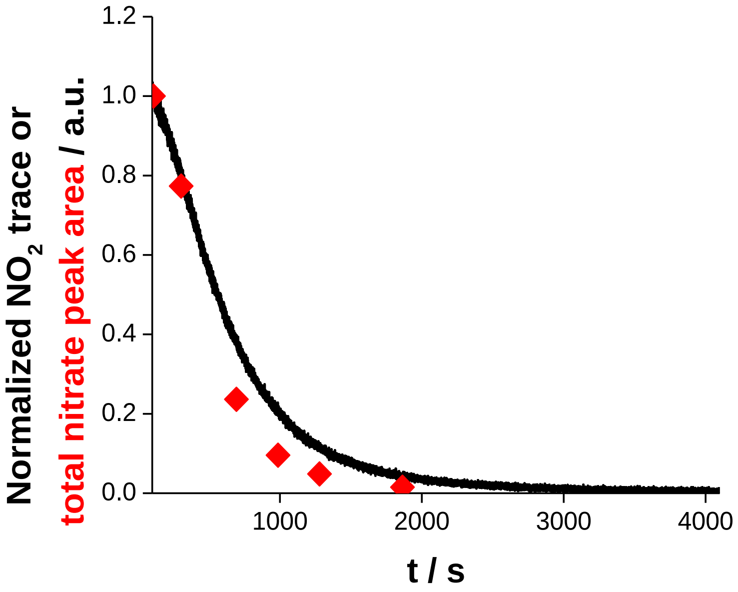

Figure 4.4.2 Overlaying the mass spectrometer trace for NO_2 (m/z = 46) with the change in the total nitrate peak area starting from steady state NO oxidation conditions (150 ppm NO, 50 ppm NO_2, 5% O_2 and 573 K) during the subsequent purge with 150 ppm NO (started at 108 s). Sample: Cu/Al = 0.3, Si/Al = 18, Cu-ZSM-5.

cm^{-1} have been assigned to the various stretching modes of different types of nitrates on Cu [13, 36, 222-224, 227, 228] or weakly adsorbed NO_2 on Cu [225, 229], while the peak at 2133 cm^{-1} is assigned to NO^+ in cationic positions within the zeolite [230] based on isotope labeling experiments. Hadjiivanov et al. [224] assigned the peaks between 1700 and 1500 cm^{-1} to nitrates because these species were thermally stable upon flushing with inert gas whereas weakly bound NO_2 would desorb from the catalyst surface during the flush. The peaks at 1626 cm^{-1} and 1601 cm^{-1} are assigned to the free N-O stretching mode of bidentate/bridged nitrates [227, 231-233] whereas the peak at 1567 cm^{-1} has been assigned to the asymmetric O-N-O stretching of a monodentate nitrate [222, 234, 235]. These nitrate peaks were observed only for those samples that showed measurable NO oxidation rates [225]. Peaks due to adsorbed NO species that are expected to appear between 1700 cm^{-1} and 1900 cm^{-1} were not observed. The role of nitrates for NO oxidation was probed by flushing the sample with 300 ppm NO while monitoring the production of NO_2 at the reactor outlet. Figure 4.4.2 shows that NO_2 production continued until all nitrates present on the catalyst surface decomposed, proving that NO reduced the surface nitrates to produce NO_2 and hence, nitrates participate in the NO oxidation reaction.

4.4.2 $^{14}NO \rightarrow {}^{15}NO$ Isotope Switch

It was essential to ensure that the NO oxidation reaction rate measured in the *operando* FTIR reactor matched with that in the plug-flow reactor (PFR) for the Cu-ZSM-5 sample with Cu/Al = 0.33 before performing any isotope labeling experiments and interpreting the results. The NO oxidation reaction rate measured at standard conditions of 300 ppm NO, 150 ppm NO_2, 10% O_2, 573 K in the PFR setup described by Verma et al.

[41] was 3 x 10^{-4} mol NO (mol Cu)$^{-1}$ s^{-1}. Standard concentrations of 150 ppm NO, 50 ppm NO_2, 5% O_2, 573 K were used for the *operando* reactor to avoid contributions from gas phase NO oxidation reaction in the measurement of NO and NO_2 concentrations, which is explained in more detail in appendix C. The measured NO oxidation rate was subsequently normalized to 300 ppm NO, 10% O_2 and 150 ppm NO_2 and compared with the corresponding value from the PFR by using the reaction orders of 1.7 for NO, -0.8 for NO_2 and 0.9 for O_2, and gave a value of 2.6 x 10^{-4} mol NO (mol Cu)$^{-1}$ s^{-1}. A comparison of the activation energy plots in the two reactors (Figure 4.4.3) shows that the rate measurements in the two reactors were in quantitative agreement with each other across the temperature range tested (543-573 K).

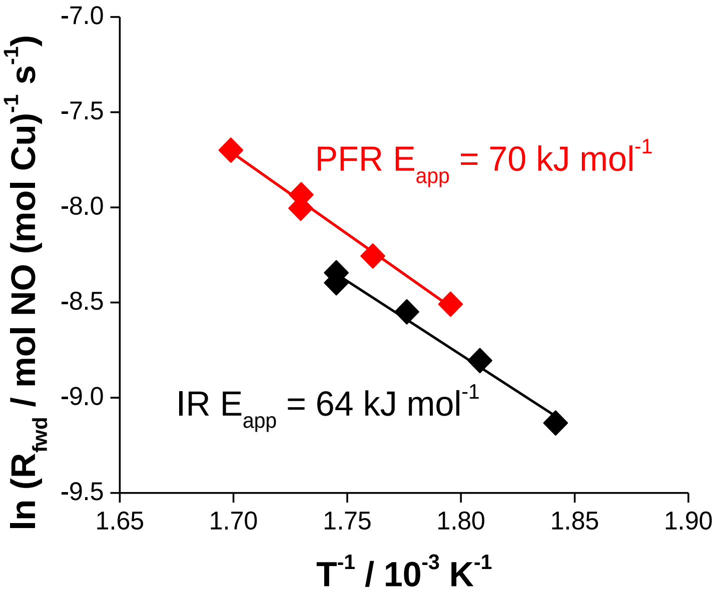

Figure 4.4.3 Comparison of the activation energy plots in (a) the *operando* IR reactor **(black diamonds)** and (b) PFR **(red diamonds)**. Sample: Cu/Al = 0.33, Si/Al = 18, Cu-ZSM-5.

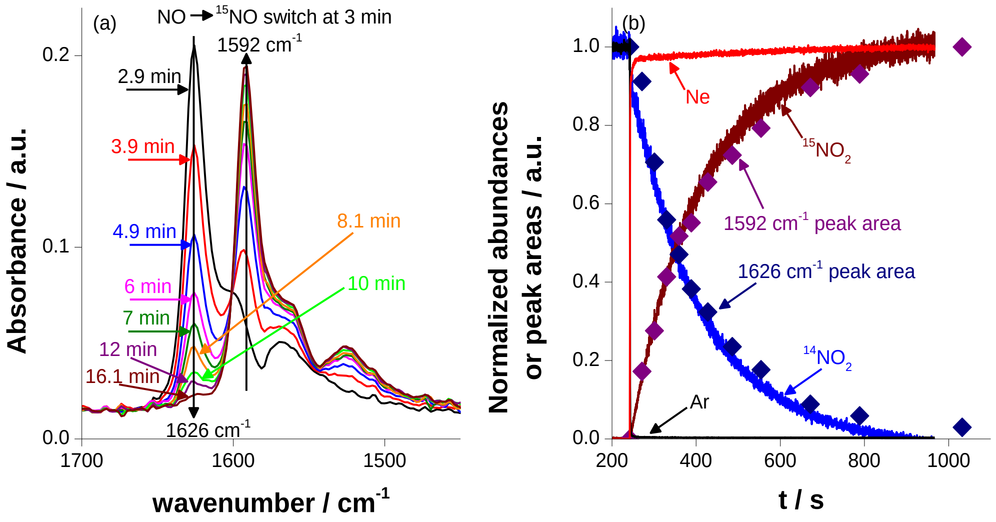

Figure 4.4.4 (a) FTIR spectra after the $^{14}NO \rightarrow ^{15}NO$ isotope switch show an immediate decrease in the 1626 cm^{-1} peak along with a concomitant increase in the 1592 cm^{-1} peak (b) Mass spectrometer traces for $^{15}NO_2$ ($m/z = 47$) and $^{14}NO_2$ ($m/z = 46$) are coincident with the areas for the 1592 cm^{-1} and 1626 cm^{-1} peaks, respectively. The corresponding Ar ($m/z = 40$) and Ne ($m/z = 20$) traces are also shown. Sample: Cu/Al = 0.3, Si/Al = 18, Cu-ZSM-5. Feed conditions: 150 ppm NO/^{15}NO, 5% O_2, 553 K.

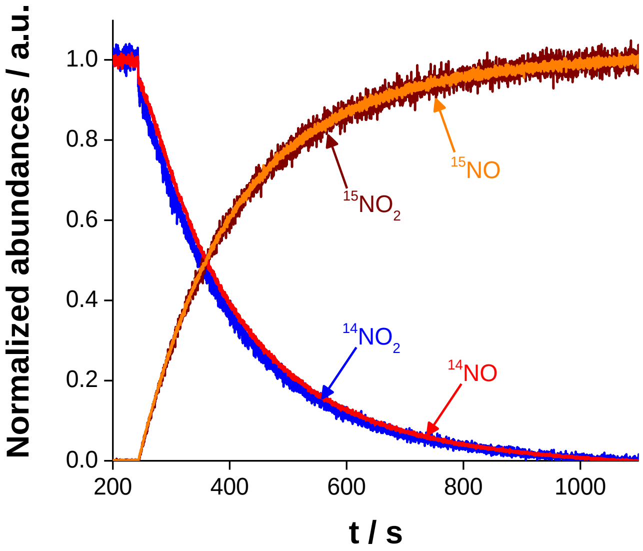

Figure 4.4.5 Mass spectrometer traces during the isotope switching experiment overlap for $^{15}NO_2$ ($m/z = 47$) – ^{15}NO ($m/z = 31$) and $^{14}NO_2$ ($m/z = 46$) – ^{14}NO ($m/z = 30$). Feed conditions: 150 ppm NO/^{15}NO, 5% O_2, 553 K.

Results from section 4.4.1 showed that nitrates are important intermediates for the NO oxidation reaction. However, three different nitrates were observed at steady state. Hence, it was of interest to identify which nitrate species were the active intermediates for NO_2 production. Since the combination of NO and O_2 or NO_2 in the feed both led to nitrates on the catalyst, NO_2 was excluded in the $^{14}NO \rightarrow {}^{15}NO$ isotope switching experiments because NO_2 would cause scrambling of the ^{15}N-labeled nitrate species with the unlabeled nitrates.

Once the catalyst reached steady state (150 ppm NO, 5% O_2 at 553 K), ^{14}NO and Ar in the feed stream was replaced with ^{15}NO and Ne at 3 min while simultaneously collecting FTIR spectra and monitoring the effluent gas species with a mass spectrometer (MS). It was important to ensure plug-flow behavior during these switching experiments in order to prevent back-mixing of the isotope gas, and to be able to interpret the product traces measured in the MS. The Ne and Ar inert tracers in Figure 4.4.4b reached 95% of their maximum and minimum signals within ~1.5 s of performing the $^{14}NO \rightarrow {}^{15}NO$ switch, thus confirming plug-flow behavior. Figure 4.4.4a shows that the peak at 1626 cm^{-1} decreased in intensity immediately after performing the switch along with a concomitant increase in a new peak at 1592 cm^{-1}, due to an isotopically labeled ^{15}N-nitrate. Applying the two atom oscillator model for the peak at 1626 cm^{-1} because it represents the N-O stretching vibration of a bridged/bidentate nitrate, its vibrational frequency is inversely proportional to the square root of the reduced masses of the N and the O atoms [236]. Thus, the calculated position of the ^{15}N-O stretching is 1595 cm^{-1}, which gives a shift of 31 cm^{-1} when a ^{14}N atom is replaced by its isotope ^{15}N in a N-O stretching vibrational mode. This is in agreement with the observed shift of 34 cm^{-1} and hence, the peak at 1592 cm^{-1} is due to the ^{15}N-bidentate/bridged nitrate species. The mass spectrometer signal showed that $^{14}NO_2$ decreased along with a simultaneous increase in $^{15}NO_2$ after the isotope switch. Furthermore, the decrease in the ^{14}N-nitrate peak area at 1626 cm^{-1} was coincident with the decreasing $^{14}NO_2$ product in the reactor effluent, while the corresponding ^{15}N-nitrate peak area at 1592 cm^{-1} coincided with the increasing $^{15}NO_2$ product. Thus, the bridged/bidentate nitrate at 1626 cm^{-1} is the probable reaction intermediate producing NO_2 during the oxidation of NO by O_2.

Additionally the average lifetime of the reactive intermediates on the catalyst surface can be obtained from the $^{15}NO_2$ product trace in the MS as shown by Shannon et al. [237] and Wang et al [200]. The average lifetime (τ), calculated by integrating the difference between the normalized MS traces of Ne (F_{Ne}) and $^{15}NO_2$ (F_{15NO2}) (equation 4.1), was 177.5 ± 7.5 s at 553 K.

$$\tau = \int \left(F_{Ne} - F_{^{15}NO_2}\right) dt \ldots\ldots 4.1$$

Further, it was observed that the MS traces in the reactor effluent for ^{15}NO and $^{15}NO_2$ overlapped with each other as well as those for ^{14}NO and $^{14}NO_2$ (Figure 4.4.5) . This occurs due to the rapid equilibrium between NO and NO_2 via surface nitrates [6, 220] according to equation 4.2. An important consequence of this result is that both ^{15}NO and $^{15}NO_2$ contribute to the total pool of ^{15}N intermediates on the catalyst surface. Thus, the total amount of ^{15}N intermediates on the catalyst surface was calculated (Table 4.4.1) from the difference between the ^{15}NO fed to the reactor and the sum of ^{15}NO and $^{15}NO_2$ concentrations detected in the reactor effluent using the MS.

$$NO + NO_3^- \rightarrow NO_2 + NO_2^- \ldots\ldots 4.2$$

Equation 4.2 implies that the catalyst surface would have coverages of both nitrates and nitrites under reaction conditions. However, we were unable to observe nitrite species on the zeolite surface because strong zeolite framework vibrations mask the infrared spectrum below 1300 cm^{-1}, which coincides with the vibrational modes of nitrites on transition metal oxides that are typically observed in the range of 1200 – 1300 cm^{-1} for CuO [238], NiO and ZrO_2 [239]. Further, repeating the isotope switching experiment at 543 K, 563 K and 573 K yielded similar results where the peak areas for the ^{14}N-nitrate peak at 1626 cm^{-1} and the ^{15}N-nitrate peak at 1592 cm^{-1} changed in unison with the corresponding $^{14}NO_2$ and $^{15}NO_2$ product traces respectively (Figure C.4.1-Figure C.4.3). Values of the average residence time and amount of ^{15}N surface reaction intermediates at each temperature are shown in Table 4.4.1.

Table 4.4.1 Average residence times (τ) at various temperatures obtained from the ^{14}NO → ^{15}NO switching experiment. Feed conditions: 150 ppm NO/^{15}NO, 5% O_2, 543 K – 573 K. Sample: Cu/Al = 0.3, Si/Al = 18, Cu-ZSM-5.

T / K	573	563	553	543
τ / s	125.6 ± 1.7	149.2 ± 2.5	177.5 ± 7.5	214.1 ± 3.5
$\theta_{\text{active intermediates}}$	0.034	0.039	0.047	0.061

Based on the results presented here about the involvement of nitrates in NO oxidation, the kinetic model proposed by Verma et al. [41] has been modified to incorporate nitrate formation and account for the fast equilibrium between gas phase NO and NO_2 via nitrates. The coverages the surface species are consistent with the predictions made by the authors in that study with O* being the most stable intermediate with a coverage of 0.5.

4.5 Conclusions

Nitrates were observed only for those Cu-ZSM-5 samples that were active for NO oxidation , but no specificity with regards to the three types of nitrates at 1626 cm^{-1}, 1601 cm^{-1} and 1567 cm^{-1} was observed [225]. NO reduced nitrates to produce NO_2, thus showing that nitrates were important participants in the NO oxidation reaction. $^{14}NO \rightarrow {}^{15}NO$ isotope switching experiments at 543 K, 553 K, 563 K and 573 K showed that the peak area for the ^{14}N-nitrate at 1626 cm^{-1} tracked with the production of $^{14}NO_2$, whereas the peak area for the corresponding ^{15}N-bridged/bidentate nitrate at 1592 cm^{-1} tracked with $^{15}NO_2$. Thus, the bridged/bidentate nitrate at 1626 cm^{-1} is the likely intermediate for the NO oxidation reaction. The results also showed that NO and NO_2 were in equilibrium with each other via nitrates on the catalyst surface. Average residence times (τ) for the reactive intermediates and the total pool of ^{15}N containing species on the catalyst surface was calculated from the $^{15}NO_2$ and ^{15}NO traces in the mass spectrometer, and showed that less than 10% of the total Cu was covered with the ^{15}N containing species between 543 K and 573 K.

4.6 Acknowledgements

We would like to acknowledge Ford Motor Co. and Dr. Giovanni Cavataio for providing us with the isotope gases and the gas regulators used in this work. We would also like to thank Dr. Jun Wang for his help and guidance with building the custom reactor unit used for these isotope switching experiments.

CHAPTER 5. RECOMMENDATIONS

Although NO and NH_3 are commonly accepted as co-reductants for standard SCR redox chemistry [30, 33], re-oxidation of Cu(I) to Cu(II) is poorly understood till date, with the only suggestions being that NO and O_2 participate in the oxidation half-cycle via formation of nitrates and nitrites [31, 33]. There is no clear consensus on what are the elementary steps for this step to occur. To probe the low temperature standard SCR (473 K) oxidation half-cycle, XAS experiments were performed as elaborated in chapter 3, which show that the oxidation of Cu(I) to Cu(II) with O_2 is a second order process in the amount of Cu(I) at any given instant. This suggests that multiple Cu moieties are required for the oxidation process during standard SCR catalysis, in agreement with the inference from the non-linear, squared dependence of the low temperature standard SCR (473 K) reaction rate on Cu content of the catalysts [34].

Chapter 2 shows that solvation by NH_3 imparts mobility to the Cu(I) ions. Hence, it is conceivable that two Cu(I) ions can activate O_2 to form Cu-oxo-dimer complexes. The enzyme literature cited in Chapter 3 shows the prevalence of a rich chemistry involving multiple types of Cu-oxo complexes. However, because of electrostatic attraction, the mobile Cu(I) ions can only move within a specific distance from the charge-compensating framework Al atoms. Hence, only Cu ions in close proximity would be able to form a paired Cu-oxo site to perform the oxidation half-cycle for standard SCR, and the fraction of such Cu out of the total ion exchanged Cu in any sample will depend on the catalyst composition (Si:Al and Cu:Al ratios). Because the reduction event occurs on single, isolated Cu(II) ions but oxidation requires multiple proximal Cu(I) sites, there may be a fraction of the total Cu under standard SCR conditions that is stuck in the Cu(I) state because of the absence of other neighboring Cu(I) ions within its sphere of mobility and hence, is inactive for standard SCR. This suggests that two different pools of Cu sites exist during steady state standard SCR, one that participates in the reaction via pairing with proximal Cu sites and the other that is inactive because of its inability to find a proximal Cu within its sphere of mobility

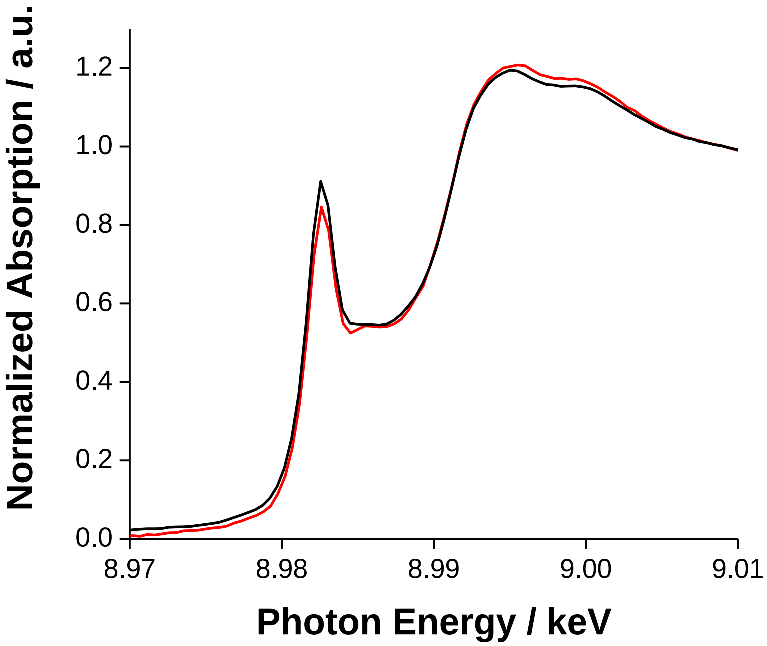

Figure 4.6.1 Standard SCR steady state *operando* XANES spectra at **10% O_2 (black)** and **60% O_2 (red)** feed concentrations. Feed conditions: 300 ppm NO, 300 ppm NH_3, 10%/60% O_2, 2% H_2O, 5% CO_2, 475 K. Sample: Cu/Al = 0.12, Si/Al = 15. Cu(I) fraction = 0.75 at 10% O_2 and 0.69 at 60% O_2.

This picture is consistent with our current and previous observations across multiple samples where we have not been able to obtain ~100% Cu(II) under any catalytic conditions, even with 60% feed O_2 concentration (Figure 4.6.1) at which point the O_2 order for this sample is 0, suggesting that not all Cu(I) can be oxidized.

An upper bound for the number of active sites that are capable of participating in the standard SCR reaction can be obtained from the O_2 titration experiment, similar to that performed in Chapter 3. This should be performed for several samples across the entire composition space with varying Si/Al and Cu/Al ratios and the SCR rates normalized to the amount of Cu(II) obtained at the end of this titration, which is the correct count for the number of active sites, rather than the total Cu content. This view of two pools of Cu sites is also consistent with previous studies in our group [28] on high Al (Si/al = 4.5) Cu-SSZ-13 catalysts because high Cu and Al contents in those samples meant that a majority of the total Cu was within close proximity to each other and hence, the standard SCR reaction rates scaled linearly with the Cu content since it was not limited by pairing of Cu sites. This implies that our initial idea of all isolated Cu sites being active for standard SCR [28] may be an over-simplification compared to the more complex actual chemistry because single Cu(II) sites can reduce to Cu(I) but two Cu(I) sites are involved during the re-oxidation to Cu(II). NO_2, however, engages all the Cu(I) sites in an identical manner regardless of the density or proximity of Cu sites in the sample (chapter 3). Thus, all Cu sites participate in the fast SCR reaction, whereas only a fraction of the total Cu sites can participate in the standard SCR reaction.

Although there is indirect evidence of Cu-oxo-dimers being responsible for oxidation of Cu(I) to Cu(II) from both the non-linear dependence of the standard SCR rate

(473 K) on the Cu content for samples that are limited by the oxidation half-cycle [34] and second order dependence of Cu(I) oxidation in the O_2 titration experiments, we have no direct spectroscopic evidence for the existence of such Cu-dimer complexes. Since a variety of Cu-dimer complexes have been reported within enzymes, and these have different signatures in UV-Vis spectra depending on the type of the dimer species that is formed, this technique would be a good way to identify dimer formation during the oxidation process with O_2. Another possible experiment to detect such dimers is to cool the samples to sub-ambient temperatures (between 148 K and 195 K) following reduction in flowing NO and NH_3 (300 ppm each, 473 K), and subsequently introducing O_2 while collecting EXAFS spectra to observe any possible Cu-Cu second shell feature as would be expected if Cu-dimers are formed. However, the absence of any such feature should not be taken as an indication that they are not formed because they are unstable and very reactive.

After understanding the oxidation of Cu(I) with O_2, the other missing piece in the standard SCR mechanism is to elucidate how the catalytic cycle closes following the oxidation of Cu(I) to Cu(II) with O_2. A direct probe of this, and a follow up for the experiments in chapter 3, is to flow NO subsequent to the O_2 titration step and monitor the time – dependent behavior of the Cu oxidation states using XANES. Preliminary calculations from Chris Paolucci at Notre Dame suggest that NO reacts with the Cu-dimers to form nitrates, and in the process half of the total Cu(II) present in the form of Cu-dimers is reduced to Cu(I) according to the following reaction:

$$\mathrm{Cu(II)}\left(\mathrm{O_2^{2-}}\right)\mathrm{Cu(II)} + \mathrm{NO} \rightarrow \mathrm{Cu(II)NO_3^-} + \mathrm{Cu(I)} \ldots\ldots 5.1$$

An increase in the Cu(I) fraction upon dosing NO to the O_2 treated catalyst would confirm that the reaction indeed proceeds via a nitrate mechanism. Further, FTIR spectroscopy can be employed to detect nitrate formation on the catalyst surface. Thus, these experiments are powerful tools in extending our understanding of the oxidation half-cycle in the standard SCR mechanism to close the catalytic cycle.

REFERENCES

REFERENCES

[1] E.S.N.A.Q.S. , http://www2.epa.gov/aboutepa/epa-sets-national-air-quality-standards, (1971).

[2] H. Sjovall, L. Olsson, E. Fridell, R.J. Blint, Selective catalytic reduction of NOx with NH3 over Cu-ZSM-5 - The effect of changing the gas composition, Appl Catal B-Environ, 64 (2006) 180-188.

[3] Final Revisions to the Primary National Ambient Air Quality Standards for NO_2, http://www.epa.gov/airquality/nitrogenoxides/pdfs/20100124presentation.pdf, (January 2010).

[4] H. Bosch, F. Janssen, Catalysis Today, 2 (1988) 369 - 531.

[5] K. Kamasamudram, N.W. Currier, X. Chen, A. Yezerets, Overview of the practically important behaviors of zeolite-based urea-SCR catalysts, using compact experimental protocol, Catalysis Today, 151 (2010) 212-222.

[6] L. Olsson, H. Sjovall, R.J. Blint, Detailed kinetic modeling of NOx adsorption and NO oxidation over Cu-ZSM-5, Appl Catal B-Environ, 87 (2009) 200-210.

[7] S. Brandenberger, O. Krocher, A. Tissler, R. Althoff, The State of the Art in Selective Catalytic Reduction of NOx by Ammonia Using Metal-Exchanged Zeolite Catalysts, Catal Rev, 50 (2008) 492-531.

[8] G. Centi, S. Perathoner, Introduction: State of the Art in the Development of Catalytic Processes for the Selective Catalytic Reduction of Nox into N-2, Stud Surf Sci Catal, 171 (2007) 1-23.

[9] C. Ciardelli, I. Nova, E. Tronconi, D. Chatterjee, B. Bandl-Konrad, M. Weibel, B. Krutzsch, Reactivity of NO/NO2-NH3 SCR system for diesel exhaust aftertreatment: Identification of the reaction network as a function of temperature and NO2 feed content, Appl Catal B-Environ, 70 (2007) 80-90.

[10] USEPA, Clean Diesel Combustion - Clean, Efficient, Cost Effective Technology (http://www.epa.gov/otaq/420f04023.pdf), EPA420-F-04-023, (2004).

[11] M. Iwamoto, H. Yahiro, K. Tanda, N. Mizuno, Y. Mine, S. Kagawa, Removal of Nitrogen Monoxide through a Novel Catalytic Process .1. Decomposition on Excessively Copper-Ion Exchanged Zsm-5 Zeolites, J Phys Chem-Us, 95 (1991) 3727-3730.

[12] M. Colombo, I. Nova, E. Tronconi, NO2 adsorption on Fe- and Cu-zeolite catalysts: The effect of the catalyst red-ox state, Appl Catal B-Environ, 111 (2012) 433-444.

[13] H. Sjovall, E. Fridell, R.J. Blint, L. Olsson, Identification of adsorbed species on Cu-ZSM-5 under NH3SCR conditions, Top Catal, 42-43 (2007) 113-117.

[14] P.T. Fanson, M.W. Stradt, J. Lauterbach, W.N. Delgass, The effect of Si/Al ratio and copper exchange level on isothermal kinetic rate oscillations for N2O decomposition over Cu-ZSM-5: a transient FTIR study, Appl Catal B-Environ, 38 (2002) 331-347.

[15] K.M. Adams, J.V. Cavataio, R.H. Hammerle, Lean NOx catalysis for diesel passenger cars: Investigating effects of sulfur dioxide and space velocity, Appl Catal B-Environ, 10 (1996) 157-181.

[16] N.-Y. Topsoe, Selective catalytic reduction of NOx by ammonia: fundamental and industrial aspects, CatTech, (1997) 125 - 134.

[17] O. Krocher, Aspects of Catalyst Development for Mobile Urea-Scr Systems - from Vanadia-Titania Catalysts to Metal-Exchanged Zeolites, Stud Surf Sci Catal, 171 (2007) 261-289.

[18] S.T. Korhonen, D.W. Fickel, R.F. Lobo, B.M. Weckhuysen, A.M. Beale, Isolated Cu2+ ions: active sites for selective catalytic reduction of NO, Chem Commun, 47 (2011) 800-802.

[19] U. Deka, A. Juhin, E.A. Eilertsen, H. Emerich, M.A. Green, S.T. Korhonen, B.M. Weckhuysen, A.M. Beale, Confirmation of Isolated Cu2+ Ions in SSZ-13 Zeolite as Active Sites in NH3-Selective Catalytic Reduction, J Phys Chem C, 116 (2012) 4809-4818.

[20] J.S. McEwen, T. Anggara, W.F. Schneider, V.F. Kispersky, J.T. Miller, W.N. Delgass, F.H. Ribeiro, Integrated operando X-ray absorption and DFT characterization of Cu-SSZ-13 exchange sites during the selective catalytic reduction of NOx with NH3, Catalysis Today, 184 (2012) 129-144.

[21] J. Szanyi, J.H. Kwak, H.Y. Zhu, C.H.F. Peden, Characterization of Cu-SSZ-13 NH3 SCR catalysts: an in situ FTIR study, Phys Chem Chem Phys, 15 (2013) 2368-2380.

[22] A. Grossale, I. Nova, E. Tronconi, D. Chatterjee, M. Weibel, The chemistry of the NO/NO2-NH3 "fast" SCR reaction over Fe-ZSM5 investigated by transient reaction analysis, J Catal, 256 (2008) 312-322.

[23] K. Rahkamaa-Tolonen, T. Maunula, M. Lomma, M. Huuhtanen, R.L. Keiski, The effect of NO2 on the activity of fresh and aged zeolite catalysts in the NH3-SCR reaction, Catalysis Today, 100 (2005) 217-222.

[24] M. Iwamoto, H. Furukawa, Y. Mine, F. Uemura, S.I. Mikuriya, S. Kagawa, Copper(Ii) Ion-Exchanged Zsm-5 Zeolites as Highly-Active Catalysts for Direct and Continuous Decomposition of Nitrogen Monoxide, J Chem Soc Chem Comm, (1986) 1272-1273.

[25] J.H. Kwak, D. Tran, S.D. Burton, J. Szanyi, J.H. Lee, C.H.F. Peden, Effects of hydrothermal aging on NH3-SCR reaction over Cu/zeolites, J Catal, 287 (2012) 203-209.

[26] G. Busca, L. Lietti, G. Ramis, F. Berti, Chemical and mechanistic aspects of the selective catalytic reduction of NOx by ammonia over oxide catalysts: A review, Appl Catal B-Environ, 18 (1998) 1-36.

[27] M. Colombo, I. Nova, E. Tronconi, V. Schmeisser, B. Bandl-Konrad, L. Zimmermann, NO/NO2/N2O-NH3 SCR reactions over a commercial Fe-zeolite catalyst for diesel exhaust aftertreatment: Intrinsic kinetics and monolith converter modelling, Appl Catal B-Environ, 111 (2012) 106-118.

[28] S.A. Bates, A.A. Verma, C. Paolucci, A.A. Parekh, T. Anggara, A. Yezerets, W.F. Schneider, J.T. Miller, W.N. Delgass, F.H. Ribeiro, Identification of the active Cu site in standard selective catalytic reduction with ammonia on Cu-SSZ-13, J Catal, 312 (2014) 87-97.

[29] V.F. Kispersky, A.J. Kropf, F.H. Ribeiro, J.T. Miller, Low absorption vitreous carbon reactors for operando XAS: a case study on Cu/Zeolites for selective catalytic reduction of NOx by NH3, Phys Chem Chem Phys, 14 (2012) 2229-2238.

[30] C. Paolucci, A.A. Verma, S.A. Bates, V.F. Kispersky, J.T. Miller, R. Gounder, W.N. Delgass, F.H. Ribeiro, W.F. Schneider, Isolation of the Copper Redox Steps in the Standard Selective Catalytic Reduction on Cu-SSZ-13, Angew Chem Int Edit, 53 (2014) 11828-11833.

[31] C. Paolucci, A.A. Parekh, I. Khurana, J.R. Di Iorio, H. Li, J. Albarracin, A. Shih, T. Anggara, W.N. Delgass, J.T. Miller, F.H. Ribeiro, R. Gounder, W.F. Schneider, Catalysis in a Cage: Condition-Dependent Speciation and Dynamics of Exchanged Cu Cations in SSZ-13 Zeolites, J Am Chem Soc, 10.1021/jacs.6b02651 (2016).

[32] F. Giordanino, P.N.R. Vennestrom, L.F. Lundegaard, F.N. Stappen, S. Mossin, P. Beato, S. Bordiga, C. Lamberti, Characterization of Cu-exchanged SSZ-13: a comparative FTIR, UV-Vis, and EPR study with Cu-ZSM-5 and Cu-beta with similar Si/Al and Cu/Al ratios, Dalton T, 42 (2013) 12741-12761.

[33] T.V.W. Janssens, H. Falsig, L.F. Lundegaard, P.N.R. Vennestrom, S.B. Rasmussen, P.G. Moses, F. Giordanino, E. Borfecchia, K.A. Lomachenko, C. Lamberti, S. Bordiga, A. Godiksen, S. Mossin, P. Beato, A Consistent Reaction Scheme for the Selective Catalytic Reduction of Nitrogen Oxides with Ammonia, Acs Catal, 5 (2015) 2832-2845.

[34] F. Gao, E.D. Walter, M. Kollar, Y.L. Wang, J. Szanyi, C.H.F. Peden, Understanding ammonia selective catalytic reduction kinetics over Cu/SSZ-13 from motion of the Cu ions, J Catal, 319 (2014) 1-14.

[35] P.S. Metkar, V. Balakotaiah, M.P. Harold, Experimental and kinetic modeling study of NO oxidation: Comparison of Fe and Cu-zeolite catalysts, Catalysis Today, 184 (2012) 115-128.

[36] T. Komatsu, T. Ogawa, T. Yashima, Nitrate Species on Cu-Zsm-5 Catalyst as an Intermediate for the Reduction of Nitric-Oxide with Ammonia, J Phys Chem-Us, 99 (1995) 13053-13055.

[37] M. Devadas, O. Krocher, M. Elsener, A. Wokaun, N. Soger, M. Pfeifer, Y. Demel, L. Mussmann, Influence of NO2 on the selective catalytic reduction of NO with ammonia over Fe-ZSM5, Appl Catal B-Environ, 67 (2006) 187-196.

[38] G. Delahay, D. Valade, A. Guzman-Vargas, B. Coq, Selective catalytic reduction of nitric oxide with ammonia on Fe-ZSM-5 catalysts prepared by different methods, Appl Catal B-Environ, 55 (2005) 149-155.

[39] J.Y. Luo, X.X. Hou, P. Wijayakoon, S.J. Schmieg, W. Li, W.S. Epling, Spatially resolving SCR reactions over a Fe/zeolite catalyst, Appl Catal B-Environ, 102 (2011) 110-119.

[40] M. Devadas, O. Krocher, M. Elsener, A. Wokaun, G. Mitrikas, N. Soger, M. Pfeifer, Y. Demel, L. Mussmann, Characterization and catalytic investigation of Fe-ZSM5 for urea-SCR, Catalysis Today, 119 (2007) 137-144.

[41] A.A. Verma, S.A. Bates, T. Anggara, C. Paolucci, A.A. Parekh, K. Kamasamudram, A. Yezerets, J.T. Miller, W.N. Delgass, W.F. Schneider, F.H. Ribeiro, NO oxidation: A probe reaction on Cu-SSZ-13, J Catal, 312 (2014) 179-190.

[42] P. Bazin, O. Marie, M. Daturi, General Features of *In Situ* and *Operando* Spectroscopic Investigation in the Particular Case of DeNO$_x$ Reactions, Stud Surf Sci Catal, 171 (2007) 97-143.

[43] U.S. Ozkan, Y.P. Cai, M.W. Kumthekar, Investigation of the Mechanism of Ammonia Oxidation and Oxygen-Exchange over Vanadia Catalysts Using N-15 and O-18 Tracer Studies, J Catal, 149 (1994) 375-389.

[44] U.S. Ozkan, Y.P. Cai, M.W. Kumthekar, Investigation of the Reaction Pathways in Selective Catalytic Reduction of No with Nh3 over V2o5 Catalysts - Isotopic Labeling Studies Using O-18(2), (Nh3)-N-15, (No)-N-15, and (No1)-N-15-O-18, J Catal, 149 (1994) 390-403.

[45] U.S. Ozkan, Y.P. Cai, M.W. Kumthekar, Mechanistic Studies of Selective Catalytic Reduction of Nitric-Oxide with Ammonia over V2o5/Tio2 (Anatase) Catalysts through Transient Isotopic Labeling at Steady-State, J Phys Chem-Us, 99 (1995) 2363-2371.

[46] J.H. Siddall, M.L. Miller, W.N. Delgass, Transient Kinetic-Analysis of Methane Synthesis over Unsupported Co and Rh/Sio2, Chem Eng Commun, 83 (1989) 261-276.

[47] S. Chansai, R. Burch, C. Hardacre, J. Breen, F. Meunier, The use of short time-on-stream in situ spectroscopic transient kinetic isotope techniques to investigate the mechanism of hydrocarbon selective catalytic reduction (HC-SCR) of NOx at low temperatures, J Catal, 281 (2011) 98-105.

[48] H.S. Taylor, A theory of the catalytic surface, P R Soc Lond a-Conta, 108 (1925) 105-111.

[49] M. Behrens, F. Studt, I. Kasatkin, S. Kuhl, M. Havecker, F. Abild-Pedersen, S. Zander, F. Girgsdies, P. Kurr, B.L. Kniep, M. Tovar, R.W. Fischer, J.K. Norskov, R. Schlogl, The Active Site of Methanol Synthesis over Cu/ZnO/Al2O3 Industrial Catalysts, Science, 336 (2012) 893-897.

[50] T. Zambelli, J. Wintterlin, J. Trost, G. Ertl, Identification of the "active sites" of a surface-catalyzed reaction, Science, 273 (1996) 1688-1690.

[51] T.F. Jaramillo, K.P. Jorgensen, J. Bonde, J.H. Nielsen, S. Horch, I. Chorkendorff, Identification of active edge sites for electrochemical H-2 evolution from MoS2 nanocatalysts, Science, 317 (2007) 100-102.

[52] J.M. Thomas, Design, synthesis, and in situ characterization of new solid catalysts, Angew Chem Int Edit, 38 (1999) 3589-3628.

[53] Y.D. Kim, A.P. Seitsonen, S. Wendt, J. Wang, C. Fan, K. Jacobi, H. Over, G. Ertl, Characterization of various oxygen species on an oxide surface: RuO2(110), J Phys Chem B, 105 (2001) 3752-3758.

[54] E.C. Tyo, C.R. Yin, M. Di Vece, Q. Qian, G. Kwon, S. Lee, B. Lee, J.E. DeBartolo, S. Seifert, R.E. Winans, R. Si, B. Ricks, S. Goergen, M. Rutter, B. Zugic, M. Flytzani-Stephanopoulos, Z.W. Wang, R.E. Palmer, M. Neurock, S. Vajda, Oxidative Dehydrogenation of Cyclohexane on Cobalt Oxide (Co3O4) Nanoparticles: The Effect of Particle Size on Activity and Selectivity, Acs Catal, 2 (2012) 2409-2423.

[55] T. Hwang, B.R. Goldsmith, B. Peters, S.L. Scott, Water-Catalyzed Activation of H2O2 by Methyltrioxorhenium: A Combined Computational-Experimental Study, Inorg Chem, 52 (2013) 13904-13917.

[56] A.M. Beale, A.M.J. van der Eerden, K. Kervinen, M.A. Newton, B.M. Weckhuysen, Adding a third dimension to operando spectroscopy: a combined UV-Vis, Raman and XAFS setup to study heterogeneous catalysts under working conditions, Chem Commun, (2005) 3015-3017.

[57] H. Topsoe, Developments in operando studies and in situ characterization of heterogeneous catalysts, J Catal, 216 (2003) 155-164.

[58] B.M. Weckhuysen, Determining the active site in a catalytic process: Operando spectroscopy is more than a buzzword, Phys Chem Chem Phys, 5 (2003) 4351-4360.

[59] I.X. Green, W.J. Tang, M. Neurock, J.T. Yates, Spectroscopic Observation of Dual Catalytic Sites During Oxidation of CO on a Au/TiO2 Catalyst, Science, 333 (2011) 736-739.

[60] A. Boubnov, H.W.P. Carvalho, D.E. Doronkin, T. Gunter, E. Gallo, A.J. Atkins, C.R. Jacob, J.D. Grunwaldt, Selective Catalytic Reduction of NO Over Fe-ZSM-5: Mechanistic Insights by Operando HERFD-XANES and Valence-to-Core X-ray Emission Spectroscopy, J Am Chem Soc, 136 (2014) 13006-13015.

[61] E.J. Peterson, A.T. Delariva, S. Lin, R.S. Johnson, H. Guo, J.T. Miller, J.H. Kwak, C.H.F. Peden, B. Kiefer, L.F. Allard, F.H. Ribeiro, A.K. Datye, Low-temperature carbon monoxide oxidation catalysed by regenerable atomically dispersed palladium on alumina, Nat Commun, 5 (2014).

[62] M.J. Rice, A.K. Chakraborty, A.T. Bell, Site availability and competitive siting of divalent metal cations in ZSM-5, J Catal, 194 (2000) 278-285.

[63] M.J. Rice, A.K. Chakraborty, A.T. Bell, Al next nearest neighbor, ring occupation, and proximity statistics in ZSM-5, J Catal, 186 (1999) 222-227.

[64] B.R. Goodman, K.C. Hass, W.F. Schneider, J.B. Adams, Statistical analysis of Al distributions and metal ion pairing probabilities in zeolites, Catal Lett, 68 (2000) 85-93.

[65] P. Sarv, C. Fernandez, J.P. Amoureux, K. Keskinen, Distribution of tetrahedral aluminium sites in ZSM-5 type zeolites: An Al-27 (Multiquantum) magic angle spinning NMR study, J Phys Chem-Us, 100 (1996) 19223-19226.

[66] D.E. Perea, I. Arslan, J. Liu, Z. Ristanovic, L. Kovarik, B.W. Arey, J.A. Lercher, S.R. Bare, B.M. Weckhuysen, Determining the location and nearest neighbours of aluminium in zeolites with atom probe tomography, Nat Commun, 6 (2015).

[67] P. Vanelderen, J. Vancauwenbergh, B.F. Sels, R.A. Schoonheydt, Coordination chemistry and reactivity of copper in zeolites, Coordin Chem Rev, 257 (2013) 483-494.

[68] M.J. Rice, A.K. Chakraborty, A.T. Bell, Theoretical studies of the coordination and stability of divalent cations in ZSM-5, J Phys Chem B, 104 (2000) 9987-9992.

[69] K.C. Hass, W.F. Schneider, Reliability of small cluster models for Cu-exchanged zeolites, J Phys Chem-Us, 100 (1996) 9292-9301.

[70] B.L. Trout, A.K. Chakraborty, A.T. Bell, Local spin density functional theory study of copper ion-exchanged ZSM-5, J Phys Chem-Us, 100 (1996) 4173-4179.

[71] A.V. Kucherov, A.A. Slinkin, D.A. Kondratev, T.N. Bondarenko, A.M. Rubinstein, K.M. Minachev, Cu-2+-Cation Location and Reactivity in Mordenite and Zsm-5-Esr-Study, Zeolites, 5 (1985) 320-324.

[72] G. Spoto, A. Zecchina, S. Bordiga, G. Ricchiardi, G. Martra, G. Leofanti, G. Petrini, Cu(I)-Zsm-5 Zeolites Prepared by Reaction of H-Zsm-5 with Gaseous Cucl - Spectroscopic Characterization and Reactivity Towards Carbon-Monoxide and Nitric-Oxide, Appl Catal B-Environ, 3 (1994) 151-172.

[73] G.T. Palomino, P. Fisicaro, S. Bordiga, A. Zecchina, E. Giamello, C. Lamberti, Oxidation states of copper ions in ZSM-5 zeolites. A multitechnique investigation, J Phys Chem B, 104 (2000) 4064-4073.

[74] D. Nachtigallova, P. Nachtigall, M. Sierka, J. Sauer, Coordination and siting of Cu+ ions in ZSM-5: A combined quantum mechanics interatomic potential function study, Phys Chem Chem Phys, 1 (1999) 2019-2026.

[75] P. Da Costa, B. Moden, G.D. Meitzner, D.K. Lee, E. Iglesia, Spectroscopic and chemical characterization of active and inactive Cu species in NO decomposition catalysts based on Cu-ZSM5, Phys Chem Chem Phys, 4 (2002) 4590-4601.

[76] B.R. Goodman, K.C. Hass, W.F. Schneider, J.B. Adams, Cluster model studies of oxygen-bridged Cu pairs in Cu-ZSM-5 catalysts, J Phys Chem B, 103 (1999) 10452-10460.

[77] P.J. Smeets, R.G. Hadt, J.S. Woertink, P. Vanelderen, R.A. Schoonheydt, B.F. Sels, E.I. Solomon, Oxygen Precursor to the Reactive Intermediate in Methanol Synthesis by Cu-ZSM-5, J Am Chem Soc, 132 (2010) 14736-14738.

[78] J.S. Woertink, P.J. Smeets, M.H. Groothaert, M.A. Vance, B.F. Sels, R.A. Schoonheydt, E.I. Solomon, A [Cu2O](2+) core in Cu-ZSM-5, the active site in the oxidation of methane to methanol, P Natl Acad Sci USA, 106 (2009) 18908-18913.

[79] M.H. Groothaert, J.A. van Bokhoven, A.A. Battiston, B.M. Weckhuysen, R.A. Schoonheydt, Bis(mu-oxo)dicopper in Cu-ZSM-5 and its role in the decomposition of NO: A combined in situ XAFS, UV-Vis-Near-IR, and kinetic study, J Am Chem Soc, 125 (2003) 7629-7640.

[80] R. Balasubramanian, S.M. Smith, S. Rawat, L.A. Yatsunyk, T.L. Stemmler, A.C. Rosenzweig, Oxidation of methane by a biological dicopper centre, Nature, 465 (2010) 115-U131.

[81] M.H. Groothaert, P.J. Smeets, B.F. Sels, P.A. Jacobs, R.A. Schoonheydt, Selective oxidation of methane by the bis(mu-oxo)dicopper core stabilized on ZSM-5 and mordenite zeolites, J Am Chem Soc, 127 (2005) 1394-1395.

[82] P. Vanelderen, R.G. Hadt, P.J. Smeets, E.I. Solomon, R.A. Schoonheydt, B.F. Sels, Cu-ZSM-5: A biomimetic inorganic model for methane oxidation, J Catal, 284 (2011) 157-164.

[83] N.V. Beznis, B.M. Weckhuysen, J.H. Bitter, Cu-ZSM-5 Zeolites for the Formation of Methanol from Methane and Oxygen: Probing the Active Sites and Spectator Species, Catal Lett, 138 (2010) 14-22.

[84] E.M.C. Alayon, M. Nachtegaal, A. Bodi, J.A. van Bokhoven, Reaction Conditions of Methane-to-Methanol Conversion Affect the Structure of Active Copper Sites, Acs Catal, 4 (2014) 16-22.

[85] E.M.C. Alayon, M. Nachtegaal, E. Kleymenov, J.A. van Bokhoven, Determination of the electronic and geometric structure of Cu sites during methane conversion over Cu-MOR with X-ray absorption spectroscopy, Micropor Mesopor Mat, 166 (2013) 131-136.

[86] E.M.C. Alayon, M. Nachtegaal, A. Bodi, M. Ranocchiari, J.A. van Bokhoven, Bis(mu-oxo) versus mono(mu-oxo)dicopper cores in a zeolite for converting methane to methanol: an in situ XAS and DFT investigation, Phys Chem Chem Phys, 17 (2015) 7681-7693.

[87] S. Grundner, M.A.C. Markovits, G. Li, M. Tromp, E.A. Pidko, E.J.M. Hensen, A. Jentys, M. Sanchez-Sanchez, J.A. Lercher, Single-site trinuclear copper oxygen clusters in mordenite for selective conversion of methane to methanol, Nat Commun, 6 (2015).

[88] P.J. Smeets, M.H. Groothaert, R.A. Schoonheydt, Cu based zeolites: A UV-vis study of the active site in the selective methane oxidation at low temperatures, Catalysis Today, 110 (2005) 303-309.

[89] M.J. Wulfers, S. Teketel, B. Ipek, R.F. Lobo, Conversion of methane to methanol on copper-containing small-pore zeolites and zeotypes, Chem Commun, 51 (2015) 4447-4450.
[90] S.T. King, Reaction mechanism of oxidative carbonylation of methanol to dimethyl carbonate in Cu-Y zeolite, J Catal, 161 (1996) 530-538.
[91] J. Dedecek, L. Capek, P. Sazama, Z. Sobalik, B. Wichterlova, Control of metal ion species in zeolites by distribution of aluminium in the framework: From structural analysis to performance under real conditions of SCR-NOx and NO, N2O decomposition, Appl Catal a-Gen, 391 (2011) 244-253.
[92] P.J. Smeets, B.F. Sels, R.M. van Teeffelen, H. Leeman, E.J.M. Hensen, R.A. Schoonheydt, The catalytic performance of Cu-containing zeolites in N2O decomposition and the influence of O-2, NO and H2O on recombination of oxygen, J Catal, 256 (2008) 183-191.
[93] B. Moden, P. Da Costa, B. Fonfe, D.K. Lee, E. Iglesia, Kinetics and mechanism of steady-state catalytic NO decomposition reactions on Cu-ZSM5, J Catal, 209 (2002) 75-86.
[94] M. Colombo, I. Nova, E. Tronconi, A comparative study of the NH3-SCR reactions over a Cu-zeolite and a Fe-zeolite catalyst, Catalysis Today, 151 (2010) 223-230.
[95] A. Shishkin, H. Kannisto, P.A. Carlsson, H. Harelind, M. Skoglundh, Synthesis and functionalization of SSZ-13 as an NH3-SCR catalyst, Catal Sci Technol, 4 (2014) 3917-3926.
[96] D.E. Doronkin, M. Casapu, T. Gunter, O. Muller, R. Frahm, J.D. Grunwaldt, Operando Spatially- and Time-Resolved XAS Study on Zeolite Catalysts for Selective Catalytic Reduction of NOx by NH3, J Phys Chem C, 118 (2014) 10204-10212.
[97] M. Koebel, M. Elsener, M. Kleemann, Urea-SCR: a promising technique to reduce NOx emissions from automotive diesel engines, Catalysis Today, 59 (2000) 335-345.
[98] G. Cavataio, J. Girard, J.E. Patterson, C. Montreuil, Y. Cheng, C.K. Lambert, Laboratory testing of Urea-SCR Formulations to Meet Tier 2 Bin 5 Emissions, SAE Technical Paper 2007-01-1575, (2007) 776-790.
[99] J.H. Kwak, R.G. Tonkyn, D.H. Kim, J. Szanyi, C.H.F. Peden, Excellent activity and selectivity of Cu-SSZ-13 in the selective catalytic reduction of NOx with NH3, J Catal, 275 (2010) 187-190.
[100] Q. Ye, L.F. Wang, R.T. Yang, Activity, propene poisoning resistance and hydrothermal stability of copper exchanged chabazite-like zeolite catalysts for SCR of NO with ammonia in comparison to Cu/ZSM-5, Appl Catal a-Gen, 427-428 (2012) 24-34.
[101] J. Luo, D. Wang, A. Kumar, A. Yezerets, Identification of two types of Cu sites in Cu/SSZ-13 and their unique responses to hydrothermal aging and sulfur poisoning, Catalysis Today, in press (2015) 10.1016/j.cattod.2015.1012.1002.
[102] H.-Y. Chen, Urea-SCR Technology for deNOx After Treatment of Diesel Exhausts; Nova, I., Tronconi, E., Eds; Fundamentals and Applied Catalysis; Springer New York, (2014) 123 - 147.
[103] C. Baerlocher, L.B. McCusker, Database of Zeolite Structures; http://www.iza-structure.org/databases/, (2016).

[104] U. Deka, I. Lezcano-Gonzalez, S.J. Warrender, A.L. Picone, P.A. Wright, B.M. Weckhuysen, A.M. Beale, Changing active sites in Cu-CHA catalysts: deNO(x) selectivity as a function of the preparation method, Micropor Mesopor Mat, 166 (2013) 144-152.

[105] E. Borfecchia, K.A. Lomachenko, F. Giordanino, H. Falsig, P. Beato, A.V. Soldatov, S. Bordiga, C. Lamberti, Revisiting the nature of Cu sites in the activated Cu-SSZ-13 catalyst for SCR reaction, Chem Sci, 6 (2015) 548-563.

[106] F. Goltl, P. Sautet, I. Hermans, Can Dynamics Be Responsible for the Complex Multipeak Infrared Spectra of NO Adsorbed to Copper(II) Sites in Zeolites?, Angew Chem Int Edit, 54 (2015) 7799-7804.

[107] R.Q. Zhang, J.S. McEwen, M. Kollar, F. Gao, Y.L. Wang, J. Szanyi, C.H.F. Peden, NO Chemisorption on Cu/SSZ-13: A Comparative Study from Infrared Spectroscopy and DFT Calculations, Acs Catal, 4 (2014) 4093-4105.

[108] F. Goltl, P. Sautet, I. Hermans, The impact of finite temperature on the coordination of Cu cations in the zeolite SSZ-13, Catalysis Today, (2015) 10.1016/j.cattod.2015.1010.1028.

[109] D.W. Fickel, R.F. Lobo, Copper Coordination in Cu-SSZ-13 and Cu-SSZ-16 Investigated by Variable-Temperature XRD, J Phys Chem C, 114 (2010) 1633-1640.

[110] J.H. Kwak, T. Varga, C.H.F. Peden, F. Gao, J.C. Hanson, J. Szanyi, Following the movement of Cu ions in a SSZ-13 zeolite during dehydration, reduction and adsorption: A combined in situ TP-XRD, XANES/DRIFTS study, J Catal, 314 (2014) 83-93.

[111] A. Godiksen, F.N. Stappen, P.N.R. Vennestrom, F. Giordanino, S.B. Rasmussen, L.F. Lundegaard, S. Mossin, Coordination Environment of Copper Sites in Cu-CHA Zeolite Investigated by Electron Paramagnetic Resonance, J Phys Chem C, 118 (2014) 23126-23138.

[112] P.N.R. Vennestrom, A. Katerinopoulou, R.R. Tiruvalam, A. Kustov, P.G. Moses, P. Concepcion, A. Corma, Migration of Cu Ions in SAPO-34 and Its Impact on Selective Catalytic Reduction of NOx NH3, Acs Catal, 3 (2013) 2158-2161.

[113] C.W. Andersen, M. Bremholm, P.N.R. Vennestrom, A.B. Blichfeld, L.F. Lundegaard, B.B. Iverson, Location of Cu2+ in CHA zeolite investigated by X-ray diffraction using the Rietveld/maximum entropy method, IUCrJ, 1 (2014) 382 - 386.

[114] F. Gao, N.M. Washton, Y.L. Wang, M. Kollar, J. Szanyi, C.H.F. Peden, Effects of Si/Al ratio on Cu/SSZ-13 NH3-SCR catalysts: Implications for the active Cu species and the roles of Bronsted acidity, J Catal, 331 (2015) 25-38.

[115] F. Gao, E.D. Walter, E.M. Karp, J.Y. Luo, R.G. Tonkyn, J.H. Kwak, J. Szanyi, C.H.F. Peden, Structure-activity relationships in NH3-SCR over Cu-SSZ-13 as probed by reaction kinetics and EPR studies, J Catal, 300 (2013) 20-29.

[116] J.H. Kwak, D. Tran, J. Szanyi, C.H.F. Peden, J.H. Lee, The Effect of Copper Loading on the Selective Catalytic Reduction of Nitric Oxide by Ammonia Over Cu-SSZ-13, Catal Lett, 142 (2012) 295-301.

[117] J. Dedecek, B. Wichterlova, Role of hydrated Cu ion complexes and aluminum distribution in the framework on the Cu ion siting in ZSM-5, J Phys Chem B, 101 (1997) 10233-10240.

[118] J.L. Fulton, M.M. Hoffmann, J.G. Darab, B.J. Palmer, E.A. Stern, Copper(I) and copper(II) coordination structure under hydrothermal conditions at 325 degrees C: An X-ray absorption fine structure and molecular dynamics study, J Phys Chem A, 104 (2000) 11651-11663.

[119] F. Goltl, R.E. Bulo, J. Hafner, P. Sautet, What Makes Copper-Exchanged SSZ-13 Zeolite Efficient at Cleaning Car Exhaust Gases?, J Phys Chem Lett, 4 (2013) 2244-2249.

[120] F. Goltl, J. Hafner, Structure and properties of metal-exchanged zeolites studied using gradient-corrected and hybrid functionals. I. Structure and energetics, J Chem Phys, 136 (2012) 064501.

[121] F. Goltl, J. Hafner, Structure and properties of metal-exchanged zeolites studied using gradient-corrected and hybrid functionals. II. Electronic structure and photoluminescence spectra, J Chem Phys, 136 (2012) 064502.

[122] F. Goltl, J. Hafner, Structure and properties of metal-exchanged zeolites studied using gradient-corrected and hybrid functionals. III. Energetics and vibrational spectroscopy of adsorbates, J Chem Phys, 136 (2012) 064503.

[123] A.M. Beale, F. Gao, I. Lezcano-Gonzalez, C.H.F. Peden, J. Szanyi, Recent advances in automotive catalysis for NOx emission control by small-pore microporous materials, Chem Soc Rev, 44 (2015) 7371-7405.

[124] J.H. Kwak, J.H. Lee, S.D. Burton, A.S. Lipton, C.H.F. Peden, J. Szanyi, A Common Intermediate for N-2 Formation in Enzymes and Zeolites: Side-On Cu-Nitrosyl Complexes, Angew Chem Int Edit, 52 (2013) 9985-9989.

[125] P. Forzatti, L. Lietti, I. Nova, E. Tronconi, Diesel NOx aftertreatment catalytic technologies: Analogies in LNT and SCR catalytic chemistry, Catalysis Today, 151 (2010) 202-211.

[126] M. Colombo, I. Nova, E. Tronconi, Detailed kinetic modeling of the NH3-NO/NO2 SCR reactions over a commercial Cu-zeolite catalyst for Diesel exhausts after treatment, Catalysis Today, 197 (2012) 243-255.

[127] M.P. Ruggeri, T. Selleri, M. Colombo, I. Nova, E. Tronconi, Identification of nitrites/HONO as primary products of NO oxidation over Fe-ZSM-5 and their role in the Standard SCR mechanism: A chemical trapping study, J Catal, 311 (2014) 266-270.

[128] M.P. Ruggeri, I. Nova, E. Tronconi, J.A. Pihl, T.J. Toops, W.P. Partridge, In-situ DRIFTS measurements for the mechanistic study of NO oxidation over a commercial Cu-CHA, Appl Catal B-Environ, 166 (2014) 181 - 192.

[129] T. Gunter, H.W.P. Carvalho, D.E. Doronkin, T. Sheppard, P. Glatzel, A.J. Atkins, J. Rudolph, C.R. Jacob, M. Casapu, J.D. Grunwaldt, Structural snapshots of the SCR reaction mechanism on Cu-SSZ-13, Chem Commun, 51 (2015) 9227-9230.

[130] R.M. Koros, E.J. Nowak, A Diagnostic Test of Kinetic Regime in a Packed Bed Reactor, Chem Eng Sci, 22 (1967) 470-&.

[131] G.M. Psofogiannakis, J.F. McCleerey, E. Jaramillo, A.C.T. van Duin, ReaxFF Reactive Molecular Dynamics Simulation of the Hydration of Cu-SSZ-13 Zeolite and the Formation of Cu Dimers, J Phys Chem C, 119 (2015) 6678-6686.

[132] A.K.S. Clemens, A. Shishkin, P.A. Carlsson, M. Skoglundh, F.J. Martinez-Casado, Z. Matej, O. Balmes, H. Harelind, Reaction-driven Ion Exchange of Copper into Zeolite SSZ-13, Acs Catal, 5 (2015) 6209-6218.

[133] W. Lowenstein, The Distribution of Aluminum in the Tetrahedra of Silicates and Aluminates, American Mineralogist, 39 (1954) 92-96.
[134] S.I. Zones, Zeolite SSZZ-13 and its method of preparation. US Patent 4544538A, (1985).
[135] J.R. Di Iorio, S.A. Bates, A.A. Verma, W.N. Delgass, F.H. Ribeiro, J.T. Miller, R. Gounder, The Dynamic Nature of Bronsted Acid Sites in Cu-Zeolites During NOx Selective Catalytic Reduction: Quantification by Gas-Phase Ammonia Titration, Top Catal, 58 (2015) 424-434.
[136] S.A. Bates, W.N. Delgass, F.H. Ribeiro, J.T. Miller, R. Gounder, Methods for NH3 titration of Bronsted acid sites in Cu-zeolites that catalyze the selective catalytic reduction of NOx with NH3, J Catal, 312 (2014) 26-36.
[137] M. Sierka, J. Sauer, Proton mobility in chabazite, faujasite, and ZSM-5 zeolite catalysts, comparison based on ab initio calculations, J Phys Chem B, 105 (2001) 1603-1613.
[138] L.J. Smith, A. Davidson, A.K. Cheetham, A neutron diffraction and infrared spectroscopy study of the acid form of the aluminosilicate zeolite, chabazite (H-SSZ-13), Catal Lett, 49 (1997) 143-146.
[139] S. Bordiga, J.G. Vitillo, G. Ricchiardi, L. Regli, D. Cocina, A. Zecchina, B. Arstad, M. Bjorgen, J. Hafizovic, K.P. Lillerud, Interaction of hydrogen with MOF-5, J Phys Chem B, 109 (2005) 18237-18242.
[140] C.G. Baes, R.E. Mesmer, Hydrolysis of cations, (Wiley New York, 1976).
[141] J.R. Di Iorio, R. Gounder, Chemistry of Materials, in press (2016) 10.1021/acs.chemmater.1026b00181.
[142] A. Auroux, V. Bolis, P. Wierzchowski, P.C. Gravelle, J.C. Vedrine, Study of the Acidity of Zsm-5 Zeolite by Micro-Calorimetry and Infrared Spectroscopy, J Chem Soc Farad T 1, 75 (1979) 2544-2555.
[143] A. Auroux, Calorimetry and Thermal Methods in Catalysis, 154 (Springer 2013) 1 - 561.
[144] S.B. Sharma, B.L. Meyers, D.T. Chen, J. Miller, J.A. Dumesic, Characterization of Catalyst Acidity by Microcalorimetry and Temperature-Programmed Desorption, Appl Catal a-Gen, 102 (1993) 253-265.
[145] C. Lee, D.J. Parrillo, R.J. Gorte, W.E. Farneth, Relationship between differential heats of adsorption and Bronsted acid strengths of acidic zeolites: H-ZSM-5 and H-Mordenite, J Am Chem Soc, 118 (1996) 3262-3268.
[146] M. Brandle, J. Sauer, R. Dovesi, N.M. Harrison, Comparison of a combined quantum mechanics/interatomic potential function approach with its periodic quantum-mechanical limit: Proton siting and ammonia adsorption in zeolite chabazite, J Chem Phys, 109 (1998) 10379-10389.
[147] S. Shwan, M. Skoglundh, L.F. Lundegaard, R.R. Tiruvalam, T.V.W. Janssens, A. Carlsson, P.N.R. Vennestrom, Solid-State Ion-Exchange of Copper into Zeolites Facilitated by Ammonia at Low Temperature, Acs Catal, 5 (2014) 16-19.
[148] D. Sun, W.F. Schneider, J.B. Adams, D. Sengupta, Molecular origins of selectivity in the reduction of NOx by NH3, J Phys Chem A, 108 (2004) 9365-9374.

[149] J. Dedecek, Z. Sobalik, B. Wichterlova, Siting and Distribution of Framework Aluminium Atoms in Silicon-Rich Zeolites and Impact on Catalysis, Catal Rev, 54 (2012) 135-223.
[150] V. Pashkova, P. Klein, J. Dedecek, V. Tokarova, B. Wichterlova, Incorporation of Al at ZSM-5 hydrothermal synthesis. Tuning of Al pairs in the framework, Micropor Mesopor Mat, 202 (2015) 138-146.
[151] S. Sklenak, J. Dedecek, C. Li, B. Wichterlova, V. Gabova, M. Sierka, J. Sauer, Aluminium siting in the ZSM-5 framework by combination of high resolution Al-27 NMR and DFT/MM calculations, Phys Chem Chem Phys, 11 (2009) 1237-1247.
[152] S. Sklenak, J. Dedecek, C.B. Li, B. Wichterlova, V. Gabova, M. Sierka, J. Sauer, Aluminum siting in silicon-rich zeolite frameworks: A combined high-resolution Al-27 NMR spectroscopy and quantum mechanics/molecular mechanics study of ZSM-5, Angew Chem Int Edit, 46 (2007) 7286-7289.
[153] J. Dedecek, D. Kaucky, B. Wichterlova, O. Gonsiorova, Co2+ ions as probes of Al distribution in the framework of zeolites. ZSM-5 study, Phys Chem Chem Phys, 4 (2002) 5406-5413.
[154] V. Gabova, J. Dedecek, J. Cejka, Control of Al distribution in ZSM-5 by conditions of zeolite synthesis, Chem Commun, (2003) 1196-1197.
[155] A. Vjunov, J.L. Fulton, T. Huthwelker, S. Pin, D.H. Mei, G.K. Schenter, N. Govind, D.M. Camaioni, J.Z. Hu, J.A. Lercher, Quantitatively Probing the Al Distribution in Zeolites, J Am Chem Soc, 136 (2014) 8296-8306.
[156] D.E. Akporiaye, I.M. Dahl, H.B. Mostad, R. Wendelbo, Aluminum distribution in chabazite: An experimental and computational study, J Phys Chem-Us, 100 (1996) 4148-4153.
[157] S. Prasad, M. Petrov, Mixed domain models for the distribution of aluminum in high silica zeolite SSZ-13, Solid State Nucl Mag, 54 (2013) 26-31.
[158] O.H. Han, C.S. Kim, S.B. Hong, Direct evidence for the nonrandom nature of Al substitution in zeolite ZSM-5: An investigation by Al-27 MAS and MQ MAS NMR, Angew Chem Int Edit, 41 (2002) 469-472.
[159] T. Yokoi, H. Mochizuki, S. Namba, J.N. Kondo, T. Tatsumi, Control of the Al Distribution in the Framework of ZSM-5 Zeolite and Its Evaluation by Solid-State NMR Technique and Catalytic Properties, J Phys Chem C, 119 (2015) 15303-15315.
[160] E.A. Eilertsen, B. Arstad, S. Svelle, K.P. Lillerud, Single parameter synthesis of high silica CHA zeolites from fluoride media, Micropor Mesopor Mat, 153 (2012) 94-99.
[161] D.W. Fickel, E. D'Addio, J.A. Lauterbach, R.F. Lobo, The ammonia selective catalytic reduction activity of copper-exchanged small-pore zeolites, Appl Catal B-Environ, 102 (2011) 441-448.
[162] S.I. Zones, Conversion of Faujasites to High-Silica Chabazite Ssz-13 in the Presence of N,N,N-Trimethyl-1-Adamantammonium Iodide, J Chem Soc Faraday T, 87 (1991) 3709-3716.
[163] S.I. Zones, R.A. Vannordstrand, Novel Zeolite Transformations - the Template-Mediated Conversion of Cubic-P Zeolite to Ssz-13, Zeolites, 8 (1988) 166-174.
[164] C.C. Chang, Z.P. Wang, P. Dornath, H.J. Cho, W. Fan, Rapid synthesis of Sn-Beta for the isomerization of cellulosic sugars, Rsc Adv, 2 (2012) 10475-10477.

[165] J.H. Kwak, H.Y. Zhu, J.H. Lee, C.H.F. Peden, J. Szanyi, Two different cationic positions in Cu-SSZ-13?, Chem Commun, 48 (2012) 4758-4760.

[166] F. Gao, Y. Wang, N.M. Washton, M. Kollar, J. Szanyi, C.H.F. Peden, Effect of Alkali and Alkaline Earth Cocations on the Activity and Hydrothermal Stability of Cu/SSZ-13 NH3-SCR Catalysts, Acs Catal, 5 (2015) 6780-6791.

[167] M. Dusselier, M.A. Deimund, J.E. Schmidt, M.E. Davis, Methanol-to-Olefins Catalysis with Hydrothermally Treated Zeolite SSZ-39, Acs Catal, 5 (2015) 6078-6085.

[168] M.H. Groothaert, K. Lievens, J.A. van Bokhoven, A.A. Battiston, B.M. Weckhuysen, K. Pierloot, R.A. Schoonheydt, Bis(mu-oxo)dicopper as intermediate in the catalytic decomposition of NO over Cu-ZSM-5, Recent Advances in the Science and Technology of Zeolites and Related Materials, Pts a - C, 154 (2004) 2449-2457.

[169] A.V. Kucherov, A.A. Slinkin, Introduction of Transition-Metal Ions in Cationic Positions of High-Silica Zeolites by a Solid-State Reaction - Interaction of Copper-Compounds with H-Mordenite or H-Zsm-5, Zeolites, 6 (1986) 175-180.

[170] F. Giordanino, E. Borfecchia, K.A. Lomachenko, A. Lazzarini, G. Agostini, E. Gallo, A.V. Soldatov, P. Beato, S. Bordiga, C. Lamberti, Interaction of NH3 with Cu-SSZ-13 Catalyst: A Complementary FTIR, XANES, and XES Study, J Phys Chem Lett, 5 (2014) 1552-1559.

[171] H.Y. Zhu, J.H. Kwak, C.H.F. Peden, J. Szanyi, In situ DRIFTS-MS studies on the oxidation of adsorbed NH3 by NOx over a Cu-SSZ-13 zeolite, Catalysis Today, 205 (2013) 16-23.

[172] G. Lamble, A. Moen, D.G. Nicholson, Structure of the Diamminecopper(I) Ion in Solution - an X-Ray-Absorption Spectroscopic Study, J Chem Soc Faraday T, 90 (1994) 2211-2213.

[173] D. Wang, L. Zhang, K. Kamasamudram, W.S. Epling, In Situ-DRIFTS Study of Selective Catalytic Reduction of NOx by NH3 over Cu-Exchanged SAPO-34, Acs Catal, 3 (2013) 871-881.

[174] I. Lezcano-Gonzalez, U. Deka, B. Arstad, A. Van Yperen-De Deyne, K. Hemelsoet, M. Waroquier, V. Van Speybroeck, B.M. Weckhuysen, A.M. Beale, Determining the storage, availability and reactivity of NH3 within Cu-Chabazite-based Ammonia Selective Catalytic Reduction systems, Phys Chem Chem Phys, 16 (2014) 1639-1650.

[175] B. Gomez-Lor, M. Iglesias, C. Cascales, E. Gutierrez-Puebla, M.A. Monge, A diamine copper(I) complex stabilized in situ within the ferrierite framework. Catalytic properties, Chemistry of Materials, 13 (2001) 1364-1368.

[176] M. Moreno-Gonzalez, B. Hueso, M. Boronat, T. Blasco, A. Corma, Ammonia-Containing Species Formed in Cu-Chabazite As Per In Situ EPR, Solid-State NMR, and DFT Calculations, J Phys Chem Lett, 6 (2015) 1011-1017.

[177] J.M. Hoover, B.L. Ryland, S.S. Stahl, Mechanism of Copper(I)/TEMPO-Catalyzed Aerobic Alcohol Oxidation, J Am Chem Soc, 135 (2013) 2357-2367.

[178] P. Chen, E.I. Solomon, O2 activation of binuclear Cu sites: Noncoupled versus exchange coupled reaction mechanisms, P Natl Acad Sci USA, 101 (2004) 13105-13110.

[179] E.I. Solomon, D.E. Heppner, E.M. Johnston, J.W. Ginsbach, J. Cirera, M. Qayyum, M.T. Kieber-Emmons, C.H. Kjaergaard, R.G. Hadt, L. Tian, Copper Active Sites in Biology, Chem Rev, 114 (2014) 3659-3853.

[180] I. Corp., Carr-Parrinello Molecular Dynamics Code; http://www.cpmd.org, (2016).

[181] J.P. Perdew, Y. Wang, Accurate and Simple Analytic Representation of the Electron-Gas Correlation-Energy, Phys Rev B, 45 (1992) 13244-13249.

[182] D. Vanderbilt, Soft Self-Consistent Pseudopotentials in a Generalized Eigenvalue Formalism, Phys Rev B, 41 (1990) 7892-7895.

[183] K. Laasonen, R. Car, C. Lee, D. Vanderbilt, Implementation of Ultrasoft Pseudopotentials in Abinitio Molecular-Dynamics, Phys Rev B, 43 (1991) 6796-6799.

[184] G. Kresse, J. Furthmuller, Efficient iterative schemes for ab initio total-energy calculations using a plane-wave basis set, Phys Rev B, 54 (1996) 11169-11186.

[185] P.E. Blochl, Projector Augmented-Wave Method, Phys Rev B, 50 (1994) 17953-17979.

[186] G. Kresse, D. Joubert, From ultrasoft pseudopotentials to the projector augmented-wave method, Phys Rev B, 59 (1999) 1758-1775.

[187] J. Heyd, G.E. Scuseria, M. Ernzerhof, Hybrid functionals based on a screened Coulomb potential, J Chem Phys, 118 (2003) 8207-8215.

[188] J. Heyd, G.E. Scuseria, M. Ernzerhof, Erratum: "Hybrid functionals based on a screened Coulomb potential", J Chem Phys, 124 (2006) 219906.

[189] A.V. Krukau, O.A. Vydrov, A.F. Izmaylov, G.E. Scuseria, Influence of the exchange screening parameter on the performance of screened hybrid functionals, J Chem Phys, 125 (2006).

[190] A. Tkatchenko, M. Scheffler, Accurate Molecular Van Der Waals Interactions from Ground-State Electron Density and Free-Atom Reference Data, Phys Rev Lett, 102 (2009).

[191] R.F.W. Bader, Oxford University Press, 36 (1990) 354 - 360.

[192] W. Tang, E. Sanville, G. Henkelman, A grid-based Bader analysis algorithm without lattice bias, J Phys-Condens Mat, 21 (2009).

[193] E. Sanville, S.D. Kenny, R. Smith, G. Henkelman, Improved grid-based algorithm for Bader charge allocation, J Comput Chem, 28 (2007) 899-908.

[194] G. Henkelman, A. Arnaldsson, H. Jonsson, A fast and robust algorithm for Bader decomposition of charge density, Comp Mater Sci, 36 (2006) 354-360.

[195] M. Yu, D.R. Trinkle, Accurate and efficient algorithm for Bader charge integration, J Chem Phys, 134 (2011).

[196] J.M. Bray, W.F. Schneider, In Chapter 2. First-principles Thermodynamic Models in Heterogeneous Catalysis; Asthagiri, A., Janik, M., Eds., Royal Society of Chemistry, (2013) 59 - 115.

[197] M.W. Penninger, C.H. Kim, L.T. Thompson, W.F. Schneider, DFT Analysis of NO Oxidation Intermediates on Undoped and Doped LaCoO3 Perovskite, J Phys Chem C, 119 (2015) 20488-20494.

[198] G. Piccini, J. Sauer, Effect of Anharmonicity on Adsorption Thermodynamics, J Chem Theory Comput, 10 (2014) 2479-2487.

[199] C.T. Campbell, J.R.V. Sellers, The Entropies of Adsorbed Molecules, J Am Chem Soc, 134 (2012) 18109-18115.

[200] J. Wang, V.F. Kispersky, W.N. Delgass, F.H. Ribeiro, Determination of the Au active site and surface active species via operando transmission FTIR and isotopic transient experiments on 2.3 wt.% Au/TiO2 for the WGS reaction, J Catal, 289 (2012) 171-178.

[201] U. Deka, I. Lezcano-Gonzalez, B.M. Weckhuysen, A.M. Beale, Local Environment and Nature of Cu Active Sites in Zeolite-Based Catalysts for the Selective Catalytic Reduction of NOx, Acs Catal, 3 (2013) 413-427.
[202] T. Tanabe, T. Iijima, A. Koiwai, J. Mizuno, K. Yokota, A. Isogai, Esr Study of the Deactivation of Cu-Zsm-5 in a Net Oxidizing Atmosphere, Appl Catal B-Environ, 6 (1995) 145-153.
[203] C. Citek, S. Herres-Pawlis, T.D.P. Stack, Low Temperature Syntheses and Reactivity of Cu2O2 Active-Site Models, Accounts Chem Res, 48 (2015) 2424-2433.
[204] S. Kieger, G. Delahay, B. Coq, B. Neveu, Selective catalytic reduction of nitric oxide by ammonia over Cu-FAU catalysts in oxygen-rich atmosphere, J Catal, 183 (1999) 267 - 280.
[205] C. Lamberti, S. Bordiga, F. Bonino, C. Prestipino, G. Berlier, L. Capello, F. D'Acapito, F.X.L.I. Xamena, A. Zecchina, Determination of the oxidation and coordination state of copper on different Cu-based catalysts by XANES spectroscopy in situ or in operando conditions, Phys Chem Chem Phys, 5 (2003) 4502-4509.
[206] R.G. Shulman, Y. Yafet, P. Eisenberger, W.E. Blumberg, Observation and Interpretation of X-Ray Absorption Edges in Iron Compounds and Proteins, Proceedings of the National Academy of Sciences of the United States of America, 73 (1976) 1384-1388.
[207] J.E. Hahn, R.A. Scott, K.O. Hodgson, S. Doniach, S.R. Desjardins, E.I. Solomon, Observation of an Electric Quadrupole Transition in the X-Ray Absorption-Spectrum of a Cu(Ii) Complex, Chem Phys Lett, 88 (1982) 595-598.
[208] P.N.R. Vennestrom, T.V.W. Janssens, A. Kustov, M. Grill, A. Puig-Molina, L.F. Lundegaard, R.R. Tiruvalam, P. Concepcion, A. Corma, Influence of lattice stability on hydrothermal deactivation of Cu-ZSM-5 and Cu-IM-5 zeolites for selective catalytic reduction of NOx by NH3, J Catal, 309 (2014) 477-490.
[209] D.J. Liu, H.J. Robota, On the mechanism of NO selective catalytic reduction by hydrocarbons over Cu-ZSM-5 via X-ray absorption spectroscopic study, J Phys Chem B, 103 (1999) 2755-2765.
[210] D.J. Liu, H.J. Robota, In-Situ Xanes Characterization of the Cu Oxidation-State in Cu-Zsm-5 during No Decomposition Catalysis, Catal Lett, 21 (1993) 291-301.
[211] Y. Kuroda, Y. Yoshikawa, S. Konno, H. Hamano, H. Maeda, R. Kumashiro, M. Nagao, Specific Feature of Copper Ion-Exchanged Mordenite for Dinitrogen Adsorption at Room-Temperature, J Phys Chem-Us, 99 (1995) 10621-10628.
[212] C. Lamberti, G. Spoto, D. Scarano, C. Paze, M. Salvalaggio, S. Bordiga, A. Zecchina, G.T. Palomino, F. DAcapito, Cu-I-Y and Cu-II-Y zeolites: A XANES, EXAFS and visible-NIR study, Chem Phys Lett, 269 (1997) 500-508.
[213] L.S. Kau, D.J. Spirasolomon, J.E. Pennerhahn, K.O. Hodgson, E.I. Solomon, X-Ray Absorption-Edge Determination of the Oxidation-State and Coordination-Number of Copper - Application to the Type-3 Site in Rhus-Vernicifera Laccase and Its Reaction with Oxygen, J Am Chem Soc, 109 (1987) 6433-6442.
[214] K. Mathisen, M. Stockenhuber, D.G. Nicholson, In situ XAS and IR studies on Cu:SAPO-5 and Cu:SAPO-11: the contributory role of monomeric linear copper(I) species in the selective catalytic reduction of NOx by propene, Phys Chem Chem Phys, 11 (2009) 5476-5488.

[215] A. Moen, D.G. Nicholson, M. Ronning, Studies on the Pre-Edge Region of the X-Ray-Absorption Spectra of Copper(I) Oxide and the Diamminecopper(I) Ion, J Chem Soc Faraday T, 91 (1995) 3189-3194.

[216] P.K. Ross, E.I. Solomon, Electronic-Structure of Peroxide-Bridged Copper Dimers of Relevance to Oxyhemocyanin, J Am Chem Soc, 112 (1990) 5871-5872.

[217] E.I. Solomon, U.M. Sundaram, T.E. Machonkin, Multicopper oxidases and oxygenases, Chem Rev, 96 (1996) 2563-2605.

[218] N. Kitajima, K. Fujisawa, Y. Morooka, K. Toriumi, Mu-Eta-2-Eta-2-Peroxo Binuclear Copper Complex, [Cu(Hb(3,5-Ipr2pz)3)]2(O2), J Am Chem Soc, 111 (1989) 8975-8976.

[219] R. Delahay, S. Kieger, N. Tanchoux, P. Trens, B. Coq, Kinetics of the selective catalytic reduction of NO by NH3 on a Cu-faujasite catalyst, Appl Catal B-Environ, 52 (2004) 251-257.

[220] H. Sjovall, R.J. Blint, L. Olsson, Detailed kinetic modeling of NH3 SCR over Cu-ZSM-5, Appl Catal B-Environ, 92 (2009) 138-153.

[221] M. Iwasaki, K. Yamazaki, H. Shinjoh, Transient reaction analysis and steady-state kinetic study of selective catalytic reduction of NO and NO + NO2 by NH3 over Fe/ZSM-5, Appl Catal a-Gen, 366 (2009) 84-92.

[222] P.T. Fanson, M.W. Stradt, W.N. Delgass, J. Lauterbach, Infrared evidence for the existence of nitrate species on Cu-ZSM5 during isothermal rate oscillations in the decomposition of N2O, Catal Lett, 77 (2001) 15-19.

[223] K. Hadjiivanov, D. Klissurski, G. Ramis, G. Busca, Fourier transform IR study of NOx adsorption on a CuZSM-5 DeNO(x) catalyst, Appl Catal B-Environ, 7 (1996) 251-267.

[224] K.I. Hadjiivanov, Identification of neutral and charged NxOy surface species by IR spectroscopy, Catal Rev, 42 (2000) 71-144.

[225] A.A. Parekh, Mechanistic Study of NO Oxidation on Copper Zeolites, MS Thesis, Purdue University, (2013).

[226] B.J. Adelman, T. Beutel, G.D. Lei, W.M.H. Sachtler, On the mechanism of selective NOx reduction with alkanes over Cu/ZSM-5, Appl Catal B-Environ, 11 (1996) L1-L9.

[227] G. Centi, S. Perathoner, Role and importance of oxidized nitrogen oxide adspecies on the mechanism and dynamics of reaction over copper-based catalysts, Catalysis Today, 29 (1996) 117-122.

[228] K. Hadjiivanov, H. Knozinger, B. Tsyntsarski, L. Dimitrov, Effect of water on the reduction of NOx with propane on Fe-ZSM-5. An FTIR mechanistic study, Catal Lett, 62 (1999) 35-40.

[229] H.Y. Liu, Z.K. Zhang, Y.Y. Xu, Y.F. Chen, X. Li, Adsorption-Oxidation Reaction Mechanism of NO on Na-ZSM-5 Molecular Sieves with a High Si/Al Ratio at Ambient Temperature, Chinese J Catal, 31 (2010) 1233-1241.

[230] K. Hadjiivanov, J. Saussey, J.L. Freysz, J.C. Lavalley, FT-IR study of NO+O-2 co-adsorption on H-ZSM-5: re-assignment of the 2133 cm(-1) band to NO+ species, Catal Lett, 52 (1998) 103-108.

[231] A. Milushev, K. Hadjiivanov, FTIR study of CO and NOx adsorption and co-adsorption on Cu/silicalite-1, Phys Chem Chem Phys, 3 (2001) 5337-5341.

[232] G.G. Ramis, G. Busca, V. Lorenzelli, P. Forzatti, Fourier-Transform Infrared Study of the Adsorption and Coadsorption of Nitric-Oxide, Nitrogen-Dioxide and Ammonia on Tio2 Anatase, Appl Catal, 64 (1990) 243-257.
[233] K.I. Hadjiivanov, D.G. Klissurski, V.P. Bushev, Ir Spectroscopic Study of No2 Adsorption on Chromia, J Chem Soc Faraday T, 91 (1995) 149-153.
[234] M.M. Kantcheva, V.P. Bushev, K.I. Hadjiivanov, Nitrogen-Dioxide Adsorption on Deuteroxylated Titania (Anatase), J Chem Soc Faraday T, 88 (1992) 3087-3089.
[235] T.J. Dines, C.H. Rochester, A.M. Ward, Infrared and Raman-Study of the Adsorption of Nh3, Pyridine, No and No2 on Anatase, J Chem Soc Faraday T, 87 (1991) 643-651.
[236] K. Nakamoto, Infrared Spectra of Inorganic and Coordination Compounds, Second Edition, Wiley-Interscience, (1970).
[237] S.L. Shannon, J.G. Goodwin, Characterization of Catalytic Surfaces by Isotopic-Transient Kinetics during Steady-State Reaction, Chem Rev, 95 (1995) 677-695.
[238] A.A. Davydov, A.A. Budneva, IR Spectra of CO and NO Adsorbed on CuO, React Kinet Catal L, 25 (1984) 121 - 124.
[239] D.V. Pozdnyakov, V.N. Filimonov, Use of IR Spectroscopy to Investigate Chemisorption of Nitric Oxide and Nitrogen Dioxide on Metallic Oxides, Kinetics and Catalysis, 14 (1973) 760 - 766.
[240] M.K. Rubin, Zeolite Beta, https://www.google.ch/patentsUS5164169, (1992).
[241] W.S. Borghard, E.W. Sheppard, H.J. Schoennagel, An Automated, High-Precision Unit for Low-Pressure Physisorption, Rev Sci Instrum, 62 (1991) 2801-2809.
[242] W.S. Borghard, P.T. Reischman, E.W. Sheppard, Argon Sorption in Zsm-5, J Catal, 139 (1993) 19-23.
[243] H. Tsukahara, T. Ishida, M. Mayumi, Gas-phase oxidation of nitric oxide: Chemical kinetics and rate constant, Nitric Oxide-Biol Ch, 3 (1999) 191-198.
[244] J. Despres, M. Koebel, O. Krocher, M. Elsener, A. Wokaun, Adsorption and desorption of NO and NO2 on Cu-ZSM-5, Micropor Mesopor Mat, 58 (2003) 175-183.

APPENDICES

APPENDIX A . Supplementary Materials to Chapter 2: Catalysis in a Cage: Condition Dependent Speciation and Dynamics of Exchanged Cu Cations in SSZ-13

A.1 HSE06-TSvdw Values for Phase Diagram Species

Bader charges were normalized to ZCu(1.00) and $Z_2Cu(2.00)$. ΔZPE is defined as the ZPE difference between the adsorbate bound site and the bare site, e.g.

$$\Delta ZPE(Z_2CuH_2O) = ZPE(Z_2CuH_2O) - ZPE(Z_2Cu) \ldots\ldots A.1$$

Table A.1.1 Calculated total energies, ZPE's of adsorbed species, and normalized Bader charges for the 2Al system.

Species	Total Energy	ΔZPE	Bader
Z2Cu	-351.11	0.00	2.00
Z2CuH2O	-369.56	0.71	2.02
Z2CuH2Ox2	-388.10	1.43	1.99
Z2CuH2Ox3	-406.84	2.13	2.05
Z2CuH2Ox4	-425.25	2.84	2.05
Z2CuH2Ox5	-443.76	3.55	1.76
Z2CuH2Ox6	-462.00	4.22	2.03
Z2CuO2	-365.30	0.11	1.70
Z2HCu	-355.98	0.32	1.05
Z2HCuH2O	-374.17	1.01	1.06
Z2HCuO	-362.56	0.35	2.02
Z2HCuO2	-370.45	0.44	1.70
Z2HCu(OH)2	-378.17	1.00	2.07
Z2CuNH3	-375.75	1.08	1.94
Z2CuNH3x2	-400.41	2.15	1.87
Z2CuNH3x3	-424.95	3.22	1.80
Z2CuNH3x4	-449.59	4.31	1.72
Z2CuNH4	-380.98	1.39	1.04
Z2NH4CuNH3	-405.62	2.46	0.96
Z2NH4CuNH3x2	-430.41	3.50	0.86
Z2NH4CuNH3x3	-454.32	4.47	0.84
Z2NH4CuNH3x4	-478.24	5.43	0.83

Table A.1.2 Calculated total energies, ZPE's of adsorbed species, and normalized Bader charges for the 2Al system.

Species	Energy	ZPE	Bader
ZCuOH	-366.87	0.35	1.80
ZCuOH-H2O	-385.20	1.03	1.92
ZCuOH-H2Ox2	-403.50	1.75	1.84
ZCuOH-H2Ox3	-421.82	2.44	1.65
ZCuOH-H2Ox4	-440.10	3.19	1.99
ZCuOH-H2Ox5	-458.67	3.90	2.04
ZCuOH-H2Ox6	-476.83	4.61	2.00
ZCu(OH)O2	-380.90	0.48	1.84
ZCu	-353.94	0.00	1.00
ZCuH2O	-372.25	0.68	1.05
ZCuO	-360.31	0.04	1.73
ZCuO2	-368.49	0.12	1.56
ZCu(OH)2	-378.82	0.72	2.11
ZCu(OH)NH3	-391.35	1.42	1.80
ZCu(OH)NH3x2	-415.84	2.49	1.73
ZCu(OH)NH3x3	-440.29	3.55	1.70
ZCu(OH)NH3x4	-463.63	4.52	1.73
ZCuNH3	-378.61	1.06	0.95
ZCuNH3x2	-403.44	2.13	0.86
ZCuNH3x3	-427.37	3.10	0.85
ZCuNH3x4	-450.95	4.05	0.83

A.2 H_2O Pressure Phase Diagrams

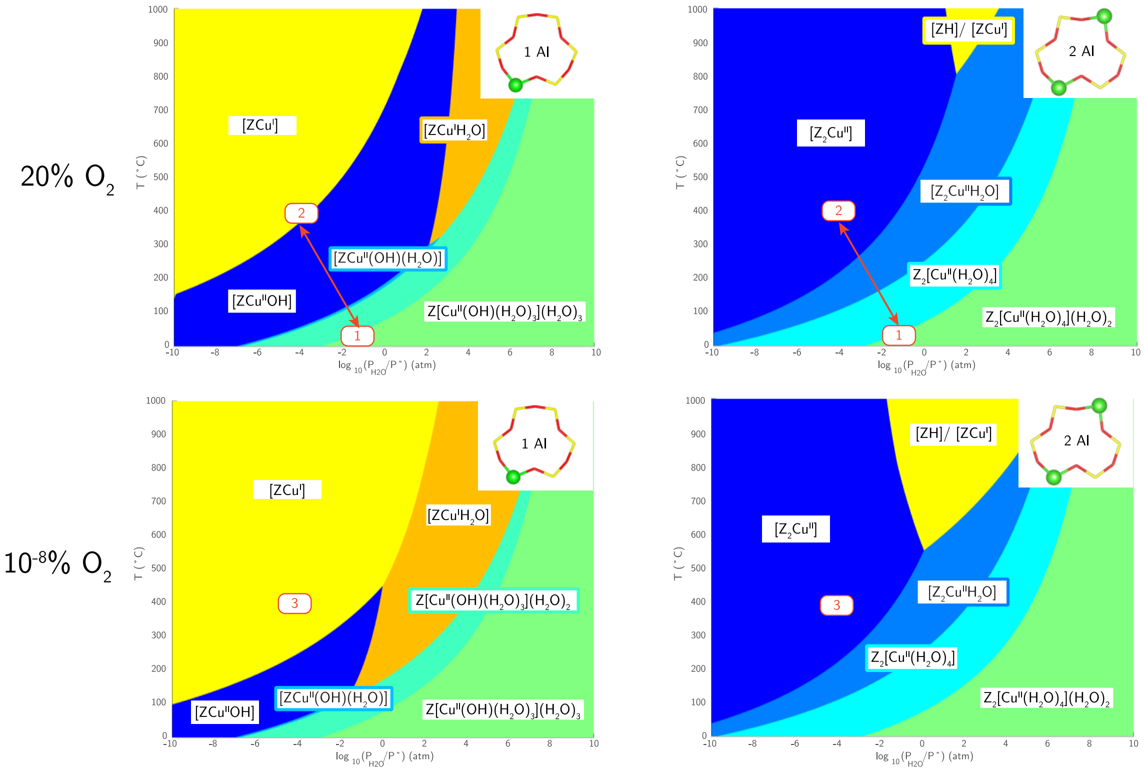

Figure A.2.1 H_2O partial pressure phase diagrams at fixed O_2 pressures.

A.3 Z_2Cu vs. ZCuOH Exchange Energetics

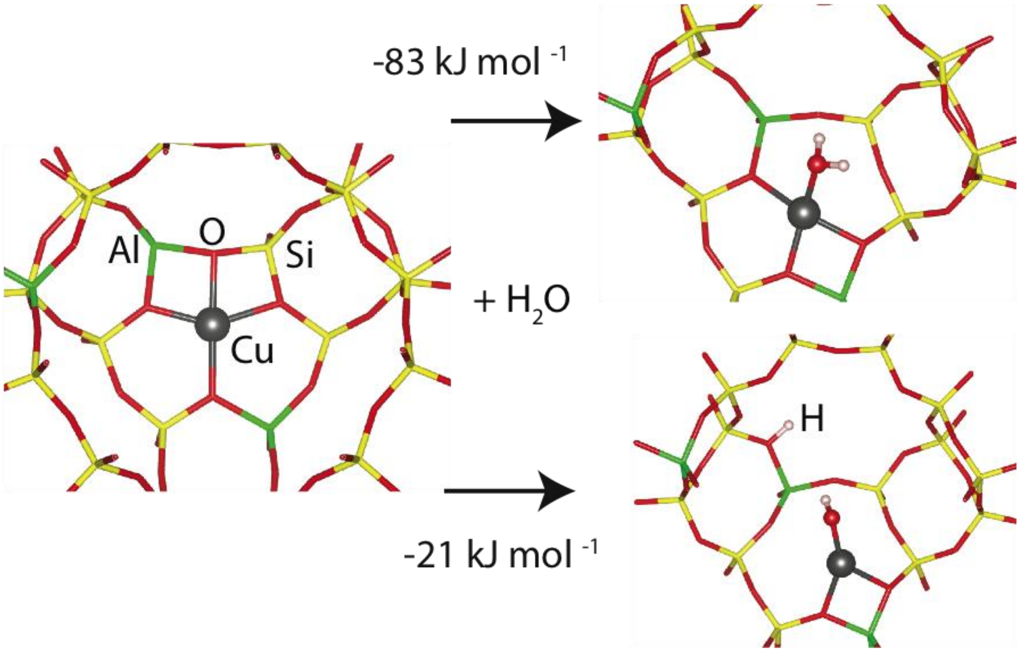

Figure A.2.2 Z_2CuH_2O vs. ZH/ZCuOH energetics in a single supercell.

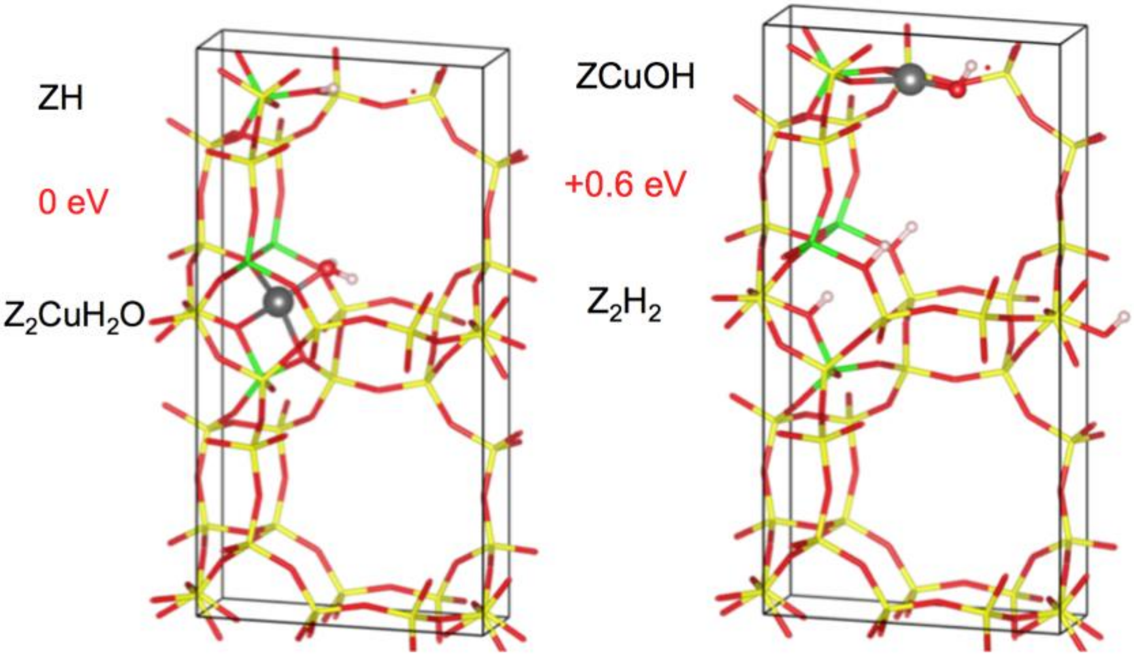

Figure A.2.3 Z_2CuH_2O vs. ZH/ZCuOH energetics in a 2 x 1 x 1 supercell.

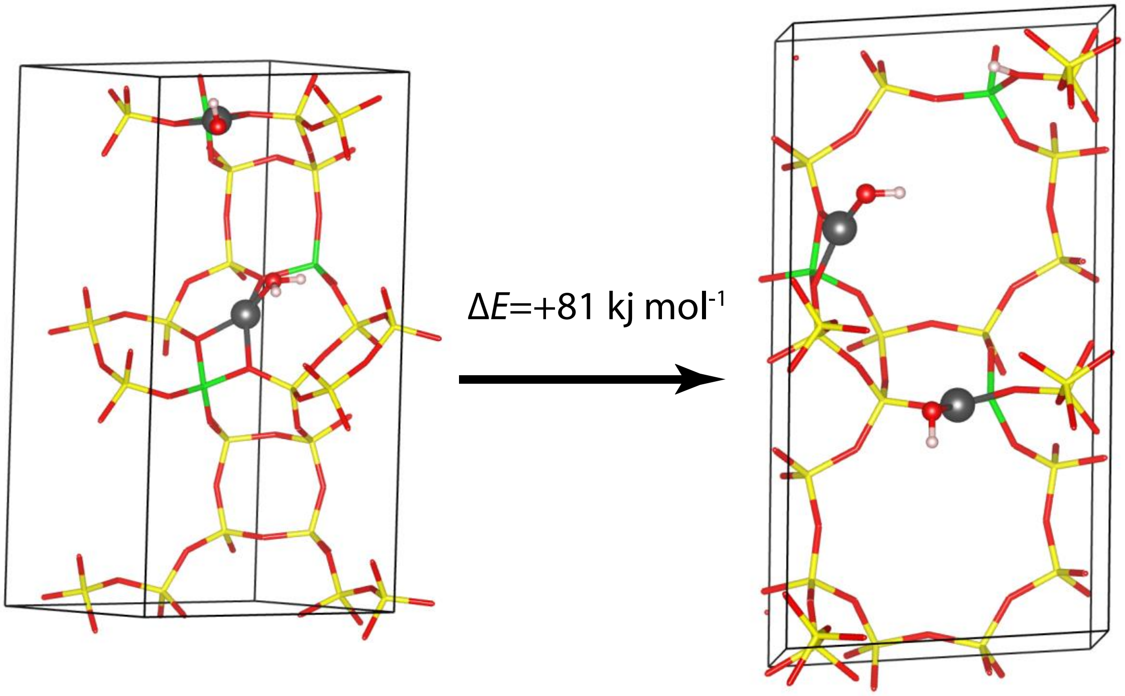

Figure A.2.4 Z_2CuH_2O/ZCuOH vs. ZH/ZCuOHx2 energetics in a 2 x 1 x 1 supercell.

A.4 XRD Spectra

Powder x-ray diffraction (XRD) data were collected on a SmartLab Rigaku diffractometer using a Cu Kα source. Approximately 0.6 g of sample were loaded in a sample holder with a depth of 2 mm. Patterns were obtained from 4 to 40° 2θ using a step size of 0.01° 2θ and a scan rate of 0.05° 2θ min^{-1} at ambient conditions.

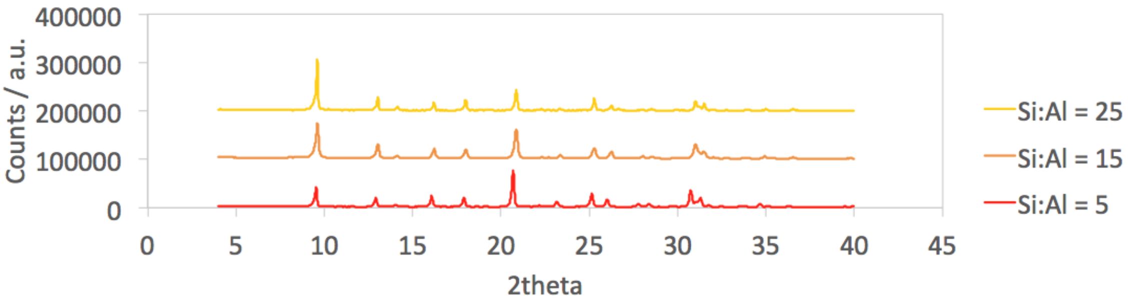

Figure A.4.1 XRD spectra on the H-form of the Si:Al = 5, 15 and 25 samples.

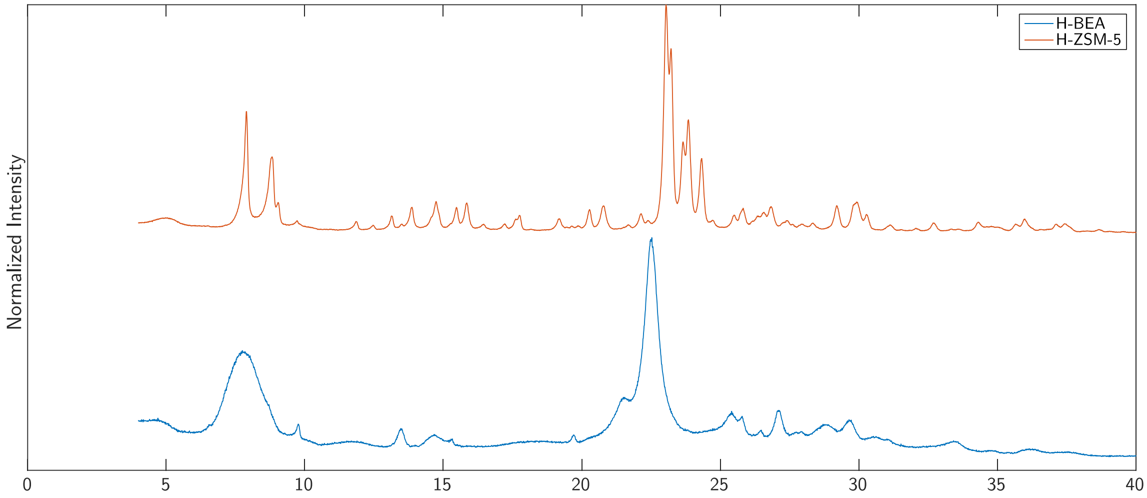

Figure A.4.2 XRD spectra on the H-form of BEA and ZSM-5 samples.

A.5 Atomic Absorptiom

Approximately 20 mg of samples were dissolved in 2 ml HF, then diluted with 50-120 ml deionized water (Millipore, Synergy UV Water Purification System, 18.2 MΩ cm^{-1} resistivity). Elemental analysis to measure the Si:Al, Co:Al and Cu:Al of the dissolved sample was performed using atomic absorption spectroscopy (AAS) on a Perkin-Elmer AAnalyst 300. Na:Al and K:Al were measured also, but not detected within error.

Table A.5.1 AA obtained Si:Al and Co:Al values after Co saturation

Si:Al	Co:Al
SSZ-13 (synthesized)	
4.5	0.19
14.8	0.10
24.1	0.04

Table A.5.2 AA obtained Si:Al and Cu:Al values on all zeolite samples

Si:Al	Cu:Al
SSZ-13 (synthesized)	
4.5	0.00
	0.02
	0.04
	0.09
	0.12
	0.16
	0.20
14.8	0.00
	0.12
	0.21
	0.37
	0.44
24.1	0.00
	0.06
	0.37
	0.44
ZSM-5 (commercial)	
12.5	0.24
	0.27
	0.35
BEA (commercial)	
13.0	0.25
	0.34
BEA (synthesized)	
13.0	0.43

A.6 FTIR Details

The IR data were collected using a Nicolet 6700 FTIR spectrometer equipped with a liquid nitrogen cooled MCT detector. Experiments were performed in a custom designed transmission FTIR cell, a detailed description of which can be found in our previous publication [200]. About 35-40 mg of each catalyst sample was loaded in the form of a self-supported wafer, 2 cm in diameter. All samples were treated with 10% O_2 (UHP grade

O_2, Indiana Oxygen diluted with UHP grade He, Indiana Oxygen) at 673 K for 30 min and then cooled down in the same gas flow to 473 K. All reported spectra were collected at 473 K with a resolution of 4 cm^{-1}, averaged over 1000 scans and baseline corrected for direct comparison. The IR spectrum of the H-form was subtracted from the corresponding spectrum for each Cu-SSZ- 13 sample to obtain a difference spectrum. The peak area for the CuOH species at 3650 cm^{-1} [32, 170] as quantified as a function of Cu loading.

All spectra were first normalized by their T-O-T vibrations between 2082 and 1589 cm^{-1}. Difference spectra were obtained by subtracting the spectrum of H/SSZ-13 from each of the individual Cu/SSZ-13 sample spectra. This clearly showed the growth of the CuOH peak at 3651 cm^{-1} with Cu loading, while the associated peak area was quantified by using a baseline between 3670 and 3635 cm^{-1}. The corresponding Brønsted OH peak area was calculated by drawing a baseline between 3627 and 3523 cm^{-1} for the difference spectra of each sample. Since both Brønsted hydroxyl peaks decreased with increasing Cu loading, the total Brønsted hydroxyl peak area was calculated rather than that for the individual peaks at 3580 or 3605 cm^{-1}.

A.7 Si:Al = 5 repeat synthesis with H:Al ratios between 0.45-0.85

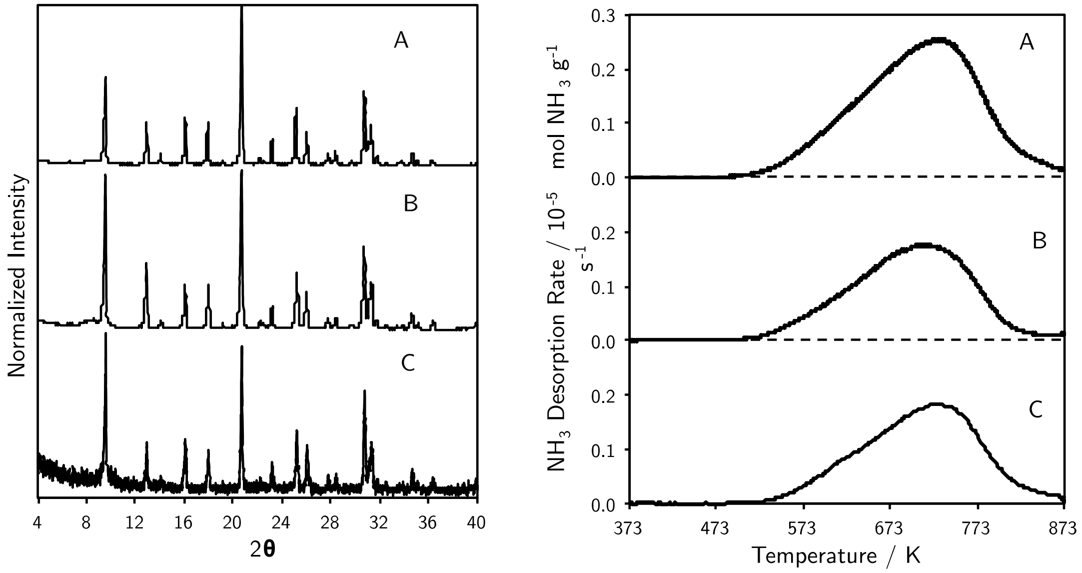

Figure A.6.1 (left) XRD spectra for Si:Al = 5 samples with H:Al ranging from 0.85 (A) to 0.65 (B) to 0.45 (C). (right) NH_3 TPDs following a purge of physisorbed NH_3 to determine H:Al

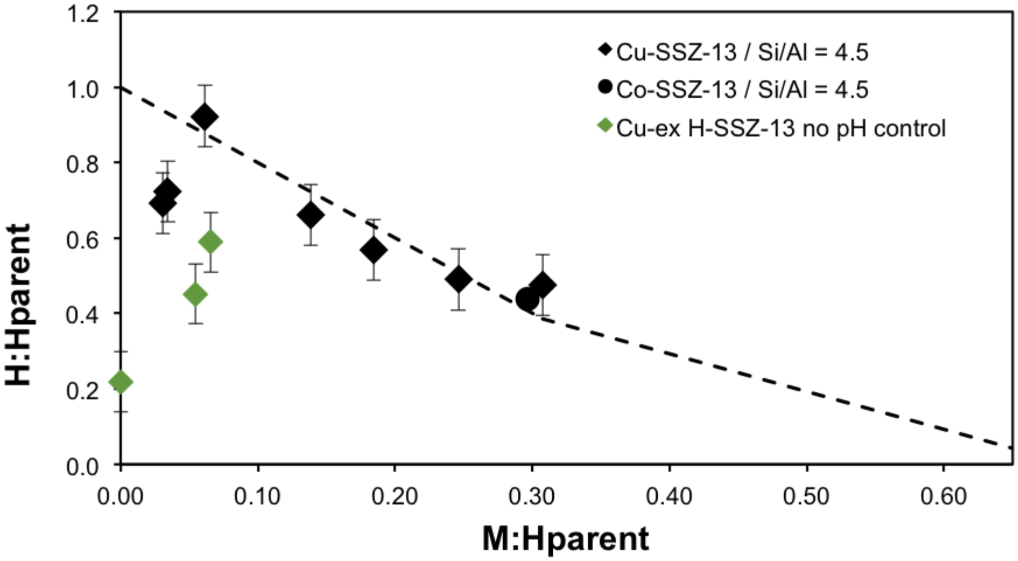

Figure A.6.2 Residual H^+ sites per parent sample H^+ from NH_3 titrations on oxidized M-SSZ-13 samples vs. extent of M/Al exchange for Si:Al = 5 at pH = 5 (black shapes) and no pH control (green shapes). Open and filled symbols denote Cu^{2+} and saturated Co^{2+} exchange, respectively. Dashed lines are model predictions.

When low concentrations of Cu(II) and NH_4^+ are present during aqueous-phase Cu exchange of H-SSZ-13 (Si:Al = 5) at ambient conditions, we observed a 40-80% decrease in th number of Brønsted acid sites relative to the parent SSZ-13 (Figure A.6.2), green diamonds). These observations suggest that significant structural changes occur to framework Al atoms (e.g. dealumination) in high Al content H-SSZ-13 zeolites synthesized by FAU-to-CHA conversion methods at low pH values and low concentrations of cations (80% loss in H^+ sites when no Cu is present), consistent with reports that cation exchange H^+ sites to stabilize framework Al against dealumination [166, 167]. The addition of NH_4OH to maintain a pH of 5 during the exchange of low concentrations of Cu cations mitigated Al structure changes and only resulted in a decrease of 25% of the number of Brønsted acid sites (black diamonds). We have previously reported NH_3 TPD data that quantified the loss of ≈0.25 H^+:Al for this SSZ-13 sample (Si:Al = 5, Cu:Al = 0.02) [166], which is much larger than expected from the Cu(II):H^+ 2:1 exchange stoichiometry (0.04 H^+:Al for a Cu:Al = 0.02). In this manuscript, we have removed this data point from the correlation in Figure 2.3.4, in light of this new evidence for the simultaneous structural changes to zeolite exchange sites (framework Al) that occur during Cu exchange procedure to prepare this sample.

A.8 XAS Details

XAS experiments were carried out at Sector 10 of the Advanced Photon Source at Argonne National Laboratory. Spectra were collected at both beamlines, 10-ID and 10-BM. The high photon flux at the ID line (approximately 100 times higher than that at the BM line) was required to perform experiments in the operando reactor to get enough transmitted

X-ray intensity through the catalyst bed. Cu metal foil spectrum was simultaneously collected while measuring sample spectra and its energy was calibrated to 8979 eV for the Cu K-edge. All spectra were collected under isothermal conditions and normalized using a 1st order polynomial in the pre-edge region and a 3rd order polynomial in the post-edge region. EXAFS data was fit from k = 2.7 to 11 $Å^{-1}$. Linear combination XANES fits to determine the Cu(I) and Cu(II) fractions under operando conditions were carried out using the appropriate references as explained in our previous publications [28-30]. 10-15 mg of each sample was loaded for in situ experiments. All spectra were collected in the step scan mode. Gas treatments were performed in the lab and the samples were transferred to the beamline and cooled down to room temperature before collecting spectra. The samples were oxidized in a 20% O_2/He (UHP grade, Airgas) flow, whereas the reducing treatments used either UHP He (Airgas) at 673 K, 3.5% H_2/He (UHP, Airgas) at 523 K or 1500 ppm NH_3 (3% NH_3/Ar, Praxair) + 1500 ppm NO (0.3% NO/N_2, Airgas) at 673 K. The total flow rate in each case was 100 ml min^{-1} and samples were exposed to the corresponding gas conditions for 45 min. A wide range of catalysts with varying Si/Al and Cu/Al ratios was used to sample the different Cu configurations and identify the response of those species to the different gas treatments. The energy range for the data collected at the 10-BM line was 8700 eV to 9890 eV.

Operando experiments were performed at the 10-ID line in a special glassy carbon tube reactor as described by Kispersky et al [29]. During these experiments XAS spectra were simultaneously collected while measuring the reaction rates for each sample to ensure that the standard SCR rate per mole Cu measured at APS matched with that measured in the lab. Typical standard SCR conditions used were 300 ppm NO, 300 ppm NH_3, 10%

O_2, 2-2.5% H_2O, 5% CO_2 with a total flow rate of 500 ml min^{-1} at 458-463 K. 9-12 mg of each sample was loaded in the reactor to ensure differential conditions (< 20% conversion). Spectra under *operando* conditions were collected in the quick scan mode and averaged over 3-5 scans. The in situ experiments with 300 ppm NH_3+10% O_2 were performed at the 10-ID line with 2.5-3% H_2O and a total flow of 500 ml min^{-1} at 673 K. The energy range for the data collected at the 10-ID line was 8700 eV to 9780 eV.

EXAFS data was fit from 2.7 to 10.5 Å^{-1} range with DWF's of 0.001 at room temperature, 0.002 at 473 K and 0.0035 at 673 K. k^2 weighting was used to convert the data into R-space, and obtain the coordination numbers and bond distances under the various gas conditions.

A.9 Mobility Calculation Details

Cu positions during the entire course of simulation are analyzed to find out its relative mobility when different ligands bind to Cu. Only Cu positions represented as 3D cartesian coordinates (x,y,z) after 60 ps of equilibration time are used for the study. To calculate the volume of space Cu traveled, the 3D cartesian space is discretized into 0.008 Å^3 cubes as illustrated in Figure 2.3.7. The number of cubes that Cu has visited at least once is counted and summed up to be the final volume. Absolute volumes Cu visited for different binding ligands are going to change according to the size of the cubes used, but relative ratio of this volume keeps the same for cube size 0.001 to 0.125 Å^3.

A.10 XANES Fitting Details

Since XAS is a bulk technique, each sample spectrum is a linear combination of the corresponding oxidation states. A mixture of Cu(I) and Cu(II) are present under standard SCR conditions and therefore, a linear combination XANES fitting of the Cu(I) and Cu(II) references was used to obtain the relative amounts of each oxidation state under various conditions. Information about how the Cu(I) and Cu(II) references were generated is provided in our previous publication [30]. EXAFS data was fit from 2.7 to 10.5 $Å^{-1}$ range with DWF's of 0.001 at room temperature, 0.002 at 473 K and 0.0035 at 673 K. k^2 weighting was used to convert the data into R-space, and obtain the coordination numbers and bond distances under the various gas conditions.

A.11 Z_2Cu Modes

The six oxygens in the 6MR are labeled from 1 through 6 clockwise to identify Cu-O coordination. The ring structures just adjacent to the 6MR are shown in Figure A.11.1, where 4MR and 8MR alternates around the 6MR. In principle any four oxygens out of the six oxygens could be coordinated with Cu, however not all combinations are energetically stable at 0K. We found that at least two out of the four Cu-O bonds must come from the oxygen pair adjacent to the Al (i.e. O_1/O_6 pair, and O_3/O_4 pair). The rest of the two bonds must come from two other oxygens that's in the neighboring 4MR. Alternatively the two oxygen pairs can all be coordinated with Cu. This is because in a 6MR without Cu interaction, the TOT angle in the neighboring 4MR prefers to be <180°, while the TOT angle in the neighboring 8MR prefers to be >180°. When Cu is introduced in the 6MR and bonding with four of the oxygens, it is energetically more favorable to distort as less as TOT angles as possible. This can be illustrated in the three stable local minima that we found as detailed below.

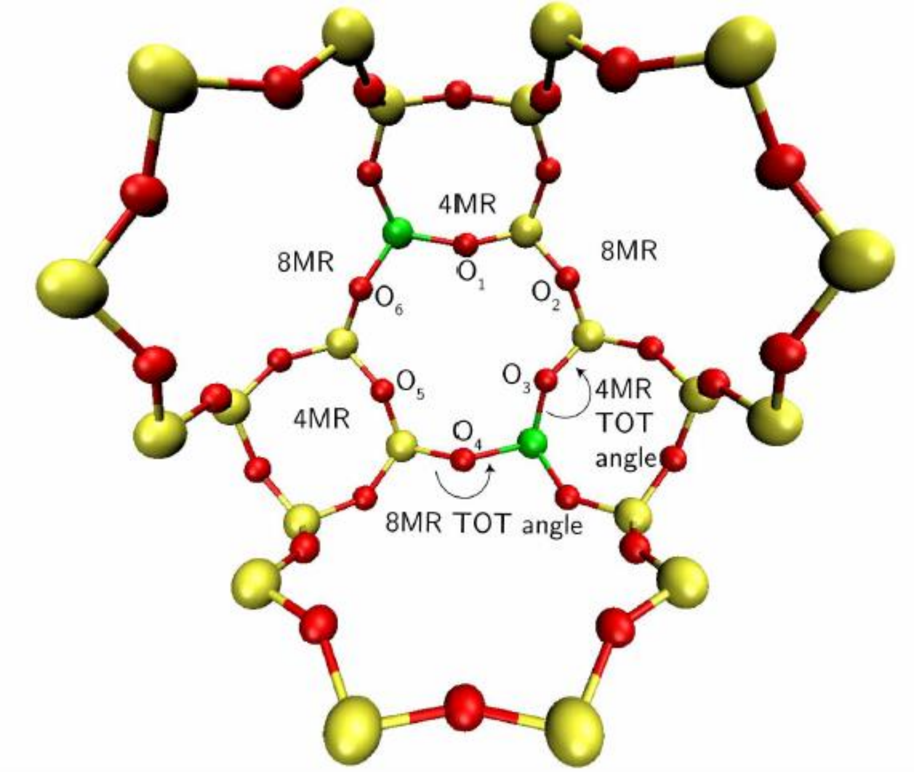

Figure A.11.1 Ring structures surrounding the 6MR, shown in perspective view for clarity. 4MR and 8MR alternates around 6MR.

In Figure A.11.2, dashed lines show Cu-O coordination and the numbering of oxygens is consistent with Figure A.11.1. In modes 1 and 2 only 8MR TOT angle is distorted and in mode 3 two 8MR TOT angles are distorted. Distortion of three 8MR TOT angles are strongly unfavorable and thus create structures high in energy. The three stable mode structures are optimized with the same computational method described in section xx. Mode 1 is slightly higher in energy than 2 and 3. But we can conclude the three modes are almost isoenergetic. Cu-O coordination information as well as relative energetics are summarized in Table A.*11.1*.

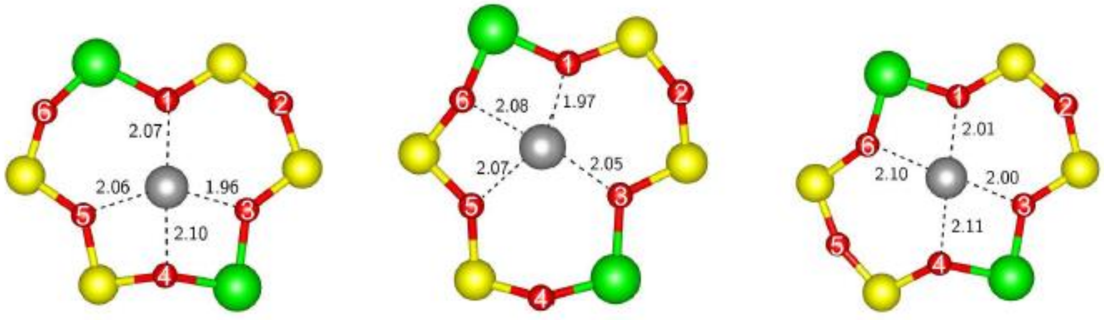

(a) mode 1 (b) mode 2 (c) mode3

Figure A.11.2 Pictures of Z_2Cu modes.

Table A.11.1 Summary of Cu-O coordination in para Z2Cu and relative energies for the three modes.

Mode	Cu-O coordination				Relative energy ($kJ\ mol^{-1}$)	Avg Cu-O distance (Å)
1	O_1	O_3	O_4	O_5	0	2.08
2			O_5	O_6	-4.6	2.08
3			O_6	O_6	-5.5	2.09

A.12 RDF calculations

Pair-wise radial distribution function (RDF) ($g_{\alpha\beta}(r)$) between Cu and other atoms (Si/Al/O/N) defines the average number of framwork Si/Al/O/N atoms in a spherical shell of radius r distance away from the Cu:

$$dn_{\alpha\beta}(r) = \frac{N_{total}}{V} g_{\alpha\beta}(r) 4\pi r^2 dr \ldots\ldots A.2$$

where R is the furthest distance away from the Cu we consider for the RDF; V is the volume of the model; N_{total} is the total number of atoms in a unit cell; $dn_{\alpha\beta}(r)$ is the number of atoms in

3 3

the shell volume averaged by number of MD trajectories; α is Cu and β is any atom from Si/Al/O/N. Hydrogens in the molecular structures are not considered in RDF calculation. To calculate the shell volume we use $4\pi r^2 dr = V_{shell} = (4/3)[(r + dr)^3 – r^3]$. $V = (4/3)\pi R^3$, where we consider R up to 4.5 Å, half of the supercell dimension, to avoid counting an atom in its periodic image. Substitute all into equation 2,

$$g_{\alpha\beta}(r) = \frac{dn_{\alpha\beta}(r)}{N_{total} \text{ x } \frac{4}{3}\pi[(r+dr)^3 - r^3] / \frac{4}{3}\pi R^3} \text{ ……A.3}$$

We calculate $g_{\alpha\beta}(r)$ for all atoms except H to obtain the overall RDF, we also calculate $g_{\alpha\beta}(r)$ for each of the Cu-Si/Cu-Al/Cu-O/Cu-N combinations to obtained de-convoluted RDF’s for each molecular structures (Figure A.12.1-Figure A.12.9).

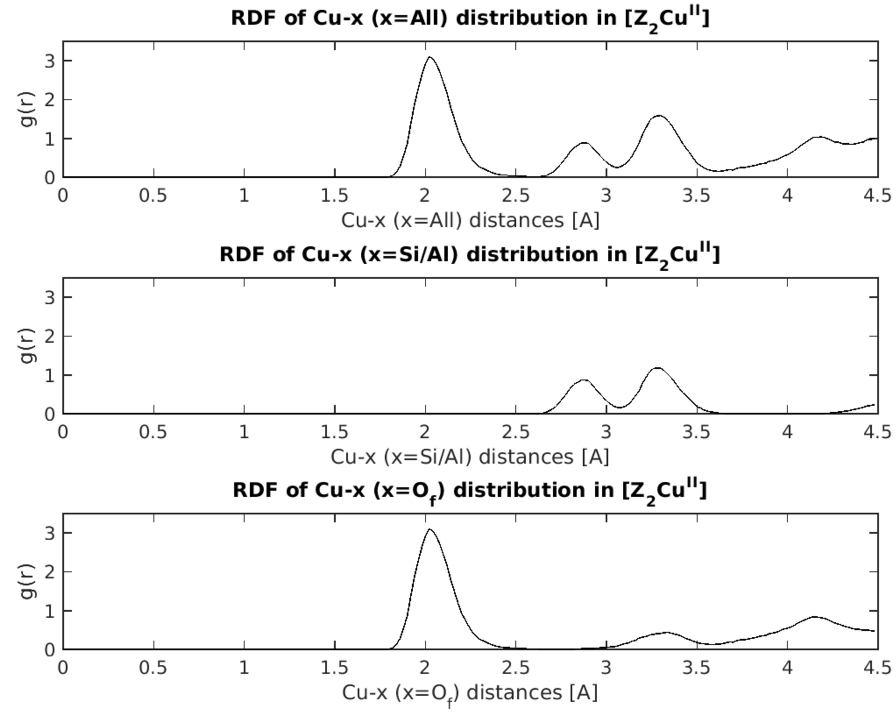

Figure A.12.1 RDF of Cu-x (x = Si, Al, O) in [Z_2Cu(II)].

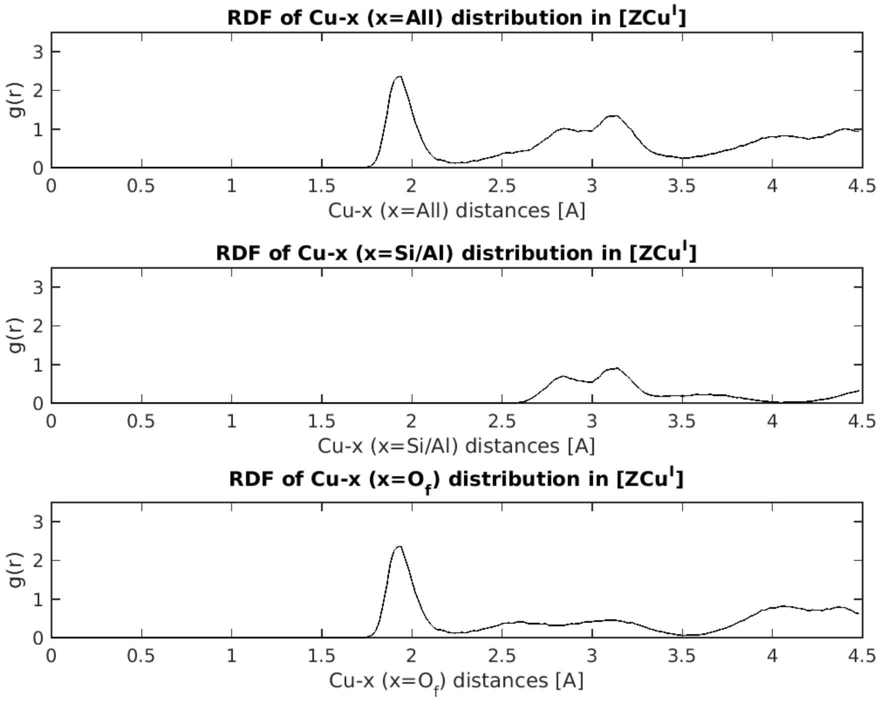

Figure A.12.2 RDF of Cu-x (x = Si, Al, O) in [ZCu(I)].

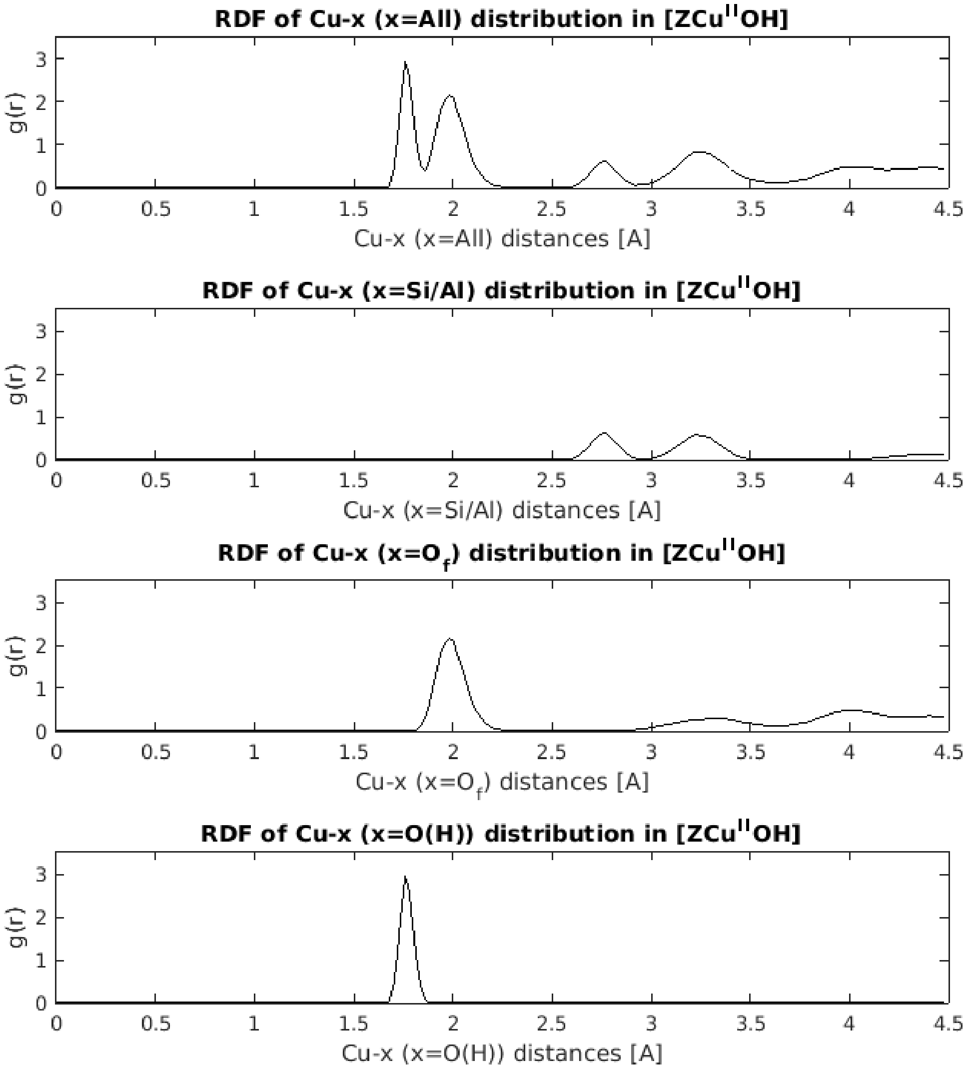

Figure A.12.3 RDF of Cu-x (x = Si, Al, O) in [ZCu(II)OH].

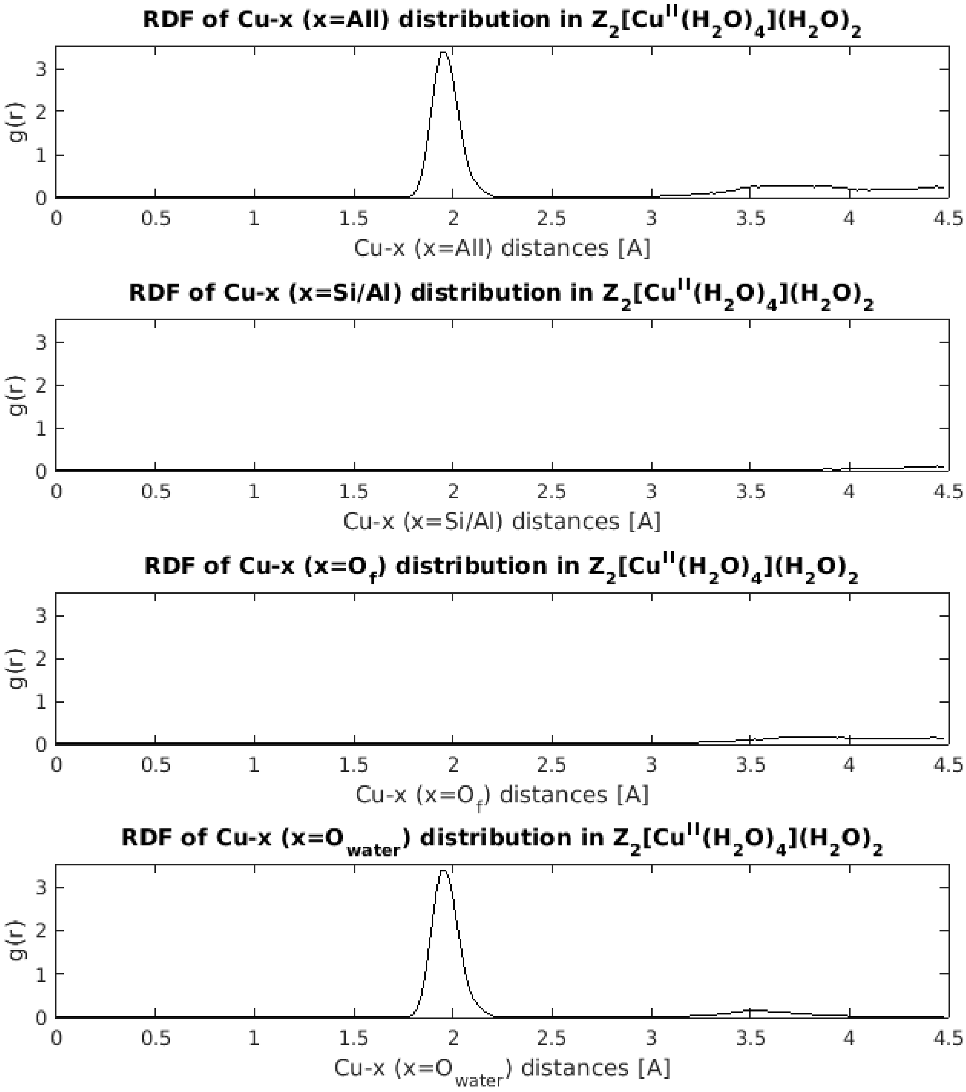

Figure A.12.4 RDF of Cu-x (x = Si, Al, O) in $Z_2[Cu(II)(H_2O)_4](H_2O)_2$.

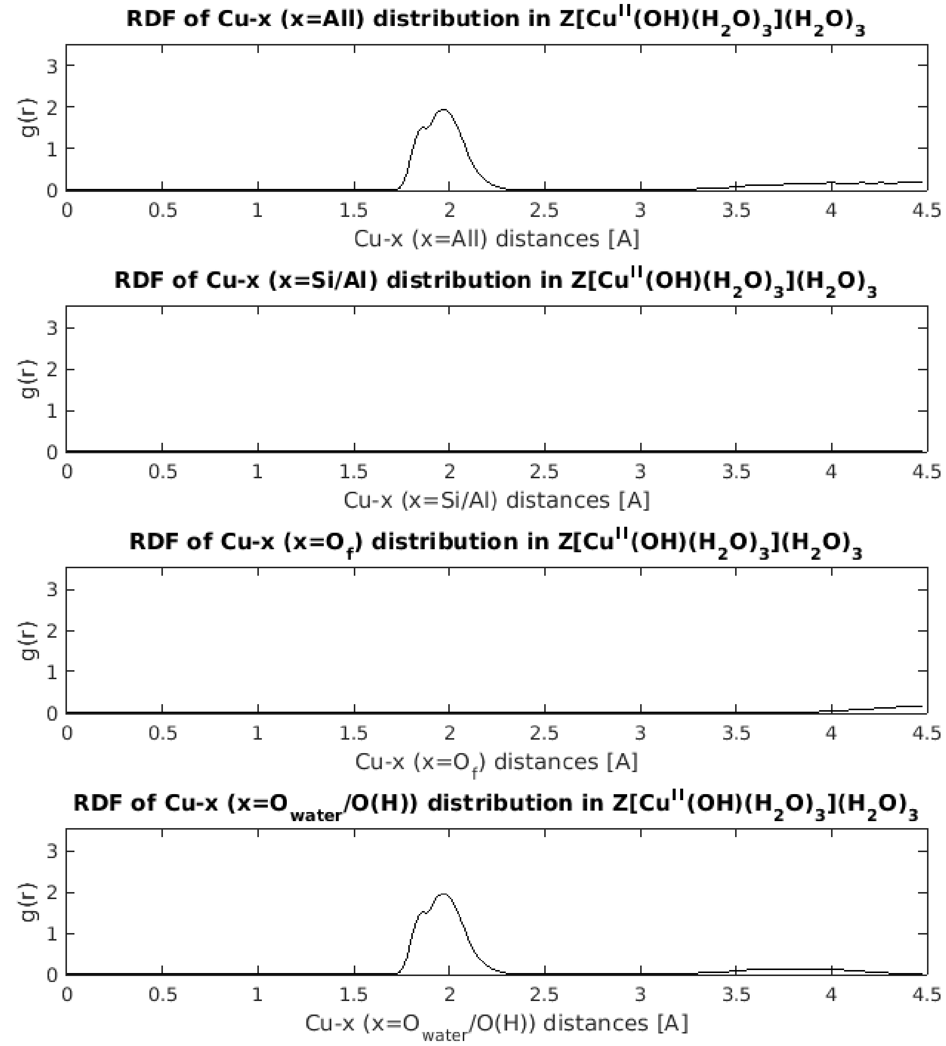

Figure A.12.5 RDF of Cu-x (x = Si, Al, O) in Z[Cu(II)(OH)(H_2O)$_3$](H_2O)$_3$.

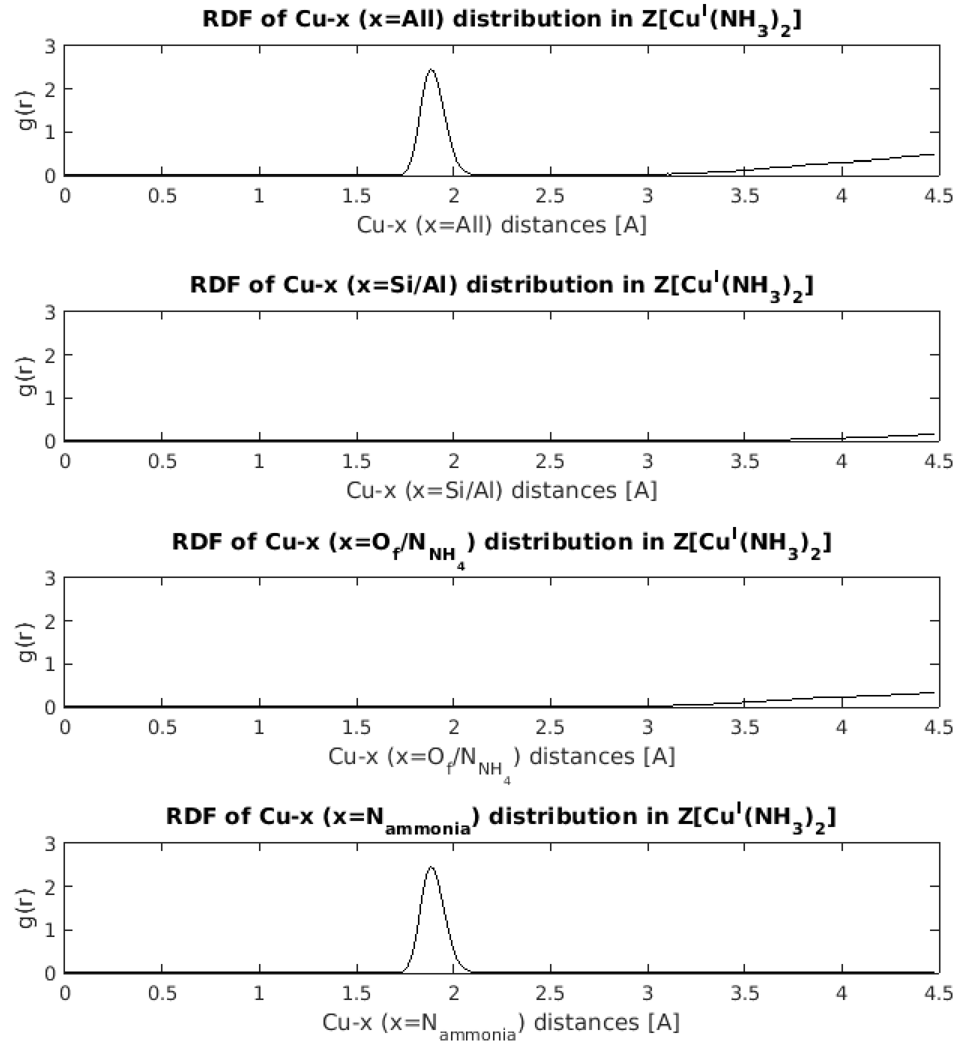

Figure A.12.6 RDF of Cu-x (x = Si, Al, O) in Z[Cu(I)(NH_3)$_2$].

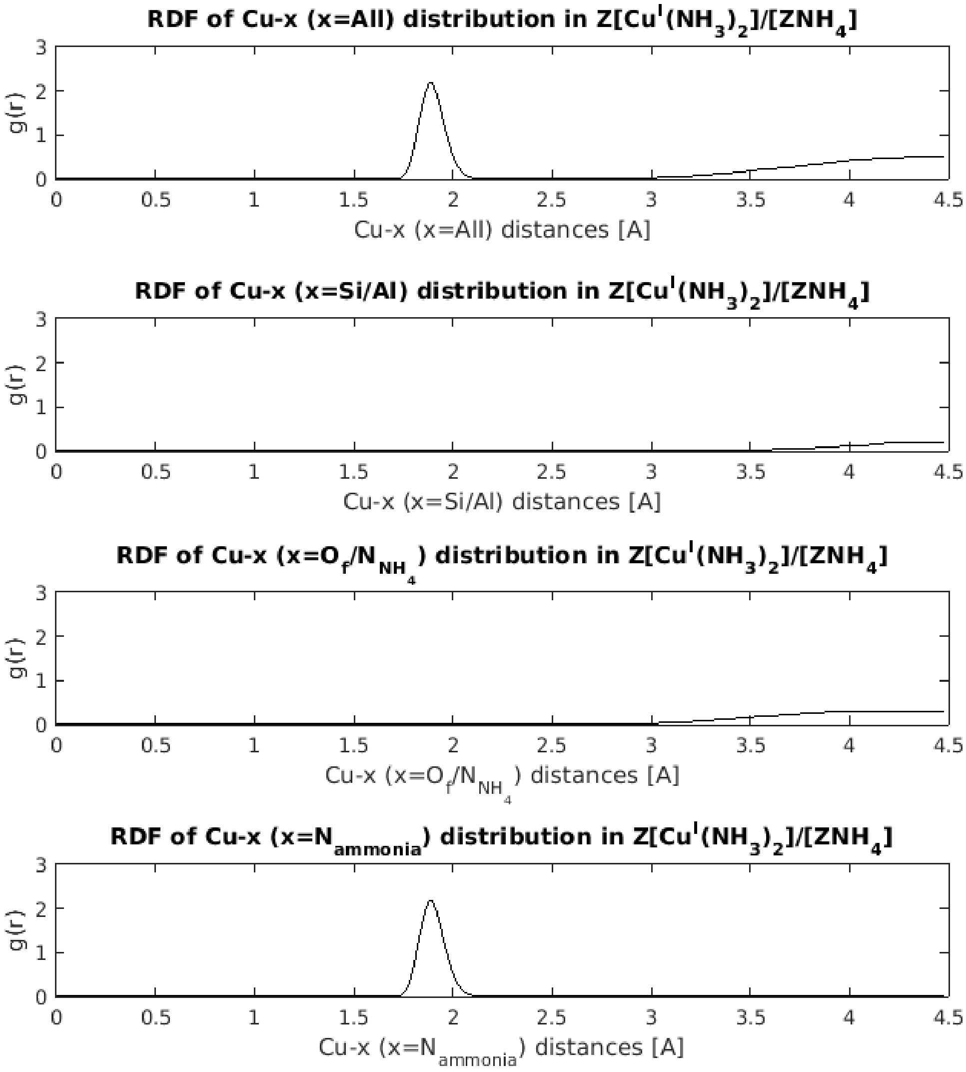

Figure A.12.7 RDF of Cu-x (x = Si, Al, O) in Z[Cu(I)(NH_3)$_2$]/[ZNH_4].

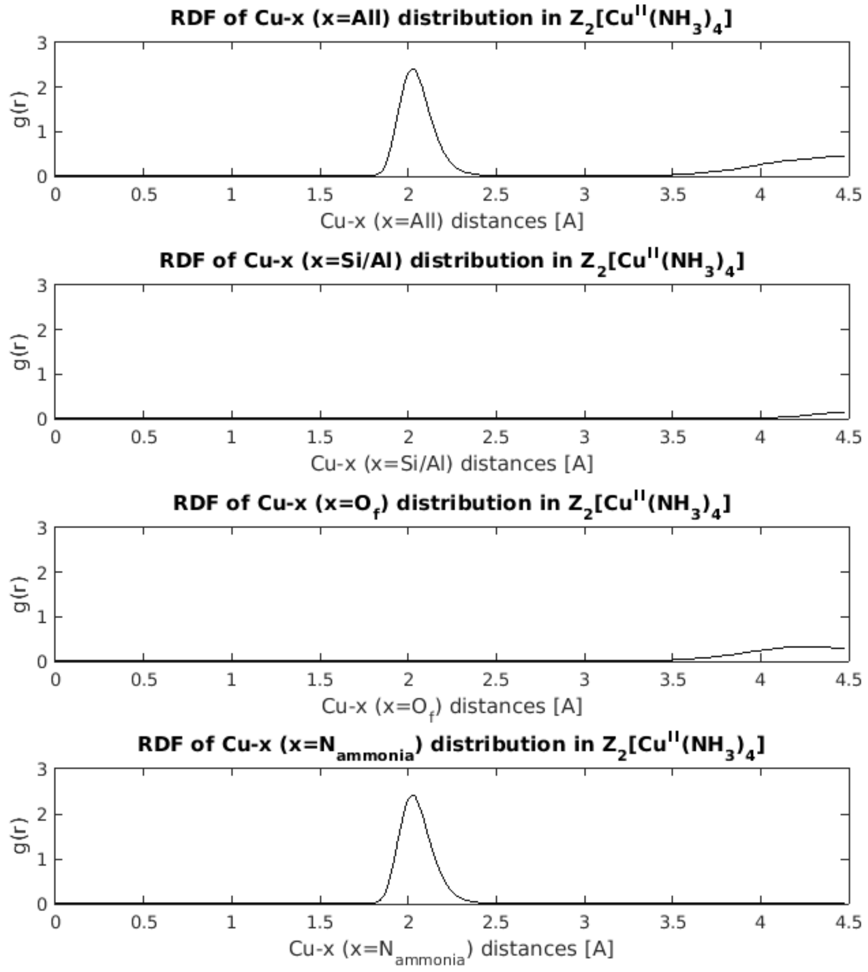

Figure A.12.8 RDF of Cu-x (x = Si, Al, O) in Z[Cu(II)$(NH_3)_4$].

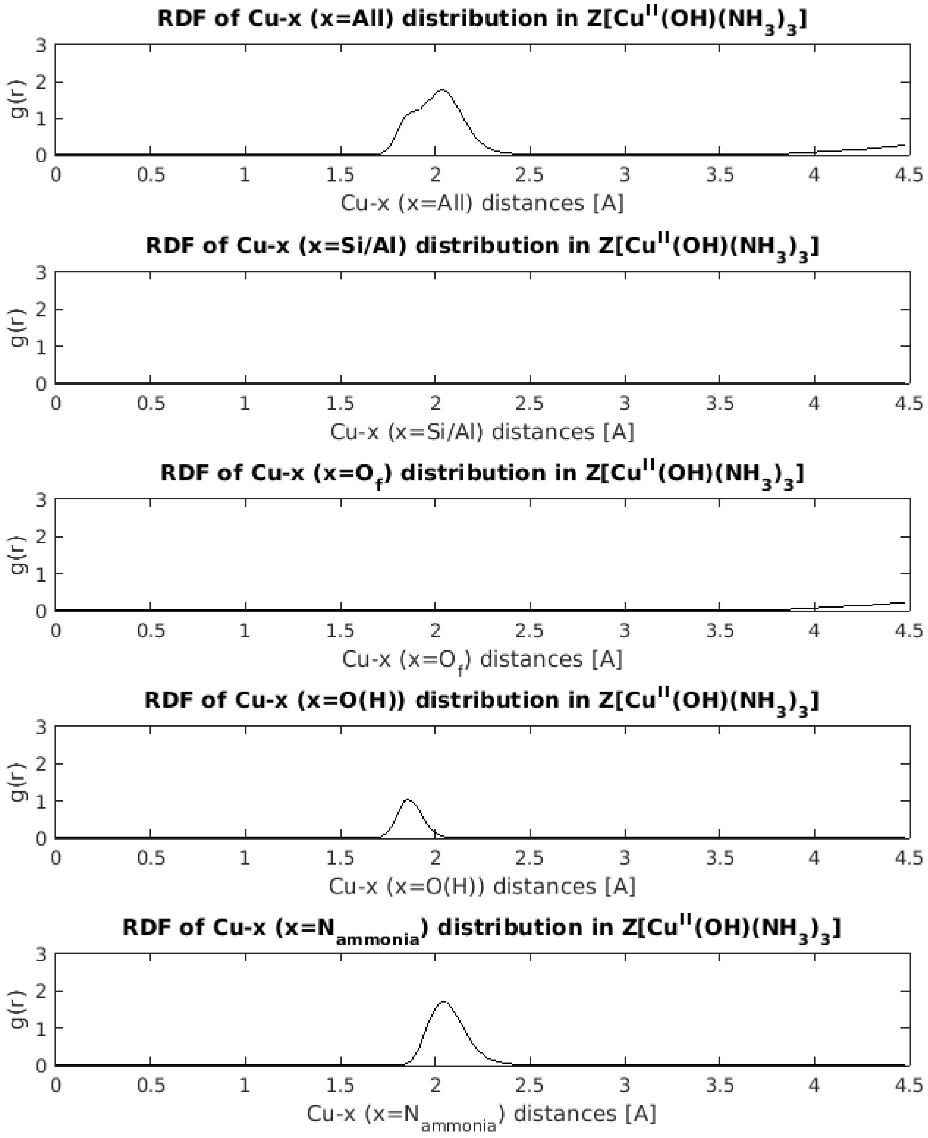

Figure A.12.9 RDF of Cu-x (x = Si, Al, O) in Z[Cu(II)(OH)(NH_3)$_3$].

A.13 XANES reversibility data

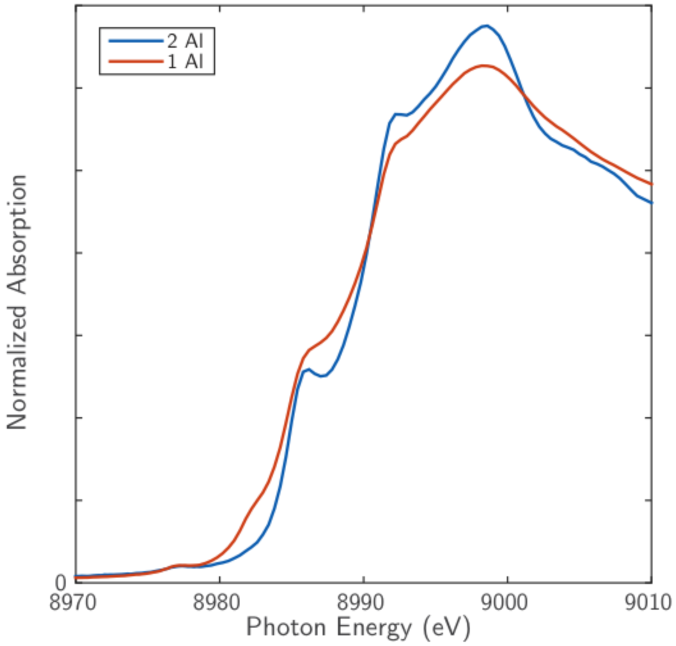

Figure A.13.1 XANES spectra collected after exposing Si:Al = 4.5 Cu:Al = 0.08 (2Al) sample and Si:Al = 15 Cu:Al = 0.44 (1Al) to 20% O_2, balance He at 673 K following pretreatment in He at 673 K.

A.14 Four-site Adsorbate Binding Energies

Table A.14.1 Binding energies (kJ mol^{-1}) for one of each of the SCR gas species on the four different adsorption site models.

	NH3	H2O	NO2	NO	N2	O2
Z2Cu	-132	-84	-35	-17	-29	-19
ZCuOH	-117	-75	-44	-73	-8	-1
ZCu	-137	-74	-134	-90	-67	-52
ZNH4/ZCu	-134	-71	-122	-69	-17	-31

A.15 NH_3 phase diagram results at exp. SCR conditions

Table A.15.1 Full free energies of formation at SCR conditions for all NH_3 2Al and 1Al phase diagram species.

2Al	ΔG (kJ/mol)	1Al	ΔG (kJ/mol)
H/(OH)2	391	OH-H2Ox6	107
H/O	114	(OH)2	73
H/O2	79	O	72
H/H2O	59	OH-H2Ox5	67
O2	42	OH-H2Ox4	67
H	36	OH-O2	67
2NH4CuNH3x4	7	OH-NH3x4	63
Clean	0	OH-(H2O)x3	36
H2Ox6	-1	NH3x4	21
H2Ox3	-5	OH-H2Ox2	16
H2Ox4	-13	O2	9
Z2NH4Cu	-20	Clean	0
H2Ox5	-22	OH/H2O	-12
H2O	-24	H2O	-15
H2Ox2	-25	OH	-29
Z2NH4Cu	-26	OH-NH3	-33
NH4/NH3x3	-36	OH-NH3x2	-35
NH4/NH3	-44	OH-NH3x3	-36
NH3	-52	NH3x3	-54
NH3x2	-73	NH3	-57
NH4/NH3x2	-80	NH3x2	-94
NH3x3	-81		
NH3x4	-96		

A.16 Cu diammine diffusion CI-NEB

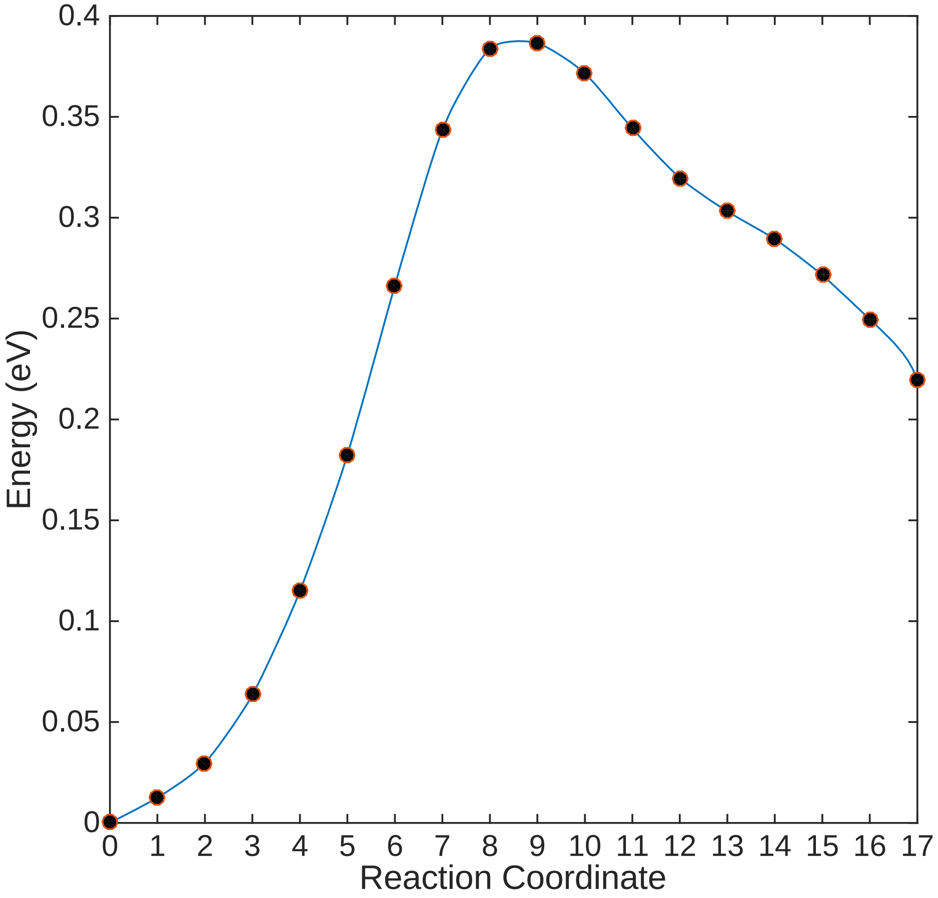

Figure A.16.1 CI-NEB for Cu diammine to traverse the 8MR.

A.17 *Operando* EXAFS

Conditions: 2% H_2O, 300 ppm NH_3, 10% O_2, 300 ppm NO Cu:Al = 0.41, Si:Al = 25, CN = 3.1. XANES: 60% Cu(I), 40% Cu(II).

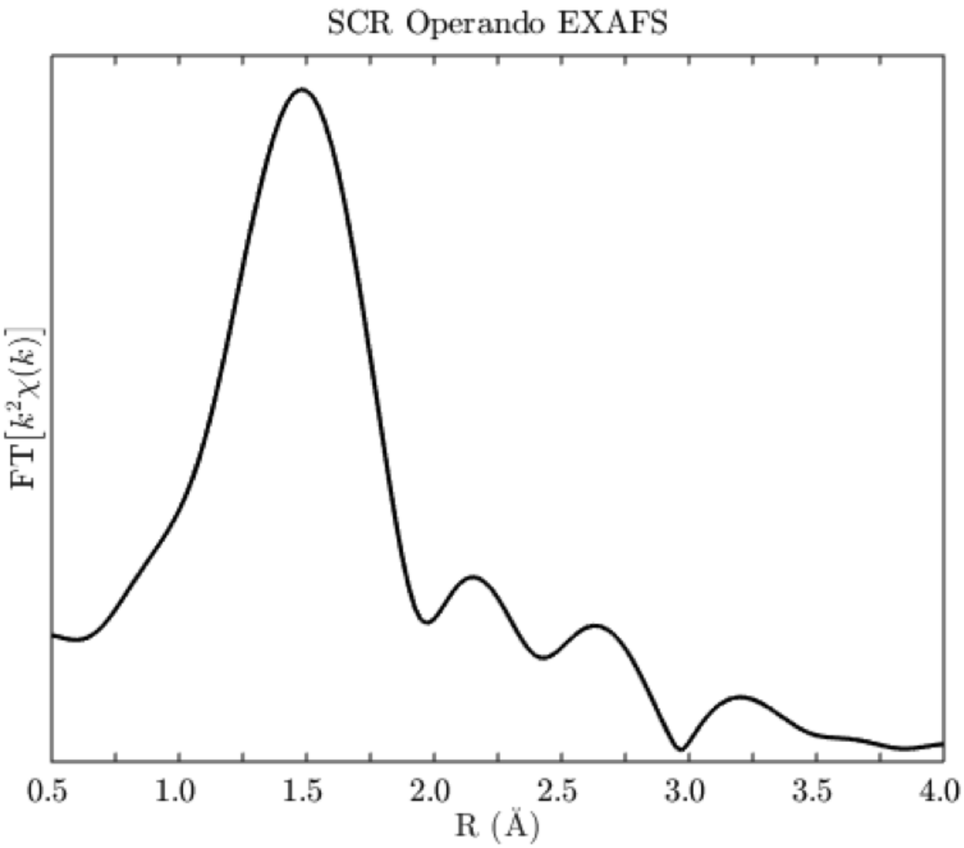

Figure A.17.1 EXAFS spectra collected at 473 K, 2% H_2O, 300 ppm NH_3, 10% O_2, 300 ppm NO on a Cu:Al = 0.41, Si:Al = 25 sample, Rate per gram catalyst is 81 x 10^{-8}.

A.18 NO+NH_3 NEBS

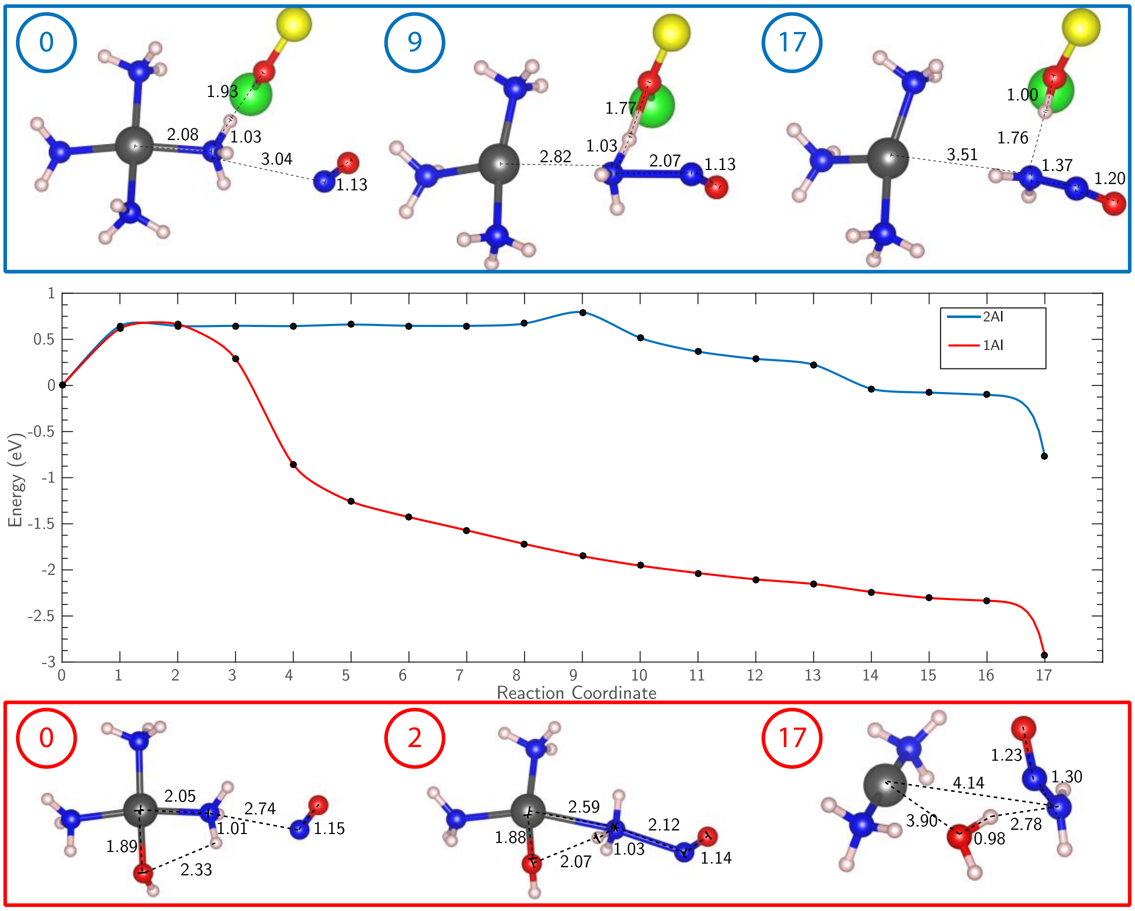

Figure A.18.1 XANES spectra collected after exposing Si:Al = 4.5 Cu:Al = 0.08 (2Al) and Si:Al = 15 Cu:Al = 0.44 (1Al) to O_2 balance He at 673 K following pretreatment in He at 673 K.

A.19 Disappearance of Proximal Sites Upon re-oxidation

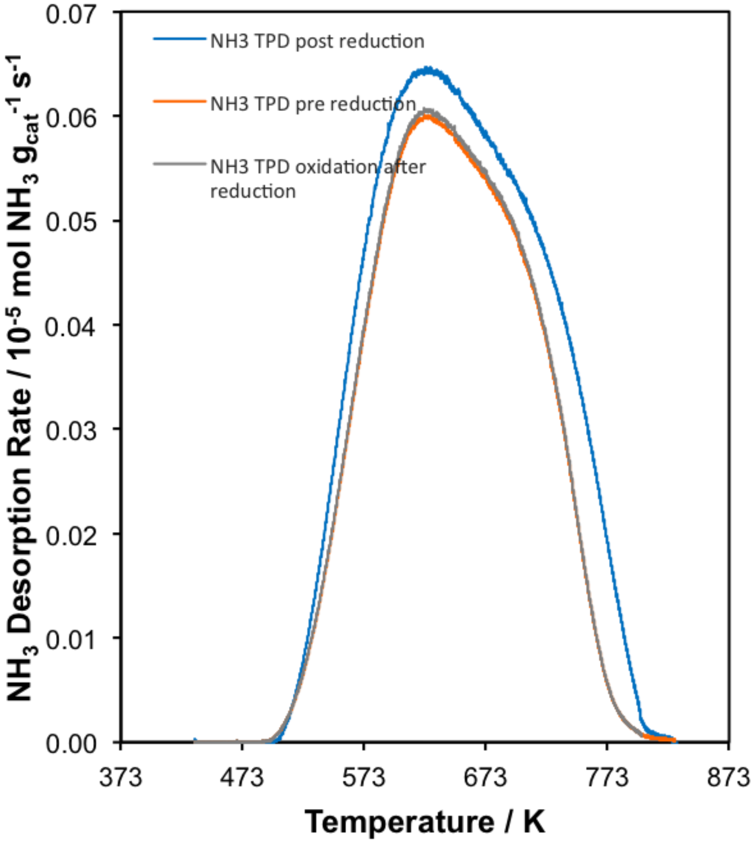

Figure A.19.1 Titration of residual Brønsted sites on a Si:Al = 5 Cu:Al = 0.21 SSZ-13 sample, before reduction in NO+NH_3, after reduction, and after reduction followed by oxidation.

A.20 Mechanism Energies

Table A.20.1 Energy for each step in the standard SCR mechanism for Z2Cu and ZCuOH.

Step	ZCu	ΔE(eV)
1	ZCuOH-NH3+2NO+2NH3+1/2O2	0
2	ZCuOH-NH3x3+2NO+1/2O2	-2.44
3	ZCuNH3x2-H2N2O+NO+1/2O2	-3.63
4	ZCuNH3x2+2H2O+N2+NO+1/2O2	-4.85
5	ZCuNO2-NH3x2+2H2O+N2	-6.32
6	ZCuOH-NH3+3H2O+2N2	-7.49
Step	Z2Cu	ΔE(eV)
1	Z2Cu-NH3x2+2NO+2NH3+1/2O2	0
2	Z2Cu-NH3x4+2NO+1/2O2	-2.64
3	Z2Cu-NH3x2/NH4/N2H2O	-3.28
4	Z2Cu-NH3x2/NH4+H2O+N2+NO+1/2O2	-5.25
5	Z2CuNO2-NH3x2/NH4+H2O+N2	-6.84
6	Z2Cu-NH3x2+3H2O+2N2	-7.49

A.21 Kinetic Data for BEA and ZSM-5

Table A.21.1 Rates, apparent orders and apparent activation energies on BEA and ZSM-5 samples (only the rate was measured on the 3.3 Cu wt.% BEA sample)

ZSM-5	Si:Al = 13					
Cu wt.%	Cu:Al	Rate per g x 10^{-8}	E_{app} (kJ mol^{-1})	NO order	NH_3 order	O_2 order
1.7	0.24	199	61±10	0.6	-0.3	0.5
1.9	0.27	232	64±10	0.7	-0.4	0.4
2.7	0.36	340	77±10	0.6	-0.5	0.4
BEA	Si:Al = 13					
Cu wt.%	Cu:Al	Rate per g x 10^{-8}	E_{app} (kJ mol^{-1})	NO order	NH_3 order	O_2 order
1.9	0.25	314	48±15	0.6	0	0.3
2.6	0.34	438	58±15	0.7	-0.1	0.3

A.22 Z_2Cu 200C vs 400C EXAFS comparison

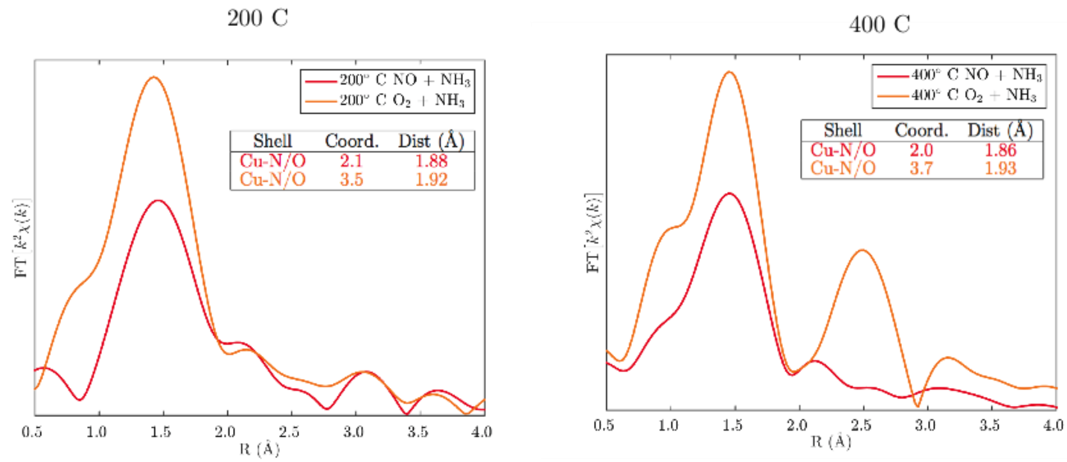

Figure A.22.1 EXAFS spectra collected after exposing Si:Al = 4.5 Cu:Al = 0.08 (2Al) to either NO+NH_3 (red) or O_2+NH_3 (orange), at (left) 200 °C and (right) 400 °C.

A.23 200 °C XANES, ZCuOH NO only

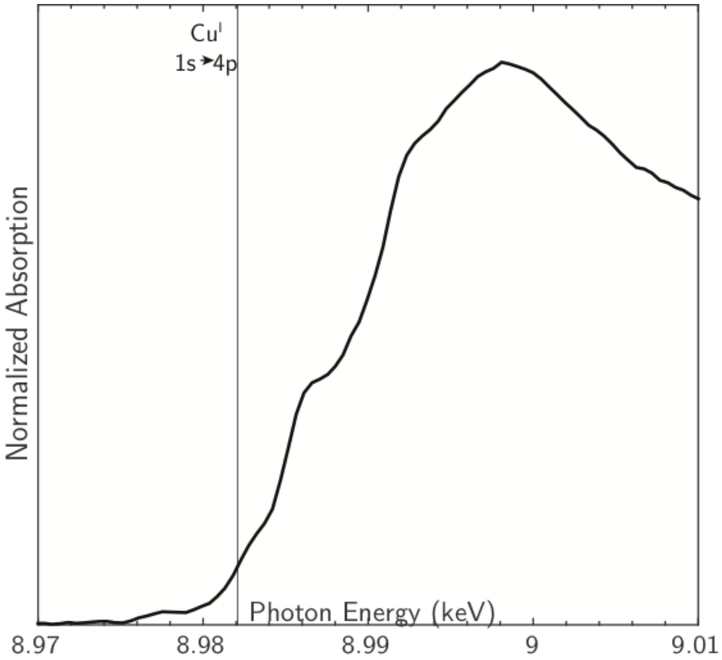

Figure A.23.1 XANES spectra collected after exposing Si:Al = 15 Cu:Al = 0.44 to 300 ppm NO, balance He at 200 °C until steady state.

A.24 Synthesis Details

CHA (SSZ-13) zeolites with a Si:Al ratio of 5 were synthesized as reported elsewhere [28, 161], which was based on a method to convert FAU to CHA using N,N,N-trimethyl-1-adamantylammonium hydroxide (TMAdaOH) developed by Zones [161, 162] and modified by Fickel et al. [109, 134, 163, 164] with molar ratios of 1 SiO_2 / 0.033 or 0.017 Al_2O_3 / 0.20 TMAdaOH / 0.17 Na_2O / 26 H_2O. A typical synthesis of SSZ-13 with Si:Al = 15 or 25 was performed by preparing an aqueous mixture of 28.4 g TMAdaOH (25 wt%, Sachem) with 77.4 g H_2O (deionized; 18.2 MΩ) in a perfluoroalkoxy alkane (PFA) plastic vessel and stirring the solution for 15 minutes under ambient conditions. 0.87 or 0.43 g (Si:Al = 15 or 25, respectively) of aluminum hydroxide (SPI Pharma) and 34.6 g of a 1M NaOH solution (Alfa Aesar) were added and the mixture was stirred for 15 minutes at ambient conditions to homogenize the contents. 10 g of fumed silica (Cab-o-Sil) were added and the mixture was stirred at ambient conditions for 2h to homogenize the mixture. The synthesis gel was loaded into four identical 45 cm^3 Teflon-lined stainless steel autoclaves (Parr Instruments) and heated under rotation at 433 K for 6 days at 60 RPM.

BEA (Beta) zeolites were synthesized with a Si:Al ratio of 13 following a modified procedure originally reported by Rubin [240]. A typical synthesis of BEA with Si:Al = 13 was prepared by dissolving 0.78 g of NaOH pellets (98%, Macron Fine Chemicals) in 92.1 g of an aqueous tetraethylammonium hydroxide (TEAOH) solution (35 wt%, Sachem) in a perfluoroalkoxy alkane (PFA) plastic vessel and stirring the solution for 15 minutes under ambient conditions. 139.0 g of colloidal silica (30 wt%, Ludox HS30, Sigma Aldrich) and 11.6 g of aluminum isopropoxide (98 wt%, Sigma Aldrich) were added to the mixture and stirred for 2h at ambient conditions to homogenize the contents. The synthesis gel was loaded into two 45 cm^3 and one 300 cm^3 Teflon-lined stainless steel autoclaves (Parr Instruments) and heated at 413 K for 8 days. BEA zeolites (Si:Al = 13, CP814E) and MFI (ZSM-5) zeolites (Si/Al = 13). After synthesis of CHA and BEA zeolites, crystalline solid products were washed by alternating deionized water and acetone (99.9 wt%, Sigma Aldrich) rinses (50 cm^3 g $solid^{-1}$) until the pH was constant between washes. Solids were recovered by centrifu- gation, dried under static air at 373 K for 24 h, and then treated in flowing dry air (100 cm^3 min^{-1} g $solids^{-1}$, 99.999% UHP, Indiana Oxygen) to 853 K (0.0167 K s^{-1}) for 10 h. All zeolite samples were converted to the NH_4-form by ion-exchange with a 1.0M aqueous NH_4NO_3 (99.9 wt.%, Sigma Aldrich) solution (100 cm^3 solution g $solids^{-1}$) for 10 h at 353 K, followed by washing the solid dix times with deionized water (50 cm^3 g $solids^{-1}$), recovery via centrifugation, and drying the solids at 373 K for 24 h. NH_4-form zeolites were converted to their H-form by treating the solids in flowing air (100cm^3 min^{-1} g $solids^{-1}$, 99.999% UHP, Indiana Oxygen) at 773K (0.0167 K s^{-1}) for 4 h.

Cu-zeolites were prepared by aqueous-phase Cu ion exchange of H-form zeolites with a $Cu(II)(NO_3)_2$ solution (0.001M-0.1M, 100 cm^3 g_{cat}^{-1}, 99.999wt.%, Sigma Aldrich) for 4 h and 300 rpm at ambient conditions, during which the pH was controlled to 4.9 ± 0.1 through dropwise addition of a 1 M NH_4OH solution (Sigma Aldrich). Co-SSZ-13 zeolites were prepared by ion exchange of H-SSZ-13 with an aqueous 0.25 M $Co(II)(NO_3)_2$ solution (150 ml g_{cat}^{-1}) for 4 h at ambient conditions, during which the pH was not controlled (pH stabilized between 3.2-3.6 after 4 h). Metal-exchanged zeolites were recovered by centrifugation and washed with deionized water six times (70 ml g_{cat}^{-1} per wash), dried at ambient temperature under flowing air, and then treated in flowing dry air (100 ml g_{cat}^{-1}) to 773 K (0.0167 K s^{-1}) for 4h. Elemental composition (Si, Al, Cu, Co) was determined using atomic absorption spectroscopy (AAS) on a Perkin-Elmer AAnalyst 300.

Commercial BEA and ZSM-5 samples with Si:Al = 13 were purchased from Zeolyst.

A.25 Micropore Volume

Zeolite samples were pelleted and sieved to obtain particles between 180-250 µm in diameter, degassed by heating 0.02-0.05 g of zeolite to 393 K (0.167 K s^{-1}) and holding under high vacuum (≈5 µm Hg) for 2 h, and then further heating to 623 K ((0.167 K s^{-1}) and holding high vacuum (≈5 µm Hg) for 8 h. Micropore volumes (cm^3 g_{solid}^{-1} at STP) were measured by extrapolating the linear volumetric gas adsorption during mesopore filling (≈0.08-0.3 P/P_0) to zero relative pressure. These estimates were in agreement with the micropore volumes derived from analyzing the semi-log derivative plot of the adsorption isotherm ($dV_{ads}/d\ln(P/P_0)$) vs. $\ln(P/P_0)$. This analysis requires determining the first maximum of ($dV_{ads}/d\ln(P/P_0)$), which corresponds to the relative pressure when micropore filling occurs, and then identifying the subsequent minimum that corresponds to the end of the micropore filling [241, 242]. The micropore volumes were determined by converting adsorbed gas volumes (STP) to liquid volumes using a density conversion factor assuming the liquid density of N_2 (77 K) or Ar (87 K) and can be found in Table A.*25.1*.

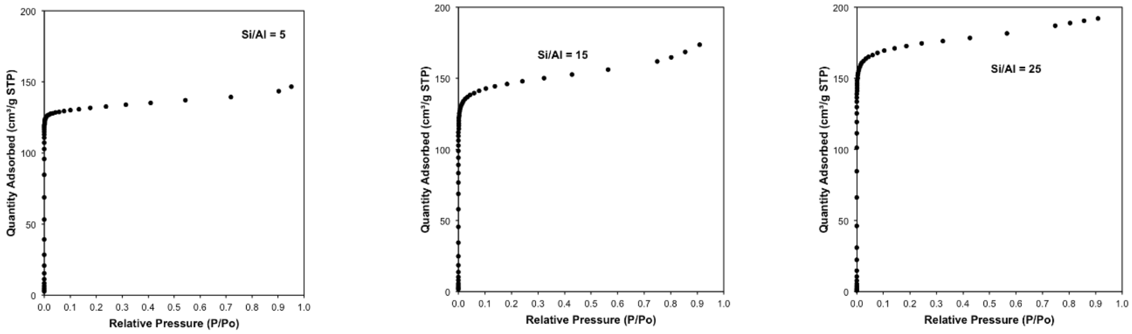

Figure A.25.1 Micropore Ar adsorption isotherms on H-SSZ-13 Si:Al = 5, 15 and 25 samples.

Table A.25.1 Micropore volumes for H-SSZ-13, H-BEA and H-ZSM-5.

Si/Al	Micropore Volume
H-SSZ-13	
5	0.16
15	0.18
25	0.2
H-BEA	
13	0.21
H-ZSM-5	
13	0.14

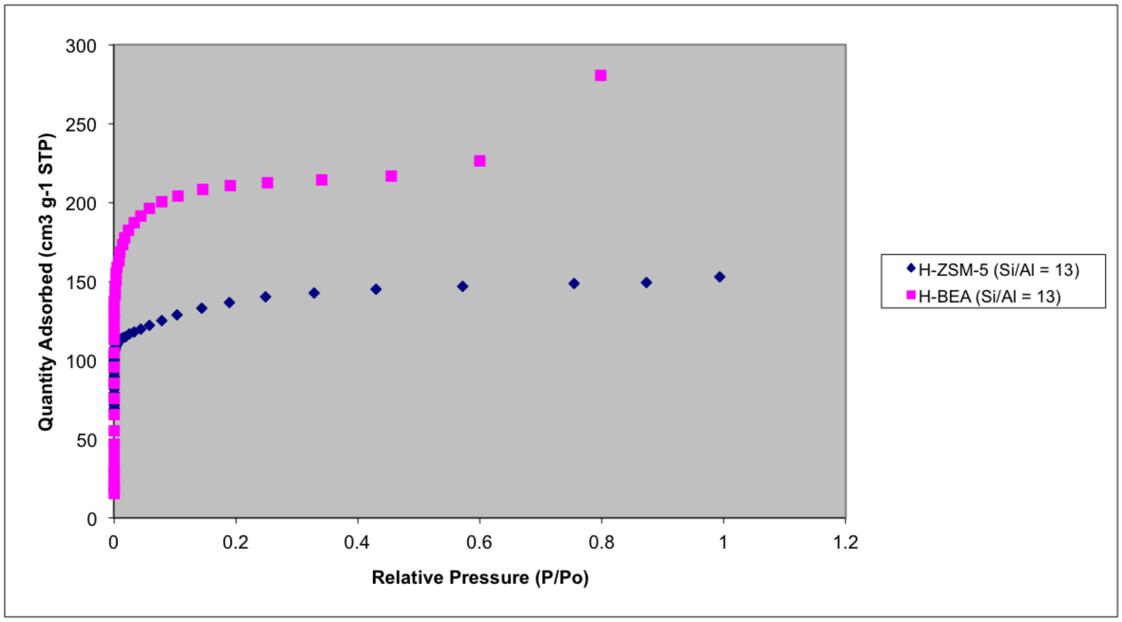

Figure A.25.2 Micropore N_2 adsorption isotherms on H-BEA and H-ZSM-5.

A.26 ^{27}Al NMR

Solid-state ^{27}Al magic angle spinning nuclear magnetic resonance (^{27}Al MAS NMR) spec- troscopy was used to estimate the fraction of framework and extraframework Al on H-form zeolites. SS NMR spectra were collected using a Chemagnetics CMX400 400 MHz spec- trometer in a wide-bore 9.4 Tesla magnet at ambient conditions from 456 scans with 12.5 μs pulses and a 2 s delay and were measured at 104.24 MHz and MAS rate of 5 kHz. Prior to packing in a 4mm ZrO_2 rotor, zeolite samples were hydrated by holding for >48 h in a desic- cator containing a saturated potassium chloride (KCl) solution. All ^{27}Al MAS NMR spectra are referenced to an aqueous 1.0M $Al(NO_3)_3$ solution. NMR spectra and quantification of extraframework Al for all H-zeolite samples can be found in Table A.*26.1*.

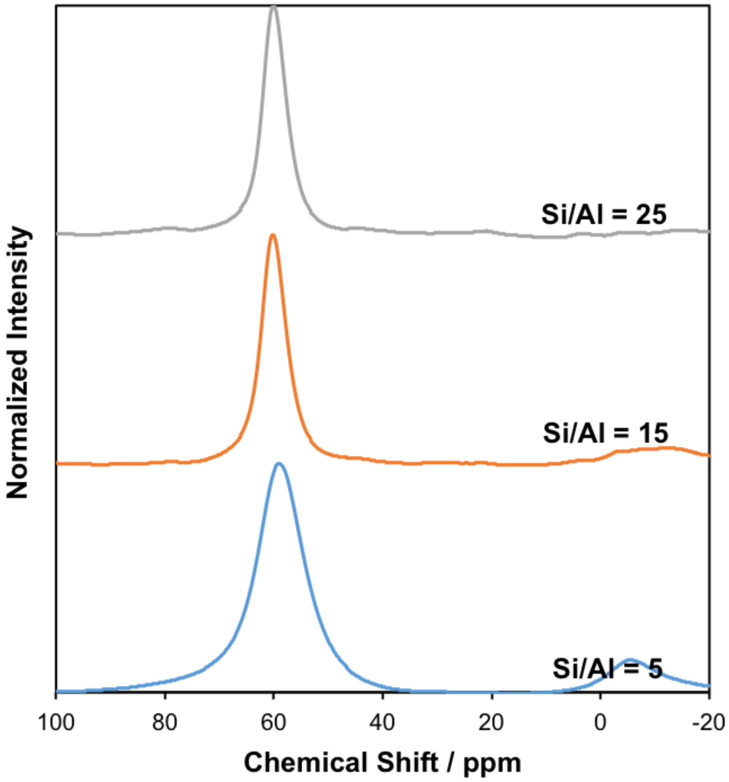

Figure A.26.1 Al ^{27}NMR spectra for SSZ-13 at Si:Al =5, 15, 25.

Table A.26.1 Fraction of extraframework Al estimated from Al ^{27}NMR.

Si/Al	5	15	25
Fractional Tetrahedral	0.85	0.95	1.00
Fractional Octahedral	0.15	0.05	0.00

A.27 NH_3 TPDs

H^+ sites on H-SSZ-13, and oxidized and reduced forms of Cu-SSZ-13 samples were measured using the NH3 titration procedure described by Di Iorio et al [135]. Oxidizing pre-treatment involved heating in synthetic air (commercial grade, Indiana Oxygen) at 773 K while the reducing pre-treatment involved flowing 500 ppm NO (from 3.6% NO/Ar, Praxair) + 500 ppm NH_3 (from 3% NH_3 in Ar, Praxair) at 473 K for 2 hr. 30-50 mg of each sample, in either its oxidized or reduced forms, was saturated with 500 ppm NH_3 diluted with UHP He (99.999% , Indiana Oxygen) at 433 K for 2 h with a total flow rate of 350 ml min^{-1}. Following this NH_3 saturation step, the sample was flushed with 2.5-3.0% water in UHP He (wet purge) for 8 h while still keeping the same total flow rate to desorb NH_3 bound to non-protonic sites [135]. Wet purge was followed by a temperature programmed desorption (TPD) in UHP He from 433 K to 820 K at a ramp rate of 0.167 K s^{-1}. NH_3 titration on the reduced form of Cu-SSZ-13 samples showed that Cu^{2+} sites balancing two Al atoms formed a Cu^+ cation and a proximal H^+ site upon reduction, while $[CuOH]^+$ sites formed a Cu^+ cation and H_2O without generating an additional H^+ sites, as proposed in the reaction scheme shown above. Thus, NH_3 titrations can be used in situ after oxidation and reduction treatments to distinguish between the Z_2Cu and $[CuOH]^+$ sites by counting the total acid sites which are equal to the sum of residual acid sites on the oxidized form of the sample and the excess acid sites generated after reduction [30].

For Co-exchanged SSZ-13 samples, the number of H^+ sites, after oxidative treatments in flowing air (773 K), were titrated in situ using a Micromeritics Autochem II 2920 Chemisorption analyzer and required the use of a lower gas flow rate than that of the H- and Cu- exchanged SSZ-13 samples. The NH_3 titration procedure involved saturating zeolite samples (30-50 mg) with 500 ppm NH_3 (500 ppm NH_3/He, Indiana Oxygen) at 433 K for 5 h and a total flow rate of 150 ml min^{-1}. Subsequently, NH_3-saturated samples were wet purged at 433 K for 8 h prior to temperature programmed desorption (TPD) experiments. TPD experiments on H-SSZ-13 and Co-exchanged SSZ-13 were performed using a Micromeritics Autochem II 2920 Chemisorption analyzer equipped with an Agilent 5975C mass selective detector (MSD) to identify the gaseous species desorbing from the catalyst samples. Catalyst samples were supported between two quartz wool plugs inside a U-shaped quartz cell held within a clam-shell furnace, held in 50 ml min^{-1} flowing UHP He at ambient temperature for 1 h, and heated to 873 K (0.167 K s^{-1}). The effluent stream from the quartz cell passed through heated transfer lines held at 383 K to the MSD for analysis. The signal at $m/z = 17$ was quantified by developing a calibration curve using four NH_4-exchanged ZSM-5 zeolites with varying Si/Al ratio [136] (Si/Al = 17-89). The total NH_3 desorbed per gram of these zeolites were determined by performing TPD experiments on a gas-phase plug flow reactor, described in the subsequent paragraph. After each TPD experiment, a 0.5 cm^3 sample loop was filled with Ar (UHP, 99.999%, Indiana Oxygen) and injected into 50 ml min^{-1} UHP He flow. The area of this Ar pulse was used as an internal standard to correct for the instrumental drift between TPD experiments. The total NH_3 desorbed per gram of catalyst was quantified from the area under the $m/z = 17$ signal, after subtracting the contribution from water at $m/z = 17$ due to fragmentation.

TPD experiments on Cu-exchanged samples were performed on a gas-phase plug flow reactor, as described by Bates et al [28]. The total moles of NH_3 desorbed during these TPD experiments were measured using on-board calibrations in a MKS Multigas 2030 gas-phase FT-IR spectrometer [136].

APPENDIX B. Supplementary Materials to Chapter 3: Copper Site Proximity Requirements for Oxidation with Dioxygen or Nitrogen Dioxide during Ammonia Selective Catalytic Reduction on Cu-SSZ-13

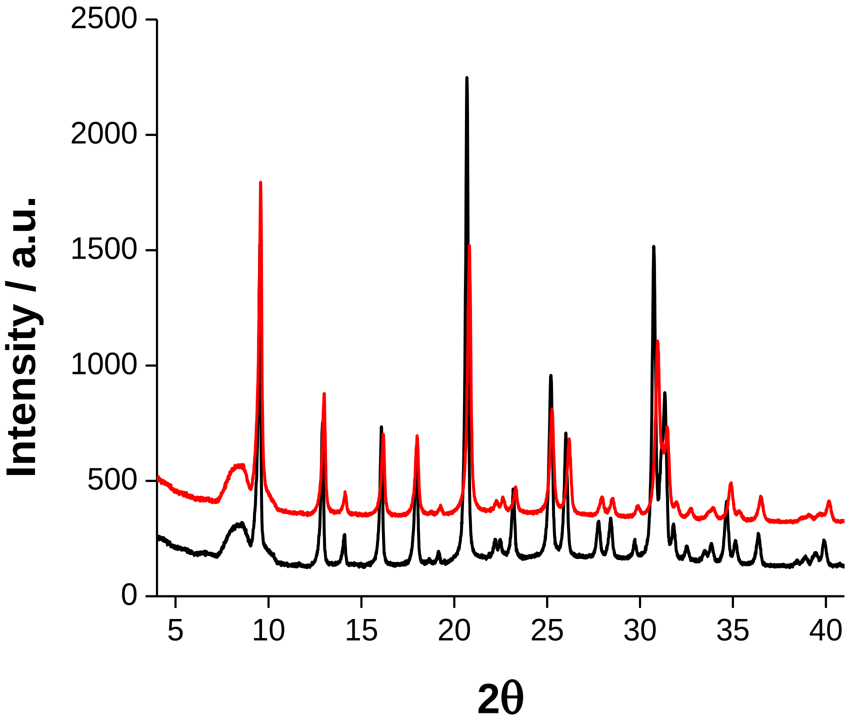

Figure B.1 X-ray diffraction (XRD) pattern for the high Al (Cu/Al = 0.08, Si/Al = 4.5) and low Al (Cu/Al = 0.09, Si/Al = 15) content samples.

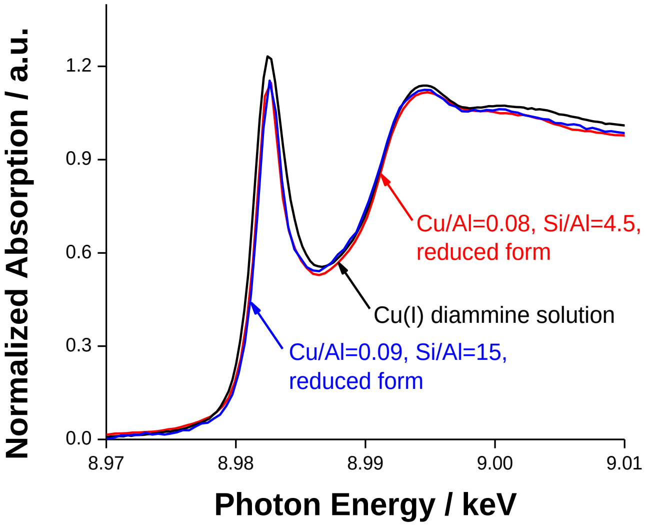

Figure B.2 Comparison of XANES spectra for diamminecopper(I) solution at room temperature with the **high Al (Cu/Al = 0.08, Si/Al = 4.5)** and **low Al (Cu/Al = 0.09, Si/Al = 15)** content samples after reduction with NO + NH_3. Feed conditions: 300 ppm NO + 300 ppm NH_3, 447 – 463 K.

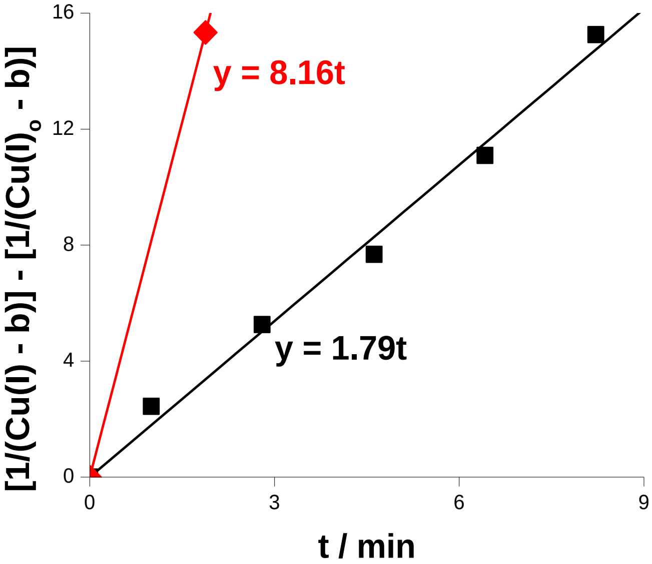

Figure B.3 A second order rate constant plot (according to equation 3.13) for the **high Al (Cu/Al = 0.08, Si/Al = 4.5, b = 0.15)** and **low Al (Cu/Al = 0.09, Si/Al = 15, b = 0.26)** content samples during oxidation with 10% O_2 at 447 K starting from Cu(I).

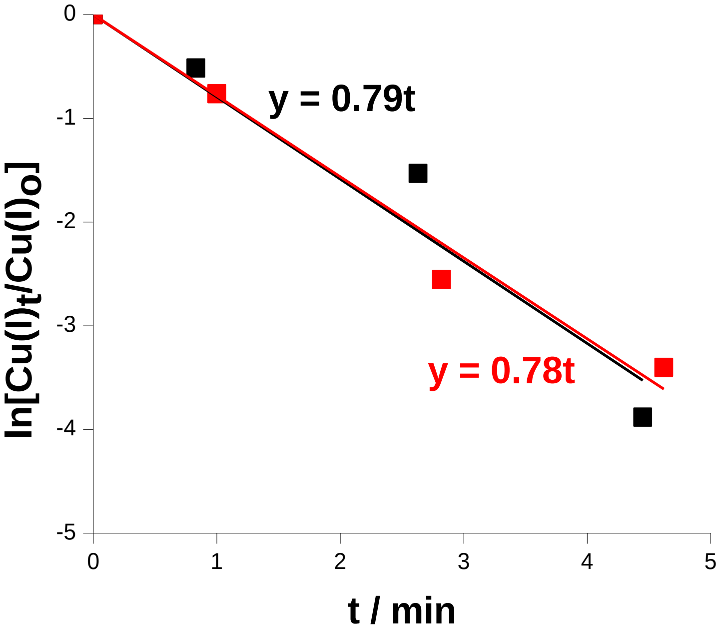

Figure B.4 A first order rate constant plot (according to equation 3.15) for the **high Al (Cu/Al=0.08, Si/Al=4.5, Cu(I)$_o$=0.9)** and **low Al (Cu/Al=0.09, Si/Al=15, Cu(I)$_o$=0.97)** content samples during oxidation with 90 ppm NO_2 at 447 K starting from Cu(I).

Determination of Sample Temperature for in situ oxidation experiments with O_2 and NO_2

Due to hardware changes at the beamline, the catalyst bed in the reactor tube was moved to the lower end of the reactor to ensure it was still in the x-ray beam path for XAS measurements. Also, the aluminum heating block used for heating the sample in the *operando* reactor setup was replaced by a heating tape instead. The section of the reactor tube that had the sample was left unwrapped and exposed so that the x-ray beam was not blocked by the heating tape or the insulation (as shown in the picture below). Consequently, there was an offset in the temperature measured by the thermocouple (not in the catalyst bed) and the actual sample temperature, which was lower due to the reactor tube being

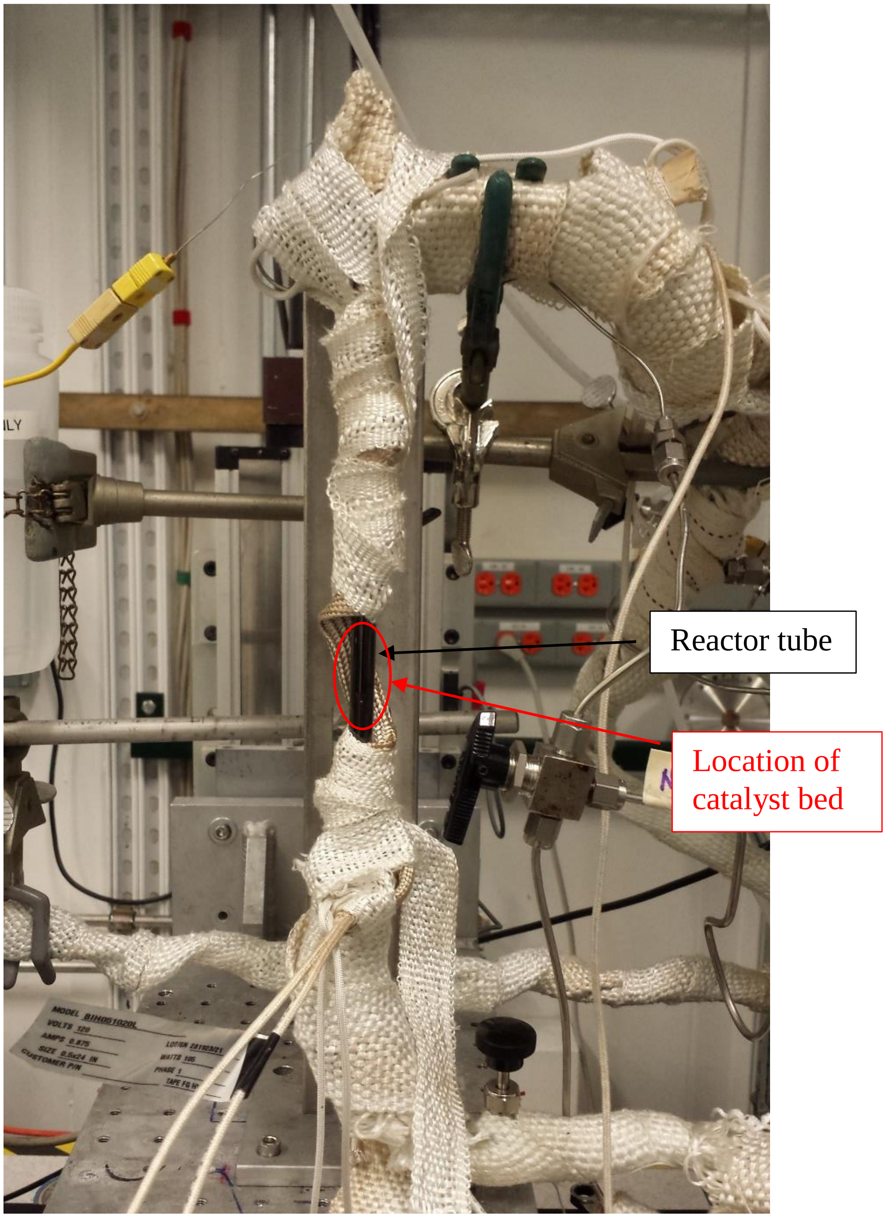

Figure B.5 Picture of the modified *operando* reactor setup in operation, with the heating tape to heat the sample to the desired temperature.

exposed to the atmosphere. The temperature controller had a setpoint of 477 K. The temperature offset was determined by measuring the reaction rate at that setpoint and using the Arrhenius plot for the same sample to match the sample temperature corresponding to the measured reaction rate. The reaction rate for the dilute Al (Cu/Al=0.09, Si/Al=15) sample was measured as 7.9 x 10^{-8} mol NO (g cat)$^{-1}$ s^{-1}, instead of the expected value of 18 x 10^{-8} mol NO (g cat)$^{-1}$ s^{-1} from Table 3.4.2. With an E_{app} of 50 kJ mol^{-1} (Table 3.4.2), the actual catalyst temperature would be 447 K.

APPENDIX C. Supplementary Materials to Chapter 4: Determining the Active Intermediates for NO Oxidation on Cu-ZSM-5 from ^{15}NO Labeling Experiments

C.1 Gas Phase NO Oxidation Reaction

The extents of gas phase NO oxidation in the 200 ml measurement cell of the 2030 Multigas FTIR analyzer at the chosen NO and O_2 concentrations and a total flow of 50 ml min^{-1} were calculated from the kinetic parameters obtained reported by Tsukahara et al. [243] shown in

Table *C.1* below. 10% O_2 and 345 ppm NO produced 35 – 36 ppm NO_2, whereas 5% O_2 and 125 ppm NO or 150 ppm NO produced 2 – 3 ppm NO_2 from the gas phase NO oxidation reaction. To maximize the amount of surface intermediates while simultaneously minimizing the gas phase reaction, 150 ppm NO and 5% O_2 were chosen as the standard concentrations for the *operando* FTIR measurements. Furthermore, the value of β, which is the dimensionless equilibrium constant for the NO oxidation reaction [41] used to ensure that the reaction is not close to equilibrium and that the rates were measured in a kinetically controlled regime, is less than 0.1 in all cases at the conditions of operation chosen for the *operando* reactor.

Table C.1 Observed and calculated extents of NO oxidation inside the 200 ml measurement cell of the MKS 2030 Multigas FTIR analyzer at the appropriate concentrations.

O_2 / %	NO / ppm	Observed gas phase NO oxidation / ppm	Calculated gas phase NO oxidation / ppm
5	125	2	2.4
5	150	3	3.4
5	200	7	6
10	345	35	36

C.2 Test for External Mass Transfer Limitations

The presence of external mass transfer limitations were tested in two separate sets of experiments. Using a CSTR formulation gives:

$$(C_o\text{-}C)*v = r*w\ldots\ldots C.1$$

where C_o is the reactor inlet concentration, C is the reactor outlet concentration, v is the total volumetric flow rate, r is the reaction rate on the catalyst and w is the weight of the catalyst sample loaded. Since $C = C_o*(1 – X)$, where X is the measured conversion

$$C_o*X*v = r*w\ldots\ldots C.2$$

Equation C.2 shows that the conversion, X, is directly proportional to the weight of the catalyst, w, loaded in the reactor or inversely proportional to the total flow rate, v. Consequently, two separate tests by varying the amount of sample loaded (Cu/Al = 0.41, Si/Al = 18, Cu-ZSM-5) and changing the total flow rate were used to identify if external mass transfer limitations were present under the conditions being tested.

First the amount of catalyst sample loaded in the reactor was varied by diluting the sample pellet loaded in the *operando* reactor with inert SiO_2 (Fisher Scientific). Pure sample, 1:1 and 1:3 ratios of sample:SiO_2 on weight basis were used for this test. A plot of the corrected conversion by normalizing to 300 ppm NO, 150 ppm NO_2, 10% O_2 versus the weight of the catalyst loaded showed a linear correlation (Figure C.2.1a). Secondly, four different total flow rates of 27 ml min^{-1}, 45 ml min^{-1}, 92 ml min^{-1} and 136 ml min^{-1} were used keeping the same NO, NO_2 and O_2 concentrations. A plot of the corrected conversion versus the inverse of the total flow rate once again showed a linear correlation (Figure C.2.1b).

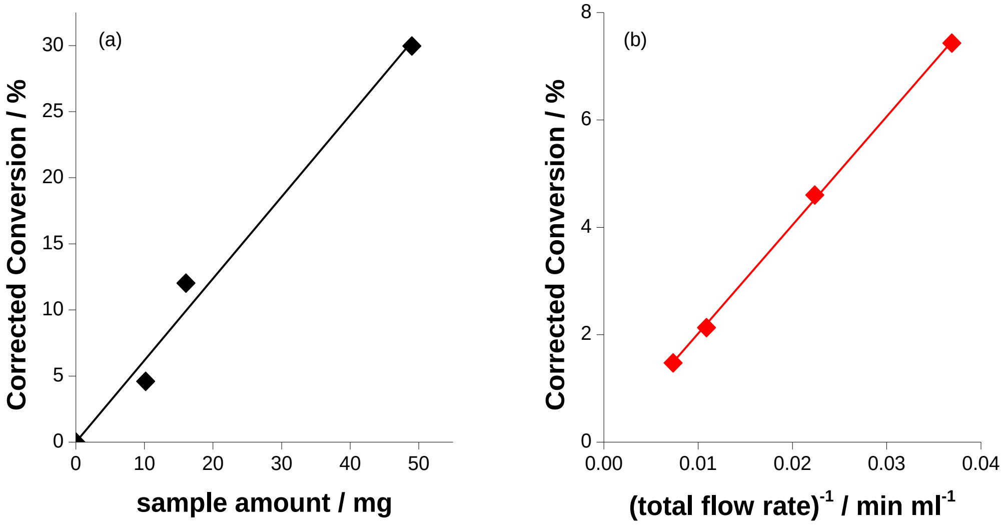

Figure C.2.1 Plots of corrected conversion versus (a) amount of sample loaded (black diamonds) in the *operando* reactor (b) inverse of the total flow rate (red diamonds) through the *operando* reactor. Sample: Cu/Al = 0.41, Si/Al = 18, Cu-ZSM-5.

C.3 NO Adsorption Capacity of the Catalyst

Since the ^{15}NO trace coincided with the $^{15}NO_2$ trace in each of the $^{14}NO \rightarrow {}^{15}NO$ switching experiments performed in this study, it was of interest to identify the storage capacity of the bare catalyst surface for NO only. Since the ^{15}NO trace coincided with the inert Ne trace (Figure C.3.1), it showed that the surface did not have any capacity for NO storage by itself at 573 K, similar to the results reported by others [6, 244]. This meant that the lag in the ^{15}NO trace compared to the Ne tracer during NO oxidation occurred because of its involvement in the surface reaction with $^{15}NO_2$ via nitrates as suggested by equation 4.2. The initial spikes in the mass spectrometer traces are observed due to adjustment of ^{15}NO concentration after its flow was started.

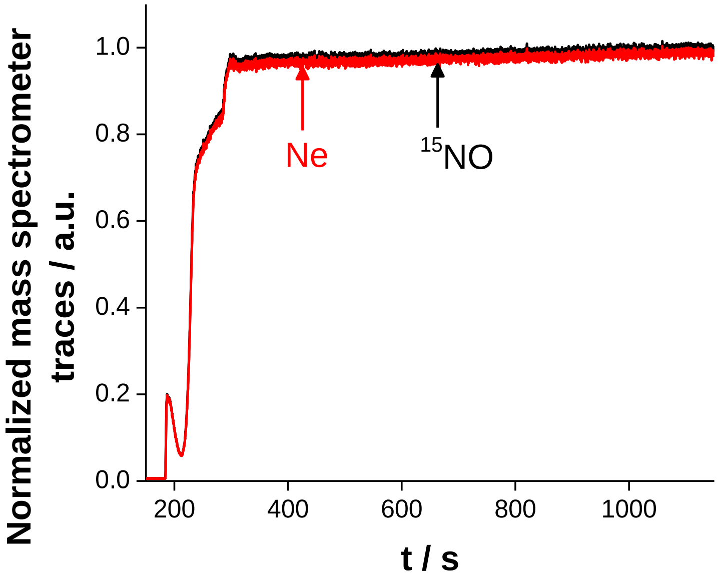

Figure C.3.1 Probing the NO storage capacity of the catalyst by flowing ^{15}NO only on the clean, calcined catalyst sample. Mass spectrometer traces for $^{15}NO_2$ (m/z = 47) and Ne (m/z = 20) are coincident with each other. Feed conditions: 300 ppm ^{15}NO, 573 K. Sample: Cu/Al = 0.33, Si/Al = 18, Cu-ZSM-5.

C.4 ^{14}NO → ^{15}NO Isotope Switch at Different Temperatures

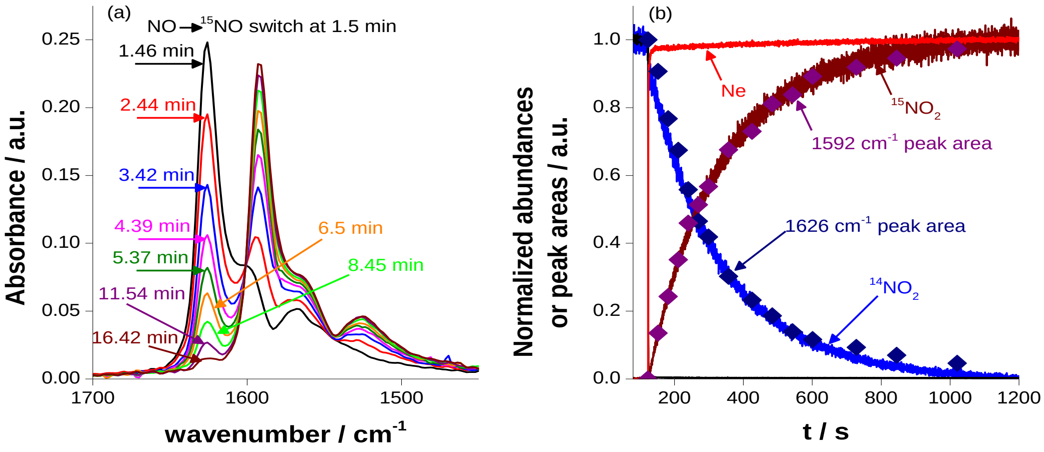

Figure C.4.1 (a) FTIR spectra after the ^{14}NO → ^{15}NO isotope switch show an immediate decrease in the 1626 cm^{-1} peak along with a concomitant increase in the 1592 cm^{-1} peak (b) Mass spectrometer traces for $^{15}NO_2$ (m/z = 47) and $^{14}NO_2$ (m/z = 46) are coincident with the areas for the 1592 cm^{-1} and 1626 cm^{-1} peaks, respectively. The corresponding Ar (m/z = 40) and Ne (m/z = 20) traces are also shown. Sample: Cu/Al = 0.3, Si/Al = 18, Cu-ZSM-5. Feed conditions: 150 ppm NO/^{15}NO, 5% O_2, 543 K.

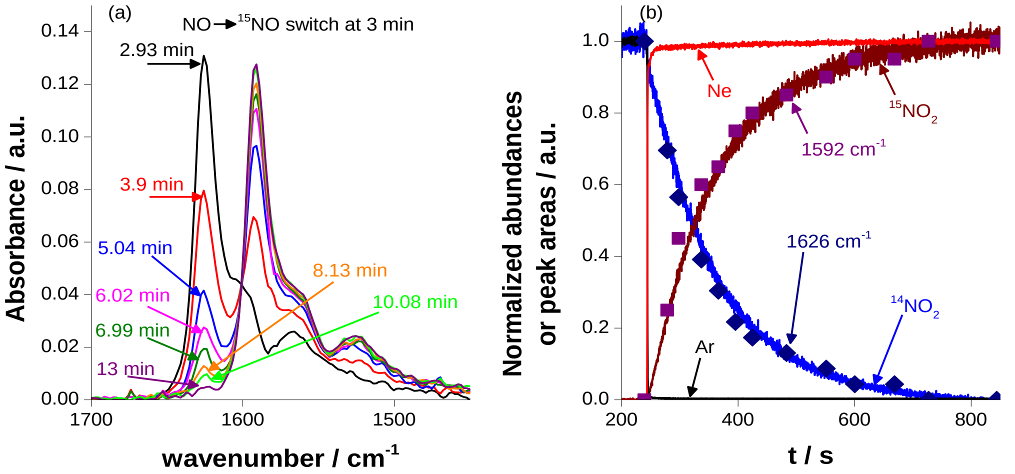

Figure C.4.2 (a) FTIR spectra after the ^{14}NO → ^{15}NO isotope switch show an immediate decrease in the 1626 cm^{-1} peak along with a concomitant increase in the 1592 cm^{-1} peak (b) Mass spectrometer traces for $^{15}NO_2$ (m/z = 47) and $^{14}NO_2$ (m/z = 46) are coincident with the areas for the 1592 cm^{-1} and 1626 cm^{-1} peaks, respectively. The corresponding Ar (m/z = 40) and Ne (m/z = 20) traces are also shown. Sample: Cu/Al = 0.3, Si/Al = 18, Cu-ZSM-5. Feed conditions: 150 ppm NO/^{15}NO, 5% O_2, 573 K.

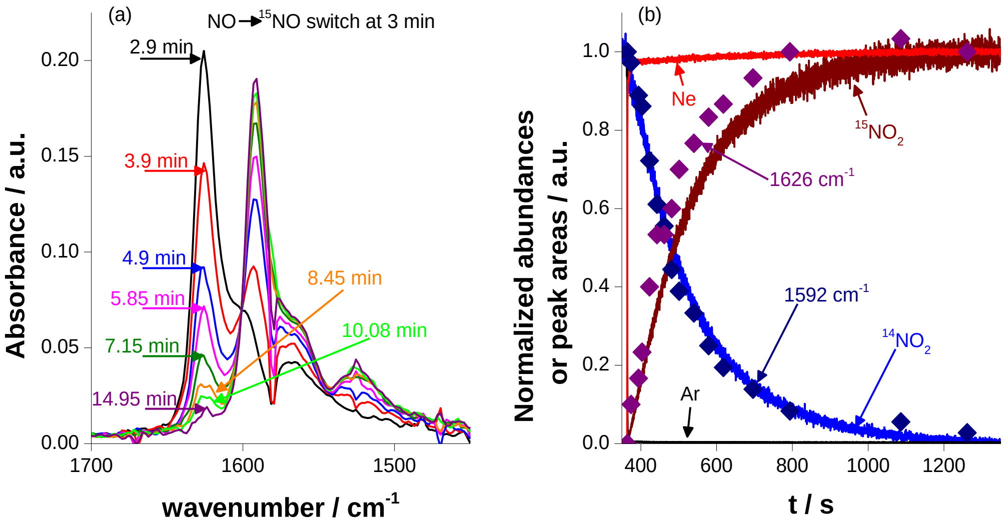

Figure C.4.3 (a) FTIR spectra after the $^{14}NO \rightarrow {}^{15}NO$ isotope switch show an immediate decrease in the 1626 cm^{-1} peak along with a concomitant increase in the 1592 cm^{-1} peak (b) Mass spectrometer traces for $^{15}NO_2$ (m/z = 47) and $^{14}NO_2$ (m/z = 46) are coincident with the areas for the 1592 cm^{-1} and 1626 cm^{-1} peaks, respectively. The corresponding Ar (m/z = 40) and Ne (m/z = 20) traces are also shown. Sample: Cu/Al = 0.3, Si/Al = 18, Cu-ZSM-5. Feed conditions: 150 ppm NO/^{15}NO, 5% O_2, 563 K.

C.5 Kinetic Model for NO Oxidation

The model proposed by Verma et al. [41] has been modified to account for the participation of nitrates in the NO oxidation reaction as well as to account for the NO – NO_2 equilibrium via nitrates. The new kinetic model, consistent with their observations as well as the current study, is as follows:

$$* + O_2 \overset{K_1}{\leftrightarrow} O_2^* \ldots\ldots C.3$$

$$O_2^* + NO \overset{k_2}{\rightarrow} NO_2 + O^* \ldots\ldots C.4$$

$$NO_2 + O^* \overset{K_3}{\leftrightarrow} NO_3^* \ldots\ldots C.5$$

$$NO_3^* + NO \overset{K_4}{\leftrightarrow} NO_2^* + NO_2 \ldots\ldots C.6$$

$$NO_2^* \overset{K_5}{\leftrightarrow} NO_2 + * \ldots\ldots C.7$$

$$\text{Overall NO Oxidation Reaction: } 2NO + O_2 \rightarrow 2NO_2 \ldots\ldots C.8$$

where * = a Cu-Cu pair without adsorbed oxygen i.e reduced Cu-Cu site. Assuming that equation C.4 is the rate determining step [41] while all other steps are in equilibrium, the rate for the NO oxidation reaction is:

$$r = k_2[NO][O_2*] \ldots\ldots C.9$$

Using equilibrium for steps C.3 and C.5 – C.7, the individual surface species can be expressed as a function of the gas phase NO, NO_2 and O_2 concentrations as follows

$$[O_2*] = K_1[O_2][*] \ldots\ldots C.10$$

$$[NO_2*] = \frac{[NO_2][*]}{K_5} \ldots\ldots C.11$$

$$[NO_3*] = \frac{[NO_2]^2[*]}{K_5K_4[NO]} \ldots\ldots C.12$$

$$[O*] = \frac{[NO_2][*]}{K_3K_4K_5[NO]} \ldots\ldots C.13$$

Equation C.6 accounts for the fast equilibrium between gas phase NO and NO_2 via nitrates. The total site balance, taking [L] as the total number of available Cu-Cu pairs for NO oxidation

$$[L] = [*] + [O*] + [O_2*] + [NO_2*] + [NO_3*] \ldots\ldots C.14$$

$$[*] = \frac{[L]}{1 + K_1[O_2] + \frac{[NO_2]}{K_5} + \frac{[NO_2]^2}{K_4K_5[NO]} + \frac{[NO_2]}{K_3K_4K_5[NO]}} \ldots\ldots C.15$$

$$r = \frac{k_2K_1[O_2][NO]^2[L]}{[NO] + K_1[O_2][NO] + \frac{[NO_2][NO]}{K_5} + \frac{[NO_2]^2}{K_4K_5} + \frac{[NO_2]}{K_3K_4K_5}} \ldots\ldots C.16$$

Thus,

$$n_{O_2} = 1 - \theta_{O_2*} \ldots\ldots C.17$$

$$n_{NO_2} = -\theta_{NO_2*} - 2\theta_{NO_3*} - \theta_{O*} \ldots\ldots C.18$$

$$n_{NO} = 2 - \theta_{*} - \theta_{O_2*} - \theta_{NO_2*} \ldots\ldots C.19$$

where θ_i is the coverage of the i^{th} species on the catalyst surface.

Using the experimentally measured reaction orders of 0.9 for O_2, -0.8 for NO_2 and 1.7 for NO the following surface coverages for each of the intermediates is obtained

$$\theta_{O_2*} = 0.1,\ \theta_{O*} = 0.5,\ \theta_{NO_3*} = 0.1,\ \theta_{NO_2*} = 0.1,\ \theta_{*} = 0.1$$

APPENDIX D. Copyright and Legal Matters

All the legal matters with permission to reproduce figures and texts from the published papers are covered in this appendix.

D.1 Chapter 2

VITA

VITA

Atish A. Parekh was born in Mumbai, India on August 21st, 1987 to parents Anil J. Parekh and Varsha A. Parekh. He attended school from grades 1 to 10 at Dr. Antonio da Silva High School in Dadar between years 1993 and 2003, following which he was admitted to Ruia College in Matunga for junior college (grades 11 and 12) between 2003 and 2005. During this time he also prepared for the Joint Entrance Examination (JEE) and secured admission to Indian Institute of Technology Bombay (IITB) in 2006. He pursued bachelor of technology (B. Tech.) in Chemical Engineering from 2006 to 2010. While at IITB, he explored his interests in music, and discovered his liking for the keyboard. He did summer internships at Hindustan Unilever Limited, Bangalore (Project Supervisor: Dr. Gurmeet Singh) and the University of Delaware, Newark (Project Supervisor: Dr. Christopher J. Roberts) to gain research experience, and an insight into whether research would be the appropriate path forward. Based on his experience at both internships he decided to pursue a Ph.D. in Chemical Engineering at Purdue University, West Lafayette under the guidance of Prof. Fabio H. Ribeiro and Prof. W. Nicholas Delgass starting August 2010 on NO_x abatement from engine exhaust of heavy-duty diesel automobiles. Along the way, he defended his thesis, and obtained a master of science (M.S.) in Chemical Engineering in August 2013. He continued further on the same project for his Ph.D. and successfully completed his thesis defense in April 2016. He got the opportunity to present his research in the form of posters and talks at various conferences such as the Chicago Catalysis Club's (CCC) spring symposium, Michigan Catalysis Society's (MCS) spring symposium, North American Meeting (NAM) and the annual meeting of the American Institute of Chemical Engineers (AIChE). He was selected as the recipient for various awards such as the Goddard Fellowship by the School of Chemical Engineering at Purdue University (Fall 2010), Richard J. Kokes award (2015), AIChE's Chemical and Reaction Engineering (CRE) division travel award (2015), outstanding oral presentation at the MCS spring symposium (2014), Eastman travel grant (2015), Purdue Gradute Student Government (PGSG) travel grant (2014), and 3rd place oral (2015) and poster (2014) presentations for the annual ChE GSO symposium. During his stay at Purdue, he was involved with several extra-curricular activities on campus that greatly enhanced his experience as a graduate student. He was the social chair for the Chemical Engineering Graduate Student Organization (ChE GSO) during August 2012 to May 2013, played the keyboard as part of the Indian Classical Music Association of Purdue (ICMAP) between August 2012 and February 2013, was a vocalist for the Indo-American a cappella group Purdue Taal from January 2013 to December 2014, formed and performed as part of the band Vertigo42 for several cultural shows on campus from September 2013 to November 2015 and volunteered for Boiler Blast during the years 2012, 2014 and ASHA for Education between August 2012 and December 2012. He was part of the Purdue Taal team that recorded a professional music album in spring 2015, due to be released in 2016. After his Ph.D. he plans to pursue an internship with Evonik Corporation at Calvert City, KY in summer 2016 following which he will head back to India to work with Shell Projects and Technology in Bangalore as a full-time employee.